國 立 交 通 大 學

應 用 化 學 研 究 所

博 士 論 文

以蒽為主體之非晶態材料雙極性載子傳輸特性與摻雜電性
研究及其在有機電激發光元件之應用

Study of Bipolar Charge Transport and Electrical Doping
Characteristics of Amorphous Anthracene-based Materials and Their
Applications in Organic Electroluminescence Devices

研 究 生：何孟寰
指導教授：陳金鑫 博士
　　　　　陳登銘 博士

中 華 民 國 九 十 九 年 八 月

以蒽為主體之非晶態材料雙極性載子傳輸特性與摻雜電性研究及
其在有機電激發光元件之應用

Study of Bipolar Charge Transport and Electrical Doping
Characteristics of Amorphous Anthracene-based Materials and Their
Applications in Organic Electroluminescence Devices

研 究 生：何孟寰　　　　　　　　Student：Meng-Huan Ho

指導教授：陳金鑫 博士　　　　　　Advisor：Dr. Chin H. Chen

　　　　　陳登銘 博士　　　　　　　　　　Dr. Teng-Ming Chen

國 立 交 通 大 學
應 用 化 學 研 究 所
博 士 論 文

A Thesis

Submitted to Institute of Applied Chemistry

College of Science

National Chiao Tung University

in Partial Fulfillment of the Requirements

for the Degree of

Doctor of Philosophy

in

Applied Chemistry

August 2010

Hsinchu, Taiwan, Republic of China

中華民國九十九年八月

以蒽為主體之非晶態材料雙極性載子傳輸特性與摻雜電性研究及其在有機電激發光元件之應用

研究生：何孟寰　　　　　　　　　　指導教授：陳金鑫 博士

　　　　　　　　　　　　　　　　　　　　　　陳登銘 博士

國立交通大學應用化學研究所

摘　　要

　　將 p 型與 n 型有機摻雜層引入由 2-methyl-9,10-*di*(2-naphthyl)anthracene (MADN) 天藍光系統與黃光材料 rubrene 所組成的雙波段白光有機電激發光元件結構中，並有效控制載子再結合區域於薄層發光層中，在亮度 1000 cd/m^2 下可得到高發光效率 10 cd/A 和 9.3 lm/W。利用有機摻雜層的 *p-n* 接面作為連接層，也可以製作出高亮度的串聯式雙波段白光有機電激發光元件。

　　但雙波段白光元件的色域與演色性無法達到全彩顯示器與固態照明應用的需求。於是我們開發出以 2-methyl-9,10-*di*(1-naphthyl)anthracene (α,α-MADN) 為主發光體材料的高效率且穩定的深藍色發光系統並應用於

三波段白光有機電激發光元件中，可得到高發光效率 8 cd/A 和寬廣的發光頻譜，CIE 色度座標為(0.34, 0.35)，色域及演色性也提升到 73.2 %和 87。

我們也利用飛行時間量測法來量測一系列以蒽(anthracene)為主體的材料的載子傳輸特性，量測結果顯示這些材料具有極快的電洞載子遷移率，其數值介於 2×10^{-3} to 9×10^{-3} cm^2/Vs 之間。同時也發現能將 C60 應用於飛行時間技術中作為電荷生成層，可大幅減少樣品中待測材料的厚度。

另一方面， 根據導納量測理論與有機材料高阻抗的特性，我們提出了雙異質介面有機元件的導納等效電路模型，並用以研究 MADN 的 p 型與 n 型薄膜摻雜層電性。 其結果顯示將氧化鎢(WO$_3$)與氟化銫(CsF)摻雜於 MADN 中，可降低載子的注入能障以及元件的操作電壓。

最後，根據飛行時間量測法與導納分析的結果，我們設計出第一個以 MADN 為單一主體材料的高效率且穩定的有機電激發光元件。

Study of Bipolar Charge Transport and Electrical Doping Characteristics of Amorphous Anthracene-based Materials and Their Applications in Organic Electroluminescence Devices

Student：Meng Huan Ho

Advisor：Dr. Chin H. Chen

Dr. Teng-Ming Chen

Department of Applied Chemistry

National Chiao Tung University

ABSTRACT

We demonstrated highly power-efficient *di*-chromatic white organic light-emitting diode (WOLED) devices composed of a sky blue doped emitter of 2-methyl-9,10-*di*(2-naphthyl) anthracene (MADN) and a yellow emitter of rubrene. By introducing *p*-doped and *n*-doped organic layers into the device architecture along with carefully controlling the carrier recombination zone in a thin layer thickness, the high efficiency of 10 cd/A and 9.3 lm/W at 1000 cd/m^2 can be achieved. A high-brightness tandem *di*-chromatic WOLED device with a connecting layer of organic *p-n* junction was also fabricated.

But the color gamut and color rendering index (CRI) of *di*-chromatic WOLEDs are not adequate for full-color display and solid state lighting

applications. Hence we developed an efficient and stable deep blue fluorescent system based on a host material of 2-methyl-9,10-*di*(1-naphthyl) anthracene (α,α-MADN) and adopted it to *tri*-chromatic WOLED devices. The color gamut and CRI of *tri*-chromatic WOLED device can be improved to 73.2% and 87, respectively, with high efficiency of 8.0 cd/A and a white $CIE_{x,y}$ coordinates of (0.34, 0.35).

The hole mobilities of ADN-type material were also measured by time-of-flight technique, and it is found that ADN-type materials have high hole mobilities in the ranges of 2×10^{-3} to 9×10^{-3} cm^2/Vs. C60 was also shown to be a useful charge generation layer and effectively reduces the layer thickness of test material for TOF measurements of hole mobilities of ADN-type materials.

We further investigated the electrical characteristics of MADN-based *p*-doped and *n*-doped organic layers by measuring current-voltage curves and temperature-dependent admittance spectroscopy. It was found that the conductive-doping can reduce the injection barrier and drive voltage when they are adopted in OLED devices.

Finally, according to all results disclosed in this thesis, an efficient and stable OLED device with simplified architecture based on a single common host of MADN was demonstrated for the first time with excellent performance.

Acknowledgements

最後最感謝我的家人讓我無後顧之憂，可以專心地學習，也謝謝你們的陪伴，有你們在背後支持，是激勵我前進的原動力，我會更加的努力，謹以此論文獻給我最愛的你們。

In addition, I was really lucky to be a visiting student in University of Rochester, NY, USA, under the supervision of Prof. Ching W. Tang for one year, who is the inventor of OLED technology. I appreciate Prof. Ching W. Tang for his insightful advice on both an academic and personal level. Prof. Tang's example of diligence, persistence, and insight has inspired me, and his guidance has also enabled me to understand the attitude for pursuing the truth. I would also like to thank Dr. David Weiss, Dr. Jason U. Wallace, Matthew J. Smith, Thomas Yung-Hsin Lee for their help of TOF experiments and discussions. I also would like to extend my thanks to my fellow graduate students who were always helpful in life and experiments. This includes Wei Xia, Sunny Hsiang-Ning Wu, Hao Lin, Hui Wang, Min-Lu Zhang, Sang-Min Lee, Lichang Zhen, Jonathan Welt, Eric Glowacki, and Mark Hsu.

Table of Contents

Chapter 3 Development of *Di*-Chromatic White Organic Light-Emitting

Diodes…………………………………………………..…..…42

Chapter 4 Development of Fluorescence Deep Blue System and *Tri-Chromatic White Organic Light-Emitting Diodes………………...67

Chapter 5 Carrier Transport Properties of Anthracne-Based Materials...100

List of Figures

List of Tables

Chapter 1

Introduction of Organic Light-Emitting Diodes

1.1   General overview of organic light-emitting diodes

The electroluminescence (EL) phenomenon was first discovered in a piece of carborundum (SiC) crystal by H. J. Round in 1907 [1]. Commercial research into light-emitting diodes (LEDs) technology started in early 1962, when Nick Holonyak Jr. created the first inorganic LED [2,3]. In 1950s, Bernanose first observed EL in organic materials by applying a high-voltage alternating current (AC) field to crystalline thin films of arcidine orange and quinacrine [4,5].

The direct current (DC) driven EL cell using single crystals of anthracene was first demonstrated by Pope and his co-workers following the discovery of LEDs made with III-V compound semiconductors [6]. Although the quantum efficiency of this device could reach 8%, the high drive voltage limited its practical application. In 1975, the first organic EL devices made with a polymer poly(*N*-vinyl carbazole) (PVK) were demonstrated [7]. In 1982, Vincett et al. [8] demonstrated the light-emitting devices fabricated by thermal evaporation of polycrystalline anthracene. The required voltage to generate light was significantly reduced due to the much thinner organic layer. However, in this device, carrier recombination zone was too close to one of the electrodes which limited its quantum efficiency to less than 0.1%.

In 1987, Tang and Van Slyke at Kodak introduced a double layered organic light-emitting device (OLED), which combined modern thin film deposition techniques with suitable materials and device structure to produce EL with moderately low bias voltages and significantly better luminance efficiency

[9,10]. Their research eventually led to the discovery of the first efficient multi-layered organic EL device based on the concept of the heterojunction architecture [10,11] which was followed by the discovery of the doped emitter using the highly fluorescent organic dyes for color tuning, efficiency and stability enhancement [12,13]. Shortly afterwards, in 1990 the Cambridge group led by Friend announced a conducting polymer-based PLED [14,15]. The polymeric thin films are fabricated by convenient wet-coating technology and permit deposition on various substrates [16,17,18,19,20].

Although the flat panel display (FPD) industry is currently dominated by liquid crystal technology (LCDs), there have been increasing interests and research activities in OLEDs, and enormous progress has been made in the improvements of color gamut, luminance as well as power efficiency and device reliability. OLED devices offer many advantages over LCDs for FPD applications:

- Thin solid-state device (less than 300 nm thick)
- Light weight
- High luminous power efficiency
- Fast response time
- Wide viewing angle
- Self-emitting
- High contrast, color tuning throughout the entire visible spectrum for full-color displays
- Mechanical flexibility for rollable display

The development of OLED technology provides a great story on how scientific concepts and discoveries can be transformed into practical

technologies and eventually impact human life in different ways. With less than 25 years, the field of OLEDs has come through concept demonstration, single device performance improvement, industrial improvement in matrix formation, color pixel formation, display architecture, and system integration. Products in both passive-matrix OLEDs (PMOLEDs) and active-matrix OLEDS (AMOLEDs) have been in commercial markets for several years, and the OLED display market is expected to be enormous in the future.

1.2 Full-color techniques for OLED Display

Since Pioneer Corporation demonstrated the first passive matrix OLED display as a character broadcasting display for car stereo in 1997, growing interest is largely motivated by the promise of the use of OLED technology in next generation FPDs. As a consequence, various OLED displays like portable smart phones, digital cameras, photo frames, small to medium size TVs have been demonstrated and some of which have already been introduced in the marketplace by Samsung, LG, Sony, AUO, CMEL and Lumiotec. In this section, some of the methods to fabricate full-color OLEDs are discussed.

1.2.1 RGB side-by-side pixelation

One common method for full-color OLED display is the separate deposition of RGB pixels [21] as shown in Figure 1-1. The basic principle is the RGB subpixels are separately patterned by means of precision shadow mask and high-accuracy mask. This method can take the full advantage of saturate emission color and luminous efficiency of organic RGB emitters. The disadvantage is the degradation situation of RGB pixels is different, therefore, color shift of display would be an issue after long-term driving. Furthermore, for pursuing of high-resolution display, it is important to make the size of each

subpixel and the distance between each of them as small as possible. Therefore, the accuracy requirements for the mask alignment and RGB subpixel pattern will restrict the yield of mass production.
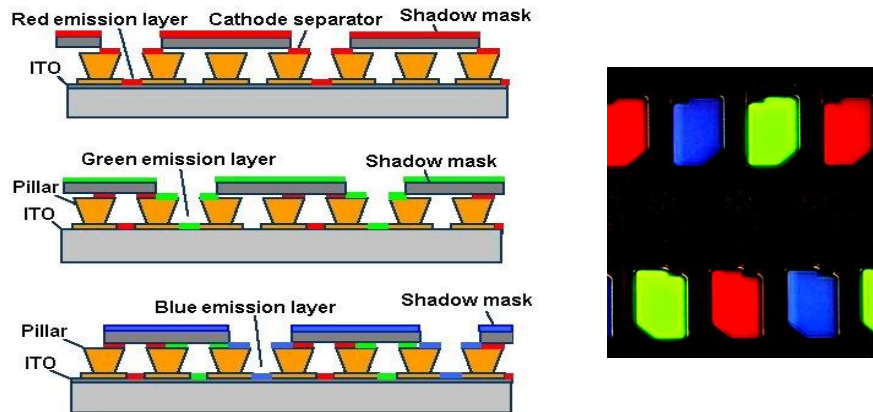
Figure 1-1 Scheme of RGB side by side pixelation.

1.2.2   WOLED backlight with color filter

One of the approaches is to use a white OLED (WOLED) cell as a backlight (see Figure 1-2). Color filters on the glass substrate, such as those used for LCDs, could be employed to filter the RGB subpixels from the white backlight. Several techniques to make white OLEDs have been proposed. Kido et al. [22] used RGB dyes dispersed in the polymer PVK. Sato [23] developed devices with multiple layers of blue-green-and orange-emitting materials. The filters can be patterned on a separate plate using photolithography, and the WOLED is directly fabricated on the substrate.

Use of color filter on the glass substrate is conventionally practiced in the LCD industry. There is no need to pattern each of the pixels other than the OLED white backlight. However, one disadvantage of this type of patterned RGB OLED display is the poor luminous power efficiency due to absorption of the light by the color filters.

1.2.3   Blue OLED backlight with color-changing medium

As shown in Figure 1-2, this method uses a blue OLED cell as backlight to change blue light into red or green photoluminescence (PL) [24]. The red and green color-changing medium (CCM) are fluorescent layers that effectively absorb blue EL. The CCM filters can be patterned independently on a glass substrate using photolithography, and then the blue OLEDs alone are fabricated on the substrate without patterning the pixels. The display using blue OLEDs with CCMs has higher quantum efficiencies than that using white OLED because the former displays directly convert from backlight to the CCM fluorescent light.

This method only needs a blue OLED as backlight, therefore, the fabrication process is simplest among all full-color OLEDs techniques. However, the requirement for efficiency and stability of blue OLEDs is also much higher than those of the other methods. Moreover, the PL quantum efficiencies of CCMs are still poor and CCMs are potentially subject to excitation by ambient light which may impact on resolution.
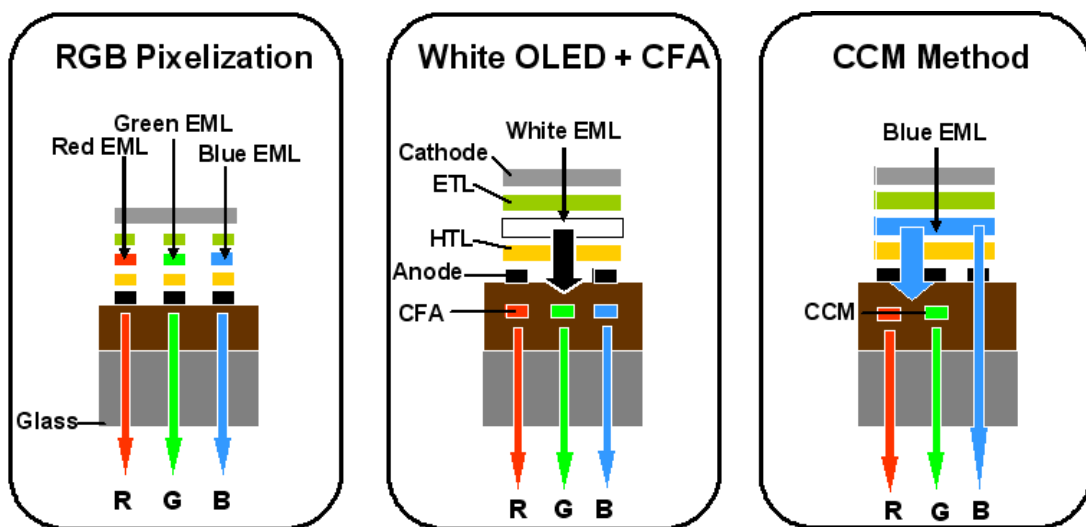
Figure 1-2 Full-color OLED techniques.

1.3   WOLEDs for lighting applications

In addition to information display and handset products, WOLEDs for lighting application emerge as one of the hottest pursuits of OLED research in recent years. According to a Display Search Report of March, 2009, the OLED lighting market is to take off in 2011 [25], with OLED lighting revenues forecast to surpass PMOLED displays in the 2013 or 2014 timeframe, reaching US$6 billion by 2018 (Figure 1-3). It is not surprising that most of the big companies such as GE, OSRAM, Philips, Konica-Minolta in the lighting business including a new company, *Lumiotec*, led by Prof. Kido of Japan have announced plans for WOLED mass production.
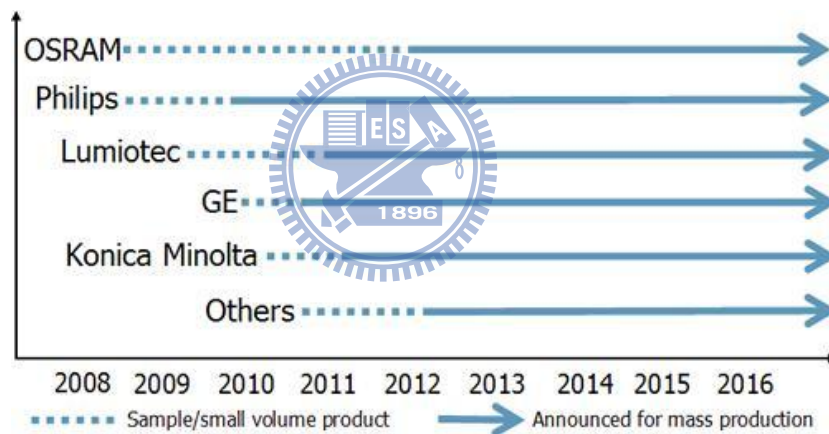
Figure 1-3 Lighting Co's announced WOLED mass production.

Although OLEDs used in lighting applications are not expected to become popular in the next few years and will initially target niche markets, the technology has several advantages over that of conventional lighting. Table 1-1 shows the comparisons of WOLEDs and several lighting sources. The major advantage is slimness. The thickness of OLED panels for lighting applications could reach less than 1 mm. Such a characteristic could allow OLED lighting placed directly on ceilings rather than hang from them. In addition, flexibility is

another advantage, which may allow OLED lighting to be used when designing for spaces with limited conditions.

Table 1-1 Comparisons of WOLED and other lighting sources.

Type	Efficiency	Life	CRI	Glare	Cost of manuf.	Cost of operation	Environ. friendl.
Incandescent	*	*	*****	*	*****	*	*****
Fluorescent	****	*****	****	**	**	***	*
HID (High Intensity Discharge)	****	*****	**	*	****	****	*
Future potential of OLEDs	*****	*****	*****	*****	*****	*****	*****

OLED   Incandescent   Fluorescent   High Intensity Discharge

Ref.: A. Duggal, (General Electric), OIDA OLED Workshop (2000)
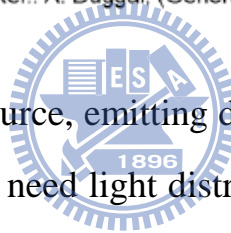
OLEDs are a flat light source, emitting diffuse light from a potentially large active area [26]. They do not need light distribution elements, thus reducing the cost for the whole lighting panel. In contrast, LEDs as main competitor are a point source technology which needs light distribution elements to achieve flat panel lighting. Additionally, OLEDs use low peak brightness on large area, LEDs provide very high brightness on small area. Due to this fact, LEDs are optimal for point-like light sources, OLEDs are more suitable for large area flat light sources. Using large-area OLED with higher efficiency will allow complete lighting solutions based on OLED technology. OLED will substitute existing lighting technologies, but will mainly generate new applications, owing to the unique properties of large-area diffuse light generating with adjustable color. Starting in the near future, OLED lighting will boost the OLED fabrication worldwide. The market research company IDTechEx expects already for 2011 a

billion dollar market.

1.4   *p*-i-*n* OLEDs

Conductive doping of organic semiconductors is achieved by dispersing strong donors and acceptors into intrinsic organic layers to improve conductivity. The operating voltage can be considerably reduced by introducing conductivity doped transport layers to OLED devices. Conducive doping has been demonstrated to be effective in increasing carrier concentrations [27], raising the conductivity of intrinsic organic layers [28,29], as well as reducing the injection barrier at electrode interfaces [30].

Similar to doping techniques developed in inorganic semiconductors, there are *p*-type and *n*-type doping for organic systems. For example, the *p*-doping hole transport layer (HTL) is typically made by co-evaporating the HTL with a strong electron acceptor such as tetrafluro-tetracyanoquinodimethane (F_4-TCNQ) [31], However, the use of highly volatile F_4-TCNQ as *p*-type dopant in thermal evaporation under high vacuum has raised serious concerns over issues of cross contamination, chamber pollution, and the thermal stability of OLEDs. Therefore, there are also some reports using inorganic metal oxide as *p*-type dopant, such as V_2O_5 [32], MoO_3 [33], and WO_3 [34]. Figure 1-4 Shows the UV-VIS-NIR absorption spectra of 200 nm thick 2-TNATA, WO_3, and 2-TNATA:WO_3 films on the quartz substrates. The absorptions of pure 2-TNATA and WO_3 film are all located at the wavelength less than 400 nm, while the 2-TNATA:WO_3 film revealed absorption peaks at around 800 and 1400 nm, which is attributed to that WO_3 can accept electron from 2-TNATA to form charge-transfer complex (WO_3^-/2-TNATA$^+$) [35,36]. The NIR absorption demonstrates that the WO_3 is also capable of accepting electron from 2-TNATA

to generate free holes in these doped films.
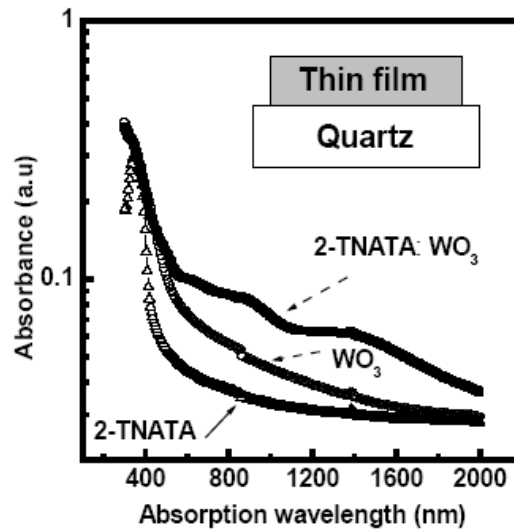
Figure 1-4 UV-VIS-NIR absorption spectra of pure and WO$_3$ doped 2-TNATA thin films [34].

The most widely investigated *n*-type dopants for the electron transoirt layer (ETL) are alkali metals, such as cesium (Cs) [37] and lithium (Li) [38]. However, they suffer from the necessity of a high doping ratio often of the order of 50% to achieve high conductivity, which often alters the host matrix properties. These methods require special equipments and care in handling reactive metals; they are thus not convenient for fabrication. In 2004, Canon Inc. reported that cesium carbonate (Cs$_2$CO$_3$) [39], either vacuum deposited as an individual layer over the organic electron transport material or co-deposited with the organic electron transport material, facilitates electron injection from a wide range of metal electrodes as shown in Figure 1-5.
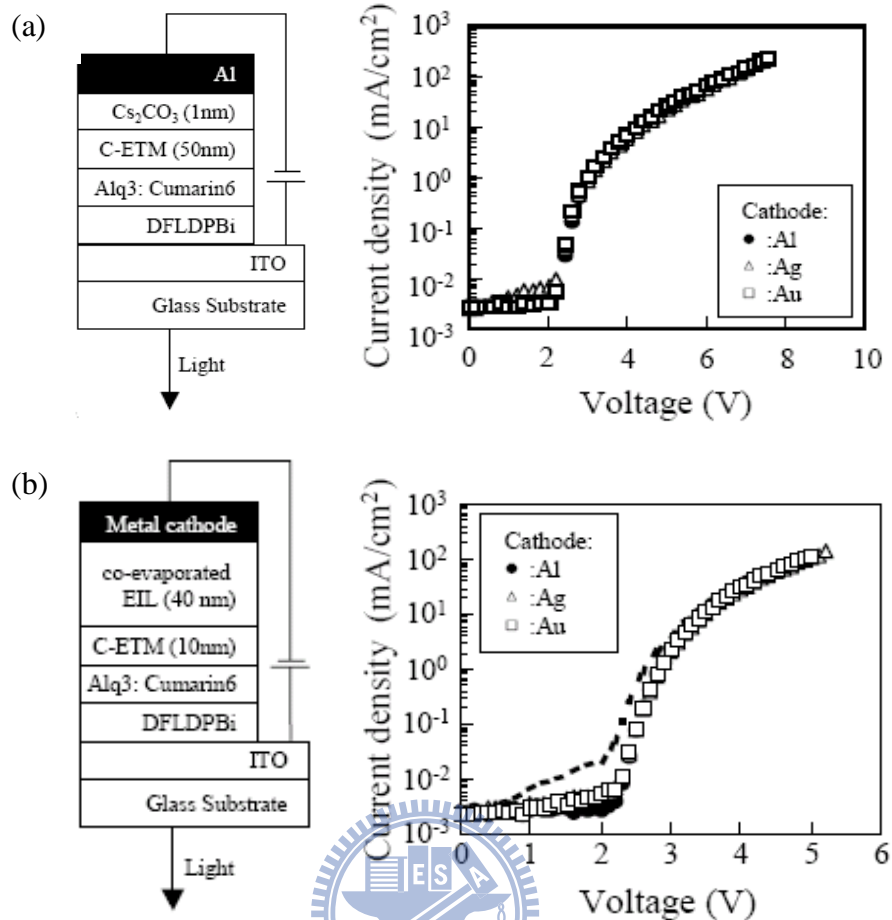
Figure 1-5 (a) Configuration of OLED with Cs_2CO_3 as electron injection layer and *J-V* characteristics. (b) Configuration of OLED with co-evaporated EIL and *J-V* characteristics [39].

Figure 1-6 depicts the common structure and energy diagram of *p*-i-*n* OLEDs. OLED devices with *p*-doped and *n*-doped layers can achieve low drive voltage, it is also necessary to keep high efficiency by preventing from the formation and non-radiative recombination of interface excitons. As a result, it is possible to solve this problem by the insertion of a thin undoped interlayer of a suitable material [40]. Moreover, the interlayer can also improve the carrier recombination in emission layer due to their carrier blocking ability.
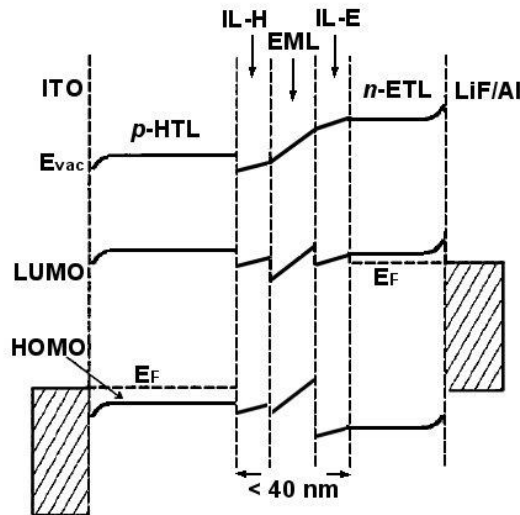
Figure 1-6 Common *p*-i-*n* OLED device structure and energy diagram.

1.5   Tandem OLEDs

OLED cells with stacked or so-called tandem structures have aroused much attention in recent years [41,42,43]. As shown in Figure 1-7, tandem OLEDs consist of multiple EL units electrically connected in series by connecting layer, and the luminance at a fixed current density increases linearly with the number of stacked and independent EL units. This can lead to a significant improvement in lifetime by reducing the degradation that accompanies the high drive currents required to achieve similarly high brightness in a single-unit device [44].
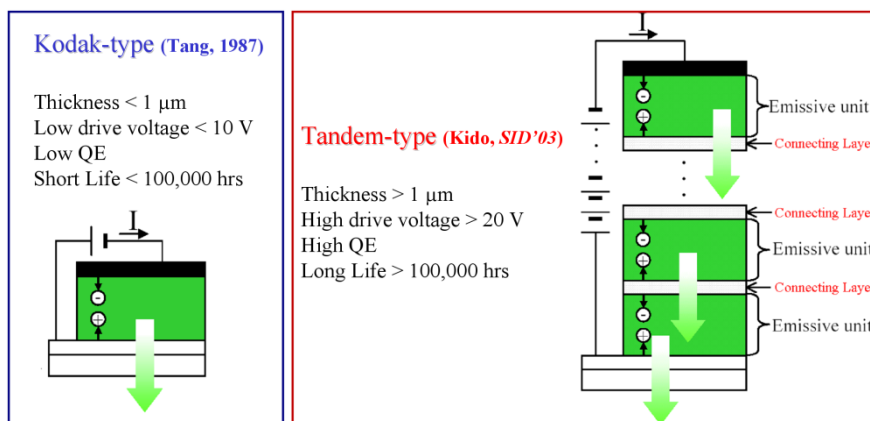
Figure 1-7 Comparison of single-unit device and tandem device.

The major challenge in tandem OLEDs in general is to prepare the effective connecting layer between emitting units so that the current can smoothly flow through without facing substantial barriers. Several effective connecting layers have been reported, such as Mg:Ag/indium zinc oxide (IZO) [45], Ag or Al/MoO$_3$ [46], n-doped organic layer/ITO, V$_2$O$_5$, WO$_3$ or Li$_2$O [47,48], and n-doped organic layer/p-doped organic layer [49]. A stable connecting layer is also an important factor for device lifetime. Liao et al. [49] found the drive voltage of their tandem device with Alq$_3$: Li/NPB: FeCl$_3$ as connecting layer would increase with operational duration. This phenomenon is caused by the n-type (Li) and p-type (FeCl$_3$) dopants inter-diffuse at the interface of organic p-n junction, which can be alleviated by inserting an additional thin metal or metal oxide layer [44].

In addition to the electrical properties of connecting layer, optical design of tandem OLED structure is also an important issue. A good connecting layer should also have high transmittance and low reflectance, thus the device performance would not be reduced due to undesirable light absorption by connecting layer. Furthermore, Wu et al. investigated theoretically and experimentally the characteristics of noncavity and microcavity tandem OLEDs as shown in Figure 1-8 [50]. They found the maximum efficiency of noncavity tandem device is 2.6 times higher than that of single-unit device. When incorporating a well-designed microcavity structure in tandem OLEDs, a fivefold enhancement in luminance could be achieved. A very high efficiency of 200 cd/A is also demonstrated with a phosphorescent microcavity two-unit green device.
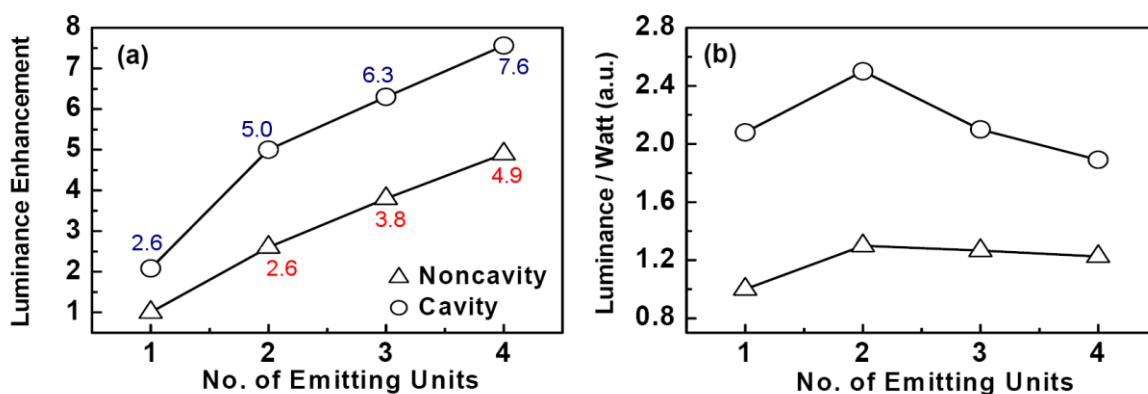
Figure 1-8 (a) Calculated luminance enhancement vs the number of emitting units. (b) Calculated power efficiency (lm/W, normalized to that of the reference device) for both noncavity and cavity tandem devices [50].

1.6　　Thesis organization

In this thesis, one anthracene-based material, 2-methyl-9,10-*di*(2-naphthyl) anthracene (MADN) developed at the OLED lab of NCTU, has been multifunctionally adopted into several OLED architectures. By taking the advantages of its large bandgap, stable thin-film morphology, reversible electrochemical properties, and bipolar charge transport nature of MADN, the OLED device structure can be further simplified by a common host of MADN for *p*-doped and *n*-doped layers as well as the emission layer.

In chapter 2, we describe the research methods and experimental details of this thesis, and also review the charge transport mechanism of disordered organic system, principle of time-of-flight transient photocurrent technique, fundamental theory of temperature-dependent admittance spectroscopy.

In chapter 3, we demonstrate a high power-efficient *di*-chromatic WOLED device by introducing *p*-doped (WO$_3$-doped NPB) and *n*-doped (Cs$_2$CO$_3$-doped BPhen) organic layers into device architecture along with carefully controlling

the carrier recombination zone in a thin layer thickness. A high-brightness tandem *di*-chromatic WOLED device with a connecting layer of organic *p-n* junction has also been fabricated.

In chapter 4, we develop an efficient and stable fluorescent deep blue host-guest system, and also adopt this deep blue system into *tri*-chromatic WOLED device architecture. The *tri*-chromatic WOLED device shows a high efficiency as well as high color gamut, and high color rendering index.

In chapter 5, we measure the carrier mobilities of anthracene-based materials by TOF technique and also demonstrate the use of C60 as a useful charge generation layer of TOF technique for hole mobilities of anthracene-based materials.

In chapter 6, we study the electrical characteristics of *p*-doped and *n*-doped organic layers by measuring current-voltage curves and temperature-dependent AS. The result shows that conductive-doping technique can greatly reduce the energy barrier and the drive voltage can also be reduced by adopting them into OLED devices.

In chapter 7, we demonstrate stable and efficient *p*-i-*n* OLED devices with a simplified architecture based on a single common host of MADN.

In chapter 8, we summarize all results and our contributions in this thesis and also propose the future works for OLED technique development.

References

[1] H. J. Round, *Electron. World* **19**, 309 (1907).

[2] N. Holonyak Jr., S. F. Bevacqua, *Appl. Phys. Lett.* **1**, 82 (1962).

[3] T. S. Perry, *IEEE Spectrum*, June 3 (2003).

[4] A. Bernanose, M. Comte, P. Vouaux, *J. Chim. Phys.* **50**, 64 (1953).

[5] A. Bernanose, *J. Chem. Phys.* **52**, 396 (1955).

[6] M. Pope, H. Kallman, P. Magnate, *J. Chem. Phys.* **38**, 2042 (1963).

[7] R. H. Partridge, *U. S. Patent* 3995299 (1976).

[8] P. S. Vincett, W. A. Barlow, R. A. Hann, G. G. Roberts, *Thin Solid films* **94**, 171 (1982).

[9] C. W. Tang, *US Patent* 4356429 (1982).

[10] C. W. Tang, S. A. VanSlyke, *Appl. Phys. Lett.* **51**, 913 (1987).

[11] S. A.VanSlyke, C. W. Tang, *US Patent* 4539507 (1985).

[12] C. W. Tang, C. H. Chen, R. Goswami, *US Patent* 4769292 (1988).

[13] C. W. Tang, S. A. VanSlyke, C. H. Chen, *J. Appl. Phys.* **65**, 3610 (1989).

[14] R. Friend, J. Burroughes, D. Bradley, *WO Patent* 9013148 (1990).

[15] R. Friend, J. Burroughes, D. Bradley, *US Patent* 5247190 (1993).

[16] G. Gustafsson, Y. Gao, G. M. Treacy, F. Klavetter, A. J. Heeger, *Nature* **357**, 477 (1992).

[17] E. Westerweele, P. Smith. A. J. Heeger, *Adv. Mater.* **7**, 788 (1995).

[18] G. Yu, K. Pakbaz, A. J. Heeger, *J. Electron. Mater.* **23**, 925 (1994).

[19] G. Yu, C. Zhang, A. J. Heeger, *Appl. Phys. Lett.* **64**, 1540 (1994).

[20] A. J. Heeger, J. Long Jr., *Optics & Photonic News* **23**, August (1996).

[21] S. Miyaguchi, et al., *Extended Abstracts 9th Int. Workshop on Inorganic and Organic Electroluminescence*, 137 (1998).

[22] J. Kido, K. Hongawa, K. Okuyama, K. Nagai, *Appl. Phys. Lett.* **64**, 815 (1994).

[23] Y. Sato, T. Ogata, S. Ichinosawa, Y. Murata, *Synth. Met.* **91**, 103 (1997).

[24] C. Hosokawa, E. Eida, M. Matuura, F. Fukuoka, H. Nakamura, T.

Kusumoto, *Proceedings of SID1997*, p. 1037 (1997).

[25] http://www.displaysearch.com.tw/

[26] A. H. Tullo, Chem. *Eng. News* **86**, 20 (2008).

[27] M. Pfeiffer, A. Beyer, T. Fritz, K. Leo, *Appl. Phys. Lett.* **73**, 3202 (1998).

[28] J. Huang, M. Pfeiffer, A. Werner, J. Blochwitz, S. Liu, K. Leo, *Appl. Phys. Lett.* **80**, 139 (2002).

[29] M. Pfeiffer, S. R. Forrest, K. Leo, M. E. Thompson, *Adv. Mater.* **14**, 1633 (2002).

[30] M. Pfeiffer, K. Leo, X. Zhou, J. S. Huang, M. Hofmann, A. Werner, J. Blochwitz, *Org. Electron.* **4**, 89 (2003).

[31] J. Blochwitz, M. Pfeiffer, T. Fritz, K. Leo, *Appl. Phys. Lett.* **73**, 729 (1998).

[32] T. Matsumoto, T. Nakada, J. Endo, K. Mori, N. Kawamura, A. Yokoi, J. Kido, *Proceedings of IDMC'03*, p. 413, Feb. 18-21 (2003), Taipei, Taiwan.

[33] C. T. Lin, G. R. Lee, C. I. Wu, T. Y. Cho, C. C. Wu, T. W. Pi, *Proceedings of IDMC'07*, p. 179, July 3-6 (2007), Taipei, Taiwan.

[34] C. C. Chang, M. T. Hsieh, J. F. Chen, S. W. Hwang, C. H. Chen, *Appl. Phys. Lett.*, **89**, 253504 (2006).

[35] C. Ganzorig, M. Fujihira, *Appl. Phys. Lett.* 77, 4211 (2000).

[36] J. Endio, T. Matsumoto, and J. Kido, *Jpn. J. Appl. Phys.* Part 2 **41**, L358 (2002).

[37] J. H. Lee, M. H. Wu, C. C. Chao, H. L. Chen, and M.K. Leung, *Cem. Phys. Lett.* **416**, 234 (2005).

[38] J. Kido, T. Matsumoto, *Appl. Phys. Lett.* **73**, 2866 (1998).

[39] T. Hasegawa, S. Miura, T. Moriyama, T. Kimura, I. Takaya, Y. Osato, H. Mizutani, *Proceedings of SID'04*, p. 154, May 23-28 (2004), Seattle,

Washington, USA.

[40] X. Zhou, M. Pfeiffer, J. Blochwitz, A. Werner, A. Nollau, T. Fritz, K. Leo, *Appl. Phys. Lett.* **78**, 410 (2001).

[41] V. Bulovic, G. Gu, P. E. Burrows, M. E. Thompson, S. R. Forrest, *Nature* **380**, 29 (1996).

[42] G. Gu, G. Parthasarathy, P. Tian, P. E. Burrows, S. R. Forrest, *J. Appl. Phys.* **86**, 4076 (1999).

[43] T. Matsumoto, T. Nakada, J. Endo, K. Mori, N. Kawamura, A. Yokoi, J. Kido, *Proceedings of IDMC'03*, p. 413, Feb. 18-21 (2003), Taipei, Taiwan.

[44] L. S. Liao, K. P. Klubek, D. L. Comfort, C. W. Tang, *US Patent* 6717358B1 (2004).

[45] S. Tanaka, C. Hosakawa, *US Patent* 6107734 (2000).

[46] C. W. Chen, Y. J. Lu, C. C. Wu, E. H. E. Wu, C. W. Chu, Y. Yang, *Appl. Phys. Lett.* **87**, 241121 (2005).

[47] C. C. Chang, S. W. Hwang, C. H. Chen, J. F. Chen, *Jpn. J. Appl. Phys.* **43**, 6418 (2004).

[48] H. Kanno, Y. Hamada, K. Nishimura, K. Okumoto, N. Saito, H. Ishida, H. Takahashi, K. Shibata, K. Mameno, *Jpn. J. Appl. Phys.* **45**, 9219 (2006).

[49] L. S. Liao, K. P. Klubek, C. W. Tang, *Appl. Phys. Lett.* **84**, 167 (2004).

[50] T. Y. Cho, C. L. Lin, C. C. Wu, *Appl. Phys. Lett.* **88**, 111106 (2006).

Chapter 2
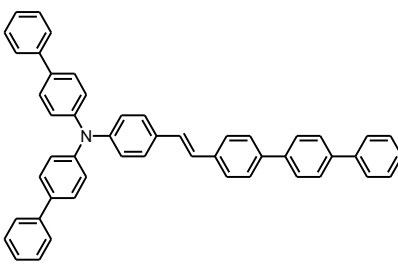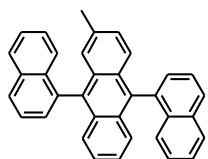
Experimental Details and Analytical Methods
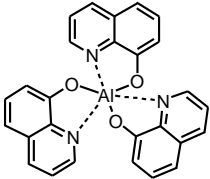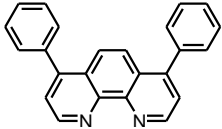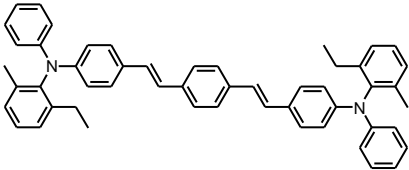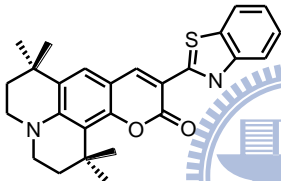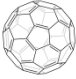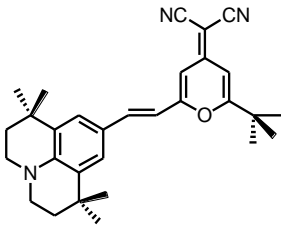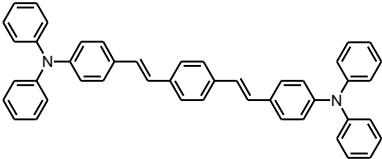
2.1 Overview
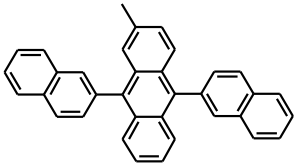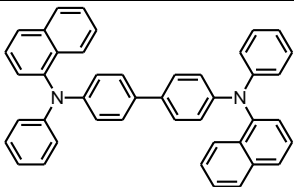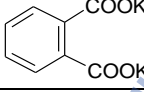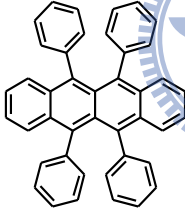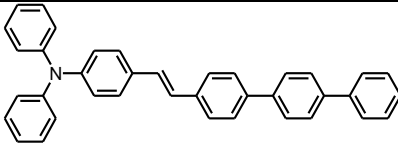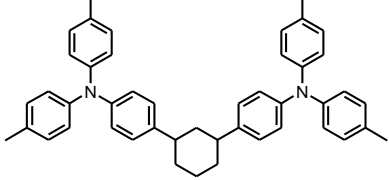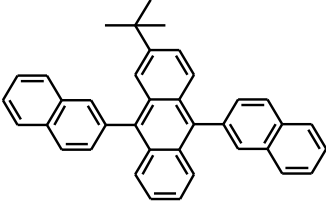
The research methods and experimental details of this thesis are described in this chapter, including (1) materials used in this thesis, (2) characterizations of material properties, (3) fabrication process and performance characterization of OLED devices. The charge transport mechanisms of disordered organic system and principles of time-of-flight (TOF) transient photocurrent technique are also reviewed in *Sections 2.6 and 2.7*. At last, a brief introduction of impedance spectroscopy (IS) and fundamental theory of thermal admittance spectroscopy (AS) are presented in *Sections 2.9 and 2.10*.

2.2 Materials used in this thesis

Table 2-1 Abbreviation, chemical structure and nomenclature of materials used in this thesis.

Abbreviation	Chemical Structure	Chemical Nomenclature	Source
2BpSA-BiPh		*di*(4,4'-biphenyl) [4-(2-[1,1';4',1"]terphenyl-4-yl-vinyl)phenyl] amine	synthesized in lab [1]
α,α-MADN		2-methyl-9,10-*di*(1-naphthyl) anthracene	synthesized in lab [2]

Abbreviation	Material Structure	Chemical Nomenclature	Source
Alq₃		*tris*-(8-hydroxyquinoline) aluminum	purchased from e-Ray
BPhen		4,7-diphenyl-1,10-phenanthroline	purchased from Lumtec
BUBD-1		*p-bis*(4-(*N*,*N*-(2-methyl-6-ethylphenyl)(phenyl)aminostryl)benzene	synthesized in lab [3]
C545T		10-(2-benzothiazolyl)-1,1,7,7-tetramethyl-2,3,6,7-tetrahydro-1*H*,5*H*,11*H*-benzo[*l*]-pyrano[6,7,8-*ij*]quinolizin-11-one	purchased from e-Ray
C60		buckminsterfullerene	purchased from Lumtec
Cs₂CO₃		cesium carbonate	purchased from Alfa Aesar
CsF		cesium fluoride	purchased from Sigma-Aldrich
DCJTB		4-(dicyanomethylene)-2-*t-butyl*-6-(1,1,7,7-tetramethyljulolidyl-9-enyl)-4H-pyran	purchased from e-Ray
DSA-Ph		*p-bis*(*p-N*,*N*-diphenyl-amino-styryl) benzene	synthesized in lab [4]
EY-53		(yellow dopant)	purchased from e-Ray

Abbreviation	Material Structure	Chemical Nomenclature	Source
ITO		indium-tin-oxide	provided by AUO
LiF		lithium fluoride	purchased from Sigma-Aldrich
MADN		2-methyl-9,10-*di*(2-naphthyl) anthracene	synthesized in lab [5]
NPB (α-NPD)		*N,N′*-Bis(naphthalen-1-yl)-*N,N′*-bis (phenyl)-benzidine	purchased from e-Ray
PAK2		dipotassium phthalate	purchased from Sigma-Aldrich
Rb		Rubrene	purchased from e-Ray
SA-BiPh		diphenyl-[4-(2-[1,1';4',1"]terphenyl-4-yl-vinyl) phenyl] amine	synthesized in lab [1]
TAPC		1,1-*bis*[*N,N*-di(*p*-tolyl)aminophenyl]cyclohexane	purchased from TCI
TBADN		2-(*t*-butyl)-9,10-*di*(2-naphthyl)anthracene	synthesized in lab [6]
WO$_3$		tungsten oxide	purchased from CERAC

2.3　　　Characterizations of material properties

2.3.1　　　UV absorption and photoluminescence spectra

The UV-vis absorption and PL spectra were measured by Hewlett Packard 8453 and Acton Research Spectra Pro-150, respectively.

2.3.2　　　Thermal properties

The thermal properties of glass transition temperature (T_g) and thermal decomposition temperature (T_d) were measured by differential scanning calorimetry (DSC) and thermogravimetric analysis (TGA), respectively. DSC was performed using Seiko SSC 5200 operated at heating and cooling rates of 10 and 30 ℃/min, respectively. Samples were scanned from 30 to 400 ℃, cooled to 30 ℃, and then scanned again from 30 to 400 ℃; T_g was determined from the second heating scan. TGA was undertaken on Seiko TG/DTA 200 under a nitrogen atmosphere, by measuring weight loss while heating at a rate of 10 ℃/min. T_d was determined as the temperature with 5% weight loss.

2.3.3　　　Electrochemical properties and HOMO/LUMO energy levels

The electrochemical properties were probed by cyclic voltammetry (CV). CV was undertaken on a CHINSTRUMENT CHI 604A instrument by using 0.1 M tetrabutylammonium hexafluorophosphat as the supporting electrolyte and ferrocene as the internal standard in dichloromethane solution.

On the basis of the onset potential for the oxidation and the band gap, HOMO and LUMO energy levels can be estimated with regard to the energy level of the ferrocene reference (4.8 eV below the vacuum level) [7]. The HOMO energy level can also be directly measured by the UV photoelectron spectroscopy (Riken Keiki Model AC-2).

2.3.4 Fluorescence quantum yield

The fluorescence quantum yield (ϕ_f) of the solid samples were measured in a HORIBA Jobin Yvon FluoroLog-3 spectrofluorometer equipped with a Xe lamp of 450 W as the excitation source, and an iHR320-FSS spectrometer equipped with a Hamamatsu R0928 PMT detector and an F-3018 integrating sphere.

2.4 Fabrication process of OLED devices

2.4.1 Cleaning procedure of ITO-glass substrate

Patterned ITO-coated glasses are provide by AU Optronics with a size of 4 cm × 4 cm, and the ITO pattern is illustrated in Figure 2-1. The thickness and sheet resistance of ITO are 75 nm and 70 $\Omega/\square$. Before the thermal evaporation of organic materials, an ultrasonic cleaning with organic solvents was used to clean the ITO-glass substrate in an effort to clean the ITO surface. The cleaning procedures are described as below: (1) ultrasonic cleaning in acetone for 5 min; (2) rinsed in deionized (DI) water for 5 min; (3) ultrasonic cleaning in detergent (purchased from Alconox): DI water (~1: 10 volume) for 5 min; (4) rinsed in DI water for 5 min; (5) washed by isopropyl alcohol (HPLC grade); (6) ultrasonic cleaning in methanol (HPLC grade) for 5 min; (7) blown by nitrogen gas flow and then baked in oven at 110 ^{0}C for 30 min.
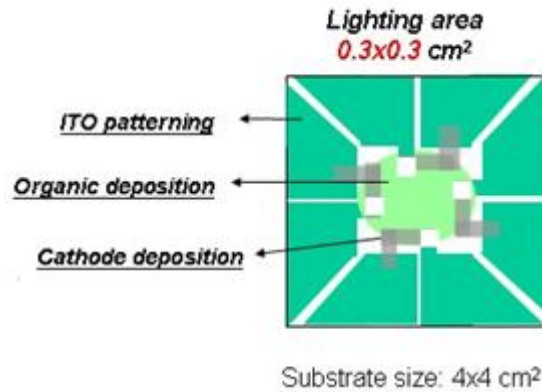
Figure 2-1 Schematic representation of device pattern.

2.4.2 Vacuum thermal evaporation of patterned films

After the routine cleaning procedure, the ITO-coated glasses were loaded on the grounded electrode of a parallel-plate plasma reactor, pretreated by oxygen plasma at 600 W for 20 sec, and then coated with a polymerized fluorocarbon film by trifluoromethane (CHF_3) plasma at 100 W for 5 sec, which can improve the hole injection from ITO anode [8]. Then organic materials were deposited by thermal evaporation at a rate of 0.1 nm/s under the base vacuum of about 10^{-6} torr in ULVAC SOLCIET coater following a published protocol [9] as illustrated in Figure 2-2. Figure 2-1 also depicts the patterns of organic layers, metal electrode, and active area. In the evaporation of emission layer, the fluorescent dopant was co-deposited with host molecule at its optimal molar ratio. After the thermal deposition of the organic layers and without a vacuum break, 150 nm of aluminum (Al) was deposited through a patterned shadow mask on top of the organic layers using separately controlled sources to complete the cathode. The active area of the OLED device is 9 mm^2, which is defined by the overlap of the ITO anode and the metal cathode.
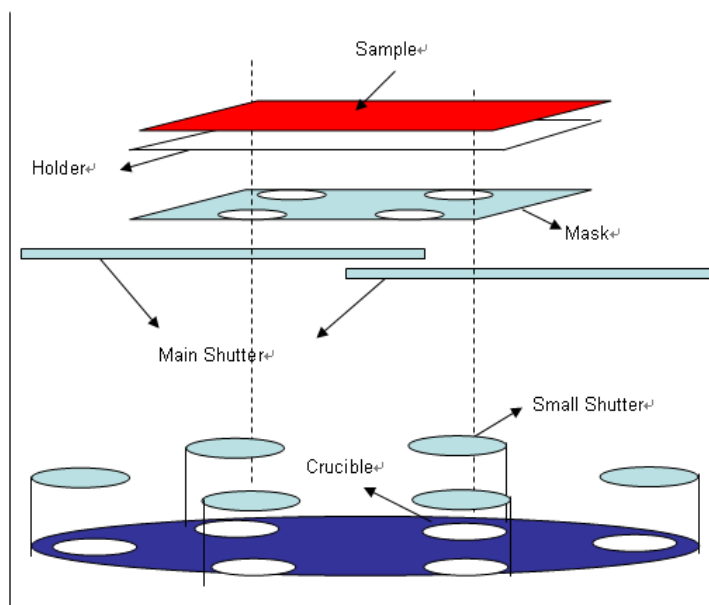
Figure 2-2 Schematic diagram of ULVAC SOLCIET coater for thermal deposition of organic materials.

2.4.3 Characterization of device performance

The luminance-current density-voltage (*L-J-V*) characteristics of the devices were measured with a diode array rapid scan system using Photo Research PR650 spectrophotometer and a DC power supply (Keithley 2400), which are controlled by a computer with a programmable software (Labview v5.1). The color rendering index of white OLED devices were measured by JETI spectroradiometer specbos 1201.

2.4.4 Encapsulation and stability measurement

All devices were sealed prior to testing as illustrated in Figure 2-3. The device lifetime was tested in glove box or in the ambient at a constant drive current density controlled by a DC power supply (Keithley 2400) and the luminance decay was detected by a photodiode connected to data acquisition instruments and a computer with a programmable software (Labview v5.1) as

shown in Figure 2-4.
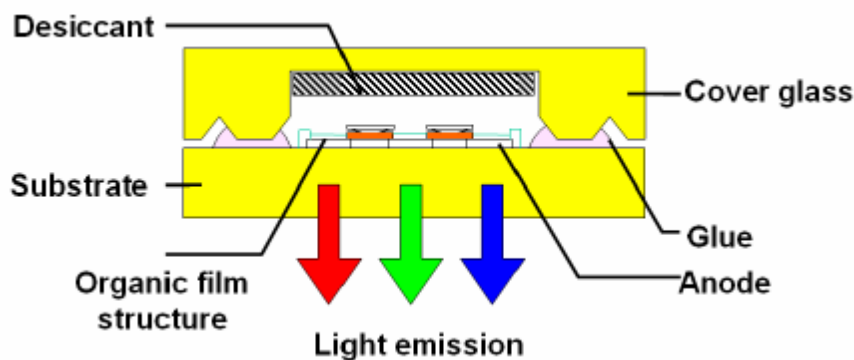
Figure 2-3 Schematic diagram of an encapsulated OLED device.
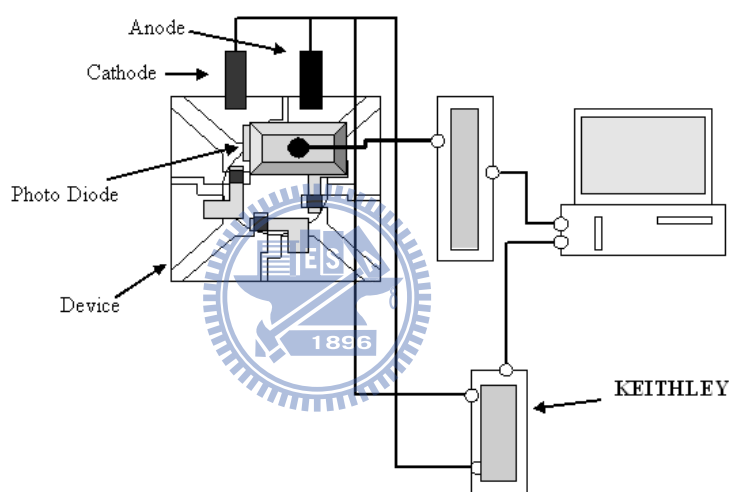
Figure 2-4 Schematic diagram of device lifetime measurement.

2.5   Charge transport mechanism in disordered organic materials

The transport of charges in disordered organic materials is described as hopping, as they quantum mechanically tunnel to other molecules in the material, sometimes even to nonadjacent ones. This hopping is like a series of redox chemical reactions. The excess electrons and holes are isolated anions and cations, respectively. These ionized species transfer this excess charge to a nearby neutral molecule, thus moving the charge through the material under the

influence of the external field even as the molecules themselves remain stationary [10]

To a certain extent theorists borrowed some equations from typical semiconductor theories while tailoring equations to account for the energetic disorder associated arrangement of organic materials. Although there are still some problems for molecular-level simulations, there are a number of characteristics of transport in organic charge transport materials that can be modeled and fit. Usually there are three main dependences of the charge carrier mobility in organics are discussed, they are namely field-dependence, temperature-dependence, and trap-concentration-dependence.

First, the charge mobility in disorder organic materials is known to be dependent on the applied field. The Poole-Frenkel conduction formalism has been shown to be applicable to organic charge transport materials for field dependence within the range of 10^4 to 10^6 V/cm [11,12,13], despite some theoretical concerns about its applicability [13]. The Poole-Frenkel dependence of the mobility (μ) is given by the following equation,

$$\mu(E) = \mu_0 \exp(\beta \sqrt{E}) \tag{2.1}$$

where μ_0 is the zero-field mobility, E is the applied field electric field, and β is the Poole-Frenkel factor.

Secondly, the carrier mobility in these materials depends on temperature. Hopping transport is thermally activated and that means the mobility increases with increasing temperatures, as additional thermal energy is provided to overcome the barriers resulting from energetic disorder. Temperature-dependence in disordered organics can first addresses by formulating a relationship based on the modified Arrhenius equation [14,15]:

$$\mu(T) = \mu_\infty \exp(-\frac{\Delta}{k_B T})$$ (2.2)

where μ_∞ is the mobility at infinite temperature and Δ is the activation energy. However, as the experimentally accessible temperature ranges are limited for this kind of measurements, other theoretically simulations with different temperature dependence have also been shown to fit well.

The most prominent model for fitting both the field and temperature dependence is Bässler's disorder formalism [16] as shown below:

$$\mu(E,T) = \mu_\infty \exp\left[-\left(\frac{2\sigma}{3k_B T}\right)^2\right] \exp\left\{C\left[\left(\frac{\sigma}{k_B T}\right)^2 - \Sigma^2\right]E^{1/2}\right\}$$ (2.3)

where the disorders in both position (including orientational effects) and energy are considered to be Gaussian distributions with widths of Σ and σ, respectively, and C is an empirical constant. The μ_∞ again represents the infinite temperature mobility and can be determined by the following equation:

$$\mu_0(T) = \mu_\infty \exp\left[-\left(\frac{T_0}{T}\right)^2\right]$$ (2.4)

The final effect on mobility that must be considered is a compositional change made to the material by altering the concentration of traps within the bulk. Extensive works have been done on molecularly doped polymers and on how the mobility increases with higher content of the active species [17]. Trap-controlled transport has also been studied, with higher concentrations and energetically deeper traps in another transport material causing greater reductions in mobility [18,19,20], as carriers are trapper more frequently and for longer amounts of time before being released (if released at all). The

Hoesterey-Letson formalism [21] is a well-known and classic equation to describe the effects on the mobility of a material with a certain relative concentration of traps, as shown below:

$$\mu_o(c) = \mu(c_0) \frac{1}{1 + c \cdot \exp\left(\dfrac{\varepsilon_t}{k_B T}\right)}$$

(2.5)

in which c is represents the concentration of dopant, $\mu(c_0)$ is the trap-free mobility, and ε_t is the trap energy below the energy level (HOMO or LUMO as relevant) of majority material.

However, there is a transition to trap-to-trap transport as the concentration of traps rises, where some charge carriers will flow primarily in hops between traps and through the material. This is the case in many mixed transport materials, with two or more charge transport compounds in nearly equal proportions. The transport in such systems is infrequently studied, but a recent theoretical treatment has covered such cases in detail with an extension of the effective medium approximation theory [22].

2.6   TOF measurement

In the field of organic electronics, the measurement of charge carrier mobility is invaluable in understanding how fast a device can respond. Over many years of research, there have been numerous methods developed to test charge transport properties of organic materials with relatively low mobility, such as steady-state space-charge-limited-current (ss-SCLC) [23] and analysis of organic field-effect transistors [24]. Besides, pulsed-radiolysis time-resolved microwave conductivity (PR-TRMC) [25,26] is an indirect method, it only measures the sum of electron and hole mobilities and cannot distinguish which

might be faster. A rather new method is admittance spectroscopy [27], it also requires an indirect analysis to obtain the mobility.

Time-of-flight (TOF) transient photocurrent technique is one of the most widely used methods for investigating carrier transport properties. The original technique, measuring charge transit time to determine mobilities for inorganic semiconductors, was first reported by Haynes and Shockley [28]. The pulsed photoconductivity technique was then extended to the measurement of mobilities of organic materials by Spear [29,30], Kepler [31] and LecBlanc [32]. The basic experimental setup is illustrated in Figure 2-5, in which the material to be measured is sandwiched between two blocking contacts, of which at least one is (semi)transparent to receive pulsed illumination (usually by a nanosecond pulsed laser) for producing a thin sheet of photo-generated carriers near the electrode. Depending on the polarity of the applied bias, selected carriers (either holes or electrons) are swept across the sample and a transient photocurrent is recorded.
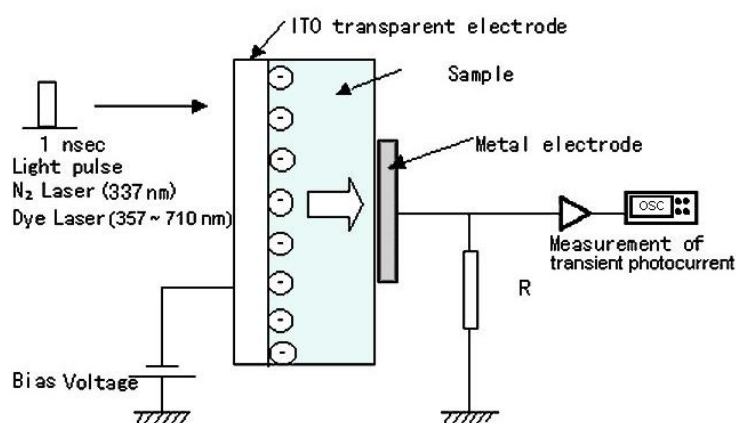
Figure 2-5 Typical TOF configuration.

In such a configuration, for unambiguous determination of the transit time from the TOF transient, the thickness of the organic layer is usually set one

order of magnitude larger than the absorption depth (the charge generation region). Then the mobility (μ) could be obtained by the well-known relationship as follow:

$$\mu = \frac{d}{E \cdot \tau_{tr}} = \frac{d^2}{V \cdot \tau_{tr}}$$

(2.6)

where d is the thickness of measured film, τ_{tr} is the flight time of carriers, and E is the applied electric field ($E = V/d$, V is the applied voltage).

There some limitations to this method that must be considered in order to effectively measure mobility. Most importantly, the electric field applied to the sample should be constant during measurement. In addition, the dielectric relaxation time (τ_{rel}) must be much longer than the TOF transit time (τ_{tr}). The dielectric relaxation time is the measured time that excess charges in a semiconducting medium to be neutralized through the conduction process. If the dielectric relaxation time is too short, built up charge in transit through the sample will be neutralized and no charge carrier transient will be observed. Fortunately, the relatively low intrinsic charge concentration in the vast majority of organic charge transport materials renders τ_{rel} extremely long, making these samples ideal for TOF measurements.

Furthermore, the generation time of the charge sheet, which takes to generate the charge sheet with an excitation pulse, must be much less than τ_{tr}. The intensity of illumination should be kept as low as possible, thus the total generated charges is less than 5% of the sample capacitor charges to avoid space charge effects which would result in non-uniform distribution of electric field across the sample. In addition, the excitation wavelength should be close to the absorption peak of the materials to ensure that the absorption coefficient is large

enough. Also, the absorption depth (which follows the Beer-Lambert law) should be as thin as possible as compared to the sample thickness.

Finally, the detail of signal across the load resistance depends on the magnitude of the resistance-capacitance (*RC*) time constant of the circuit, where $C = \varepsilon A/L$ is the capacitance of the sample with area A of the active area. It is required that the *RC* time constant must be much less than the transit time to avoid distortion induced by the *RC* response of the measurement circuit.

2.7 Non-dispersive and dispersive transit signals

The information of carrier transport in organic film can be derived from the transit photocurrent signal measured by TOF technique. As shown in Figure 2-6(a), the non-dispersive photocurrent signal shows a clear plateau and subsequent drop. This behavior indicates the charge sheet spreads slightly and exits the sample almost at the same time. Fitting non-dispersive signal is typically done on a linear scale [10], which fits lines to the plateau and a linear region intersecting at the transit time as referred to t_0.

In contrast with the non-dispersive case, if there exist some deep traps and the carrier detrapping time is comparable to the transit time, the number of charge carriers would decrease during transport. In this case, the photocurrent signals are often dispersive without any definite cusp as illustrated in Figure 2-6(b), which usually cannot be fit on a linear scale. According to Scher-Montroll theory [33], the transit time can be evaluated from the intersection point of the asymptotes to the tail in the double logarithmic (*log-log*) plots as shown in the inset of Figure 2-6(b). However, if the concentration of deep traps is so high that most carriers are caught by traps rapidly, the signal will drop too fast to be resolved and it is hard to evaluate the transit time.
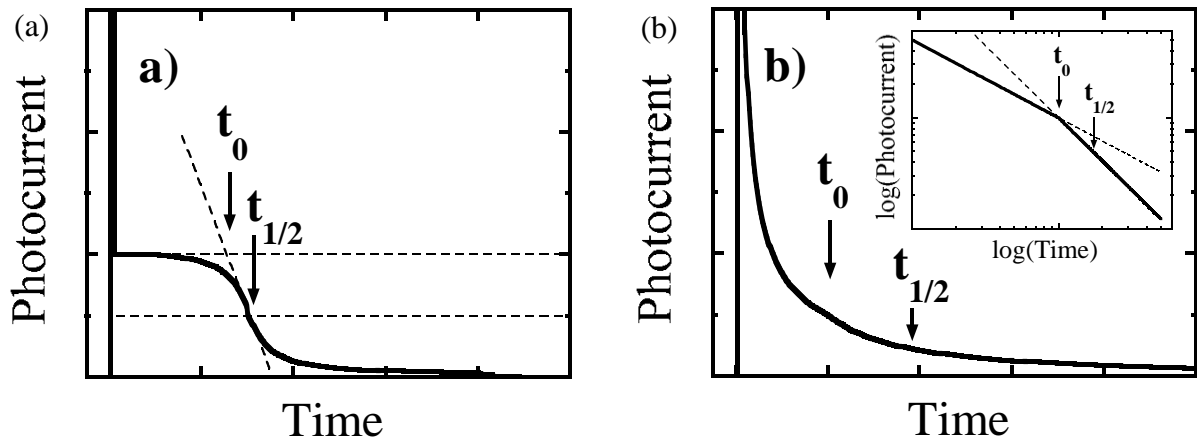
Figure 2-6 Example TOF transit signals for (a) non-dispersive curve, and (b) dispersive curve with an inset of a *log-log* scale.

2.8   Experiments of TOF measurement

The TOF experiments in this thesis were measured at room temperature in Prof. Ching W. Tang's laboratory (University of Rochester, NY, USA). The whole TOF system are shown in Figure 2-7, including a digital storage oscilloscope (Tektronix TDS 2024B), nitrogen (N_2) laser, optical components, vacuum sample holder, and a dc power supply (Hewlett Packard 6100A).

In our experiments, the samples were prepared by thermal evaporation on ITO substrates. The general sample structure was ITO/organic material (~10 μm)/Al (150 nm). During the film deposition, the chamber pressure is maintained at 10^{-6} torr and the evaporation rate was monitored by quartz crystal sensor. The thickness of organic layer was measured by Ambios XP-200 profilometer. After thermal evaporating, the sample was immediately housed inside a cryostat for TOF measurements. All samples were measured under 10^{-3} to 10^{-6} torr. A DC power supply is used for the relevant carrier detection. A N_2 laser of 337 nm was used to generate a sheet of free charges near one side of the sample. A current sensing resistor R in series with the sample converted and

magnified the photocurrent to voltage readings. The injected carriers moved through the sample under the external electric field and drifted to the counter electrode. The value of R was adjusted between 1 and 1 MΩ, so that the RC time constant should be at least 20 times less than the carrier transient time. The digital oscilloscope was used capture the voltage across R.
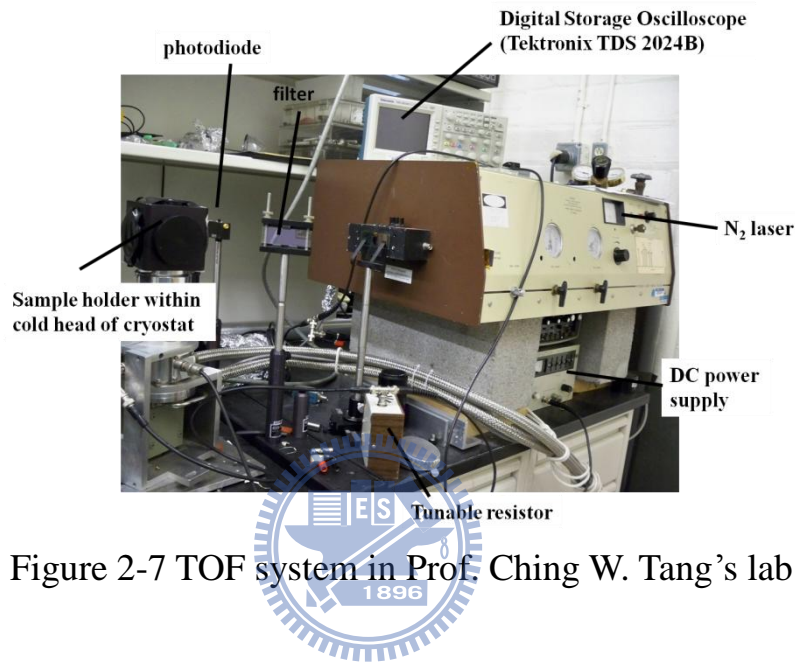
Figure 2-7 TOF system in Prof. Ching W. Tang's lab.

2.9   Introduction of impedance spectroscopy and admittance spectroscopy

Impedance is defined as the frequency domain ratio of the voltage to the current. In other words, it is the voltage-current ratio for a single complex exponential at a particular frequency (ω). The concept of electrical impedance was first introduced by O. Heaviside [34] in the 1880s and was soon after developed in terms of vector diagrams and complex representation by A. E. Kennelly [35]. Impedance is a more general concept than resistance because it takes phase differences into account, and it has become a fundamental and essential concept in electrical engineering.

In general, impedance is a complex number as represented as Z, and has the same unit as resistance, ohm (Ω). As shown in Figure 2-8, the polar form shows both magnitude and phase characteristics,

$$Z = |Z|e^{j\theta}$$

(Polar form, 2.7)

$$Z(\omega) = \frac{V_{ac}}{i_{ac}} = R(\omega) + iX(\omega)$$

(Cartesian form, 2.8)

where the magnitude $|Z|$ is the ratio of the voltage amplitude to the current amplitude, j is the imaginary unit and θ is the phase difference between voltage and current. In Cartesian form, the real part of impedance is the resistance R and the imaginary part is the reactance X.
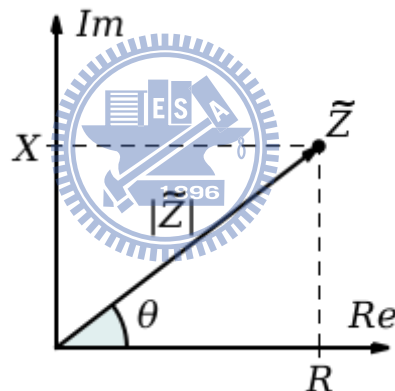
Figure 2-8 Graphical representation of the complex impedance plane.

Impedance spectroscopy (IS) is a relatively new and powerful method of characterizing many of the electrical properties of materials and their interfaces with electronically conducting electrodes. It may be used to investigate the dynamics of bound and mobile charge in the bulk or interfacial regions of any kind of solid or liquid material: ionic, semiconducting, mixed electronic-ionic, and even insulators (dielectrics). Any intrinsic property that influences the conductivity of an electrode-materials system, or an external stimulus, can be

studied by IS. The parameters derived from an IS spectrum fall generally into two categories: (1) those pertinent only to the material itself, such as conductivity, dielectric constant, mobilities of charges, equilibrium concentrations of the charged species, and bulk generation-recombination rates; and (2) those pertinent to an electrode-material interface, such as adsorption-reaction rate constants, capacitance of the interface region, and diffusion coefficient of neutral species in the electrode itself.

The most common approach of IS is to measure impedance by applying a single-frequency voltage or current to the interface and measuring the phase shift and amplitude, or real and imaginary parts, of the resulting current at that frequency using either analog circuit or fast Fourier transform (FFT) analysis of the response. Commercial instruments are available which measure the impedance as a function of frequency automatically in the frequency ranges of about 1 mHz to 1 MHz. The advantages of this approach are the availability of these instruments and the ease of their use, as well as the fact that the experimentalist can achieve a better signal-to-noise ratio in the frequency range of most interest.

There several other measured or derived quantities related to impedance which often play important roles in IS, all of them are generically called immittances. One of them is the admittance, the complex admittance Y is the reciprocal of the impedance Z and is also related to the voltage and current as follows:

$$Y(\omega) = \frac{1}{Z(\omega)} = \frac{i_{ac}}{v_{ac}} = G(\omega) + iB(\omega) = G(\omega) + i\omega C(\omega) \qquad (2.9)$$

where G is the conductance, B is the susceptance, C is the capacitance, f is the

frequency, and $\omega = 2\pi f$ is the angular frequency.

Admittance spectroscopy (AS) is also a well-known and powerful technique for determining material properties and geometries of semiconductor devices and heterojunctions [36]. Recently, AS based on small signal space-charge-limited current (SCLC) theory has also been proposed to characterize carrier dynamics [37,38,39] and investigate the charge-carrier transport properties of organic materials with high resistivity [27,40,41,42,43,44].

2.10   Model for thermal admittance spectroscopy study

Thermal admittance spectroscopy (TAS) [45,46] is a technique for the measurement of deep trap levels within *pn* junctions. By measuring the small-signal ac admittance of the junction under different conditions, e.g., with small-signal frequency and sample temperatures as parameters, one can extract the density of states, activation energy, and capture cross sections of the traps. According to the applied dc voltage, zero- and nonzero- bias AS are distinguished.

Trap levels in the space charge region of a *p-n* junction contribute to its admittance as follows: They are filled with electrons up to the Fermi level and correspond to the nearest band edge by thermal capture and emission of carriers. A small-signal AC voltage applied to the junction modulates the position of the Fermi level with respect to the band edges, so the trap levels in the vicinity of the Fermi level change their state of occupancy accordingly. Thus, their charge state also changes and an additional AC charge component is generated, which increases the total junction capacitance, i.e., the imaginary part of the admittance.

As the filling and emptying of the traps takes place with the emission rate e_T or time constant $\tau = 1/e_T$, the trapped AC charge lags behind the applied voltage at frequencies above the emission rate. This phase shift first means ohmic losses, so the traps also contribute to the junction conductance at higher frequency. Second, the trapped charge decreases, because the trap occupancy can no longer follow the rapid jitter of the Fermi level. Consequently, the trap capacitance decreases with increasing frequency. A nonzero bias voltage shifts the mean Fermi level such that trap levels at a different depth in the band gap are measured.

The terms "high frequency" and "low frequency" depend strongly on temperature, since the emission rate e_T of a discrete hole trap is given by

$$e_T = \sigma_p v_{th} N_V \exp(-\frac{E_a}{k_B T}) \tag{2.10}$$

where σ_p designates the thermal capture cross section for holes, N_V is the effective density of states in the valence band, v_{th} is the thermal velocity of the electrons, T is the temperature, k_B is the Boltzmann constant, and E_a is the activation energy. For an ideally discrete level, the usual first-order small-signal approximation [46,47,48] leads to a capacitance contribution C_T as shown below:

$$C_T = \frac{C_0}{1+(\frac{\omega}{\omega_{co}(T)})^2} \tag{2.11}$$

with the excitation angular frequency ω and the cutoff angular frequency ω_{co}. For the latter, the calculation yields [45,47],

$$\omega_{co}(T) = 2e_T = 2\xi_0 \exp(-\frac{E_a}{k_B T}) \tag{2.12}$$

in which the emission factor ξ_0 comprises the temperature-independent parts of the product $\sigma_p v_{th} N_V$ and is proportional to the capture cross section, which is assumed to be constant.

Due to its strong dependence on temperature and frequency, the admittance of a discrete trap level can easily be separated from other contributions to the total junction admittance by using an equivalent circuit model.

In our experiments, we investigate the electrical properties, such as resistance and activation energy, of *p*-doped and *n*-doped organic layers and demonstrate their effects on carrier injection barrier by temperature-dependent AS measurements. Then, we also apply these conductive-doped organic layers into OLED devices

2.11   Experiments of temperature-dependent AS measurement

The AS experiments in this thesis were measured in Prof. Jenn-Fang Chen's laboratory (Department of Electrophysics, National Chiao Tung University, Hsinchu, Taiwan). The admittances of the devices were measured using HP 4192A LF impedance analyzer. The amplitude of the test signal was 50 mV, which was superimposed on the operating DC bias, and the measurement frequency is in the range from 100 Hz to 10 MHz. All the measurements were carried out in the dark and shielded environment.

In our experiments, the samples were prepared by thermal evaporation on ITO substrates in ULVAC SOLCIET coater. During the film deposition, the chamber pressure was maintained at 10^{-6} torr and the evaporation rate was monitored by quartz crystal sensor. After thermal evaporating, the samples were hermetically sealed and immediately housed inside a vacuum cryostat for AS measurements. The temperature-dependent experiments were measured under

vacuum and controlled by LakeShore 330 temperature controller.

References

[1] M. T. Lee, C. H. Liao, C. H. Tsai, C. H. Chen, *Adv. Mater.* **17**, 2493 (2005).

[2] M. H. Ho, Y. S. Wu, S. W. Wen, M. T. Lee, T. M. Chen, C. H. Chen, K. C. Kwok, S. K. So, K. T. Yeung, Y. K. Cheng, Z. Q. Gao, *Appl. Phys. Lett.* **89**, 252903 (2006).

[3] M. F. Lin, L. Wang, L. W. K. Wong, K. W. Cheah, H. L. Tam, M. T. Lee, C. H. Chen, C. H. *Appl. Phys. Lett.* **89**, 121913 (2006).

[4] M. T. Lee, H. H. Chen, C. H. Tsai, C. H. Liao, C. H. Chen, *Appl. Phys. Lett.* **85**, 3301 (2004).

[5] M. T. Lee, Y. S Wu, H. H. Chen, C. H. Tsai, C. H. Liao, C. H. Chen, *Proceedings of SID2004*, p. 710, May 23-28 (2004), Seattle, WA, USA.

[6] B. Banumathy, W. J. Shen, C. H. Chen, *Tetrahedron Lett.* **44**, 5747 (2003).

[7] J. Pommerehne, H. Vestweber, W. Guss, R. F. Mahrt, H. Bässler, M. Porsch, J. Daub, *Adv. Mater.* **7**, 551 (1995).

[8] L. S. Hung, L. R. Zheng, M. G. Mason, *Appl. Phys. Lett.* **78**, 673 (2001).

[9] S. A. Van Slyke, C. H. Chen, C. W. Tang, *Appl. Phys. Lett.* **69**, 2160 (1996).

[10] Y. Shirota, H. Kageyama, *Chem. Rev.* **107**, 953 (2007).

[11] A. J. Mozer, P. Denk, M. C. Scharber, H. Neugebauer, N. S. Sariciftci, *J. Phys. Chem. B* **108**, 5235 (2004).

[12] D. M. Pai, *J. Chem. Phys.* **52**, 2285 (1970).

[13] W. D. Gill, *J. Appl. Phys.* **43**, 5033 (1972).

[14] V. Coropceanu, J. Cornil, D. da Silva Filho, Y. Olivier, R. Silbey, J. L. Bredas, *Chem. Rev.* **107**, 926 (2007).

[15] W. Zhu, S. J. Singer, Z. Zheng, A. T. Conlisk, *Phys. Rev. E* **71**, 041501 (2005).

[16] H. Bässler, *Phys. Status Solidi B* **175**, 15 (1993).

[17] P. M. Borsenberger, D. S. Weiss, *Organic Photoreceptors for Imaging Systems*, New York: Marcel Dekker, (1993).

[18] F. W. Schmidlin, *Phys. Rev. B* **16**, 2362 (1977).

[19] L. Li, G. Meller, H. Kosina, *Sol.-Stat. Elec.* **51**, 445 (2007).

[20] A. Fleissner, H. Schmid, C. Melzer, H. von Seggern, *Appl. Phys. Lett.* **91**, 242103 (2007).

[21] D. C. Hoesterey, G. M. Letson, *J. Phys. Chem. Solids* **24**, 1609 (1963).

[22] I. I. Fishchuk, A. K. Kadashchuk, A. Vakhnin, Y. Korosko, H. Bässler, B. Souharce, U. Scherf, *Phys. Rev. B* **73**, 115210 (2006).

[23] D. M. Burland, *Phys. Rev. Lett.* **33**, 833 (1974).

[24] M. Abkowitz, D. M. Pai, *Philos. Mag. B* **53**, 193 (1986).

[25] P. G. Schouten, J. M. Warman, M. P. de Haas, *J. Phys. Chem.* **97**, 9863 (1993).

[26] J. M. Warman, M. P. de Haas, G. Dicker, F. C. Grozema, J. Piris, M. G. Debije, *Chem. Mater.* **16**, 4600 (2004).

[27] S. W. Tsang, S. K. So, J. B. Xu, *J. Appl. Phys.* **99**, 013706 (2006).

[28] J. R. Haynes, W. Shockley, *Phys. Rev.* **81**, 835 (1951).

[29] W. E. Spear, *Proc. Phys. Soc. B* **70**, 1139 (1957).

[30] W. E. Spear, *Proc. Phys. Soc.* **76**, 826 (1960).

[31] O. H. Le Blanc, *J. Chem. Phys.* **33**, 626 (1960).

[32] R. G. Kepler, *Phys. Rev.* **119**, 1226 (1960).

[33] H. Scher, E. W. Montroll, *Phys. Rev. B* **12**, 2455 (1975).

[34] O. Heaviside, *The Electrician*, AMS Bookstore (1886).

[35] A. E. Kennelly, *Impedance*, IEEE (1893).

[36] L. Y. Leu, S. R. Forrest, *J. Appl. Phys.*, **64**, 5030 (1988).

[37] H. C. F. Martens, H. B. Brom, P. W. M. Blom, *Phys. Rev. B* **60**, R8489 (1999).

[38] S. Berleb, W. Brütting, *Phys. Rev. Lett.* **89**, 286601 (2002).

[39] H. H. P. Gommans, M. Kemerink, G. G. Andersson, R. M. T. Pijper, *Phys. Rev. B* **69**, 155216 (2004).

[40] K. L. Tong, S. W. Tsang, K. K. Tsung, S. C. Tse, S. K. So, *J. Appl. Phys.* **102**, 093705 (2007).

[41] Oliver J. Weiß, Ralf K. Krause, Arvid Hunze, *J. Appl. Phys.* **103**, 043709 (2008).

[42] N. D. Nguyen, M. Schmeit, *Phys. Rev. B* **75**, 075307 (2007).

[43] M. Schmeit, *J. Appl. Phys.* **101**, 084508 (2007).

[44] K. K. Tsung, S. K. So, *J. Appl. Phys.* **106**, 083710 (2009).

[45] D. L. Losee, *J. Appl. Phys.* **46**, 2204 (1975).

[46] J. Barbolla, S. Duenas, L. Bailon, *Solid-State Electron.* **35**, 285 (1992).

[47] T. Walter, R. Herberholz, C. Müller, H. W. Schock, *J. Appl. Phys.* **80**, 4411 (1996).

[48] J. J. Shiau, R. H. Bube, *Solid-State Electron.* **29**, 1153 (1986).

Chapter 3

Development of *Di*-Chromatic White Organic Light-Emitting Diodes

3.1   Introduction

Solid-state organic devices are at the vanguard of a generation of electronic components that promise to be as easily manufactured as colorful magazines and newspapers. These common printed products are produced using roll-to-roll technologies, where continuous rolls of paper measuring several feet in diameter are fed into machines to be cut, pressed, dyed, and packaged. Similar mass-production techniques for organic electronics may eventually replace traditional semiconductor batch processes, and thereby allow electronics to compete with well-established and inexpensive devices such as the incandescent bulb, and electronic identification tags for low-cost and disposable products.

One device that is on the cusp of widespread use is the OLED. Research over the last twenty years has paved the way for the implementation of efficient blue, green, and red OLEDs in passive and active matrix displays. Low-information-content OLED displays fabricated by Philips, TDK, Nippon Seiki, Sanyo, and Pioneer have already been commercialized, and various OLED displays like portable smart phones, digital cameras, photo frames, small to medium size TVs have been demonstrated and some of which have already been introduced in the marketplace by Samsung, LG, Sony, AUO, CMEL and Lumiotec.

Interest in the application of WOLED technology for general solid-state lighting applications and FPD backlights is also steadily increasing. Coupled to

the increase in published work in the area of WOLEDs, the power efficiency of WOLEDs has steadily increased over the last ten years and has attained a level requisite WOLED acceptance into lighting market; hence, there is a greater appreciation for potential of energy saving, thin, flexible WOLEDs to replace traditional incandescent white light sources.

3.2   Characteristics of white light

White light has three main characteristics: (1) $CIE_{x,y}$ coordinates; (2) color temperature; and (3) color rendering index (CRI). However, to be meaningful, both the color temperature and CRI should be quoted as the CRI is measured relative to a reference of a given color temoerature.

3.2.1   CIE 1931 chromaticity diagram

The emission color of OLED devices can determined and differentiated by CIE 1931 chromaticity diagram, created by Commission Internationale de l'Eclairage in 1931 [1]. As shown in Figure 3-1, the diagram represents all of the chromaticities visible to the average person. These are shown in color and this region is called the gamut of human vision. The gamut of all visible chromaticities on the CIE plot is the horseshoe-shaped figure shown in color. The curved edge of the gamut is called the *spectral locus* and corresponds to monochromatic light, with wavelengths listed in nanometers. The straight edge on the lower part of the gamut is called the line of purples. These colors, although they are on the border of the gamut, have no counterpart in monochromatic light. Less saturated colors appear in the interior of the CIE chart and the white point is at the center and is defined as (0.33, 0.33).

The major disadvantage of this diagram is the color difference is not in average, the green area is much larger than other color on the chart. So it is

difficult to tell the amount of color difference directly from the diagram.
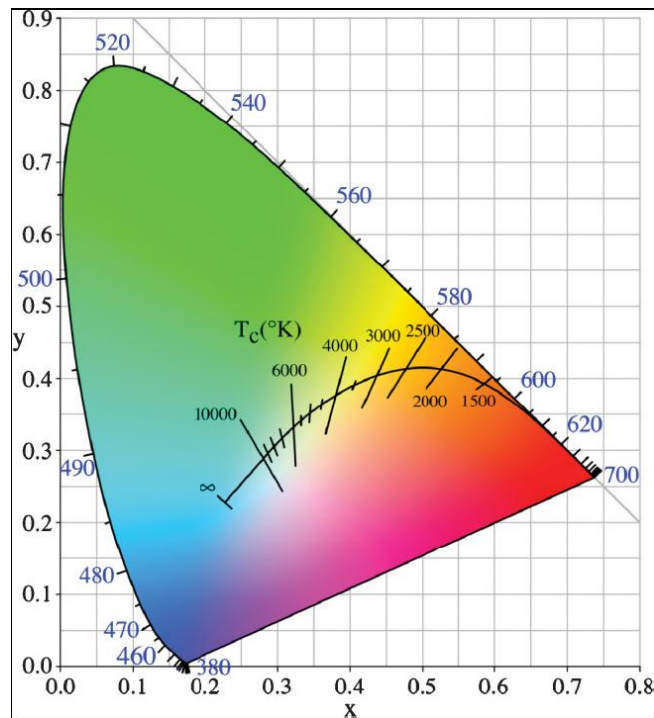
Figure 3-1 CIE$_{x,y}$ chromaticity diagram. All the colors in the visible spectrum lie within or on the boundary of this diagram. The internal arc is the Planckian locus, which is the plot of the coordinates of black body radiation at the temperatures shown, described as color-correlated temperatures.

3.2.2   Color temperature

The color temperature of a light source is the temperature of an ideal black-body radiator that radiates light of comparable hue to that light source. The temperature is conventionally stated in units of absolute temperature, kelvin (K). Color temperature is related to Planck's law [2] and Wien's displacement law [3]. Higher color temperatures (5000 K or more) are called *cool colors* (blueish white color); lower color temperatures (2700-3000 K) are called *warm colors* (yellowish white through red color).

However, most light sources, such as incandescent bulb, inorganic light-emitting diodes and even OLEDs are not a real and ideal black-body radiator, thereby, these nearly-Planckian light sources can be judged by the correlated color temperature (CCT), which the temperature of the Planckian radiator whose perceived color most closely resembles that of a given stimulus at the same brightness and under specified viewing conditions. As shown in Figure 3-1, CCT can be estimated from the lines project out from the Planckian locus in CIE 1931 chromaticity diagram.

3.2.3 Color rendering index

The color rendering index (CRI) is a numerical measurement of how true colors look when viewed with the light source and can be determined from the output spectrum of the light source. A black-body radiator has a maximum CRI value of 100. Typically the CRI value is higher than 80 for a high quality light source. Moreover, for commercial viability, color temperature and CRI of a light source need to be stable over the source lifetime [4,5].

3.3 Performances of state-of-the-art WOLEDs

Since the first reports of white-emitting devices by the group of Kido [6,7], many approaches to generating white light from organics have been described in the literature. The initial devices exhibited efficiencies of < 1 lm/W, but this value has grown to > 50 lm/W over the last few years [8]. The challenges facing WOLED technology are due, in large part, to the fact that fluorescence or phosphorescence emission from typical organic materials only spans about one third of the visible spectrum. Color tuning molecules to emit in the blue, green, or red portion of the visible spectrum can be accomplished with a variety of molecular structures and their derivatives, however, a single molecule has not

been designed that efficiently emits over the entire visible spectrum, such that high-quality white light is produced. Given the limited spectral bandwidth of single dopants, there are numerous WOLED architectures that combine the emission from multiple dopants. White emission from OLEDs can now be achieved in both small molecule and polymer systems and some review articles which focus on thermally evaporated small molecules and solution-processed polymers have been published [9,10,11].

In recent years, WOLEDs are being considered as practical solid-state light sources and could play a significant role in reducing global energy consumption. The detailed performances of state-of-the-art WOLEDs of some leading companies in the world are summarized in Table 3-1.

Table 3-1 Performances of state-of-the-art WOLEDs

Company	Size (cm^2)	Power Eff. (lm/W)	CIE$_{x,y}$ or CCT	Lifetime	Reference
Universal Display Corporation	15×15	50@1000 nits	(0.44, 0.44) 3055 K	T$_{70}$ = 10000 hr @1000 nits	[12]
Philips		28@1000 nits	(0.42, 0.46)		[13]
Panasonic Electric Works	1×1	37@1000 nits	(0.36, 0.36)	> 40000 hr @1000 nits	[14]
OSRAM	radius = 4 cm	25	2800 K	T$_{50}$ = 5000 hr	

3.4 Conventional *di*-chromatic WOLED device

In our lab, the conventional *di*-chromatic white OLED device is composed of *p*-bis(p-N,N-diphenyl-aminostyryl)benzene (DSA-Ph) doped 2-methyl-9,10-*di*(2-naphthyl) anthracene (MADN) sky-blue system [15] and 5,6,11,12-tetraphenylnaphthacene, known as rubrene [16] (abbreviation as Rb in this thesis), as the yellow emitter (device architecture is illustrated in Figure 3-2). By making use the bipolar characteristic of Rb molecular [17], doping RB molecules into the hole transport layer of *N,N'-bis*(1-naphthyl)-*N,N'*-diphenyl-1,1'-biphenyl-4,4'- diamine (NPB) in sky-blue device can directly obtain a *di*-chromatic white emission.
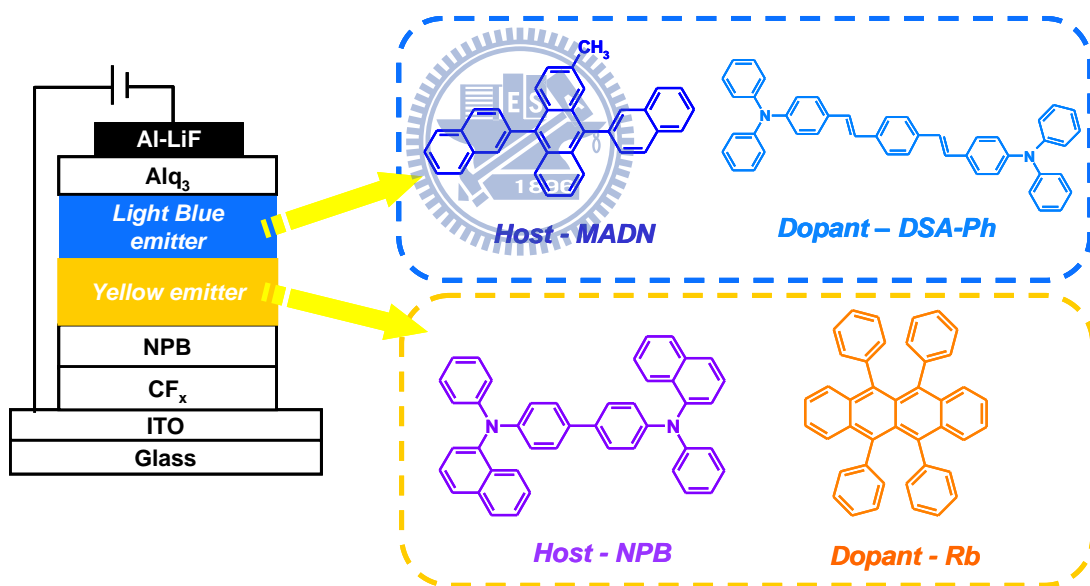
Figure 3-2 Conventional WOLED device architecture and molecular structures of key materials.

After the optimization of layer thickness and doping concentration, the structure of conventional white device is ITO/CF$_x$/NPB (50 nm)/NPB: 1.2% Rb (20 nm)/MADN: 3% DSA-Ph (40 nm)/aluminum *tris*(8-hydroxyquinoline)

(Alq$_3$, 10 nm)/lithium fluoride (LiF, 1 nm)/Al (200 nm). As shown in Figure 3-3(a), this white device shows a broad EL spectrum in visible region with two distinct peaks, clearly indicating the emissions of DSA-Ph and Rb at 456, 476, 520, and 620 nm, respectively. The device can achieve an EL efficiency of 9 cd/A with CIE$_{x,y}$ coordinates of (0.32, 0.41) at 6.4 V and 20 mA/cm^2. Moreover, the color stability should be also considered for a white device, because human eyes can sensitively tell the difference when the CIE$_{x,y}$ color change (ΔCIE$_{x,y}$) is larger than ±(0.04, 0.04). As shown in Figure 3-3(b), the color shift (ΔCIE$_{x,y}$) of this white device is only of ±(0.02, 0.01) under the wide range of 2 to 300 mA/cm^2, indicating the emission color of this white device is stable.
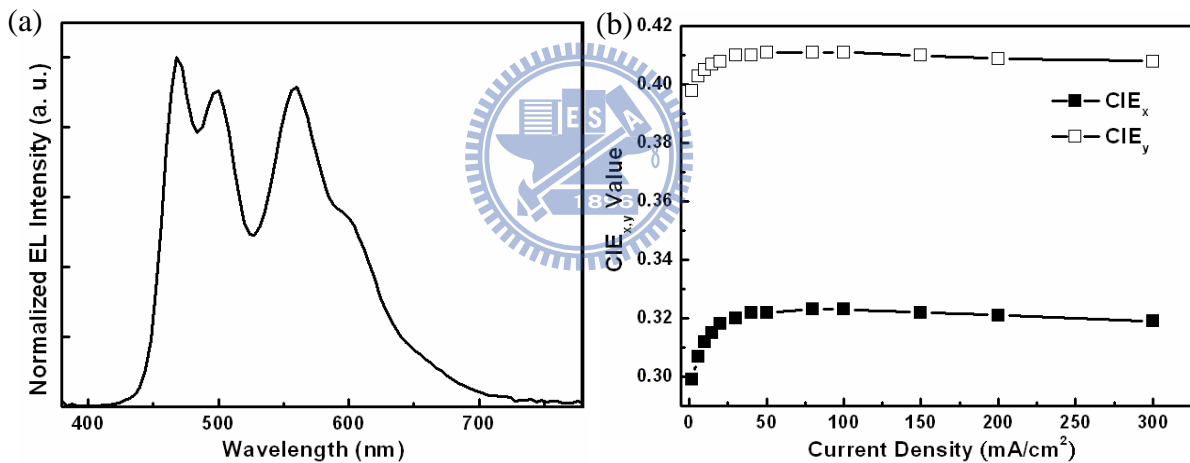
Figure 3-3 (a) EL spectrum at 20 mA/cm^2 and (b) CIE$_{x,y}$ coordinates *vs* current density characteristics of conventional WOLED device.

When the device is attached with color filter (provided by Allied Material Technology Corp.), the CIE$_{x,y}$ coordinates of RGB and white colors are (0.64, 0.35), (0.28, 0.60), (0.11, 0.17), and (0.35, 0.38), respectively [see Figures 3-4(a) and 3-4(b)]. For full-color display applications, the color gamut should be considered. Color gamut is the range of color a display can reproduce and is

commonly expressed as percentage of National Television System Committee (NTSC) specification [(0.67, 0.33), (0.21, 0.71), (0.14, 0.08), and (0.310, 0.316) for RGB and white points, respectively] as shown in Figure 3-4(c), 100% of NTSC refers to the full range of color that can theoretically be displayed. Usually, CRTs is about 70% of NTSC.
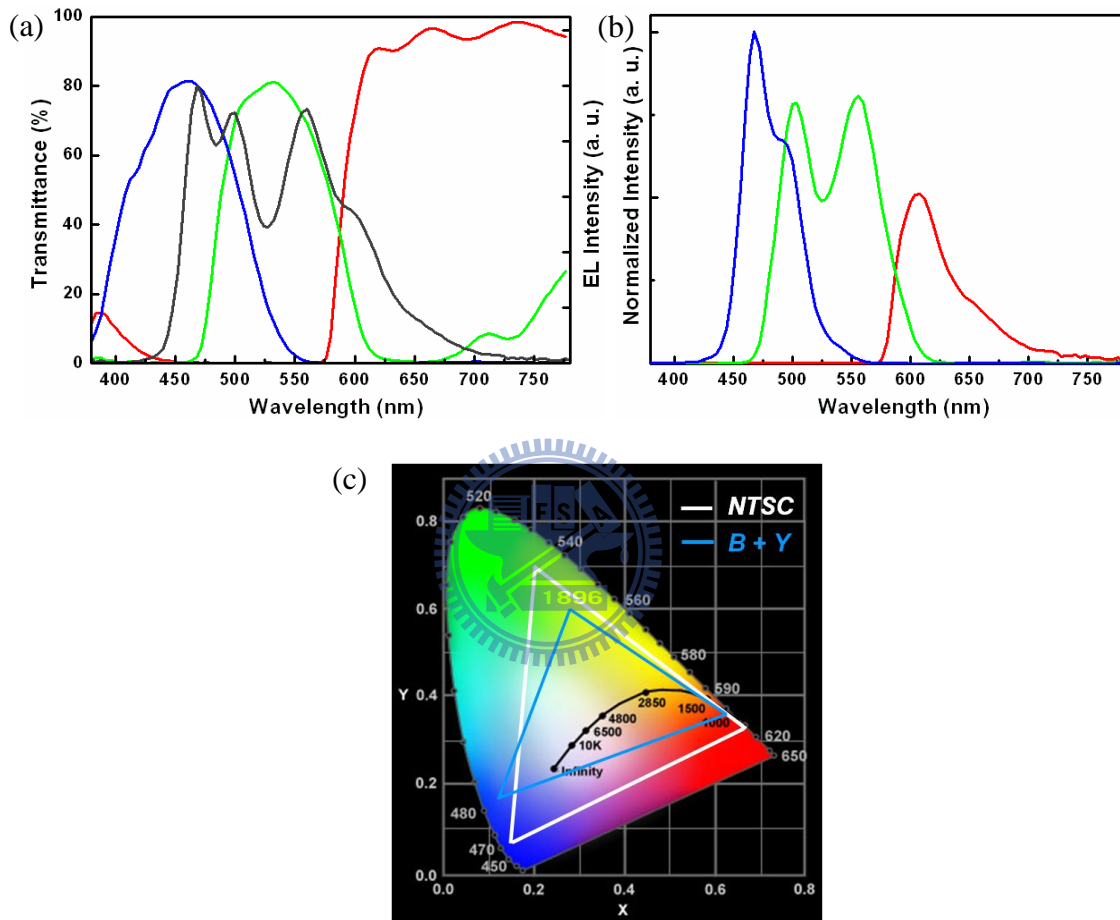
Figure 3-4 (a) The transmittance of RGB color filters and EL spectrum of conventional WOLED device. (b) Spectra of RGB colors after attaching color filters (c) The color gamut of NTSC standard and conventional WOLED device.

After calculation, the color gamut of our conventional WOLED device is 61.3% of NTSC standard, such low NTSC ratio can be attributed to this white emission is only composed of sky-blue and yellow colors, which obviously lacks

of the green color at wavelength of 520 nm. In addition, the weak intensity of blue region at wavelength < 450 nm and red region at wavelength > 620 nm, also leading to the poor saturation of blue and red colors.

For portable electronics, power consumption is one important issue should be considered, which means the electronic devices should possess high brightness at low drive voltage. However, the luminance of our conventional WOLED device is only 1200 cd/m^2 at a drive voltage of 6 V. Therefore, it is worthy to research on how to achieve high power efficiency of WOLED devices.

In this chapter, we introduce the *p*-doped [tungsten oxide (WO$_3$)-doped NPB] and *n*-doped [cesium carbonate (Cs$_2$CO$_3$)-doped 4,7-diphenyl-1,10-phenanthroline (BPhen)] organic layers into the device architecture of *di*-chromatic WOLED to achieve high power efficiency. The highly conductive *p*- and *n*-doped layers could enhance the charge injection from the contacts and reduce the ohmic losses in these layers [18]. To further reduce the drive voltage in *p*-i-*n* OLEDs, the thickness of low conductive layer based on organic materials should be as thin as possible. In addition, careful control of the location of exciton recombination zone (RZ) and the energy-transfer between the host and dopant molecules have been shown to be critical in obtaining a balanced white emission of high efficiency [19,20]. However, it is difficult for WOLEDs with multi-emission layer to achieve a stable white color due to the shift of RZ in thin organic layer, which often leads to undesired CIE$_{x,y}$ color change with respect to drive current.

3.5   Development of *p*-i-*n di*-chromatic WOLED device

In this section, we demonstrate a dual emission layer (DEML) system for

p-i-*n* WOLEDs in which the first emission layer is the co-dopant emitting layer with MADN: 5% NPB: 3% DSA-Ph: 0.2% Rb and the second one is a blue emitting layer of MADN: 5% NPB: 3% DSA-Ph. Three types of *p*-i-*n* WOLED devices were fabricated as depicted in Figure 3-5. The total thickness of DEML in these *p*-i-*n* devices is only 15 nm. Device I is the *p-i-n* WOLED without co-deposited NPB in the DEML system while device II is the *p-i-n* WOLED with the DEML system. The pure NPB layer of device II was replaced with 1,1-*bis*[*N*,*N*-di(*p*-tolyl)aminophenyl]cyclohexane (TAPC) [21] as electron-blocker in device III. In our *p*-i-*n* architecture, Cs_2CO_3 is co-evaporated with BPhen [22], which has a high electron mobility of 2.4×10^{-4} cm^2/Vs, as the *n*-doped electron transport layer (*n*-ETL). BPhen also possesses a deep highest occupied molecular orbital (HOMO) of 6.4 eV, which can effectively block hole carriers in emission layer. On the other hand, NPB doped with WO_3 is used as the *p*-doped hole transport layer (*p*-HTL) [23]. In the DEML system, MADN, NPB, DSA-Ph and Rb were used as host material, assistant dopant, blue and yellow fluorescent dopants, respectively.
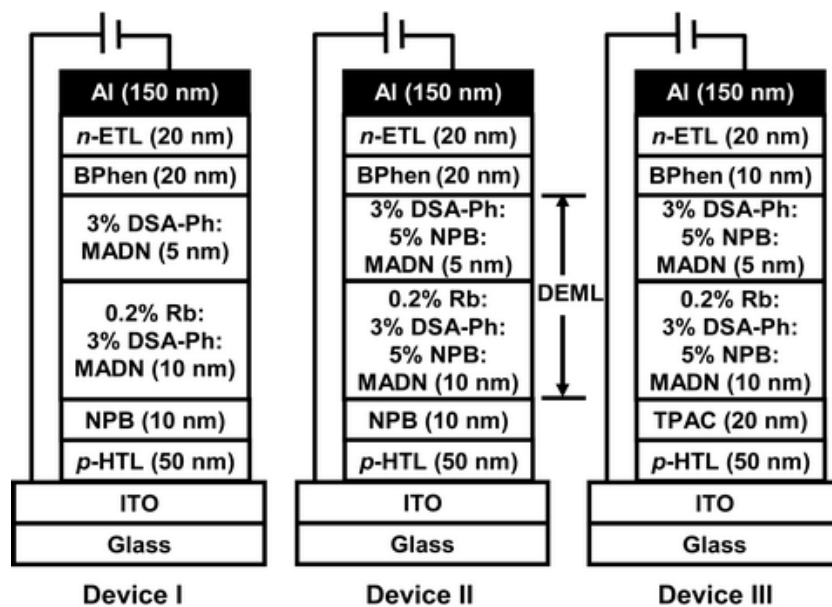
Figure 3-5 Schematic device architecture of *p*-i-*n* WOLEDs.

It is known that Rb with LUMO/HOMO of 3.2/5.4 eV can be a carrier trap for electrons, especially at low electric field [24], which will cause the problematic white emission color change with various drive currents in thin emission layer of *p*-i-*n di*-chromatic WOLEDs. In order to alleviate the unstable color issue associated with the carrier-trapping property of Rb, we have purposely co-evaporated Rb with low doping concentration of 0.2% and 3% DSA-Ph in MADN, which would cause the yellow emission generated by the energy-transfer process from blue to yellow emitter.

The energy-transfer process can be demonstrated by the solid-state emission spectra depicted in Figure 3-6, the thin film composed of MADN: 3% DSA-Ph: 0.2% Rb (90 nm) emits intense yellow emission and relatively weak blue-greenish emission. It is evident that the emission of MADN around 430 nm essentially quenched and there is an effective energy-transfer characteristic from DSA-Ph to Rb, which is primarily due to the favourable spectral overlap between the emission peak of DSA-Ph and the absorption peak of Rb at 495 nm [25].
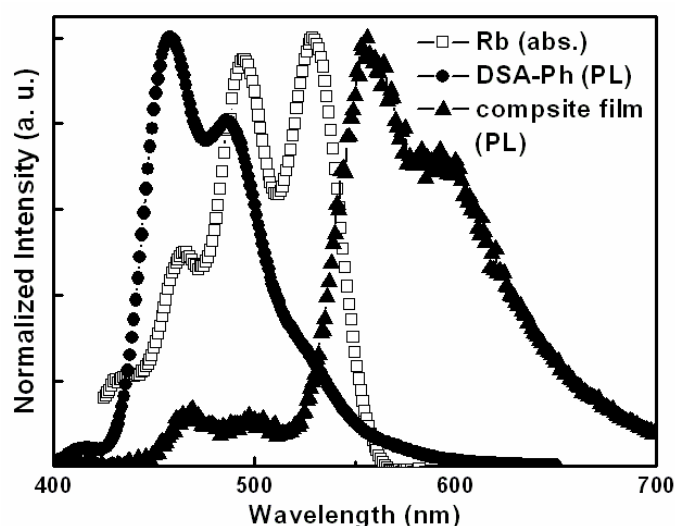
Figure 3-6 Absorption spectrum of Rb and solid PL spectra of DSA-Ph and composite thin film.

Therefore, we designed and developed a DEML system by inserting a blue emitting layer of MADN: 3% DSA-Ph after the co-evaporated EML into the structure of device I to enhance the blue emission intensity. From Figure 3-7(a), the EL spectrum of device I indeed shows the enhancement of the blue emission intensity with respect to the solid PL of co-evaporated thin film. However, the yellow emission intensity is still much higher than the blue emission, leading to undesirable white emission with $CIE_{x,y}$ coordinates of (0.37, 0.47). Furthermore, a significant EL color shift of device I is observed with respect to various drive currents as the $CIE_{x,y}$ coordinates is shifted from (0.410, 0.496) at 1 mA/cm^2 to (0.321, 0.419) at 100 mA/cm^2 with $\Delta CIE_{x,y} = \pm(0.089, 0.077)$ as shown in Figure 3-7(b), in which the yellow emission intensity decreases with the increasing current density. We inferred the unstable EL color is due to the RZ shifts towards the blue emitting layer under high current stress.
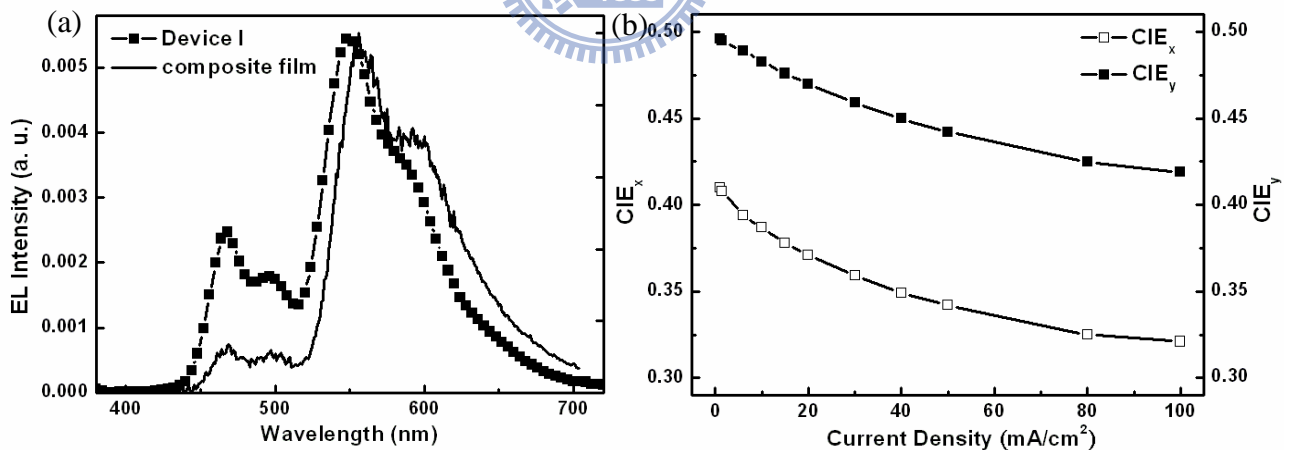
Figure 3-7 (a) Solid PL spectrum of composite film and EL spectra of device I at 20 mA/cm^2. (b) $CIE_{x,y}$ coordinates *vs* current density characteristics of device I.

Therefore, we co-deposited 5% NPB in the DEML system of device II as the assistant dopant with the purpose of shifting the RZ towards the blue

emitting layer to balance the blue and yellow emission intensity under low current density. Figure 3-8(a) reveals that device II also has a better J-V characteristic than device I which indicates that NPB molecules play an important role in enhancing the hole-transport in the DEML system. In addition, the EL spectrum of device II depicted in Figure 3-8(b) shows a more balanced white emission with $CIE_{x,y}$ of (0.33, 0.43) at 20 mA/cm^2 and the relative intensity of blue light has been increased as compared with device I. This phenomenon exhibits the co-deposited NPB molecules can indeed shift the RZ to the blue emitting layer and improve white $CIE_{x,y}$ coordinates. Moreover, the EL color shift with respect to varying drive currents has also been improved to $\Delta CIE_{x,y} = \pm(0.05, 0.04)$ from 1 mA/cm^2 to 100 mA/cm^2 as shown in Figure 3-8(c). However, the reduced relative intensity of yellow emission leads to a lower EL efficiency of 7.4 cd/A at 20 mA/cm^2.
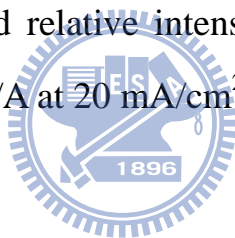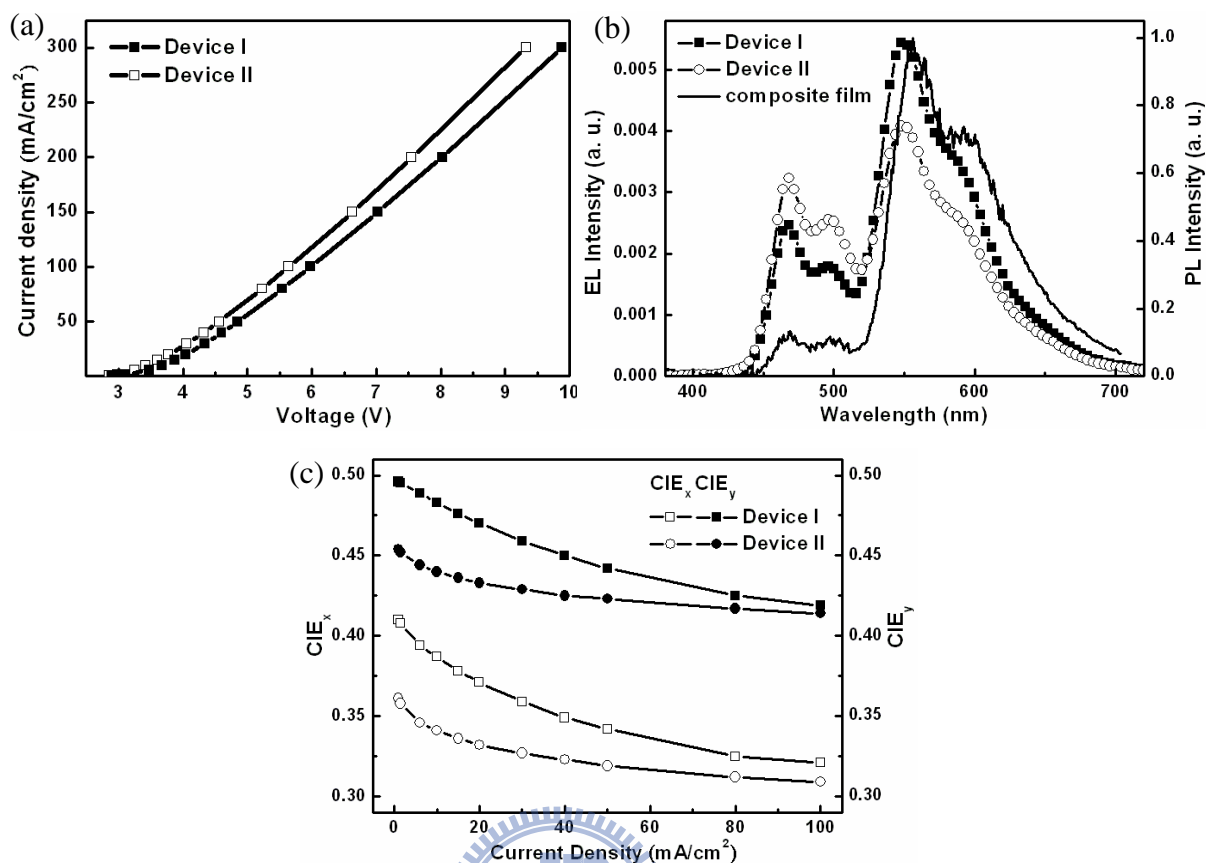
Figure 3-8 (a) *J-V* characteristics of devices I and II. (b) Solid PL spectrum of composite thin film and EL spectra of device I and II at 20 mA/cm². (c) CIE$_{x,y}$ coordinates *vs* current density characteristics of device I and II.

To further enhance the efficiency and improve the color stability of these *p*-i-*n* white devices, we turn to refine the exciton confinement in device III, in which the NPB layer was replaced by TAPC with a high LUMO energy level (2.0 eV) and high hole mobility (10^{-4}–10^{-3} cm²/Vs) [21], which can be an effective electron-blocking as well as hole transport material. Indeed, both blue and yellow intensity of device III have been enhanced as shown in Figure 3-9(a) and its emission achieved a white CIE$_{x,y}$ of (0.32, 0.43). Furthermore, the EL performance can be boosted to 9.9 cd/A and 8.2 lm/W at 20 mA/cm². It is also observed that the white emissive color becomes more stable with respect to

drive current density as the EL color shift is only of $\Delta CIE_{x,y} = \pm(0.013, 0.009)$ from 1 mA/cm^2 to 100 mA/cm^2 as shown in Figure 3-9(b).
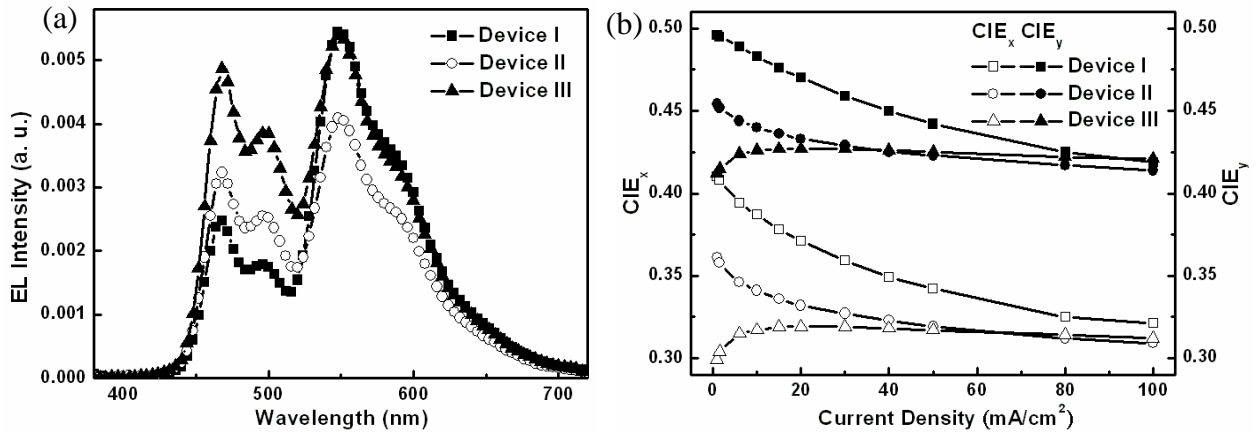
Figure 3-9 (a) EL spectra at 20 mA/cm^2. (b) CIE$_{x,y}$ coordinates *vs* current density characteristics of devices I, II, and III.

Detailed EL performances of these devices are summarized in Table 3-2. The voltage, current efficiency, power efficiency, external quantum efficiency (E. Q. E.), and color coordinates were measured at 20 mA/cm^2. All *p*-i-*n* white devices show a much lower drive voltage and a dramatic gain in power efficiency as compared with those of conventional white device. Device III can achieve 10 cd/A and 9.3 lm/W at 1000 cd/m^2 which are considerably better than those of device II with 7.3 cd/A and 6.8 lm/W. It is noteworthy that both *L-V* and *J-V* curves of device III are steeper than those of conventional white device as depicted in Figure 3-10. The threshold voltage of device III is around 2.9 V. When driven at 6 V, device III can reach 10000 cd/m^2 which is nearly 8 times brighter than the conventional device. These results prove that the efficient exciton confinement is one of the most important factors in controlling the RZ shift under various drive currents and it is also indispensable for the

development of a highly efficient and color stable *p-i-n* WOLED.

Table 3-2 EL performances of *p*-i-*n* white OLED devices at 20 mA/cm^2.

Device	Voltage (V)	Current Eff. (cd/A)	Power Eff. (lm/W)	E. Q. E. (%)	CIE$_{x,y}$
Conventional	6.4	9.0	4.4	3.5	(0.32, 0.41)
I	4.4	9.1	7.1	3.0	(0.37, 0.47)
II	3.6	7.4	6.4	2.7	(0.33, 0.43)
III	3.8	9.9	8.2	3.6	(0.32, 0.43)
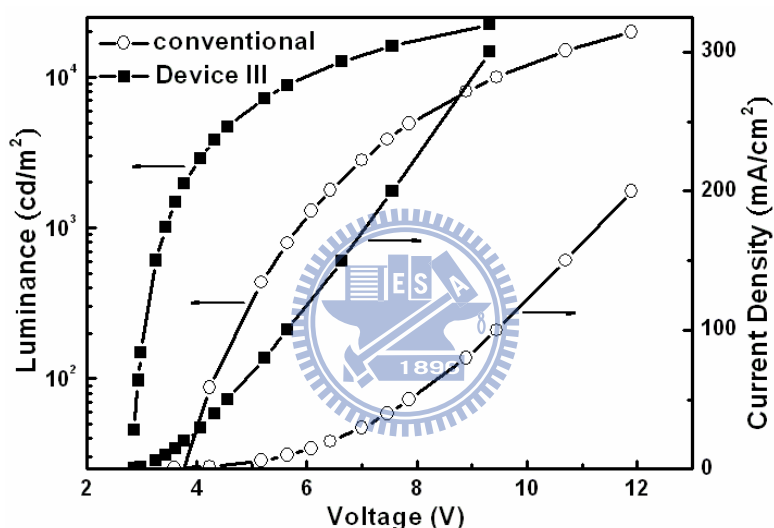
Figure 3-10 *L-J-V* characteristics of conventional white device and device III.

3.6   Development of tandem *p*-i-*n di*-chromatic WOLED device

For applications of WOLEDs, it is important that WOLEDs possess high brightness and EL efficiency at a lower current density and stable spectral characteristics in a wide range of injection current. In the past years, many monochrome tandem OLEDs have been reported to be useful for providing high luminance [26,27], the luminance at a fixed current density increases linearly with the number of stacked and independent OLED elements. This can lead to a

significant improvement in lifetime by reducing the degradation that accompanies the high drive currents required to achieve similarly high brightness in a single-unit device.

In this section, we consolidate both the structural features of *p*-i-*n* technique and that of the tandem device concept into one WOLED device to modify the high drive voltage issue of reported tandem WOLEDs [28,29]. The major challenge in tandem OLEDs in general is to prepare the effective connecting layer between emitting units so that the current can smoothly flow through without facing substantial barriers. The organic doped bilayer in this study encompasses an *n*-doped organic layer and a *p*-doped organic layer to form a doped organic *p-n* junction at their contact interface, and offers several advantages, including excellent optical and electrical properties, as well as the ease of fabrication by thermal evaporation.

The architectures of the WOLED devices are shown in Figure 3-11. Device III is the standard *p-i-n* WOLED unit with a DEML system as we discussed in last section, which gives rise to a balance white emission in a thin thickness of 15 nm. The DEML system comprises one co-dopant emitting layer with MADN: 5% NPB: 3% DSA-Ph: 0.2% Rb and one blue emitting layer of MADN: 5% NPB: 3% DSA-Ph. Device IV is the tandem *p*-i-*n* WOLED with stacking two WOLED units by a bilayer of organic doped thin film with optimized thickness consist of BPhen: 2% Cs_2CO_3/NPB (20 nm): 50 % (v/v%) WO_3 (70 nm). The *n*-type doped layer and the *p*-type doped layer are in contact with each other to form a doped organic *p-n* junction at their contact interface.
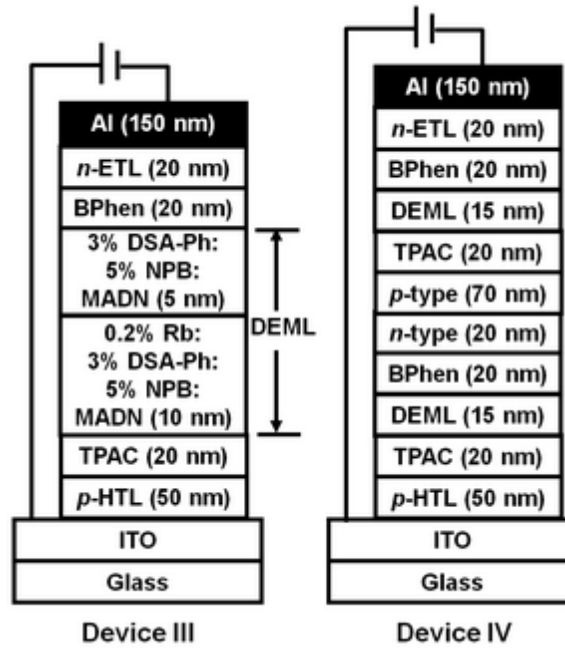
Figure 3-11 Device architecture of devices III and IV.

Figure 3-12 shows the transmittance of BPhen: 2% Cs_2CO_3 (20 nm)/NPB: 50 % (v/v%) WO_3 (70 nm) bilayer thin film and the connecting layer is transparent in the visible region from 420 nm to 750 nm, which is essential to achieve an efficient tandem WOLED. As shown in Figure 3-13(a), devices III and IV achieved 2105 cd/m^2 and 4.5 V, 4780 cd/m^2 and 9.6 V at 20 mA/cm^2, respectively. As expected, the luminance and drive voltage increases with the increasing number of active units. Both devices III and IV show near flat current efficiency versus current density response as shown in Figure 3-13(b). Device IV with tandem structure achieved a current efficiency of 23.9 cd/A and an E. Q. E. of 8.5% at 20 mA/cm^2, which is about 2.3 times greater than those of device III (10.5 cd/A and 3.9%). The enhanced EL efficiency is attributed to the effectiveness of the conductive p-n junction in electrically connecting two emitting units. Both light emissive units can efficiently produce light under the same current driving. It can also be observed that the power efficiency of device

IV (7.8 lm/W at 20 mA/cm^2) is much higher than those of the reported fluorescent tandem WOLEDs [28,29] due to the *p*-i-*n* structure of device IV, which can effectively reduce the high drive voltage issue of tandem OLED device.
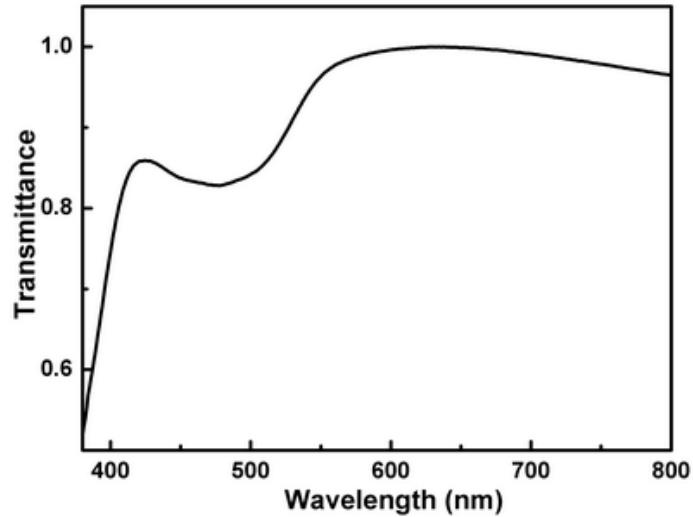
Figure 3-12 Transmittance spectrum of BPhen: Cs$_2$CO$_3$ (20 nm)/NPB: WO$_3$ (70 nm) thin film.
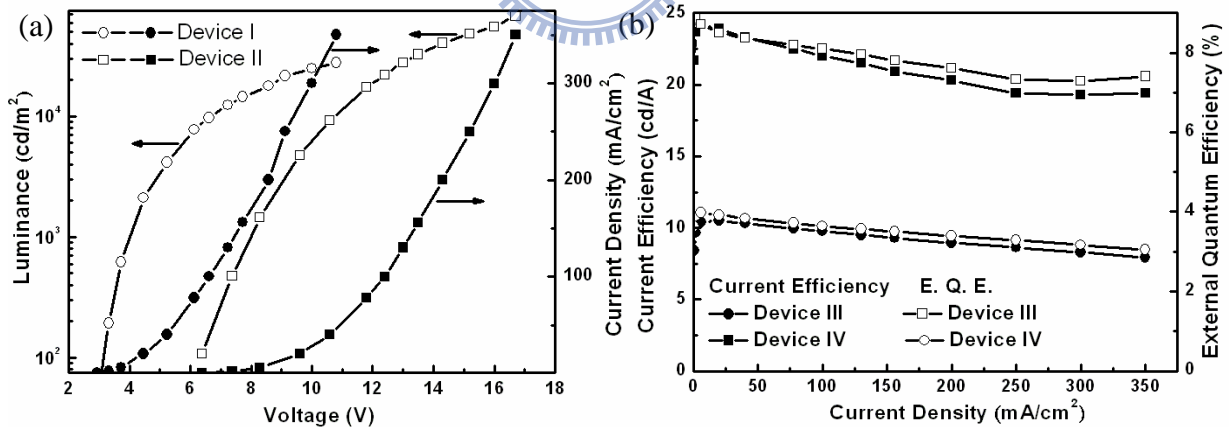
Figure 3-13 (a) *L-J-V* and (b) current efficiency and external quantum efficiency *vs* current density characteristics of devices III and IV.

Figure 3-14(a) shows the EL spectra of devices III and IV at 20 mA/cm^2 in the forward direction. With respect to device III, device IV also simultaneously emits a balanced white color and an essentially identical EL spectrum with

CIE$_{x,y}$ coordinates of (0.30, 0.43) and no unexpected peak-shift was observed, except the relative intensity of blue emission is slightly reduced and the full width of half maximum of device IV (136 nm) is smaller than that of device III (144 nm). This phenomenon is not expected to result from shifting of the RZ because these devices were all driven at a fixed current. We attribute this slight spectrum change to the optical interference and minor microcavity effect in multilayer devices, which has been reported in tandem OLEDs [30]. As shown in Figure 3-14(b), under different levels of luminance, device IV also reveals a stable EL color with ΔCIE$_{x,y}$ of ±(0.024, 0.030) from (0.303, 0.430) to (0.297, 0.400) at a broad range from 4700 cd/m^2 to 67800 cd/m^2 and nearly no current-induced quenching was observed either as depicted in Figure 3-13(b).
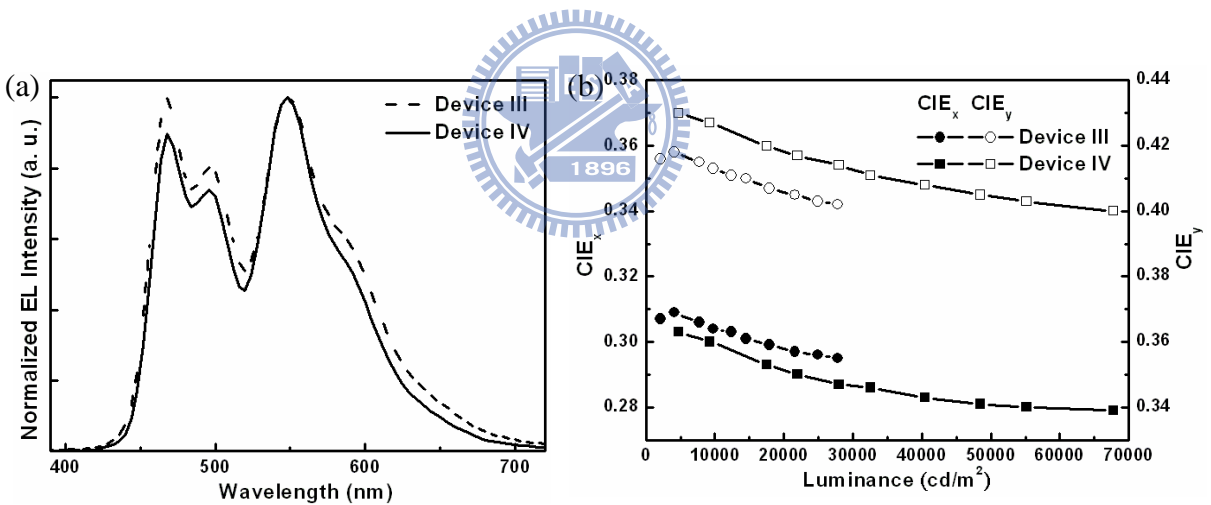
Figure 3-14 (a) EL spectra at 20 mA/cm^2 and (b) CIE$_{x,y}$ coordinates *vs* luminance characteristics of devices III and IV.

Another important factor of tandem WOLED devices is to obtain high EL efficiency and stable EL color with acceptable angular dependency characteristics. Figure 3-15(a) shows the normalized EL efficiency versus the viewing angle characteristics of tandem device IV. It is generally assumed that

the EL emission pattern from OLEDs is approximately Lambertian [31,32] and it is clear that the angular dependence of device IV is well fitted by a Lambertian distribution. The EL spectra of device IV under different viewing angles of 0°, 30°, and 60° were also shown in Figure 3-15(b). It is noteworthy that the emission shows less angular dependence in device IV as two main peaks of white emission at different viewing angles remain the same. The shifts in CIE x and y coordinates of device IV from the viewing angle of 0° to 60° are only 0.024 and 0.01, respectively. In a strong microcavity effect, OLED devices potentially yield a non-Lambertian emission profile and cause a large angular-dependent color shift. According to our observation of the angular dependence of intensity and color, the microcavity effect is minor in this tandem device which is in agreement with previous report [30].
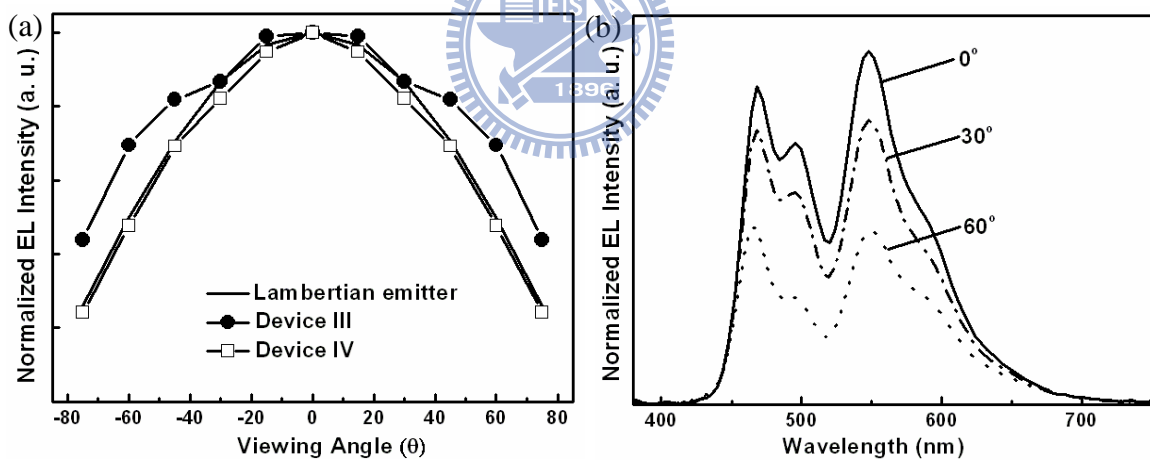
Figure 3-15 (a) Normalized EL intensity *vs* viewing angle characteristics of devices III and IV. (b) EL spectra of device IV under viewing angles of 0°, 30°, and 60° off the surface normal.

3.7   Summary

Detailed EL performances of *di*-chromatic WOLED devices discussed in this chapter are summarized in Table 3-3. It is apparent that introducing *p*-i-*n*

system into OLED device architecture can indeed reduce the drive voltage. To carefully control the RZ location in a thin layer thickness, we demonstrated highly efficient *p*-i-*n* WOLEDs with a DEML system, in which the co-deposited NPB molecules in the DEML were used as the assistant dopant (NPB) to shift the RZ towards the blue emitting layer and balance the blue and yellow emission intensity. The refined exciton confinement of *p*-i-*n* WOLED device III has been shown to significantly improve the EL performance, giving rise to 10 cd/A and 9.3 lm/W at 1000 cd/m^2 and a stable white color under various drive conditions.

Table 3-3 EL performances of WOLED devices at 20 mA/cm^2

Device	Voltage (V)	Current Eff. (cd/A)	Power Eff. (lm/W)	E. Q. E. (%)	CIE$_{x,y}$	NTSC (%)	CRI
Conventional	6.4	9.0	4.4	3.5	(0.32, 0.41)	61.3	66
III (one unit)	3.8	9.9	8.2	3.6	(0.32, 0.43)	62	67
IV (two units)	9.6	23.9	7.8	8.5	(0.30, 0.43)	61.9	67

We also developed a tandem *p*-i-*n* WOLED device IV consists of two individual *p*-i-*n* WOLED units connected electrically with an optical transparent and doped organic *p-n* junction utilizing BPhen: Cs$_2$CO$_3$/NPB: WO$_3$. The charge-carriers for recombination of this tandem WOLED are well-balanced under various current densities due to the DEML system in each individual *p*-i-*n* WOLED, giving rise to one of the best EL efficiency of 23.9 cd/A and 7.8 lm/W with CIE$_{x,y}$ coordinates of (0.30, 0.43). The EL color of the tandem device IV will not change significantly with respect to drive current variation and forward viewing angle.

Based on these results, we conclude that WOLEDs with *p*-i-*n* structure

really has the potential to be applied in portable electronics due to its high power efficiency. In addition, WOLEDs with tandem structure also can be one candidate of solid-state light source due to its high brightness at low current density. However, these *di*-chromatic WOLEDs still have drawbacks, such as low color gamut about 61-62% and low CRI value of 67. These undesirable properties will affect their applications in full-color display and light source. Therefore, to improve the color gamut and CRI value, our experiments will focus on developing *tri*-chromatic WOLED device in next chapter.

References

[1] *Commission internationale de l'Eclairage proceedings*, Cambridge: Cambridge University Press (1931).

[2] G. B. Rybicki, A. P. Lightman, *Radiative Processes in Astrophysics*, New York: John Wiley & Sons (1979).

[3] J. Mehra, H. Rechenberg, *The Historical Development of Quantum Theory*, **1**, New York: Springer-Verlag (1982).

[4] G. Wyszelki, W. S. Siles, *Color Science*, 2nd edition, New York: Wiley (1982).

[5] A. R. Duggal, J. J. Shiang, C. M. Heller, D. F. Foust, *Appl. Phys. Lett.* **80**, 3470 (2002).

[6] J. Kido, K. Hongawa, K. Okuyama, K. Nagei, *Appl. Phys. Lett.* **64**, 815 (1994).

[7] J. Kido, M. Kimura, K. Nagei, *Science* **267**, 1332 (1995).

[8] R. F. Service, *Science* **310**, 1762 (2005).

[9] B. W. D'Andrade, S. R. Forrest, *Adv. Mater.* **16**, 1585 (2004).

[10] I. ul Haq Raja, J. Y. Lee, I. T. Kim, S. H. Lee, *Monatsh. Chem.* **139**, 725 (2005).

[11] K. T. Kamtekar, A. P. Monkman, M. R. Bryce, *Adv. Mater.* **22**, 572 (2010).

[12] P. A. Levermore, V. Adamovich, K. Rajan, W. Yeager, C. Lin, S. Xia, G. S. Kottas, M. S. Weaver, R. Kwong, R. Ma, M. Hack, J. J. Brown, *Proceedings of SID2010*, p. 786, May 23-28 (2010), Seattle, WA, USA.

[13] P. Loebl, V. van Elsbergen, H. Boerner, C. Goldmann, S. Grabowski, D. Bertram, *Proceedings of SID2010*, p. 782, May 23-28 (2010), Seattle, WA, USA.

[14] T. Komoda, H. Tsuji, N. Ito, T. Nishimori, N. Ide, *Proceedings of SID2010*, p. 993, May 23-28 (2010), Seattle, WA, USA.

[15] M. T. Lee, H. H. Chen, C. H. Tsai, C. H. Liao, C. H. Chen, *Appl. Phys. Lett.* **85**, 3301 (2004).

[16] Y. Sato, *Semicond. Semimetals* **64**, 209 (2000).

[17] H. Murata, C. D. Merritt, Z. H. Kafafi, *IEEE J. Sel. Top. Quantum Electron.* **4**, 119 (1998).

[18] J. Huang, M. Pfeiffer, A. Werner, J. Blochwitz, S. Liu, K. Leo, *Appl. Phys. Lett.* **80**, 139 (2002).

[19] C. H. Kim and J. Shinar, *Appl. Phys. Lett.* **80**, 2201 (2002).

[20] J. T. Lim, N. H. Lee, Y. J. Ahn, G. W. Kang, C. H. Lee, *Curr. Appl. Phys.* **2**, 295 (2002).

[21] P. M. Borsenberger, L. Pautmeier, R. Richert, Bässler, *J. Chem. Phys.* **94**, 8276 (1991).

[22] T. Yasuda, Y. Yamaguchi, D. C. Zou, T. Tsutsui, *Jpn. J. Appl. Phys. Part 1* **41**, 5626 (2002).

[23] C. C. Chang, M. T. Hsieh, J. F. Chen, S. W. Hwang, C. H. Chen, *Appl. Phys. Lett.* **89**, 253504 (2006).

[24] B. Wei, K. Furukawa, M. Ichikawa, T. Koyama, Y. Taniguchi, Mol. *Cryst. Liq. Cryst.* **426**, 295 (2005).

[25] Y. S. Wu, T. H. Liu, H. H. Chen, C. H. Chen, *Thin Solid Films* **496**, 626 (2006).

[26] L. S. Liao, K. P. Klubek, C. W. Tang, *Appl. Phys. Lett.* **84**, 167 (2004).

[27] T. Y. Cho, C. L. Lin, C. C. Wu, *Appl. Phys. Lett.* **88**, 111106 (2006).

[28] C. C. Chang, J. F. Chen, S. W. Hwang, C. H. Chen, *Appl. Phys. Lett.* **87**, 253501 (2005).

[29] F. Guo and D. Ma, *Appl. Phys. Lett.* **87**, 173510 (2004).

[30] V. Bulovic, V. B. Khalfin, G. Gu, P. E. Burrows, D. Z. Garbuzov, S. R. Forrest, *Phys. Rev. B* **58**, 3730 (1998).

[31] J. S. Kim, P. K. H. Ho, N. C. Greenham, R. H. Friend, *J. Appl. Phys.* **88**, 1073 (2000).

[32] K. Saxena, D. S. Mehta, R. Srivastava, M. N. Kamalasanan, *Appl. Phys. Lett.* **89**, 061124 (2006).

Chapter 4

Development of Fluorescent Deep Blue System and *Tri*-Chromatic White Organic Light-Emitting Diodes

4.1   Introduction

For full-color OLED display applications, it is essential to deliver a set of primary RGB emitters with sufficiently high luminous efficiency, properly balanced color chromaticity, as well as sufficient operational stability. Such a set of emitters has been amply demonstrated by using a guest-host doped emitting system which encompasses a single or cohost matrix dispersed with various highly fluorescent or phosphorescent guest dopants leading to EL with the desirable hues [1]. With the discovery and rapid improvement of phosphorescent dopant materials along with their matching host, hole-blocker and device architecture capable of harvesting both the singlet and triplet excitons electro-generated in the doped emitter, in today's OLEDs, to achieve high efficiency and color saturation for the *red* and *green* emitters is no longer a major problem. The decision by Pioneer in 2003 announcing the use of one of United Display Corporation's (UDC) red phosphorescent dopants coupled with a BAlq-based host material in its new 1.1-in passive matrix 96 RGB 72 full-color subdisplay cellular phone has all but removed the last skepticism hanging over the intrinsic stability issue of phosphorescent materials worthy of production [2]. In 2009, UDC disclosed their improvement for red phosphorescent devices (26 cd/A) with operational stability of 500000 h at an initial luminance of 1000 cd/cm^2 and CIE$_{x,y}$ coordinates close to (0.24, 0.36) [3]. Similar improvement of extremely efficient green phosphorescent devices (64

cd/A) with operational stability of 150000 h at an initial luminance of 1000 cd/cm^2 and CIE$_{x,y}$ coordinates close to (0.35, 0.61) has also been achieved by UDC [3]. It is expected that, in the future, we would also find one of these red and green phosphorescent materials ending up in some forms of OLED products in the marketplace.

Unfortunately, the same cannot be said for the state-of-the-art of the phosphorescent blue emitter which remains to be the weakest link in the development of RGB phosphorescent materials. At the International Display Manufacturing Conference (IDMC) 2005, held in Taipei, Taiwan, Samsung SDI managed to disclose for the first time [4] a deep blue phosphorescent emitter with (0.15, 0.15) but only can last for 150 h. To date, the best triplet blue emitter reported is due to UDC [5] which claimed to have achieved a luminous efficiency of about 69 cd/A at 1000 cd/m^2 with a sky blue emission at wavelength of 474 nm, unfortunately, there is no lifetime data for this new blue emitter. Part of the problems in producing a decent saturated blue phosphorescent emitter is due to the fact that there is simply no good host material available that possesses sufficiently large triplet bandgap energy (3 eV) to effectively prevent triplet exciton of the dopant from quenching by back energy transfer, and the limitation of short–conjugated ligand selection for synthesizing transition metal-based metal–ligand charge-transfer (MLCT) complexes serves only to compound the already grave and aggravated situation [6]. All things considered, it suffices to predict that the advent of a robust phosphorescent blue emitter with all of the necessary attributes for high efficiency, saturated color, as well as device stability would be extremely difficult.

Recently, several approaches to high-efficiency WOLEDs have been demonstrated, foremost among them introduces a blue fluorescent dopant together with red and green phosphorescent dopants in the emission layer (EML) [7,8]. In that device, the blue fluorescent dopant harvests a majority of singlet excitons, with the remainder of lower energy triplets diffusing through the conductive host to directly excite the green and red phosphors. This architecture allows for increased power efficiency by resonant energy transfer from the conductive host into both the singlet and triplet energy levels. Indeed, this architecture eliminates exchange energy losses of 0.5-1.0 eV resulting from intersystem crossing from the host singlet into a blue phosphor triplet state.

It is mainly for this reason that developing fluorescent blue OLEDs with high efficiency, deep-blue color, and long operational lifetime is indispensable and is always being considered. There have been many reports on blue host materials have been reported, such as anthracene (will be introduced in next section), *di*(styryl)arylene [9], *tetra*(phenyl)pyrene [10], terfluorenes [11,12], and *tetra*(phenyl)silyl derivatives [13,14].

In this chapter, we design and develop a new blue anthracene-based host for fluorescent deep blue emitter and adopt this efficient deep blue system into *tri*-chromatic WOLED device architecture.

4.2 Prominent blue fluorescence OLED materials based on anthracene core structure

Anthracene has a rigid ring structure that minimizes vibronic energy levels to give very high fluorescence quantum efficiency as well as color purity. In addition, chemical modification of anthracene is relatively easier than most other rigid aromatics due to its better solubility in common organic solvents.

Furthermore, anthracene possesses 14π-electron aromaticity, thus it is relatively stable in terms of thermal and electrochemical properties. However, anthracene by itself with no substituent attached is highly crystalline, fluoresces in the near UV and has a propensity to crystallize in thin-films, which greatly limits its application in OLED. Therefore, various studies have been focused on derivatizing anthracene core with aromatic substituents on 9-, 10- and/or bulky steric substituents on 2-, 6- positions as shown in Figure 4-1 to prevent its crystallization and stabilize its thin-film morphology upon thermal evaporation into thin-films. One of the best deep blue fluorescent derivative among these is 9,10- *di*phenylanthracene known as DPA which has near unity fluorescence quantum efficiency in dilute solution and is also highly fluorescent in the solid state. But its fluorescence is too deep in the blue and it is prone to crystallize in solid-state thin film [15,16], thereby limiting its OLED applications. This is because crystalline formation in solid-state device destroys thin-film homogeneity, creates pin-holes and raises electrical resistance that ultimately leads to device failure [17]. It is well known that amorphous thin film materials as applied to OLEDs having high T_g are almost always less vulnerable to heat and, hence, their devices perform more stably [18,19,20,21]. Thus, there have been numerous anthracene derivatives designed and synthesized with strategically positioned bulky groups which were beneficial to stabilize their amorphous solid-state by virtue of their dissymmetrical molecular shape that mitigates intermolecular interaction and crystal formation. Later, studies also showed that the introduction of bulky spacer can alleviate unfavorable excimer emission [22].
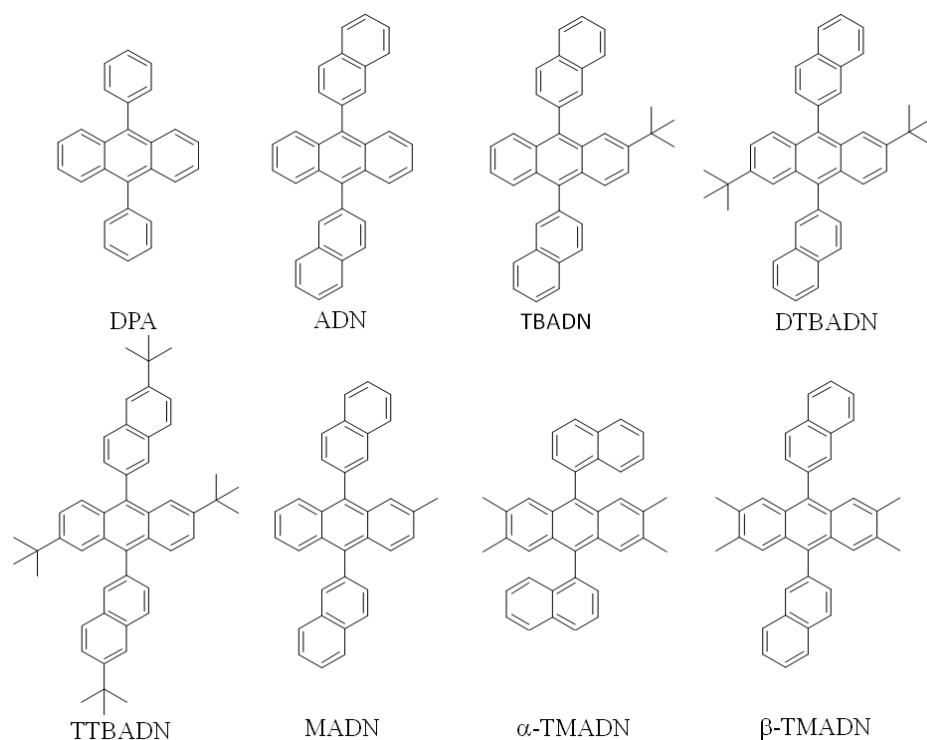
Figure 4-1 Structures of anthracene-based blue host materials.

In 2002, Shi and Tang at Kodak [23] reported the first stable blue OLED emitter using 2, 5, 8, 11-*tetra*(*t*-butyl)perylene (TBP) blue dopant and 9,10-*di*(2-naphthyl)anthracene (ADN) as blue host material. Their device structure was ITO/copper phthalocyanine (CuPc) (25 nm)/NPB (50 nm)/ADN:TBP (30 nm)/Alq$_3$ (40 nm)/Mg:Ag (9:1, 200 nm), which achieved a luminance efficiency of 3.5 cd/A with CIE$_{x,y}$ coordinates of (0.15, 0.23). The device operational lifetime reported was about 4000 hrs with an initial luminance of 636 cd/m^2, which was the best ever published in a formal journal and a blue OLED record of its time.

After the disclosure of this pioneering report, many researchers started to focus and pursue materials based on anthracene with better, hopefully improved EL performance than that of ADN. It was soon discovered that the morphology of thin-film ADN as blue host material is unstable and tends to deteriorate

(crystallize) under prolonged electrical stress or annealing at elevated temperatures (95 ℃), and its blue EL color is also not pure with $CIE_{x,y}$ of (0.17, 0.17) [24]. Quickly, in attempts to improve the emissive color, the *tert*-butyl substituted derivative at *C*-2 position of anthracene namely, 2-(*t*-butyl)-9,10-*di*(2-naphthyl)anthracene (TBADN), was reported by the Kodak group in an European patent [25]. Using the same dopant and device configuration, TBADN was able to generate a deeper blue emission of $CIE_{x,y}$ (0.13, 0.19), but its efficiency was considerably lower than that of ADN, and unfortunately neither morphological nor device stability data was disclosed in that patent.

In 2004, two isomeric anthracene derivatives, 2,3,6,7-*tetra*methyl-9,10-*di*(1-naphthyl) anthracene (α-TMADN) and 2,3,6,7-*tetra*methyl-9,10-*di*(2-naphthyl) anthracene (β-TMADN) were reported to provide highly efficient blue emission with similar design concept [26,27]. In the device structure of ITO/NPB (50 nm)/blue emitter (15 nm)/4,7-diphenyl-1,10-phenanthroline (BPhen, 40 nm)/Mg:Ag, α-TMADN device achieved a current efficiency of 3.1 cd/A with $CIE_{x,y}$ of (0.15, 0.21). The efficiency of β-TMADN was better with 4.5 cd/A and CIE coordinates of (0.16, 0.22). The experimental results clearly demonstrated that the introduction of four methyl groups to the molecular structure of ADN appears to be beneficial in producing improved device performance. The reason may be that the twisted nonplanar molecular structures of α-TMADN and β-TMADN which is distorted by the steric effect of the four methyl substituents could prevent the undesirable molecular aggregation [28]. Additionally, it was revealed that when the blend of β-TMADN and α-TMADN was used as the light-emitting material, the device

performance can be further improved to 5.2 cd/A with $CIE_{x,y}$ of (0.15, 0.23). The improved efficiency was attributed to the higher fluorescent quantum yield of β-TMADN. (The fluorescence quantum yields of α-TMADN and β-TMADN were measured to be 0.50 and 0.65, respectively.)

In an effort to improve the thin-film morphological stability of ADN by molecular engineering, several multi-*t*-butyl-substituted ADN derivatives, such as 2,6-*di*(*t*-butyl)-9,10-*di*(2-naphthyl)anthracene (DTBADN) and 2,6-*di*(*t*-butyl)-9,10-*di*[6-(*t*-butyl)-2-naphthyl]anthracene (TTBADN) were synthesized and compared with ADN and TBADN [29] (structures are shown in Figure 4-1). It was discovered, however, by virtue of its inductive effect, that the *t*-butyl groups could induce significant bathochromic shift of ADN's fluorescence in both of these derivatives and consequently lower its PL quantum efficiency. It was also suggested that the greenish color and low EL efficiency of DTBADN and TTBADN could be due to the bulky *t*-butyl groups which tend to twist the chromophore of ADN as revealed by computer simulations using the Quantum CAChe (v. 5.02) program.

To search for derivatives of ADN without adversely impacting on its EL emission, efficiency and charge-carrier mobility, a systematic study of alkyl substitution on the 2-position of ADN was launched in our lab. It was found that the best way to stabilize the morphology of ADN was to strategically place a relatively small methyl-group at *C*-2 position of the anthracene moiety, MADN, which can readily be synthesized by Suzuki coupling of the 2-methyl-9,10-dibromo-anthracene with 2-(napthyl)boronic acid according to a known procedure [30]. By computer simulation, it was found that the symmetry and close molecular packing of ADN is disrupted by the *methyl* substituent

which results in the increase of the intermolecular distance. As a result, the thin-film surface morphology of MADN is considerably more robust than that of ADN as revealed by the AFM photographs before and after annealing (as shown in Figure 4-2). The small methyl substituent imparts no effect on the LUMO/HOMO level of ADN which remains at 2.5/5.5 eV with a bandgap energy of 3 eV. Table 4-1 compares the solution PLs of various substituted ADN derivatives in toluene along with its thermal properties. In comparison with their solution PL fluorescence and relative quantum efficiency in toluene, both MADN and TBADN have better efficiency than those of ADN. Low-temperature PL studies revealed also that both MADN and TBADN have different vibronic levels which hypsochromic-shift their luminescence peaks significantly enough that their CIE color coordinates move to deeper blue and therefore have potential for deep blue OLED application [31].
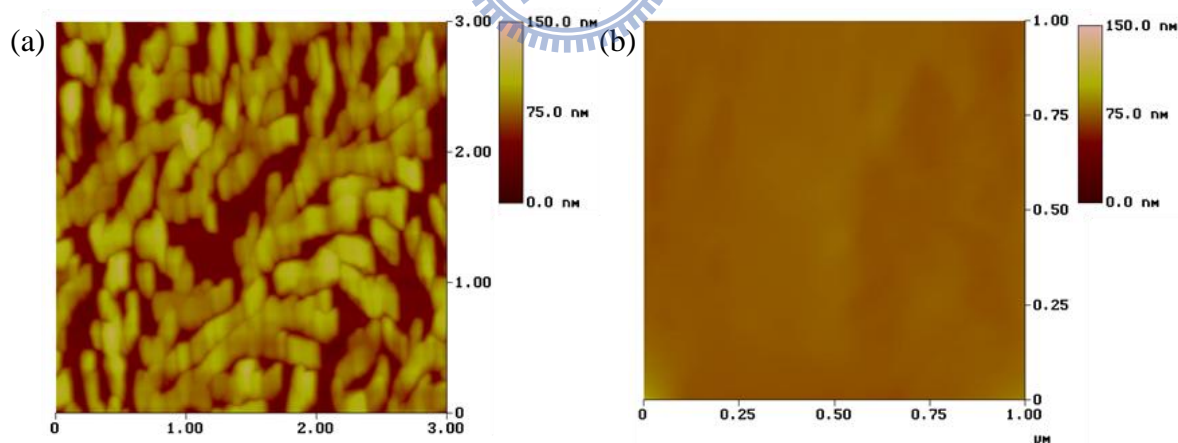
Figure 4-2 AFM images of (a) ADN and (b) MADN after heating at 95 ^{0}C for 1 hr.

Table 4-1 PL and thermal properties of ADN derivatives.

Compound	Relative (η_f)	Emission (nm)	T_d (℃)	T_m (℃)	T_g (℃)
ADN	1	427	396	388	-
TBADN	1.2	430	408	291	128
DTBADN	1.2	442	413	-	-
TTBADN	1.3	446	450	-	-
MADN	1.2	430	397	295	127

Comparison of their EL performance in an optimized device structure of ITO/CF$_x$/NPB (70 nm)/blue host (40 nm)/Alq$_3$ (10 nm)/LiF(1 nm)/Al (200 nm) showed that MADN had the best luminous efficiency of 1.4 cd/A and the lowest drive voltage of 6.2 V (measured at 20 mA/cm^2) with also the bluest color of (0.15, 0.10) that is identical to that of TBADN, as shown in Figure 4-3(a). Device stability data of all three *nondoped* devices depicted in Figure 4-3(b) confirms that MADN stands out as the best in the diarylanthracene-type of blue hosts with a projected lifetime of about 7000 hr at an initial luminance of 100 cd/m^2, which is nearly 3 and 7 times longer than those of ADN and TBADN, respectively.
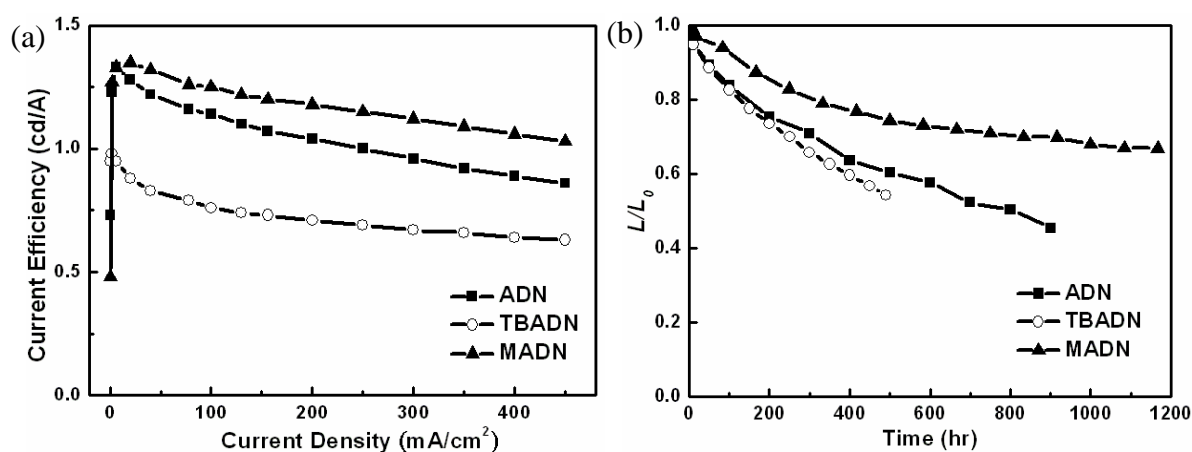
Figure 4-3 (a) EL efficiency and (b) device stability comparisons of ADN, TBADN, and MADN.

When MADN doped with the sky blue dopant, *bis*[(diphenyl)aminostyryl]benzene emitter (DSA-Ph, structure is shown in Table 2-1) [32], its EL performance can reach as high as 9.7 cd/A and 5.5 lm/W at 20 mA/cm^2 with CIE$_{x,y}$ of (0.16, 0.32). It is believed that the high efficiency is due to the good overlap between the absorption spectrum of DSA-Ph and the emission spectrum of MADN, which is an important factor for efficient Förster energy transfer. The stability of this sky blue device is projected to be able to last for 46,000 hr at $L_0 = 100$ cd/m^2.

4.3　　Development of host material for deep blue emitter

The deep-blue color is defined arbitrarily as having a blue EL emission with a CIE coordinates of *y* value (CIE$_y$) < 0.15. Such an emitter can effectively reduce the power consumption of a full-color OLED and also be utilized to generate light of other colors by energy cascade to a suitable emissive dopant [33,34].

Unfortunately, literature with full disclosure on deep blue OLED dopant/host material structures is rather rare and sketchy. One notable example was by Idemitsu Kosan Co. recently presented a styrylamine-based dopant BD-3 to produce an EL efficiency of 7.2 cd/A and a blue color of (0.14, 0.16) [35] and likewise, Kodak also presented about one of their best deep blue devices performance with dopant BK-9 in host BH-3 which achieved an efficiency of 7.4 cd/A and a blue color of (0.14, 0.17) [36]. Neither of them disclosed in these presentations any useful structural information that was needed to substantiate their great device performances.

In 2005, our group disclosed that MADN doped with an *unsymmetrical mono*(styryl)amine fluorescent dopant, *di*(4,4'-biphenyl)

[4-(2-[1,1';4',1"]terphenyl-4-yl-vinyl)phenyl] amine (SA-BiPh), achieved an EL efficiency of 2.2 cd/A at 20 mA/cm^2 with a saturated blue CIE$_{x,y}$ of (0.15, 0.12) and a normalized operational lifetime of 10000 hrs at an initial brightness of 100 cd/m^2 [37].

Although SA-BiPh doped MADN emitter could achieve a saturated deep blue color, the device efficiency is still low and inadequate. It is well known that a guest–host doped emitter system can significantly improve device performance in terms of EL efficiency and emissive color [32]. Therefore, key for developing deep blue OLEDs is not only finding the highly fluorescent deep blue dopant but also the appropriate matching host material in order to enhance the probability of carrier recombination as well as the efficiency of Förster energy-transfer from the host to the dopant molecule.

Therefore, we developed a new anthracene-based wide band gap host material, 2-methyl-9,10-*di*(1-napthyl)anthracene (α,α-MADN) in which the 2-(naphthyl)-substutuent of MADN is replaced by the sterically more demanding 1-(naphthyl)-substutient. The small methyl-substituent at *C*-2 position of the anthracene moiety is preserved with the purpose of disrupting the symmetry of ADN and suppressing its problematic crystallization. The thermal properties of MADN and α,α-MADN are summarized in Table 4-2, in which TGA revealed that the T_d of α,α-MADN was 397 ℃. During DSC measurements, α,α-MADN underwent a glass transition at a relatively high T_g of 133 ℃ and also showed a high melting temperature (T_m) at 315 ℃. The higher thermal properties of α,α-MADN, with respect to those of MADN are essential for morphological stability of thin films.

As we know, the thin-film morphological stability is very sensitive to

pin-hole formation due crystallization or any interfacial change that might be induced by Joule heating [38] during device operation which may in turn impact adversely on the lifetime of the device. The result of AFM measurement as shown in Figure 4-4 indicated that an evaporated film of α,α-MADN possessed a uniform surface that did not undergo any morphological changes when heated at 95 °C for 1 hr. The root-mean-square surface roughness of heated α,α-MADN film is 0.21 nm.

Table 4-2 Thermal, optical, and electrochemical Properties of MADN and α,α-MADN.

Material	T_g (℃)	T_m (℃)	T_d (℃)	$\lambda_{abs,\ max}$ (nm)	$\lambda_{em,\ max}$ (nm)	HOMO LUMO (eV)	E_g (eV)	ϕ_f
MADN	127	257	378	360 378 398	413	5.5 2.55	2.95	0.22
α,α-MADN	133	315	397	358 376 397	430	5.6 2.6	3.0	0.16
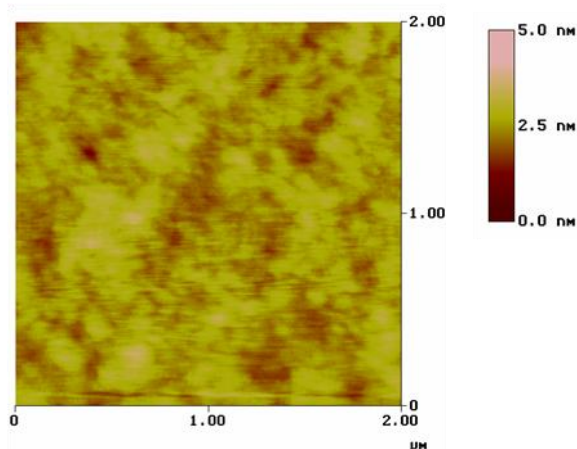
Figure 4-4 AFM topographic images of α,α-MADN thin film deposited on silicon wafers (50 nm) after heating at 95 °C for 1 hr.

Figure 4-5 shows the absorption spectra and solution fluorescence spectra of MADN and α,α-MADN in toluene. The band gap of α,α-MADN is found to be 3.0 eV, which can be determined from the optical absorption threshold and is slightly larger than that of MADN (2.95 eV). In addition, it is obvious that α,α-MADN has a smaller stoke-shift and the fluorescence wavelength λ_{max} of α,α-MADN is 413 nm which is blue-shifted around 17 nm with respect to that of MADN. The principal cause of the hypsochromic-shift is most likely due to the stronger *H atom-H atom* repulsions between the 1-(naphthyl)-substituent and anthracene moiety of α,α-MADN which causes the naphthyl-group to de-conjugate from the anthracene chromophore in the ground state.
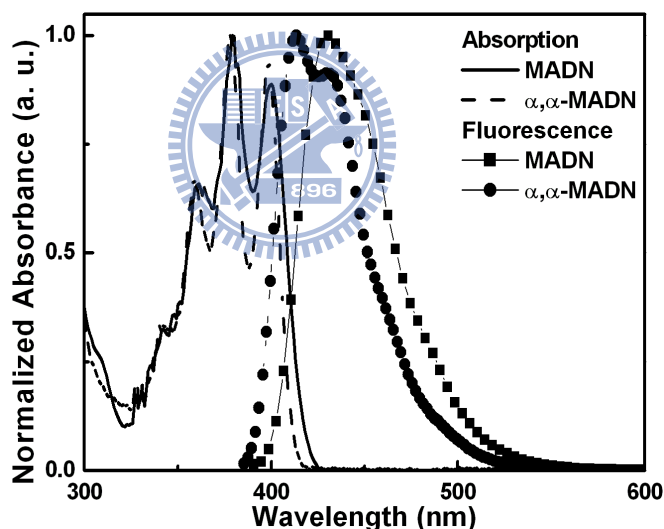
Figure 4-5 Normalized absorption and fluorescence spectra of MADN and α,α-MADN in toluene.

The electrochemical properties of MADN and α,α-MADN were probed by CV as depicted in Figure 4-6. Both of MADN and α,α-MADN exhibited reversible oxidation potentials (E_{ox}) of 1.05 V and 1.12 V, respectively. On the basis of the onset potential for the oxidation and the band gap, we estimated the

HOMO and LUMO energy levels of MADN and α,α-MADN (see Table 4-2) with regard to the energy level of the ferrocene reference (4.8 eV below the vacuum level) [39].
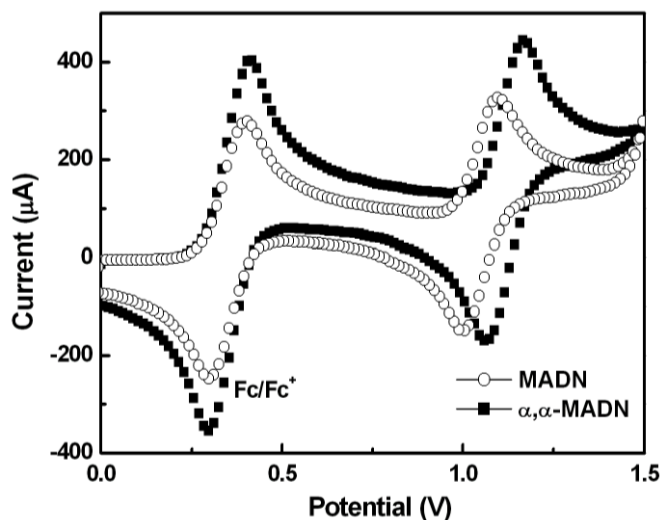
Figure 4-6 Cyclic voltammograms of MADN and α,α-MADN.

4.4   Energy transfer between blue host-guest materials

One of the key developments in the advancement of OLED display technology can be attributed to the discovery of the guest-host doped emitter system [1]. This is because a single host material with optimized transport and luminescent properties may be used together with a variety of highly fluorescent guest dopants leading to EL of desirable hues with very high efficiencies. Another advantage of the doped emitter system in OLEDs is the enhancement of its operational stability by transferring the electrogenerated exciton to the highly emissive and stable dopant site thus minimizing its possibility for non-radiative decay [40].

For fluorescent guest-host doped emitter system, the rate of Förster energy transfer (K_{ET}) can be determined as the following equation:

$$K_{ET} \text{ (Coulmbic)} = k \frac{\kappa^2 k_D^0}{R_{DA}^0} J(\varepsilon_A) \qquad (4.1)$$

the term k is a constant determined by experimental conditions such as the solvent index of refraction and concentration. The term κ^2 takes into account the fact that the interaction between two oscillating dipoles depends on the orientation of the dipoles in space. k_D^0 is the rate constant of donor molecule. R_{DA} is the distance between donor and acceptor. $J(\varepsilon_A)$ is the integrated overlap of the experimental absorption and emission curves [41], which is given by

$$J(\varepsilon_A) = \int_0^\infty I_D \, \varepsilon_A d \, \bar{v} \qquad (4.2)$$

where I_D is the experimental emission spectrum of donor molecule, and ε_A is the experimental absorption spectrum of acceptor molecule, both platted on an energy scale (usually cm^{-1}), and normalized so that complete overlap would correspond to $J = 1.00$.

Therefore, in order to study the energy transfer between our blue hosts (MADN and α,α-MADN) and deep blue emitter SA-BiPh, the absorption spectrum of SA-BiPh and the solution PL spectra of MADN and α,α-MADN in toluene are depicted in Figure 4-7. It is apparent that the spectral overlap between the absorption of SA-BiPh and emission of MADN is poor and the Förster energy-transfer from host to dopant is not expected to be efficient. On the other hand, the *hypsochromic*-shifted emission of α,α-MADN is found to overlap well with the absorption spectrum of SA-BiPh, the overlap area is almost two times larger than the overlap of MADN and MADN, which is essential for efficient Förster energy-transfer. To study the energy-transfer between our hosts and dopant, the emission spectra of 5% SA-BiPh doped MADN and α,α-MADN thin films (spin-coated with PMMA) are depicted in

Figure 4-8. We find that the emissive intensity of SA-BiPh/α,α-MADN film is 1.2 times higher than that of SA-BiPh/MADN film confirming that the Förster energy-transfer is indeed more efficient between α,α-MADN and SA-BiPh, albeit the relative fluorescence quantum yield of α,α-MADN is considerable lower to the extent of only 73% of MADN [The fluorescence quantum yields (ϕ_f) of MADN and α,α-MADN are measured by calibrated integrating sphere, and the values are shown in Table 4-2].
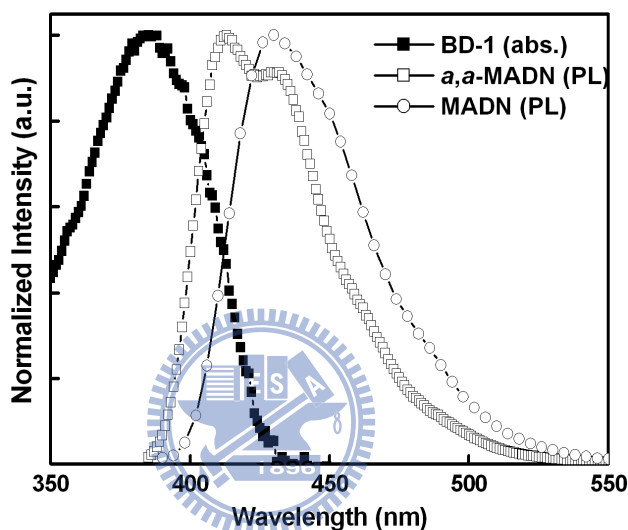
Figure 4-7 Absorption spectrum of SA-BiPh and emission spectra of MADN and α,α-MADN in toluene.
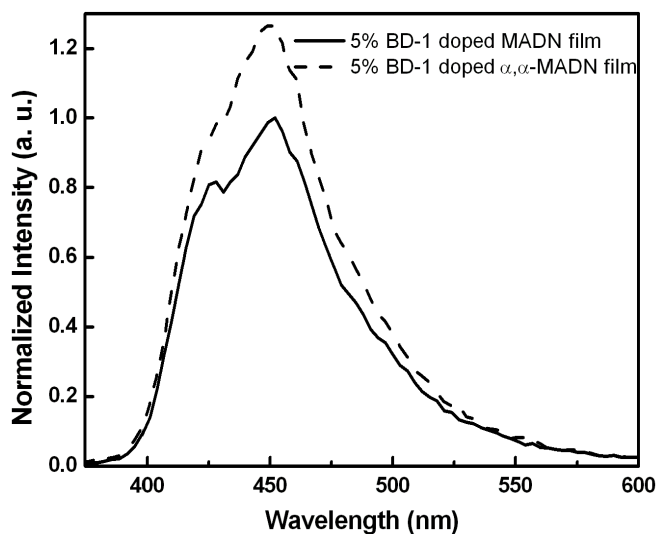
Figure 4-8 Thin-film solid PL spectra of SA-BiPh doped MADN and α,α-MADN in PMMA.

4.5   Device performances of deep blue OLED devices

To demonstrate the efficiency of α,α-MADN as host material for deep blue emitter, four blue devices with the structure of ITO/CF$_x$/NPB (50 nm)/EML (40 nm)/Alq$_3$ (10 nm)/LiF (1 nm)/Al (200 nm) were fabricated. There are two standard blue devices with undoped MADN and α,α-MADN as EML, while other two devices are blue-doped devices with 3% SA-BiPh/MADN and 3% SA-BiPh/α,α-MADN, respectively. CF$_x$, NPB, and Alq$_3$ were used as the hole injection material [42], hole and electron transport materials, respectively.

The detailed EL performances measured at 20 mA/cm^2 are summarized in Table 4-3. The EL efficiency of the undoped α,α-MADN device is only 0.7 cd/A and 0.3 lm/W at 6.7 V with a CIE$_{x,y}$ of (0.15, 0.08). But the SA-BiPh doped α,α-MADN system produced EL efficiencies of 3.3 cd/A and 1.3 lm/W at 6.5 V with a CIE$_{x,y}$ of (0.15 0.13) that is 1.5 times higher than that of SA-BiPh/MADN system of 2.2 cd/A.
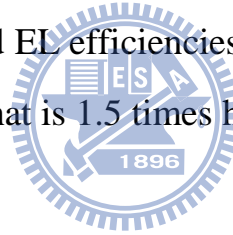
Table 4-3 EL performances of blue devices at 20 mA/cm^2.

Device	Voltage (V)	Current Eff. (cd/A)	Power Eff. (lm/W)	E. Q. E. (%)	CIE$_{x,y}$
undoped-MADN	6.4	1.3	0.6	1.7	(0.15, 0.10)
undoped-α,α-MADN	6.7	0.7	0.3	1.0	(0.15, 0.08)
MADN/ SA-BiPh	6.1	2.2	1.1	2.3	(0.15, 0.12)
α,α-MADN/ SA-BiPh	6.5	3.3	1.3	3.0	(0.15, 0.13)

It is interesting to note that devices of α,α-MADN have a higher applied voltage than devices of MADN (see Table 4-3). For studying the transport phenomenon, two additional carrier-only devices were also fabricated. The electron-only device structure was ITO/2,9-dimethyl-4,7-diphenyl-1,10-phenanthroline (BCP) (30 nm)/neat α,α-MADN or MADN (60 nm)/Alq$_3$ (20 nm)/LiF (1 nm)/Al (200 nm) and the hole-only device structure was ITO/CF$_x$/NPB (20 nm)/neat α,α-MADN or MADN (60 nm)/NPB (20 nm)/Al (200 nm). To explore the underlying physics further, we studied the *J-V* characteristics of the carrier-only devices. The HOMO/LUMO of α,α-MADN and MADN are 5.8/2.8 eV and 5.6/2.6 eV, respectively, and the energy diagrams of carrier-only devices are illustrated in Figure 4-9. Figure 4-10(a) shows *J-V* characteristics of the electron-only devices which reveal that the device of α,α-MADN has a lower applied voltage under high current density (over 40 mA/cm^2). The result can be rationalized by the lower energy barrier (0.1 eV) between the LUMO's of α,α-MADN (2.8 eV) and electron-transporting Alq$_3$ (2.9 eV), which provides an effective pathway for electron to inject from Alq$_3$ to α,α-MADN, especially under high current drive conditions. On the contrary, Figure 4-10(b) shows that α,α-MADN hole-only device has a higher applied voltage than that of the MADN under the same drive current density. We attribute this to the higher energy barrier (0.4 eV) between the HOMO's of hole-transporting NPB (5.4 eV) and α,α-MADN (5.8 eV), which makes holes injection more difficult from NPB to α,α-MADN. From the *J-V* characteristics of the carrier-only devices, we conclude that the deeper HOMO of α,α-MADN is the primary reason for causing the high applied voltage of α,α-MADN devices.
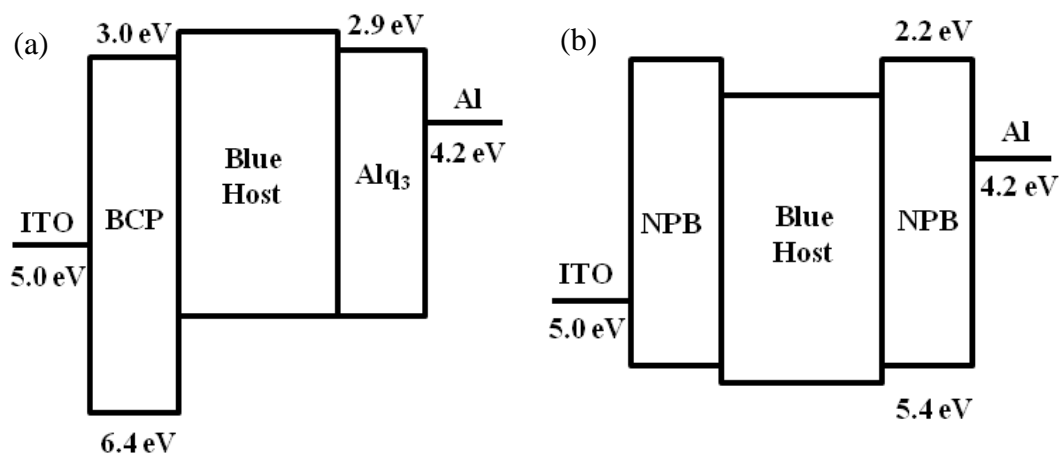
Figure 4-9 Energy diagrams of (a) electron-only and (b) hole-only devices.
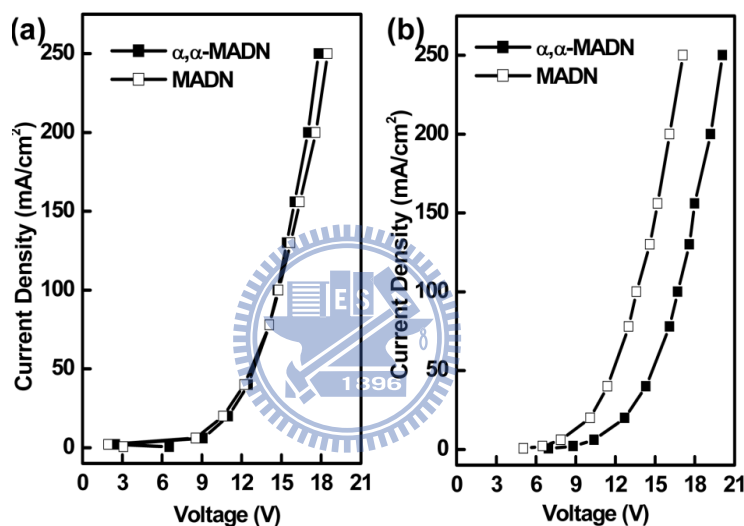
Figure 4-10 *J-V* characteristics of (a) electron-only devices and (b) hole-only devices.

Further, in most Alq$_3$-based OLED devices, the dominant carrier is often the injected hole. With the low-lying HOMO of α,α-MADN which creates a high barrier (0.4 eV) for hole to inject from the hole-transport layer of NPB to the emitter, the probability of carrier recombination near the NPB/α,α-MADN interface where there will be more hole accumulated would be much increased. This restraint of hole injection can also make the hole-electron recombination more efficient in the emitting layer of α,α-MADN device than

that of MADN. We believe that the more balanced carrierr recombination in α,α-MADN device is another reason for the enhanced device efficiency in addition to the more effective Förster energy-transfer.

Figure 4-11 shows the operational lifetime of the four blue devices under a constant current density of 20 mA/m^2 monitored in a dry box. The t_{80} (the time for the luminance to drop to 80% of initial luminance) and initial luminance (L_0) measured for devices of undoped-MADN, undoped-α,α-MADN, MADN doped with SA-BiPh, α,α-MADN doped with SA-BiPh, were 210 hrs @ L_0 = 288 cd/m^2, 85 hrs @ L_0 = 126 cd/m^2, 435 hrs @ L_0 = 484 cd/m^2, and 350 hrs @ L_0 = 660 cd/m^2, respectively. It is apparent that the α,α-MADN device stability can be significantly improved with SA-BiPh doping and can become as stable as the SA-BiPh/MADN device. Assuming scalable coulombic degradation [43], driving at a L_0 value of 100 cd/m^2, the half-lifetime ($t_{1/2}$) of devices MADN doped with SA-BiPh and α,α-MADN doped with SA-BiPh are projected to be 10000 hrs and 9600 hrs, respectively.
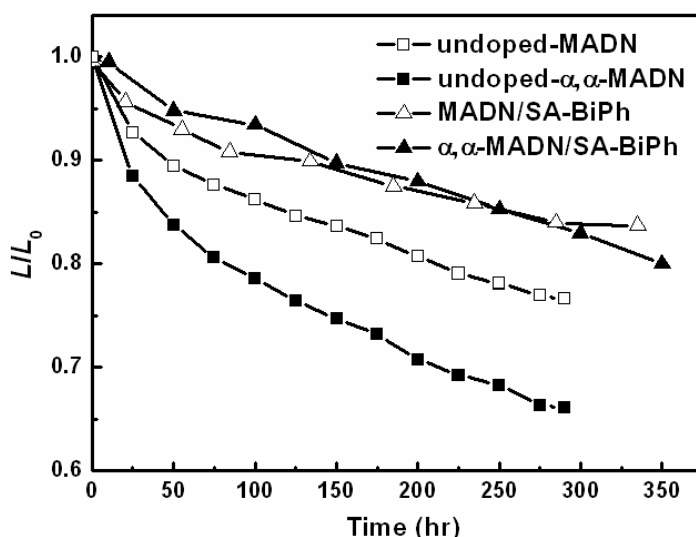
Figure 4-11 Device operational stability of the blue devices.

4.6   Development of *tri*-chromatic WOLED device

In previous experiments, we already developed an efficient and stable fluorescent deep blue system. By taking the advantage of the efficient and saturate blue color, we fabricated *tri*-chromatic white OLED device composed of red, green and blue colors to improve the low NTSC ratio and CRI value of conventional *di*-chromatic white OLED devices, In our *tri*-chromatic white OLED device, we used 4-(dicyanomethylene)-2-*t*-*butyl*-6-(1,1,7,7-tetramethyljulolidyl-9-enyl)-4H-pyran (DCJTB) doped into co-host system of Rb/Alq_3 as red emission layer [44], Alq_3 doped 10-(2-benzothiazolyl)-1,1,7,7-tetramethyl-2,3,6,7-tetrahydro-1*H*,5*H*,11*H*-benzo[*l*]-pyrano[6,7,8-*ij*]quinolizin-11-one (C545T) as green emission layer, in particular, the sky blue emission system (MADN doped DSA-Ph) is replaced by our new deep blue emission system developed in previous section. We used 2BpSA-BiPh as deep blue emitter and α,α-MADN as blue host material. The chemical structures of red, green, and deep blue emitters are shown in Table 2-1. The deep blue device with structure of $ITO/CF_x/NPB$ (50 nm)/α,α-MADN: 5% 2BpSA-BiPh (40 nm)/Alq_3 (10 nm)/LiF (1 nm)/Al (200 nm) shows the EL efficiency of 4.6 cd/A and 2.3 lm/W with an emission peak at 456 nm and $CIE_{x,y}$ of (0.14, 0.15) at 6.3 V and 20 mA/cm^2. Figure 4-12 depicts the EL spectrum of this deep blue device.
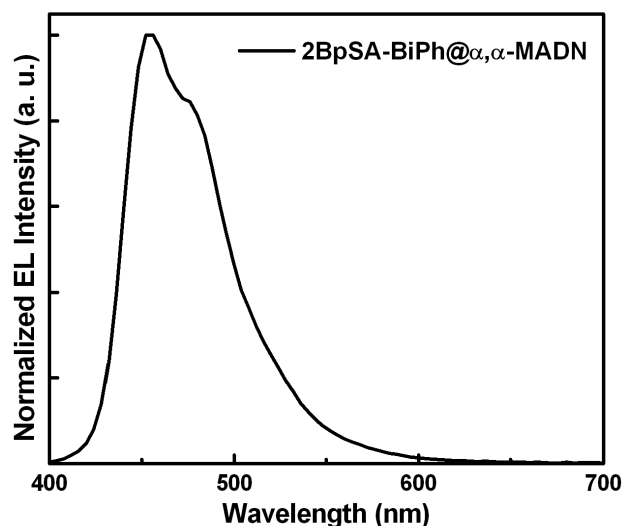
Figure 4-12 EL spectrum of 2BpSA-BiPh doped deep blue device at 20 mA/cm^2.

Firstly, we fabricated a white device with structure of ITO/CF$_x$/NPB (100 nm)/α,α-MADN: 5% 2BpSA-BiPh (25 nm)/Alq$_3$: 1% C545T (10 nm)/60% Alq$_3$: 40% Rb: 1% DCJTB (5 nm)/BPhen (25 nm)/LiF (1 nm)/Al (200 nm). The sequence of three emission layers is blue, green, and red (B/G/R). The device can achieve an EL efficiency of 5.1 cd/A and 2.1 lm/W at 7.6 V and 20 mA/cm^2. The EL spectrum covers a wide range of visible region as shown in Figure 4-13(a), however, the blue emission intensity is much weaker than the red emission, leading to undesirable white emission with CIE$_{x,y}$ coordinates of (0.44, 0.41). Furthermore, a significant EL color shift of this B/G/R device is observed with respect to various drive currents as the CIE$_{x,y}$ coordinates is shifted from (0.521, 0.410) at 2 mA/cm^2 to (0.384, 0.404) at 300 mA/cm^2 with ΔCIE$_{x,y}$ = $\pm$(0.137, 0.006) as shown in Figure 4-13(b). The red emission dominates the EL spectrum at low current density of 2 mA/cm^2, and the intensity of blue and green emission intenisty increase gradually with the increasing current density. We inferred the unstable EL color is due to the RZ shifts toward the blue emitting

layer under high current stress.
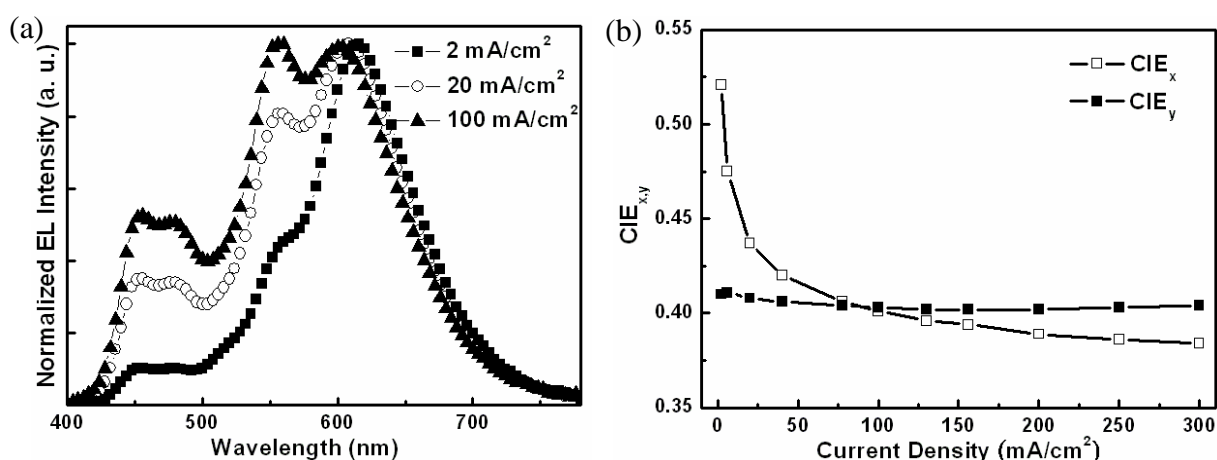
Figure 4-13 (a) EL spectrum of B/G/R device at different current density. (b) CIE$_{x,y}$ coordinates *vs* current density characteristics of B/G/R device.

This phenomenon can be rationalized by the injected holes are often the dominate carriers in most OLED devices, because of the easier hole injection from ITO anode and higher hole mobility of hole transport materials as compared to the electron injection from metal cathode and electron mobility of electron transport materials. Therefore, the carrier RZ is expected to be close to the red emission layer which is nearby the cathode side. In addition, it is known that Rb with LUMO/HOMO of 3.2/5.4 eV and DCJTB with LUMO/HOMO of 2.7/4.9 eV can be carrier traps for holes and electrons as illustrated in Figure 4-14, especially at low electric field [45], which easily cause the problematic white emission color change with various drive currents in white OLED device with multi-emission-layer structure.
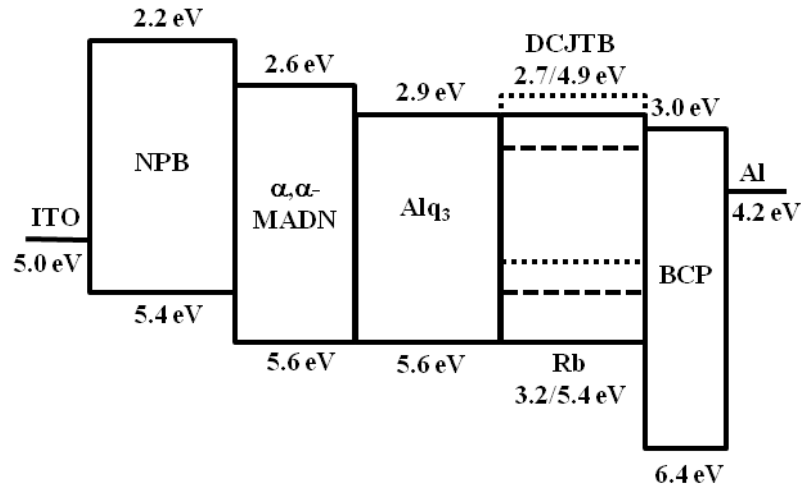
Figure 4-14 Energy diagram of B/G/R device.

In order to alleviate the unstable color issue associated with the undesirable carrier-trapping characteristic of red emission layer, we switched the sequence of three emission layers to red, blue, and green, (R/B/G) and also inserted an additional thin NPB layer (3.5 nm) between red and blue emission layers as an electron-blocking layer to enhance the carrier recombination probability in blue and green emission layer. The device structure is ITO/CF$_x$/NPB (80 nm)/60% Alq$_3$: 40% Rb: 1% DCJTB (10 nm)/NPB (3.5 nm)/α,α-MADN: 5% 2BpSA-BiPh (20 nm)/Alq$_3$: 1% C545T (10 nm)/BPhen (25 nm)/LiF (1 nm)/Al (200 nm). Figure 4-15(a) plots the EL spectrum of this R/B/G device, it shows a more balanced white emission with of CIE$_{x,y}$ of (0.36, 0.36) at 20 mA/cm^2 and the relative intensity of blue light has been increased as compared with the previous device. This phenomenon exhibits the recombination zone indeed shift toward the blue emission layer by switching the sequence of emission layers and improve white CIE$_{x,y}$ coordinates. Moreover, albeit the red emission still dominates the EL spectrum at low current density due to carrier-trapping effect, the EL color shift with respect to varying drive currents has also been improved

90

to $\Delta CIE_{x,y} = \pm(0.033, 0.097)$ from 2 mA/cm^2 to 300 mA/cm^2 as shown in Figure 4-15(b). However, the reduced relative intensity of yellow emission leads to a lower EL efficiency of 4.4 cd/A at 20 mA/cm^2 as compared to the B/G/R device.
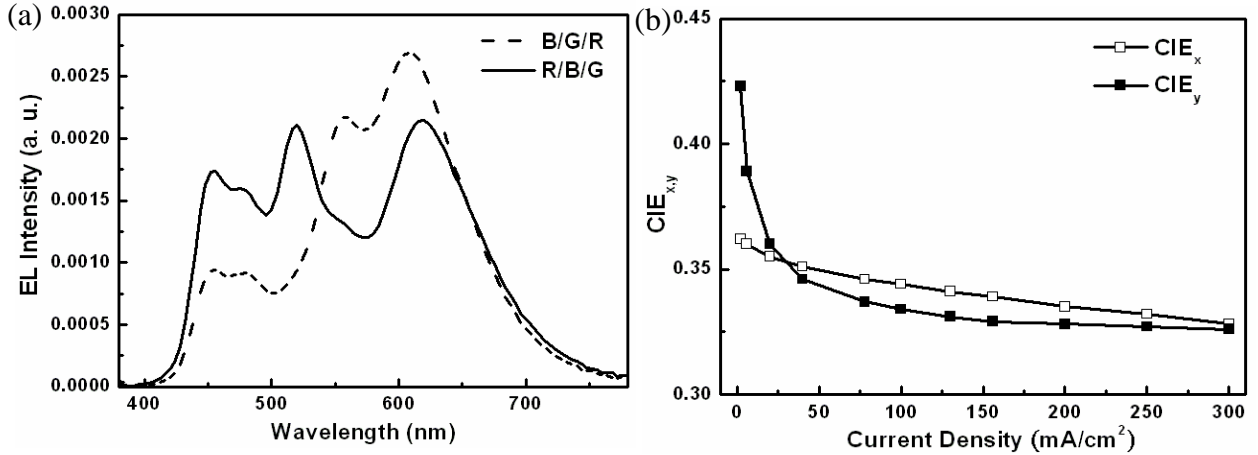
Figure 4-15 (a) EL spectrum of R/B/G device at different current densities. (b) $CIE_{x,y}$ coordinates *vs* current density characteristics of R/B/G device.

To further enhance the power efficiency of our *tri*-chromatic white OLED, we introduce *p*-i-*n* structure into device architecture, in which 50% v/v WO$_3$ doped NPB [46] and 2% Cs$_2$CO$_3$ doped BPhen [47] were used as the *p*-doped transport layer and *n*-doped transport layer, respectively. We also optimized the device structure by tuning the thickness of *p*-doped and *n*-doped layers, the optimized device structure is ITO/*p*-HTL (20 nm)/NPB (10 nm)/60% Alq$_3$: 40% Rb: 1% DCJTB (10 nm)/NPB (4 nm)/α,α-MADN: 5% 2BpSA-BiPh (20 nm)/Alq$_3$: 1% C545T (10 nm)/BPhen (25 nm)/*n*-ETL (20 nm)/Al (200 nm).

As shown in Figure 4-16, this *p*-i-*n* R/B/G white device shows a broad EL spectrum in visible region with three main peaks, clearly indicating the emissions of 2BpSA-BiPh, C545T, and DCJTB at 456, 476, 520, and 620 nm, respectively. Detailed EL performances of these devices measured at 20 mA/cm^2

are summarized in Table 4-4. The *p*-i-*n* R/B/G white device shows a much lower drive voltage and a dramatic gain in power efficiency as compared with other *tri*-chromatic white devices. The *p*-i-*n* R/B/G white device can achieve 8 cd/A and 4.5 lm/W at 5.5 V and 20 mA/cm^2 with a white CIE$_{x,y}$ of (0.34, 0.35).
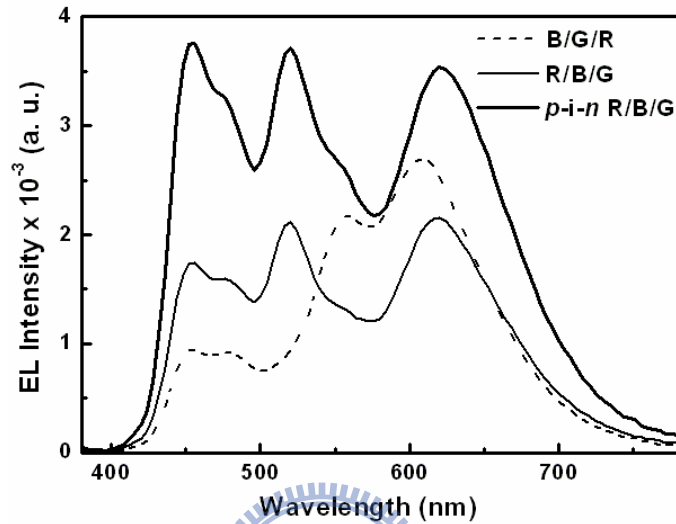
Figure 4-16 EL spectra of *tri*-chromatic white devices at 20 mA/cm^2.

Table 4-4 EL performances of *tri*-chromatic WOLED devices at 20 mA/cm^2.

Device	Voltage (V)	Current Eff. (cd/A)	Power Eff. (lm/W)	E. Q. E. (%)	CIE$_{x,y}$
B/G/R	7.6	5.1	2.1	2.3	(0.44, 0.41)
R/B/G	5.8	4.4	2.4	2.4	(0.36, 0.36)
p-i-*n* R/B/G	5.6	8.0	4.5	4.3	(0.34, 0.35)

Based on these results, we conclude that: (1) due to the smallest bandgap and carrier-trapping characteristic of red emitter, the position and thickness of red emission layer is important; (2) the efficient exciton confinement is one of the most important factors in controlling the RZ shift under various drive currents; (3) the device structure can be optimized by tuning the thickness of

p-doped and *n*-doped layers without affecting *J-V* characteristic because of their high conductivity.

We also tested the operational device lifetime of devices I and II under a constant current density of 20 mA/cm^2 in a dry box as plotted in Figure 4-17. After driving of 200 hr, the luminance decay of R/B/G device and *p*-i-*n* R/B/G device are 15% and 22%, respectively. Assuming the scalable law of Coulombic degradation [45] for driving at L_0 of 100 cd/m^2, the half-decay lifetime ($t_{1/2}$) of R/B/G device and *p*-i-*n* R/B/G device are projected to be around 11518 hrs and 16000 hrs, respectively.
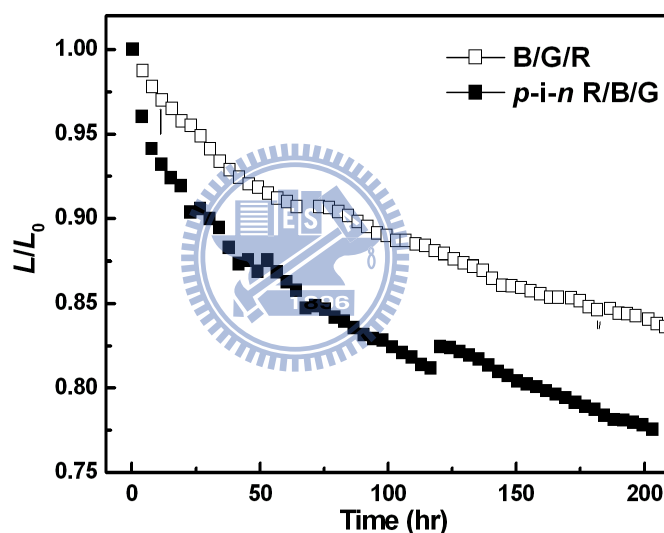
Figure 4-17 Device operational lifetime of B/G/R and *p*-i-*n* R/G/B devices.

4.7 Summary

In this chapter, we developed α,α-MADN as an effective wide bandgap host material for doped deep blue OLED device. We found α,α-MADN can be more efficient in Förster energy-transfer to the deep blue dopant (SA-BiPh). It can also make the injected carriers for recombination more balanced in the emitting layer due to its low-lying HOMO level, resulting in significant improvement in

EL performance giving rise to blue OLED with EL efficiencies of 3.3 cd/A and 1.3 lm/W and a deep blue $CIE_{x,y}$ color coordinates of (0.15, 0.13).

In addition, we also demonstrated one *tri*-chromatic WOLED device composed of our new deep blue system, green, and red emitters. Detailed EL performances of *di*- and *tri*-chromatic WOLED devices are summarized in Table 4-5. The lower current efficiency of *tri*-chromatic WOLED device is attributed to the less intensity around the emission wavelength of 555 nm, which is the most sensitive light for human eyes. However, the *tri*-chromatic WOLED device achieved a higher E. Q. E. of 4.3% and radiance of 0.79 W/Srm^2 as compared to those of conventional WOLED and *p*-i-*n di*-chromatic WOLED device (0.67 W/Srm^2 and 0.68 W/Srm^2, respectively).

Table 4-5 EL performances of WOLED devices at 20 mA/cm^2.

Device	Voltage (V)	Current Eff. (cd/A)	Power Eff. (lm/W)	E. Q. E. (%)	$CIE_{x,y}$	NTSC (%)	CRI
conventional	6.4	9.0	4.4	3.5	(0.32, 0.41)	61.3	66
p-i-*n* B/Y (*di*-chromatic)	3.8	9.9	8.2	3.6	(0.32, 0.43)	62	67
p-i-*n* R/B/G (*tri*-chromatic)	5.6	8.0	4.5	4.3	(0.34, 0.35)	73.2	87

As shown in Figure 4-18, it is evident that the weak intensity at wavelength < 450 nm and > 620 nm of conventional WOLED has been enhanced and a wider EL spectrum can be obtained by introducing deep blue system and red co-host system (MADN:SA-BiPh and Alq$_3$:Rb:DCJTB) into the WOLED device. Thereby, the CRI value of *tri*-chromatic WOLED can be enhanced to 87. Furthermore, after attaching color filters, the color gamut of *p*-i-*n* R/B/G device

can reach 73.2% of NTSC standard and CIE$_{x,y}$ coordinates of RGB and white points are (0.66, 0.33), (0.27, 0.62), (0.13, 0.13), and (0.36, 0.36), respectively,. These results indicate the *tri*-chromatic WOLEDs with high power efficiency, high CRI, and high color gamut indeed have the potential to be used for full-color display and light source applications.
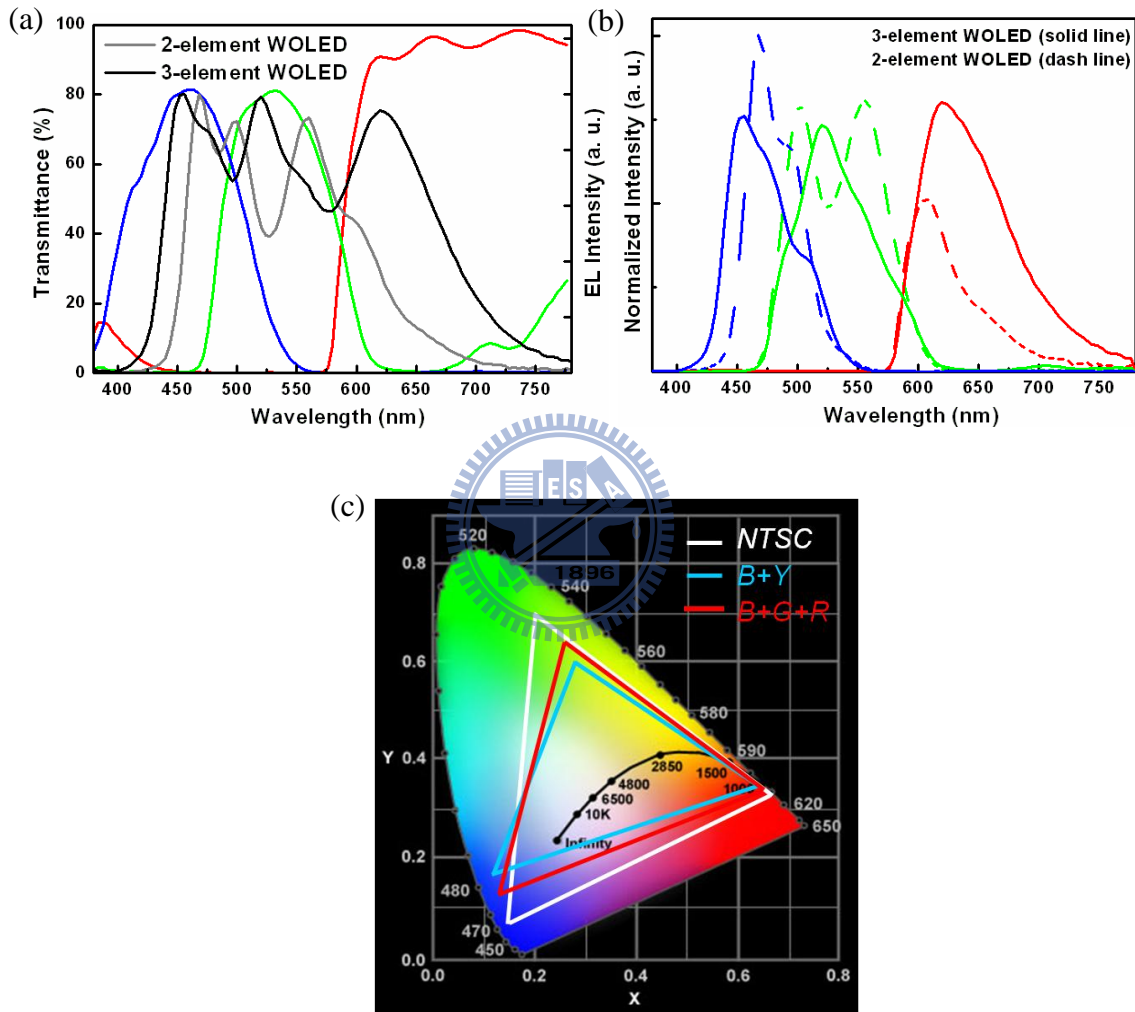
Figure 4-18 (a) The transmittance of RGB color filters and EL spectra of *di*-chromatic and *tri*-chromatic WOLEDs. (b) Spectra of RGB colors after attaching color filters. (c) The color gamut of *di*-chromatic and *tri*-chromatic WOLEDs.

References

[1] C. W. Tang, S. A. VanSlyke, C. H. Chen, *J. Appl. Phys.* **65**, 3610 (1989).

[2] T. Tsuji, S. Kawami, S. Miyaguchi, T. Naijo, T. Yuki, S. Matsuo, H. Miyazaki, *Proceedings of SID2004*, p. 900, May 23-28 (2004), Seattle, WA, USA.

[3] M. S. Weaver, V. Adamovich, J. J. Brown, K. H. Lee, C. W. Lim, S. C. Kim, *Proceedings of SID2009*, p. 314, May 31-June 5 (2009), San Antonio, TX, USA.

[4] J. Y. Lee, J. H. Kwon, *Proceedings of IDMC2005*, p. 329, Feb 21-24 (2005), Taipei, Taiwan.

[5] P. A. Levermore, V. Adamovich, K. Rajan, W. Yeager, C. Lin, S. Xia, G. S. Kottas, M. S. Weaver, R. Kwong, R. Ma, M. Hack, J. J. Brown, *Proceedings of SID2010*, p. 786, May 23-28 (2010), Seattle, WA, USA.

[6] S. J. Yeh, M. F. Wu, C. T. Chen, Y. H. Song, Y. Chi, M. H. Ho, S. F. Hsu, C. H. Chen, *Adv. Mater.* **17**, 285 (2005).

[7] Y. Sun, N. C. Giebink, H. Kanno, B. Wa, M. E. Thompson, S. R. Forrest, *Nature* **440**, 908 (2006).

[8] H. Kanno, N. C. Giebink, Y. Sun, S. R. Forrest, *Appl. Phys. Lett.* **89**, 023503 (2006).

[9] C. Hosokawa, H. Higashi, H. Nakamura, T. Kusumoto, *Appl. Phys.Lett.* **67**, 3853 (1995).

[10] C. C. Yeh, M. T. Lee, H. H. Chen, C. H. Chen, *Proceedings of SID2004*, p. 789, May 23-28 (2004), Seattle, WA, USA.

[11] C. C. Wu, Y. T. Lin, K. T. Wong, R. T. Chen, Y. Y. Chien, *Adv. Mater.* **16**, 61 (2004).

[12] T. C. Chao, Y. T. Lin, C. Y. Yang, T. S. Hung, H. C. Chou, C. C. Wu, K. T.

Wong, *Adv. Mater.* **17**, 992 (2005).

[13] L. H. Chan, H. C. Yeh, C. T. Chen, *Adv. Mater.* **13**, 1637 (2001).

[14] J. U. Kim, H. B. Lee, J. S. Shin, Y. H. Kim, Y. K. Joe, H. Y. Oh, C. G. Park, S. K. Kwon, *Synth. Met.* **150**, 27 (2005).

[15] I. B. Berlan, *Handbook of Fluorescence Spectra of Aromatic Molecules*, 2nd ed.; Academic Press: New York (1971).

[16] B. Balaganesan, W. J. Shen, C. H. Chen, *Tetrahedron Lett.* **44**, 5747 (2003).

[17] M. D. Joswick, I. H. Campbell, N. N. Barashkov, J. P. Ferraris, *J. Appl. Phys.* **80**, 2883 (1996).

[18] S. Tokito, H. Tanaka, K. Noda, A. Okada, Y. Taga, *Appl. Phys. Lett.* **70**, 1929 (1997).

[19] J. Salbeck, N. Yu, J. Bauer, F. Weissörtel, H. Bestgen, *Synth. Met.* **91**, 209 (1997).

[20] B. E. Konne, D. E. Loy, M. E. Thompson, *Chem. Mater.* **10**, 2235 (1998).

[21] Y. Shirota, *J. Mater. Chem.* **10**, 1 (2000).

[22] Y. H. Kim, S. J. Lee, S. Y. Jung, K. N. Byeon, J. Kim, S. C. Shin, S. K. Kwon, *Bull. Korean Chem. Soc.* **28**, 443 (2007).

[23] J. Shi, C. W. Tang, *Appl. Phys. Lett.* **80**, 3201 (2002).

[24] W. J. Shen, B. Banumathy, H. H. Chen, C. H. Chen, *Proceedings of IDMC2003*, p. 741 (2003), Taipei, Taiwan.

[25] J. Shi, *Eur. Patent* 1156536 (2001).

[26] Y. Kan, L. Wang, Y. Gao, L. Duan, G. Wu, Y. Qiu, *Synth. Met.* **141**, 245 (2004).

[27] Y. Kan, L. Wang, L. Duan, Y. Hu, G. Wu, Y. Qiu, *Appl. Phys. Lett.* **84**, 1513 (2004).

[28] L. S. Hung, C. H. Chen, *Mater. Sci. Eng R.* **39**, 143 (2002).

[29] B. Banumathy, W. J. Shen, C. H. Chen, *Tetrahedron Lett.* **44**, 5747 (2003).

[30] M. T. Lee, Y. S Wu, H. H. Chen, C. H. Tsai, C. H. Liao, C. H. Chen, *Proceedings of SID2004*, p. 710, May 23-28 (2004), Seattle, WA, USA.

[31] K. F. Li, K. W. Cheah, K. T. Yeung, Y. K. Cheng, Y. S. Wu, C. H. Chen, *Proceedings of IDMC2005*, p. 136, Feb 21-24 (2005), Taipei, Taiwan.

[32] M. T. Lee, H. H. Chen, C. H. Tsai, C. H. Liao, C. H. Chen, *Appl. Phys. Lett.* **85**, 3301 (2004).

[33] Y. Kijima, N. Asai, S. I. Tamura, *Jpn. J. Appl. Phys. Part 1* **38**, 5274 (1999).

[34] Y. J. Tung, T. Ngo, M. Hack, J. J. Brown, N. Koide, Y. Nagara, Y. Kate, H. Ito, *Proceedings of SID2004*, p. 48, May 23-28 (2004), Seattle, WA, USA.

[35] T. Arakane, M. Funahashi, H. Kuma, K. Fukuoka, K. Ikada, H. Yamamoto, F. Moriwaki, and C. Hosokawa, *Proceedings of SID2006*, p. 37, San Francisco, California, USA (2006).

[36] L. S. Liao, K. P. Klubek, M. J. Helber, L. Cosimbescu, and D. L. Comfort, *Proceedings of SID2006*, p. 1197, San Francisco, California, USA (2006).

[37] M. T. Lee, C. H. Liao, C. H. Tsai, and C. H. Chen, *Adv. Mater.* **17**, 2493 (2005).

[38] J. W. Choi, J. S. Kim, S. Y. Oh, H. W. Rhee, W. H. Lee, S. B. Lee, *Thin Solid Films* **363**, 271 (2000).

[39] J. Pommerehne, H. Vestweber, W. Guss, R. F. Mahrt, H. Bässler, M. Porsch, J. Daub, *Adv. Mater.* **7**, 551 (1995).

[40] J. Shi, C.W. Tang, *Appl. Phys. Lett.* **70**, 1665 (1997).

[41] A. A. Lamola, *Energy Transfer and Organic Photochemistry*, New York: Interscience (1969).

[42] L. S. Hung, L. R. Zheng, M. G. Mason, *Appl. Phys. Lett.* **78**, 673 (2001).

[43] S. A. Van Slyke, C. H. Chen, and C. W. Tang, *Appl. Phys. Lett.* **69**, 2160 (1996).

[44] T. H. Liu, C. Y. Iou, C. H. Chen, *Appl. Phys. Lett.* **83**, 5241 (2003).

[45] B. Wei, K. Furukawa, M. Ichikawa, T. Koyama, Y. Taniguchi, Mol. *Cryst. Liq. Cryst.* **426**, 295 (2005).

[46] C. C. Chang, M. T. Hsieh, J. F. Chen, S. W. Hwang, C. H. Chen, *Appl. Phys. Lett.* **89**, 253504 (2006).

[47] S. Y. Chen, T. Y. Chu, J. F. Chen, C. Y. Su, C. H. Chen, *Appl. Phys. Lett.* **89**, 053518 (2006).

Chapter 5

Carrier Transport Properties of Anthracene-Based Materials

5.1　　　Bipolar nature of anthracene-based materials

The charge carrier (hole and electron) transport property is a key factor in determining the performance of OLEDs [1,2]. Two widely used theories for describing the charge mobilities in organic materials are coherent band theory [3,4] and incoherent hopping model [5,6], respectively. In the former, the charges transfer through valence or conduction bands is formed by the overlapping molecular orbital with strong coupling between neighboring molecules. In contrast, the latter is a dominant mechanism at room temperature because the dynamic structure disorder invalidates the band model due to a strong coupling of the lattice phonons with charge motion. Accordingly, the hopping model is suitable for most organic materials, and the theoretical prediction of mobility is in good agreement with experimental observations [7]. Generally, organic π-conjugated materials are assumed to transport charge at room temperature via a thermally activated hopping-type mechanism. The hole and electron transfer process between adjacent spatially separated segments can be summarized as follows:

$$A^+ + A \rightarrow A + A^+, A^- + A \rightarrow A + A^- \tag{5.1}$$
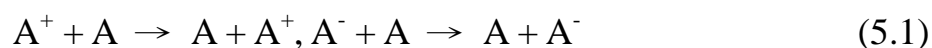
where A represents the neutral species undergoing charge transfer, and the A^+/A^- species contains the hole/electron. Assuming the temperature is sufficiently high to reasonably treat vibrational modes classically, the rate (K_{ET}) of intermolecular charge hopping can be described by the Marcus theory [8] in following equation:

$$K_{ET} = \frac{t^2}{\hbar} \sqrt{\frac{\pi}{\lambda k_B T}} \exp\left(\frac{-\lambda}{4 k_B T}\right) \tag{5.2}$$

where λ is the reorganization energy, k_B is the Boltzmann constant, T is the temperature, t is the electronic coupling matrix element between the two species, dictated largely by orbital overlap. Obviously, λ and t are the two most important parameters and have a dominant impact on the charge-transfer rate. An evaluation of t would require the relative positions of the molecules in the solid state as it is related to the energetic splitting of the frontier orbitals of the interacting molecules, and it can be obtained by two approaches: one is to resort to Koopmans' theorem [9,10]; the other is to directly calculate the coupling matrix element of the frontier orbitals [11,12]. Due to organic materials are arranged randomly in the manner of an amorphous film in OLED devices, the range of intermolecular charge transfer in the solid state is limited. The mobility of charges has been demonstrated to be largely related to the reorganization energy (λ) for OLED materials and in general, it has good agreement with the experimental observations [6,7,13,14].

The reorganization energy (λ) reflects the changes in the geometry of the two molecules when going from the initial to the final state. This term originates from the fact that the geometry of a charged π-conjugated molecule differs significantly from that of the corresponding neutral molecule, owing to a marked redistribution of the π-electron bond densities. The reorganization energy for hole transport (λ_+) can be estimated as the sum of two terms [15], as illustrated in Figure 5-1: (1) the relaxation energy (λ_1) between the energy of the charged molecule in its fully relaxed cation geometry and that in the geometry characteristic of the ground state, and (2) the relaxation energy (λ_2) between the

energy of the neutral molecule in its equilibrium geometry and that in the geometry characteristic of the charged system. In general, these two contributions are nearly equal to one another. Similarly, the reorganization energy for electron transport (λ_-) equals the sum of the two relaxation energies λ_3 (neutral to anion) and λ_4 (anion back to neutral).
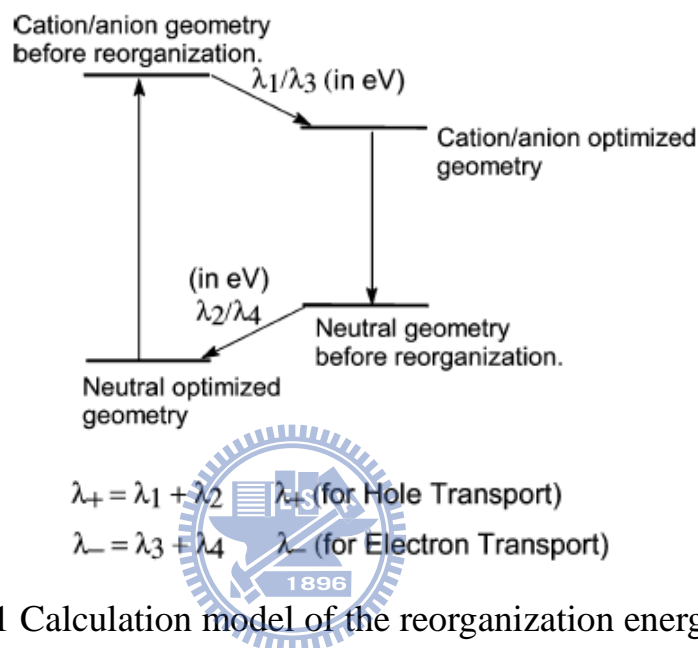
Figure 5-1 Calculation model of the reorganization energy [15].

Cornil et al. [14] calculated the reorganization energies of oligoacenes containing from 3 to 5 rings for holes and electrons and compared to the results extracted from gas-phase UV photoelectron spectroscopy spectra for holes [16] as shown in Figure 5-2. There is a very good quantitative agreement between theory and experiment for holes; importantly, the λ values have globally the same order of magnitude for electrons and holes. In general, λ varies in the range 0.1–0.5 eV; the smaller values are obtained, as expected, when the extent of geometric deformations is minimal when going from the neutral to the charged state. This is the case, for instance, for oligoacenes [16] or phthalocyanines [17]. Table 5-1 summarizes the reorganization energies of

benzene, naphthalene and anthracene. As expected, as the size of the molecule increases, there is in general a decrease in the reorganization energy due to the more rigid molecular geometry (Figure 5-2 also shows the same trend). It can also be observed that the molecular reorganization energy values do not provide markedly different contributions to hole and electron transport in organic conjugated materials, indicating these materials possess bipolar charge transport nature.
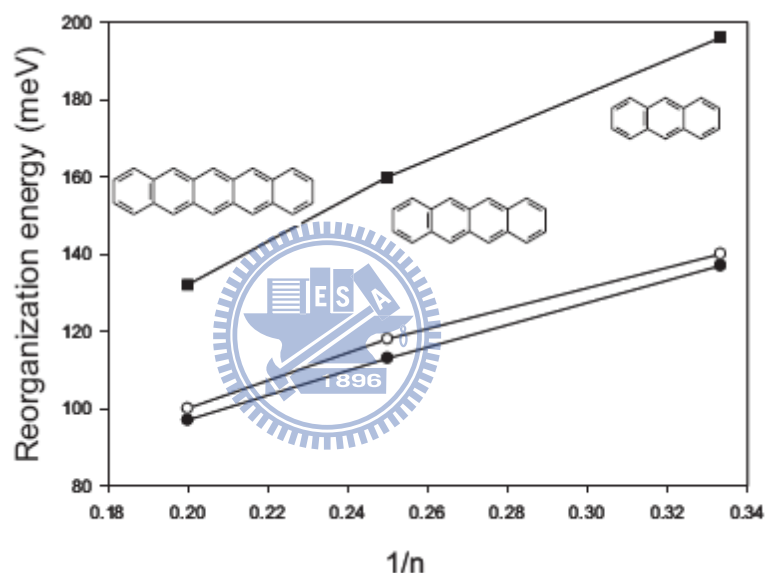
Figure 5-2 Evolution of the internal reorganization energy in oligoacenes as a function of the inverse number of rings, as calculated at the density functional theory level for holes (●) and electrons (■) [14] , and estimated as twice the relaxation energy extracted from gas-phase UV photoelectron spectroscopy measurements (○) for holes [16].

Table 5-1 Theoretical evaluation of the reorganization energies (λ, eV) for hole and electron transport for anthracene-based materials [15,18].

Molecule	λ_1	λ_2	λ_+	λ_3	λ_4	λ_-
benzene	0.153	0.149	**0.302**	0.201	0.202	**0.403**
naphthalene	0.092	0.092	**0.184**	0.129	0.129	**0.258**
anthracene	0.068	0.068	**0.136**	0.097	0.097	**0.194**
MAT	0.151	0.156	**0.307**	0.186	0.202	**0.388**
TAT	0.205	0.133	**0.338**	0.220	0.183	**0.403**
MAN	0.232	0.148	**0.380**	0.224	0.207	**0.431**
TAN	0.228	0.138	**0.366**	0.235	0.191	**0.426**
DPA	0.151	0.120	**0.271**	0.155	0.148	**0.303**
α-ADN	0.125	0.137	**0.262**	0.117	0.146	**0.263**
β-ADN	0.222	0.135	**0.357**	0.286	0.179	**0.465**
α-TMADN	0.087	0.104	**0.191**	0.135	0.150	**0.285**
β-TMADN	0.165	0.115	**0.280**	0.318	0.186	**0.504**

In 2008, Yang et al. calculated the reorganization energies of aryl-substituted anthracene derivatives (MAT and TAT) and triphenylamine-substituted anthracene derivatives [18] (MAN and TAN, values are shown in Table 5-1 and structures are shown in Figure 5-3). These reorganization energies are all two or three times higher than that of anthracene for either λ_+ or λ_-. This increasing reorganization energy indicates lower charge-carrier mobility than that of unsubstituted anthracene. We can also see that there is a large difference of reorganization energies between these anthracene-based materials, indicating the various substituents on 9-/10- positions of anthracene moiety would really affect the conformation of molecular packing and further change the charge-carrier transport abilities of each molecule. Furthermore, all these aryl-substituted and triphenylamine-substituted anthracene derivatives are found to have a more

similar reorganization energy for hole and electron transport, which indicates that these anthracene-based materials could be expected to possess the bipolar nature of a balanceable hole and electron transport property. Raghunath et al. did the similar calculations on the reorganization energy of isomeric ADN-type derivatives [15] (values are also summarized in Table 5-1 and structures can be found in Figure 4-1). From Table 5-1, DPA, α-ADN, β-ADN, and β-TBADN all have similar reorganization energy for hole and electron transport property like those aryl-substituted and triphenylamine-substituted anthracene derivatives discussed above. It can be also observed that the difference between λ_+ and λ_- of α-TMADN and β-TMADN are slightly larger than those of other compounds listed in the table, suggesting that the intense steric effect of four methyl substituents to the molecular structure of ADN would strongly affect the optimized geometry either ground state or charged state, thereby, further influence the reorganization energy. The results also indicate that the charge-carrier transport property of ADN-type materials could be tuned by modification of molecular structure, even for the design of an electron transport material. On the other hand, there are some reports about *ambi*polar materials [19,20,21], which have been proven to have similar reorganization energies of λ_+ or λ_-. Therefore, we can conclude that most anthracene-based materials have the potential to be bipolar compound, due to its similar reorganization energies for hole and electron transport (λ_+ and λ_-) from computational results.

MAT   MAN

TAT   TAN
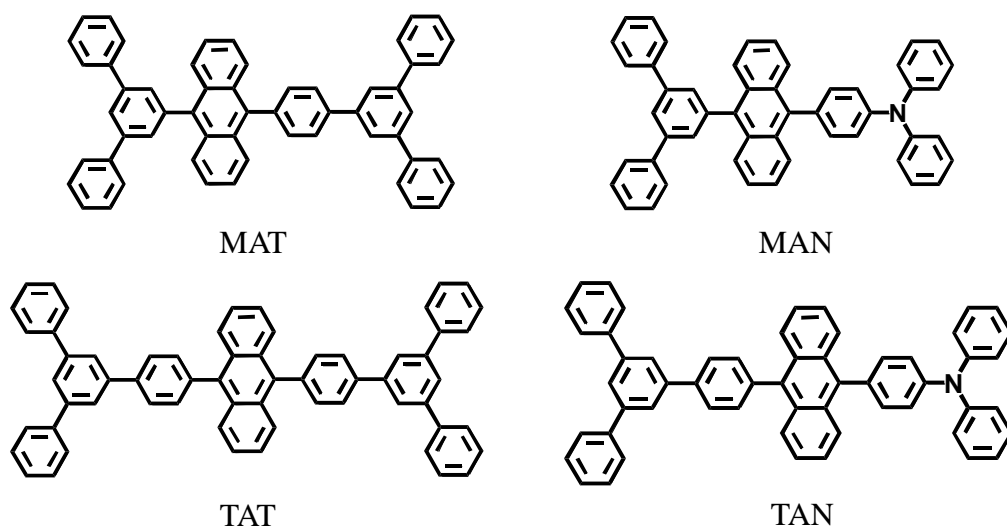
Figure 5-3 Chemical structures of aryl-substituted anthracene derivatives and triphenylamine-substituted anthracene derivatives.

5.2 Mobility measurements of anthracene-based materials in literatures

In 2006, So et al. examined the influence of various number of t-butyl substituents of ADN-type host materials on their charge-carrier transport properties by time-of-flight (TOF) measurements [22,23]. The general sample structure was [ITO/ADN compound (5~7 μm)/Al (15 nm)]. The anthracene-based compounds were: ADN, TBADN, DTBADN, and TTBADN, respectively (structures are shown in Figure 4-1). The transition time (τ) of these compounds are determined from Figure 5-5(a) and all carrier mobilities of ADN compounds at 290 K are depicted in Figure 5-5(b), which all obey the Poole-Frenkel behavior [24,25],

$$\mu(E) = \mu_0 \exp(\beta\sqrt{E})$$

(5.3)

where β is the Poole-Frenkel factor, and μ_0 is the zero field mobility.
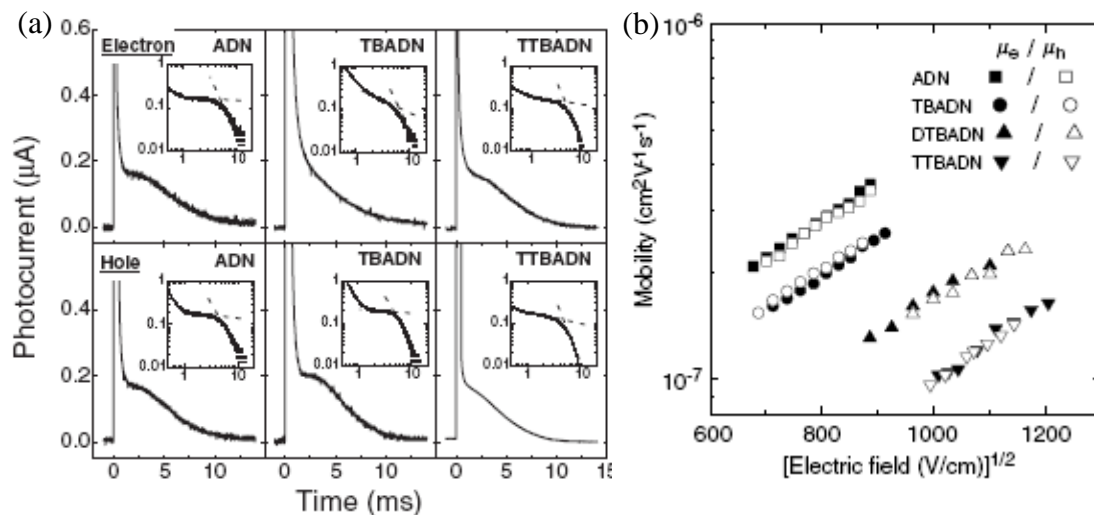
Figure 5-4 (a) TOF transient signals of ADN, TBADN and TTBADN at 290K under applied field strengths of 0.56, 0.58, and 1.45 MV/cm, respectively [22]. (b) Field dependent electron and hole mobilities of ADN, TBADN, DTBADN and TTBADN at 290 K [23].

Interestingly, from the results, all ADN-type compounds are *ambipolar* and have similar Poole–Frenkel slope β (similar results were obtained in the cases of MADN and α,α-MADN [26]). Their hole and electron mobilities as reported have values in the range $(1–5) \times 10^{-7}$ cm^2/Vs at $E = (5–8) \times 10^{5}$ V/cm. Furthermore, a systematic reduction in both the hole and electron mobilities can be observed as the number of *t*-butyl group increases. From the frontier orbitals of ADN and TTBADN as shown in Figure 5-6, it depicts that the HOMO and LUMO in both ADN compounds are localized on the anthracene moiety and do not involve the naphthyl and *t*-butyl groups. In other words, the naphthyl and *t*-butyl groups effectively act mostly as inert spacers for charge-carrier transport. As holes hop among HOMOs while electrons hop in LUMOs in adjacent molecules, it is expected that carrier transports only occur on the anthracene moieties and have similar spatial extents in all cases. As a result, all these

ADN-type compounds behave similarly and have almost identical PF slope. Furthermore, the presence of the two or four *t*-butyl group, increases the average intermolecular separation over which charge hopping from one site (anthracene moeity) to another localized on another molecule would be more difficult. Therefore, electron and hole mobilities are effectively reduced with bulky substituents. Similar observations have also been reports previously in hole transport of rubrene and tetra (*t*-butyl) rubrene [27].

(a)

HOMO   LUMO

(b)
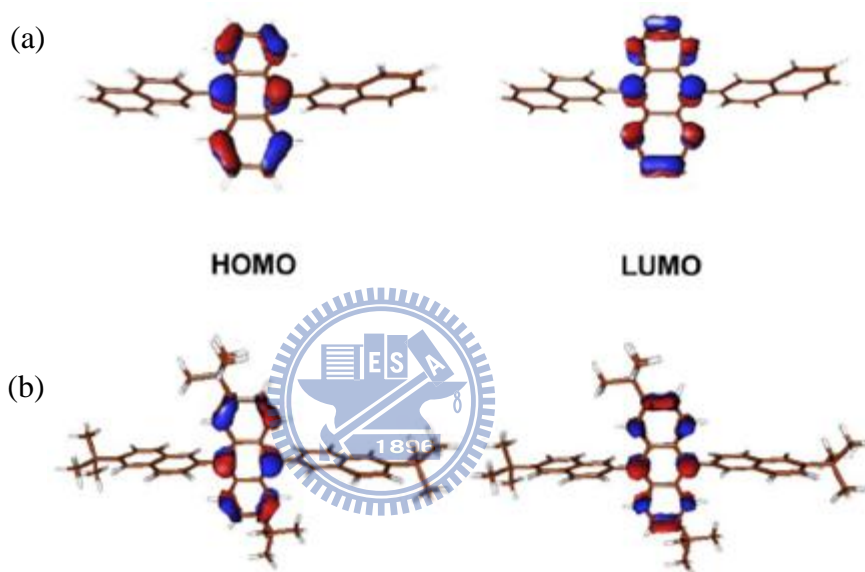
Figure 5-5 The frontier orbitals of (a) ADN and (b) TTBADN.

In 2006, Wu et al. also reported ADN's mobility data by using terfluorene [structure can be found in Figure 5-6(a)] as the charge-generation material (CGL) for TOF measurement [28]. The large bandgap terfluorene material was found to possess mobility over 10^{-3} cm^2/Vs for both carriers. Its large absorption coefficients of $>10^5$ cm^{-1} at 325–375 nm, which well matches the emission wavelength of N$_2$ laser (337 nm), suggests that terfluorene would be an ideal CGL for TOF. Therefore, the mobilities of ADN could be also obtained in the sample structure of glass substrate/Ag (30 nm)/terfluorene (0.2 μm)/ADN (2

μm)/Al (150 nm), in which sample material consumption has been greatly reduced as compared to that of the conventional TOF system. The TOF transient exhibits nondispersive hole-transport characteristics and high hole mobility of $(1–3) \times 10^{-3}$ cm^2/Vs at $E = (2.3–4.7) \times 10^5$ V/cm [as shown in Figures 5-6(b) and 5-6(c)], which is even higher than that of commonly used hole-transport material NPB [29]. However, the electron-transient of ADN is highly dispersive and no transient time and electron mobility could be extracted.
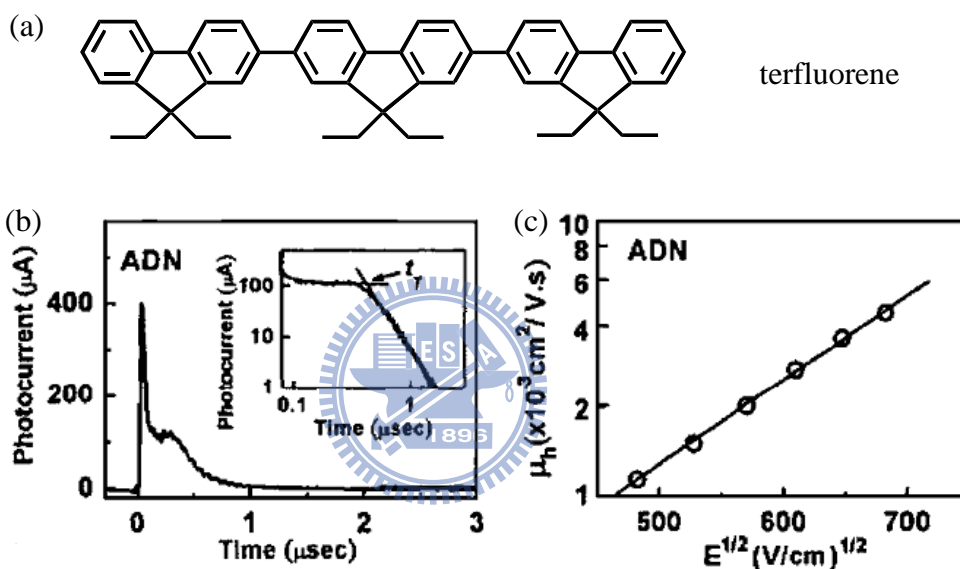
Figure 5-6 (a) Chemical Structure of terfluorene. (b) Representative TOF transients for holes of ADN at $E = 3.3 \times 10^5$ V/cm. (c) Hole mobilities vs $E^{1/2}$ of ADN [28].

On the other hand, Culligan et al. reported the hole mobility data of ADN and two anthracene-based derivatives with different fluorene substituents, ANF and ADF by transient EL measurement [30]. Contrary to typical transient OLEDs, the frequency-domain response was used to measure the hole mobility [31]. The decrease in EL intensity at high frequencies of the DC voltage pulses

was apparently the result of fewer holes reaching the Alq$_3$/C545T layer. The hole-transit time was estimated from the intercept of the tangents of the light-output versus frequency curves. The mobility was then calculated based on the film thickness and the applied field. The results of transient EL measurement are shown in Figure 5-7.The hole mobilities are measured by transient EL method to be 3.1×10^{-4}, 8.9×10^{-5}, 3.6×10^{-5} cm^2/Vs for ADN, ANF, and ADF, respectively.
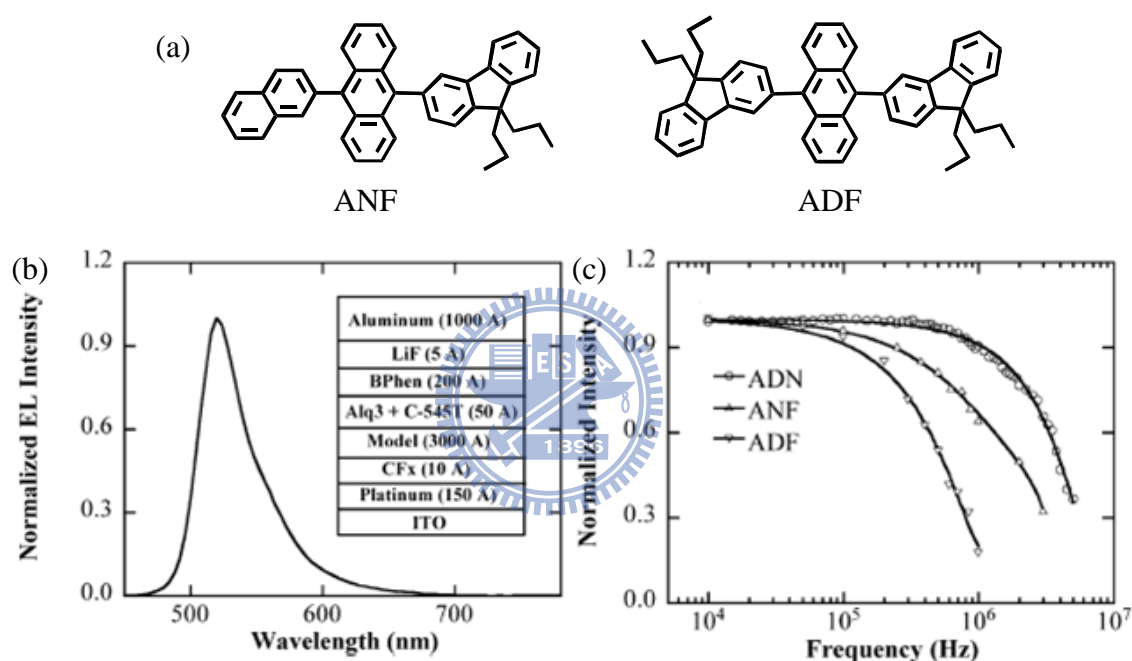
Figure 5-7 (a) Chemical Structure of ANF and ADF. (b) Steady-state EL spectrum of a typical transient OLED. Inset: transient OLED device structure. (c) Frequency-dependent EL quenching upon application of 8 V square-wave DC voltage pulses of increasing frequency, 50% duty cycle; solid curves represent the best fits to polynomials [30].

The reported mobility data of ADN-type derivatives are summarized in Table 5-2. It is interesting to note that although ADN-type materials are widely used in OLEDs, there are few reports of direct characterization of their carrier

transport properties. Furthermore, the obvious inconsistency of ADN-type compounds' mobilities recorded in different literatures at different laboratories is quite apparent in Table 5-2. We believe that a direct and detailed re-investigation into the charge-carrier mobilities of ADN-type materials would be a significant and valuable contribution, despite most ADN-type materials are known to have bipolar nature and have been utilized as carrier transport materials in OLED devices.

Table 5-2 The reported mobility data of ADN-type derivatives.

Molecule	Hole Mobility (μ_h, cm^2/Vs)	Electron Mobility (μ_e, cm^2/Vs)	Measurement Method	Reference
ADN	$(2-4) \times 10^{-7}$	$(2-4) \times 10^{-7}$	TOF	[22,23]
TBADN	$(1.5-2.5) \times 10^{-7}$	$(1.5-2.5) \times 10^{-7}$	TOF	[22,23]
DTBADN	$(1.2-2.2) \times 10^{-7}$	$(1.2-2.2) \times 10^{-7}$	TOF	[23]
TTBADN	$(1-2) \times 10^{-7}$	$(1-2) \times 10^{-7}$	TOF	[22,23]
MADN	$(2-3) \times 10^{-7}$	$(2-3) \times 10^{-7}$	TOF	[26]
α,α-MADN	$(4-6) \times 10^{-7}$	$(2-4) \times 10^{-7}$	TOF	[26]
ADN	$(1-3) \times 10^{-3}$	-	TOF with CGL	[28]
ADN	3.1×10^{-4}	-	Transient EL	[30]
ANF	8.9×10^{-5}	-	Transient EL	[30]
ADF	3.6×10^{-5}	-	Transient EL	[30]

5.3 Mobility measurements of anthracene-based materials by TOF technique

Carrier Transport properties of ADN-type materials in this study were investigated by TOF technique at room temperature in Prof. Ching W. Tang's laboratory (University of Rochester, NY, USA). The structures of ADN-type

materials can be found in Table 2-1. The carrier mobility can be evaluated from the intersection point of two asymptotes to the plateau and the tail sections in the double logarithmic representation of the transient photocurrent signal.

5.3.1 Absorption coefficient and absorption depth

In TOF measurements, the thickness of the sheet of charges is not zero and should be considered. Practically, the thickness of the sheet of charges is approximately the absorption depth (δ), the reciprocal of the absorption coefficient, which is the distance of light drops to about 36% of its original intensity, or alternately has dropped by a factor of 1/e. Therefore, we measured the absorption spectra of the MADN film (vacuum deposited on quartz substrate) as shown in Figure 5-8, in which the excitation wavelength of N_2 laser at 337 nm is close to the absorption minimum between absorption bands of MADN with a rather small absorption coefficient of 20805 cm^{-1} at 337 nm. As a result, the δ of MADN is 0.48 μm.
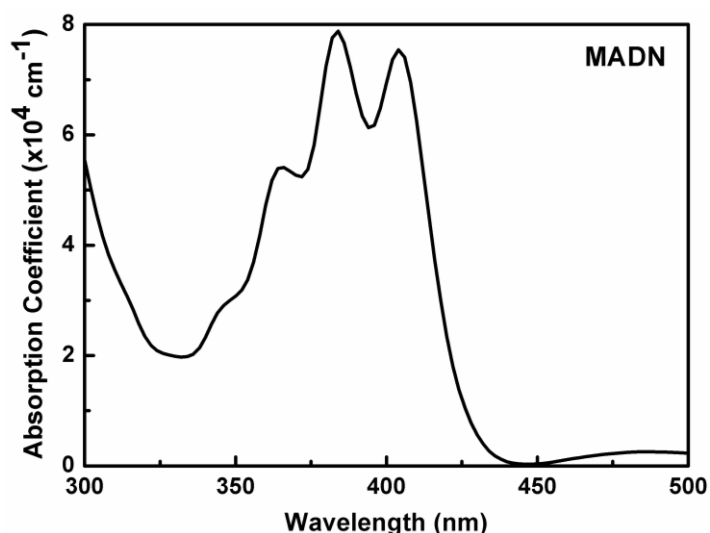
Figure 5-8 Absorption spectrum of MADN film.

Furthermore, we can also estimate the relationship of δ and transmitted light

by Beer-Lambert law [32],

$$I = I_0 e^{-\alpha l} \qquad (5.4)$$

where I_0 and I are the intensity of the incident light and the transmitted light, respectively; α is the absorption coefficient; l is the distance of the light travels through the material, such as the path length. Here l can be seen as the δ when we already know the absorption coefficient α.
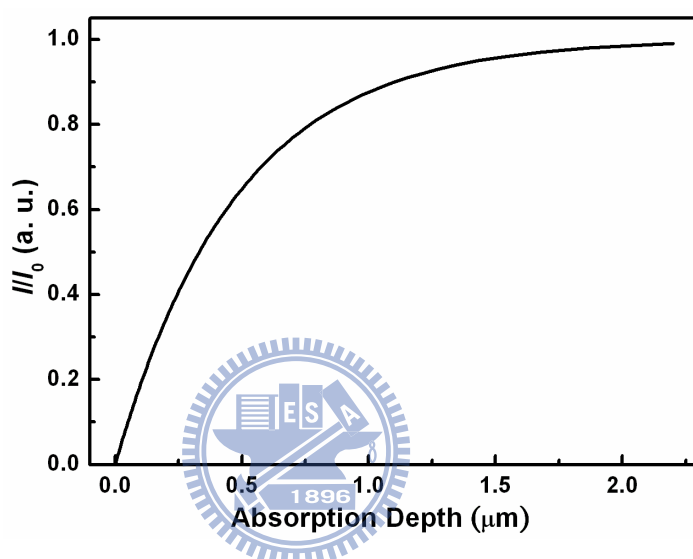
Figure 5-9 The relationship of transmitted light intensity at 337 nm and absorption depth of MADN film.

As plotted in Figure 5-9, the δ of MADN film is 1.45 μm when 95% N$_2$ laser is absorbed. To ensure the thickness of the sheet of charges would not affect the reliability of TOF measurement, the thickness of measured film (d) should be much larger than that of sheet of charges [i. e. $d \gg \delta$]. Therefore, the general sample structure in this study is ITO/ADN-based compounds (~10 μm)/Al (150 nm) for TOF measurement.

5.3.2   TOF results of MADN

The sample structure of MADN is ITO/MADN (8.1 μm)/Al (120 nm).

Figure 5-10(a) is the representative TOF transient signals of holes for MADN measured at an applied field of 3.7 $\times$ 10^5 V/cm. The double logarithmic representation of photocurrents is shown in the inset of Figure 5-10(a). The photocurrent transients for holes of MADN exhibit non-dispersive behaviors as characterized by a plateau and a well-defined turning point at $t = \tau_{tr}$.
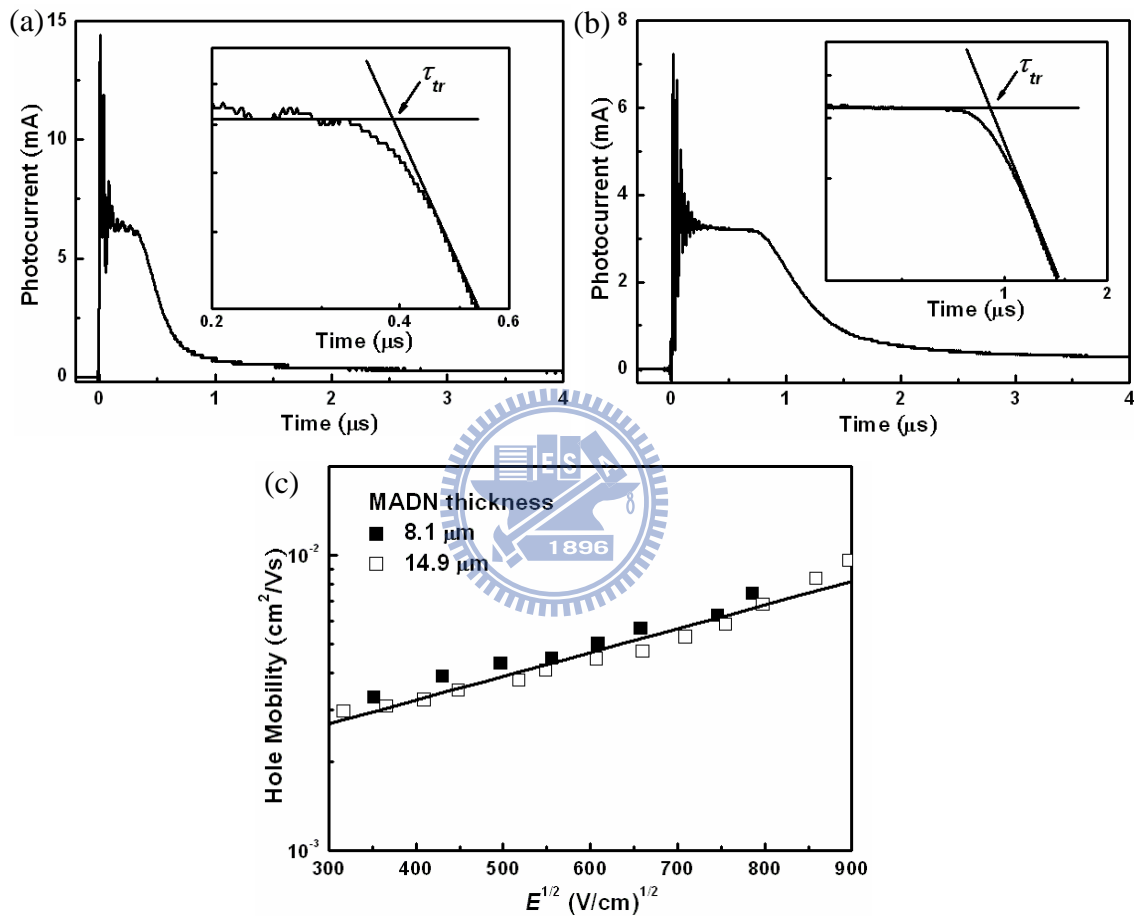
Figure 5-10 Representative TOF transient for holes of MADN at (a) $E = 3.7 \times 10^5$ V/cm (8.1 μm). (b) $E = 3.69 \times 10^5$ V/cm (14.9 μm). (c) Hole mobilities *vs* $E^{1/2}$ of MADN.

We also fabricated another MADN sample with structure of ITO/MADN (14.9 μm)/ITO (120 nm), in which the MADN layer is much thicker than that of

previous sample. Figure 5-10(b) is the representative TOF transient signals of holes for MADN measured at an applied field of 3.69 $\times$ 10^5 V/cm. The double logarithmic representation of photocurrents is shown in the inset of Figure 5-10(b). The photocurrent transients for holes of MADN exhibit non-dispersive behaviors as characterized by a plateau and a well-defined turning point at $t = \tau_{tr}$. Figure 5-10(c) depicts the dependence of the hole mobilities on the electric field of MADN. MADN exhibits a hole mobility of (2.8-9.6) $\times$ 10^{-3} cm^2/Vs at an electric field from 6.71 $\times$ 10^4 V/cm to 8.05 $\times$ 10^5 V/cm.

It is apparent that the results of two samples are consistent, indicating the layer thickness would not affect the carrier transport. It can also be observed that τ_{tr} is rather short due to the high hole mobility of MADN, which is in the range of < 1 µs. Despite a small resistance of 60 Ω is already used in the measurents, the transient signal is still close to the *RC* time constant of the circuit, especially at high electric field. Therefore, the thicker sample with a slightly longer τ_{tr} shows a more clear plateau, which is much easlier to evaluate the hole mobility.

On the other hand, Figure 5-11 is the representative TOF transient signals of electrons for MADN (14.9 µm) measured at an applied field of 2.01 $\times$ 10^5 V/cm. As compared to the hole transients, the photocurrent signal intensity of electrons is much weaker and it shows a highly dispersive behavior. Unfortunately, there is no transit time and electron mobility for MADN can be extracted.
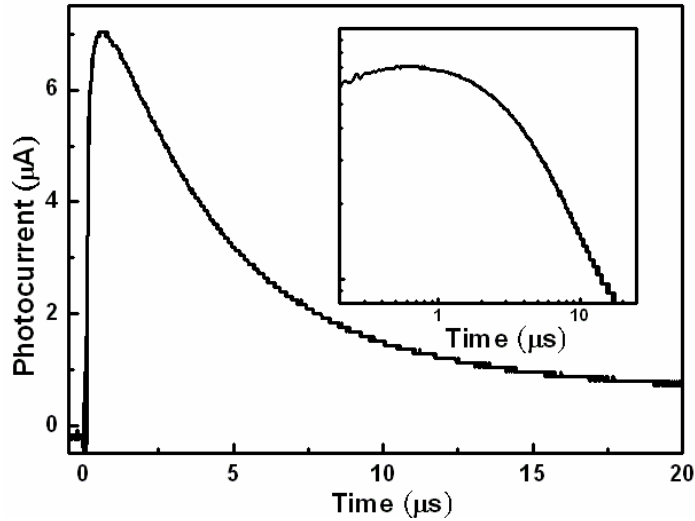
Figure 5-11 Representative TOF transient for electrons of MADN (14.9 μm) at $E = 2.01 \times 10^5$ V/cm.

5.3.3 TOF results of TBADN

The sample structure of TBADN is ITO/TBADN (14.5 μm)/Al (120 nm). Figure 5-12(a) is the representative TOF transient signals of holes for TBADN measured at an applied field of 4.15×10^5 V/cm. The double logarithmic representation of photocurrents is shown in the inset of Figure 5-12(a). The photocurrent transients for holes of TBADN exhibit non-dispersive behaviors as characterized by a plateau and a well-defined turning point at $t = \tau_{tr}$. Figure 5-12(b) depicts the dependence of the hole mobilities on the electric field of TBADN. TBADN exhibits a hole mobility of $(2.0\text{-}4.4) \times 10^{-3}$ cm^2/Vs at an electric field from 1.71×10^5 V/cm to 6.12×10^5 V/cm.

On the other hand, the TOF transient for electron of TBADN are highly dispersive and no transit time and electron mobility can be extracted.

Figure 5-12 (a) Representative TOF transient for holes of TBADN at $E = 4.15 \times 10^5$ V/cm. (b) Hole mobilities $vs\ E^{1/2}$ of TBADN.

5.3.4 TOF results of ADN

The sample structure of ADN is ITO/ADN (14 μm)/Al (120 nm). However, we found the ADN vacuum-deposited film is easily crystallized as shown in Figure 5-13(a), this phenomenon fully agrees with the literature report [33], and the crystallization heavily affects the TOF transients for both holes and electrons. Figure 5-13(b) is the representative TOF transient signals of holes for ADN measured at an applied field of 2.14×10^5 V/cm. The hole transient of ADN is highly dispersive and no transit time and hole mobility can be extracted.
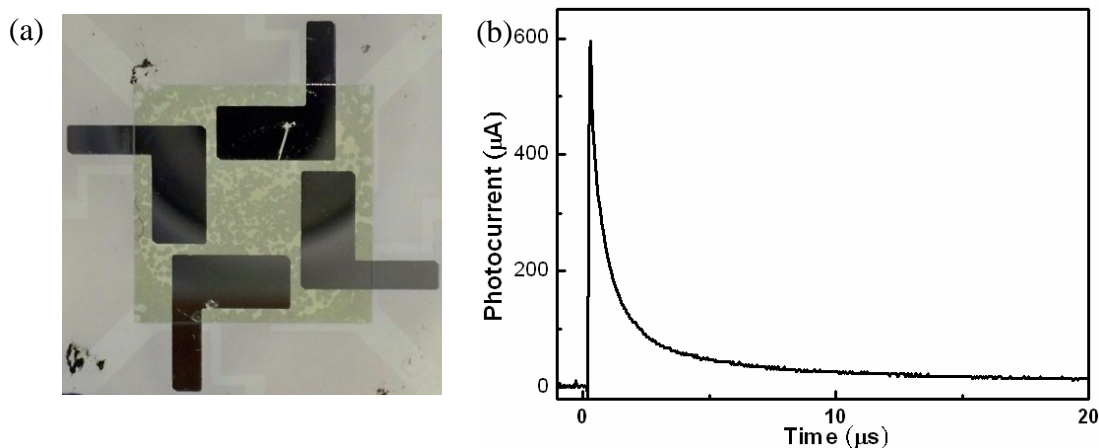
Figure 5-13 (a) Picture of crystallized ADN sample. (b) Representative TOF transient for holes of ADN at $E = 2.14 \times 10^5$ V/cm.

5.3.5 Discussions

Figure 5-14 shows the dependence of the hole mobilities on the electric field of MADN and TBADN. It is apparent that TBADN with a bulky *tert*-butyl substitution at 2-position of anthracene moiety has a lower hole mobility of 3.6×10^{-3} cm^2/Vs respect to MADN. Both of MADN and TBADN exhibit non-dispersive hole-transport behaviors, and the field dependence of hole mobilities follows the Poole-Frenkel relationship (*Equation 5.3*): mobility (μ) is proportional to the square root of the applied electric field ($E^{1/2}$). The fitted value of the zero-field mobility (μ_0), and the Poole-Frenkel factor (β) of MADN and TBADN are summarized in Table 5-3.
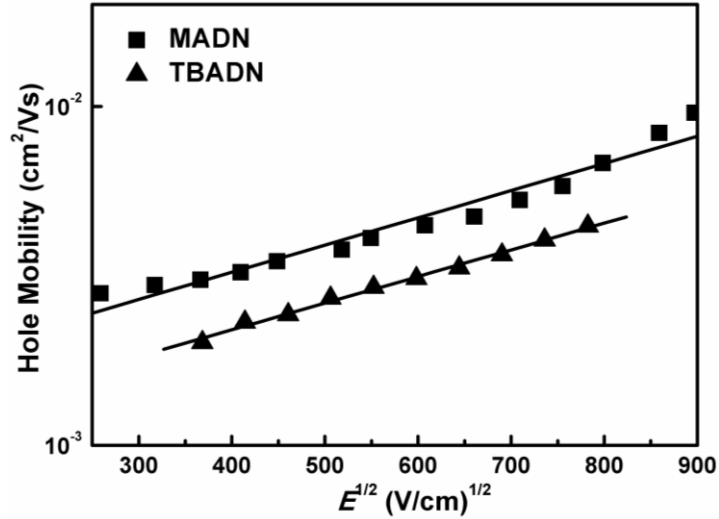
Figure 5-14 Hole mobilities *vs* $E^{1/2}$ of MADN and TBADN.

Table 5-3 The fitted values of zero-field hole mobility, Poole-Frenkel factor, and relative film density ofMADN and TBADN.

Material	zero-field mobility (μ_0, cm²/Vs)	Poole-Frenkel factor [β, (cm/V)$^{1/2}$]	relative film density (mole/volume)
MADN	1.55×10^{-3}	1.85×10^{-3}	1
TBADN	1.06×10^{-3}	1.81×10^{-3}	0.89

The Poole-Frenkel factors for holes (β_h) of MADN and TBADN are all smaller than the β_h of NPB [9.22×10^{-3} (cm/V)$^{1/2}$] and β_e of Alq$_3$ [3.45×10^{-3} (cm/V)$^{1/2}$] [29], indicating that the field dependence for hole mobility of these ADN-type materials is weaker than those common-used charge transport materials.

In addition, we also estimated the relative thin-film density (mole/volume) of these ADN-type materials to understand the molecular packing condition. The relative thin-film density of MADN and TBADN are 1 and 0.89, respectively. The large thin-film density implies the short distance between two adjacent

molecules, which is beneficial to charge-carrier transport. Table 5-3 clearly shows the trend of thin-film density of these two materials is in good agreement with the TOF results. Based on these results, the following conclusions can be made from the experimental and computational results: (1) the hole mobilities for ADN-type materials are all in the ranges of 2×10^{-3} to 9×10^{-3} cm^2/Vs and have almost identical Poole-Frenkel factors. As holes hop between HOMOs in adjacent molecules, it is expected that hole transports only occur on anthracene moieties; (2) the presence of *tert*-butyl group would increase the average intermolecular separation. Hence, it is more difficult for a charge hopping from on site to another site localized on another molecule. Therefore, the hole mobility of TBADN is reduced. Similar observations have been reports previously in hole transport of rubrene and (*t*-butyl) rubrene [27].

Unfortunately, all electron transients of ADN-type materials show highly dispersive behavior, and we cannot obtain transit time and electron mobility at all. One of the reasons could be attributed to the thick layer thickness of AND-type materials, the charge sheet might spread slightly in thin layer thickness, and the behavior of charge transport would become more dispersive when the sample thickness is increased. Therefore, the electron mobilities of AND-type materials might be obtained by using other excitation light source whose wavelength can fit the maximum absorption coefficients of AND-type materials well, which can effectively reduce the sample thickness. Another reason could be attributed to the lack of encapsulation for test samples, and the samples inevitably contact the ambient before they are put in vacuum sample holder for TOF measurement. Since oxygen (O$_2$) is a well-known electron trap and is inevitably present in the ambient and affect the TOF results. As a result, in

order to from stable anions in organic solids, it requires that the reduction potential for the test material must be lower than that of oxygen to reduce trapping. This might be the reason that much less electron transport materials were published in the literatures.

5.4   Using buckminsterfullerene (C60) as charge generation layer

Although TOF technique has been widely used to extract carrier mobility of organic materials, however, as the material of interest may not have a large enough absorption coefficient at the available excitation wavelength, the technique generally requires a thick (> 5 μm) film in order to have a well-defined flight distance. One will then face the issues of an impractically large sample thickness and a huge consumption of precious materials. Alternatively, one may set up an excitation light source with wavelengths tunable to match the absorption of materials, which however involves more complicated and costly instrumentation.

The better alternative is to incorporate between the electrode and the material under test a thin CGL with strong absorption coefficient at the available excitation wavelengths. In such a configuration, optical absorption and photocarrier generation occur in the CGL and the CGL material is also desired to have a large ionization potential and a small electron affinity for hole injection and electron injection into most organic materials, respectively, and efficient bipolar carrier transport (high carrier mobilities for both holes and electrons) without trapping photogenerated carriers.

As we discussed in previous section (see Figure 5-8), the excitation wavelength of N_2 laser at 337 nm is close to the absorption minimum of MADN. Hence, MADN has rather small absorption coefficients at 337 nm. Without

using a CGL, it would require an impractical sample thickness about 10 μm to obtain accurate TOF results for these ADN-type materials.

In this section, we demonstrate the use of buckminsterfullerene (C60) in the TOF technique as CGL to measure hole mobilities of ADN-type materials. The absorption spectrum of the vacuum-deposited C60 film is shown in Figure 5-15, in which large absorption coefficients of $> 10^5$ cm^{-1} are observed at 300-460 nm. Such wavelength matches that of the nitrogen laser at 337 nm, which is used as the excitation light in our TOF measurements. From literatures, it can also be found that C60 possesses high mobilities over 1 cm^2/Vs for both carriers [34,35]. Furthermore, the HOMO/LUMO energy levels of C60 are 6.2/3.6 eV [36], respectively, such deep HOMO level of C60 suggests that it shall be feasible for photo-generated holes in C60 to inject into the HOMO energy levels of ADN-type materials.
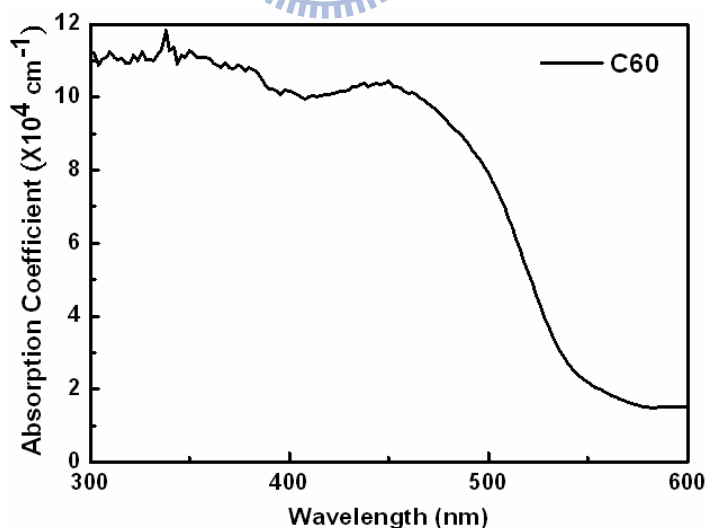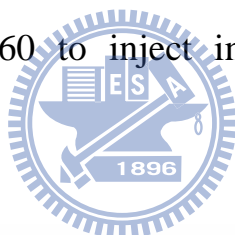
Figure 5-15 Absorption spectra of C60 film.

5.4.1 TOF results of MADN with C60 as CGL

The sample structure of MADN is ITO/C60 (0.5 μm)/MADN (5.5 μm)/Al (120 nm). The thicknesses of organic materials under testing were still set substantially larger than that of C60 so that the total transit time is larger than the time resolution of the electronic system and the transit time across the C60 layer is negligible in comparison with the total transit time.

Figure 5-16(a) is the representative TOF transient signals of holes for MADN measured at an applied field of 2.12×10^5 V/cm. The double logarithmic representation of photocurrents is shown in the inset of Figure 5-16(a). The photocurrent transients for holes of MADN exhibit non-dispersive behaviors as characterized by a plateau and a well-defined turning point at $t = \tau_{tr}$. Figure 5-16(b) depicts the dependence of the hole mobilities on the electric field of MADN. MADN exhibits a hole mobility of $(2.7\text{-}3.8) \times 10^{-3}$ cm^2/Vs at an electric field from 6.43×10^4 V/cm to 2.61×10^5 V/cm.
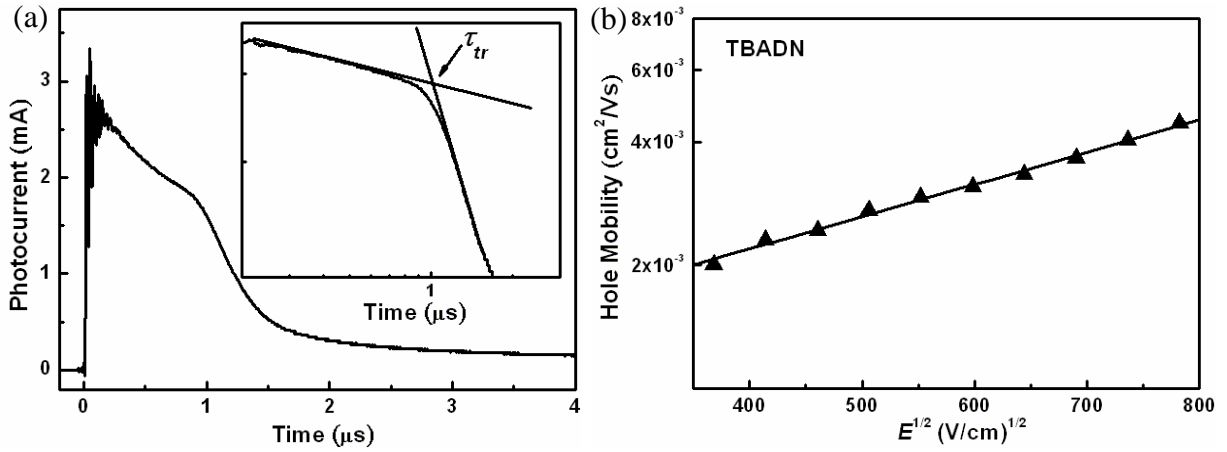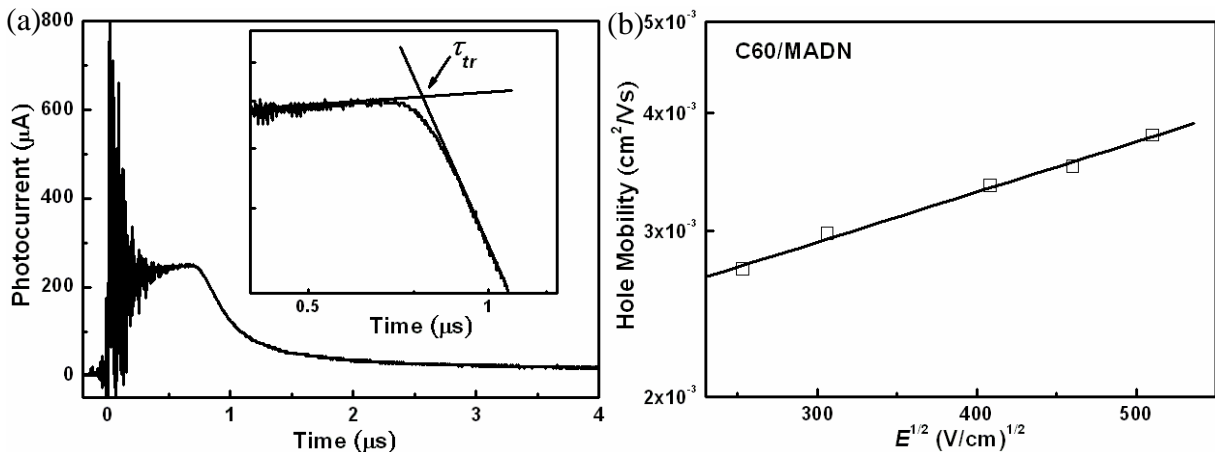

Figure 5-16 (a) Representative TOF transient for holes of MADN at $E = 2.12 \times 10^5$ V/cm. (b) Hole mobilities vs $E^{1/2}$ of MADN.

5.4.2　　　　TOF results of TBADN with C60 as CGL

The sample structure of TBADN is ITO/C60 (0.25 μm)/TBADN (3.4 μm)/ITO (120 nm). Figure 5-17(a) is the representative TOF transient signals of holes for TBADN measured at an applied field of 2×10^5 V/cm. The double logarithmic representation of photocurrents is shown in the inset of Figure 5-17(a). The photocurrent transients for holes of TBADN exhibit non-dispersive behaviors as characterized by a plateau and a well-defined turning point at $t = \tau_{tr}$. Figure 5-17(b) shows the dependence of the hole mobilities on the electric field of TBADN. TBADN exhibits a hole mobility of $(1.5\text{-}2.9) \times 10^{-3}$ cm^2/Vs at an electric field from 7.21×10^4 V/cm to 3.39×10^5 V/cm.
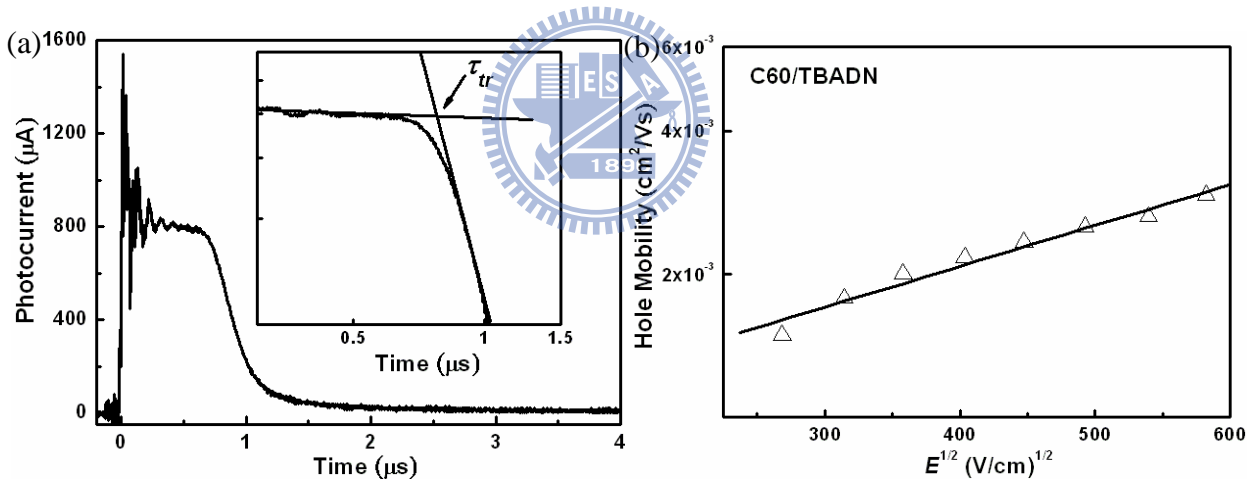
Figure 5-17 (a) Representative TOF transient for holes of TBADN at $E = 2 \times 10^5$ V/cm. (b) Hole mobilities vs $E^{1/2}$ of TBADN.

5.4.3　　　　Discussions

As shown in Figure 5-18, MADN and TBADN exhibit non-dispersive hole-transport behaviors, and the field dependence of hole mobilities follows the Poole-Frenkel relationship (*Equation 5.3*): mobility (μ) is proportional to the

square root of the applied electric field ($E^{1/2}$). The fitted value of the zero-field mobility (μ_0), and the Poole-Frenkel factor (β) of MADN and TBADN with C60 as CGL are summarized in Table 5-4. It is apparent that the CGL-TOF results almost identical to the results of typical TOF. Moreover, by incorporating C60 as the CGL, a more practical thickness of 3~5 μm for MADN and TBADN were used in the TOF sample configuration, indicating C60 is useful as the general CGL for hole TOF measurements of ADN-type materials.
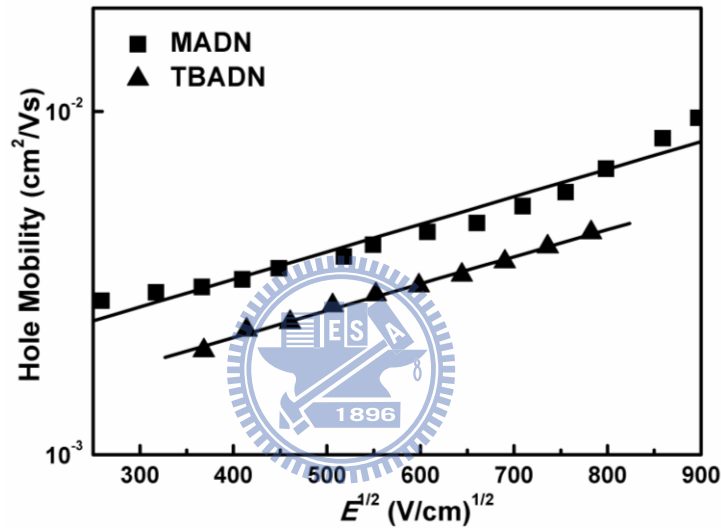
Figure 5-18 Hole mobilities *vs* $E^{1/2}$ of MADN and TBADN.

Table 5-4 The fitted values of zero-field hole mobility and Poole-Frenkel factor of MADN and TBADN.

sample structure	zero-field mobility (μ_0, cm^2/Vs)	Poole-Frenkel factor [β, (cm/V)$^{1/2}$]
MADN	1.55×10^{-3}	1.85×10^{-3}
C60/MADN	2.02×10^{-3}	1.22×10^{-3}
TBADN	1.06×10^{-3}	1.81×10^{-3}
C60/TBADN	9.41×10^{-4}	1.98×10^{-3}

However, the hole transients of ADN are still highly dispersive due to the same crystallization problem even using this CGL technique, and no transit time and electron mobility can be extracted. On the other hand, it is difficult for the photo-generated electrons to inject into ADN-type materials from C60 due to the large energy barrier between the LUMOs of C60 and ADN-type materials (LUMOs of C60 and ADN-type materials are 3.6 eV and 2.5 eV, respectively), suggesting that C60 is not suitable to be a CGL for electron TOF measurements of ADN-type materials.

5.5   Summary

In this chapter, we measured the hole mobilities of MADN and TBADN by TOF technique, and we found that ADN-type materials have high hole mobilities in the ranges of 2×10^{-3} to 9×10^{-3} cm^2/Vs, and have almost identical and small Poole-Frenkel factors. Furthermore, the various substituents on anthracene moiety would affect the conformation of molecular packing and further change the charge-carrier transport abilities of each molecule. For instance, the bulky *t*-butyl substitution is an effective means of tuning hole mobility in ADN-type compounds, which can increase the intermolecular distance and further suppress hole mobility. In addition, we also have shown that C60 is useful as the CGL of TOF measurements for hole mobilities of ADN-type materials. Such a scheme shall have the advantages of simplifying the instrument and reducing material consumption in the TOF mobility measurements.

References

[1] M. A. Baldo, D. F. O'Brien, Y. You, A. Shoustikov, S. Sibley, M. E.

Thompson, S. R. Forrest, *Nature* **395**, 151 (1998).

[2] H. Aziz, Z. D. Popovic, N. X. Hu, A. M. Hor, G. Xu, *Science* **283**, 1900 (1999).

[3] J. L. Bredas, J. P. Calbert, D. A. da Silva, J. Cornil, *Proc. Natl. Acad. Sci. U.S.A.* **99**, 5804 (2002).

[4] Y. C. Cheng, R. J. Silbey, D. A. da Silva, J. P. Calbert, J. Cornil, J. L. Bredas, *J. Chem. Phys.* **118**, 3764 (2003).

[5] S. F. Nelsen, D. A. Trieber, R. F. Ismagilov, Y. Teki, *J. Am. Chem. Soc.* **123**, 5684 (2003).

[6] B. C. Lin, C. P. Cheng, Z. P. M. Lao, *J. Phys. Chem. A* **107**, 5241 (2003).

[7] W. Q. Deng, W. A. Goddard, *J. Phys. Chem. B* **108**, 8614 (2004).

[8] R. A. Marcus, *J. Chem. Phys.* **24**, 966 (1956).

[9] D. N. Beratan, *J. Am. Chem. Soc.* **108**, 4321 (1986).

[10] J. N. Onuchic, D. N. Beratan, *J. Am. Chem. Soc.* **109**, 6771 (1987).

[11] A. A. Voityuk, N. Rosch, M. Bixon, J. Jortner, *J. Phys. Chem. B* **104**, 9740 (2000).

[12] A. Troisi, G. Orlandi, *Chem. Phys. Lett.* **344**, 509 (2001).

[13] M. Malagoli, J. L. Bredas, *Chem. Phys. Lett.* **327**, 13 (2000).

[14] J. Cornil, J. L. Brédas, J. Zaumseil, H. Sirringhaus, *Adv. Mater.* **19**, 1791 (2007).

[15] P. Raghunath, M. A. Reddy, C. Gouri, K. Bhanuprakash, V. J. Rao, *J. Phys. Chem. A* **110**, 1152 (2006).

[16] V. Coropceanu, M. Malagoli, D. A. da Silva, N. E. Gruhn, T. G. Bill, J. L. Bredas, *Phys. Rew. Lett.* **89**, 275503 (2002).

[17] J. Tant, Y. H. Geerts, M. Lehmann, V. De Cupere, G. Zucchi, B. W. Laursen,

T. Bjornholm, V. Lemaur, V. Marcq, A. Burquel, E. Hennebicq, F. Gardebien, P. Viville, D. Beljonne, R. Lazzaroni, J. Cornil, *J. Phys. Chem. B* **109**, 20315 (2005).

[18] B. Yang, S. K. Kim, H. Xu, Y. I. Park, H. Y. Zhang, C. Gu, F. Z. Shen, C. L. Wang, D. D. Liu, X. D. Liu, M. Hanif, S. Tang, W. J. Li, F. Li, J. C. Shen, J. W. Park, Y. G. Ma, *Chemphyschem* **9**, 2601 (2008).

[19] Y. Sun, L. Duan, P. Wei, J. Qiao, G. Dong, L. Wang, Y. Qiu, *Org. Lett.* **11**, 2069 (2009).

[20] X. Q. Ran, J. K. Feng, Y. L. Liu, A. M. Ren, L. Y. Zou, C. C. Sun, *J. Phys. Chem. A* **112**, 11904 (2008).

[21] X. Q. Ran, J. K. Feng, A. M. Ren, W. C. Li, L. Y. Zou, C. C. Sun, *J. Phys. Chem. A* **113**, 7933 (2009).

[22] S. C. Tse, S. K. So, M. Y. Yeung, C. F. Lo, S. W. Wen, C. H. Chen, *Jpn. J. Appl. Phys.* **45**, 555 (2006).

[23] S. C. Tse, S. K. So, M. Y. Yeung, C. F. Lo, S. W. Wen. C. H. Chen. *Chem. Phys. Lett.* **422**, 354 (2004).

[24] W. D. Gill, *J. Appl. Phys.* **43**, 5033 (1972).

[25] H. Bässler, *Phys. Status Solidi B* **175**, 15 (1993).

[26] M. H. Ho, Y. S. Wu, S. W. Wen, M. T. Lee, T. M. Chen, C. H. Chen, K. C. Kwok, S. K. So, K. T. Yeung, Y. K. Cheng, Z. Q. Gao, *Appl. Phys. Lett.* **89**, 252903 (2006).

[27] H. H. Fong, S. K. So, W. Y. Sham, C. F. Lo, Y. S. Wu, C. H. Chen, *Chem. Phys.* **289**, 119 (2004).

[28] W. Y. Hung, T. H. Ke, Y. T. Lin, C. C. Wu, T. H. Hung, T. C. Chao, K. T. Wong, C. I. Wu, *Appl. Phys. Lett.* **88**, 064102 (2006).

[29] B. Chen, C. S. Lee, S. T. Lee, P. Webb, Y. C. Chan, W. Gambling, H. Tian, W. Zhu, *Jpn. J. Appl. Phys.* **39, 1**190 (2000).

[30] S. W. Culligan, A. C. A. Chen, J. U. Wallace, K. P. Klubek, C. W. Tang, S. H. Chen, *Adv. Funct. Mater.* **16**, 1481 (2006).

[31] A. J. Pal, R. Osterbacka, K. M. Kallman, H. Stubb, *Appl. Phys. Lett.* **71**, 228 (1997).

[32] J. D. J. Ingle, S. R. Crouch, *Spectrochemical Analysis*, New Jersey: Prentice Hall (1988).

[33] W. J. Shen, B. Banumathy, H. H. Chen, C. H. Chen, *Proceedings of IDMC2003*, p. 741 (2003), Taipei, Taiwan.

[34] E. Frankevich, Y. Maruyama, H. Ogata, *Chem. Phys. Lett.* **214**, 39 (1993).

[35] J. H. Schön, *Synth. Met.* **122**, 157 (2001)

[36] J. Y. Lee, J. H. Kwon, *Appl. Phys. Lett.* **88**, 183502 (2006).

Chapter 6

Admittance Spectroscopy Measurements for Conductive-Doped Organic Layers

6.1 Introduction

As an alternative to inorganic semiconductors, organic materials have recently gained much attention [1]. Originally, much of the research has concentrated on single crystals, which can show mobilites of a few cm^2/Vs at room temperature and even much higher values at low temperature, as shown in the pioneering work of Karl [2]. However, for practical applications as thin films, organic semiconductors with disordered structures, such as evaporated small-molecule materials of polymers processed from solution are prevailing. In photoconductors for copiers and laser printers, organic semiconductors are already broadly applied.

Organic semiconductors have unique physical properties, which offer many advantages to inorganic semiconductors: (1) The extremely high absorption coefficients in the visible range of some dyes offer the possibility to prepare very thin photodetectors and photovoltaic cells [3]. Due to the small thickness of the layers, the requirements on chemical and structural perfection are reduced since the excitation energy does not have to travel long ways. (2) Many fluorescent dyes emit strongly red shifted to their absorption. Thus, there are almost no reabsorption losses in OLEDs [4], which, together with the low index of refraction, circumvents the key problems of inorganic LED. (3) Since organic semiconductors consist of molecular structures with saturated electron systems, the number of intrinsic defects in disordered systems is much lower than in

inorganic amorphous semiconductors, where a large number of dangling bonds exist. (4) There is a nearly unlimited number of chemical compounds available, and it is possible to tailor materials.

It is worthwhile to remind that the breakthrough of the classical silicon technology came in the very moment the conduction type was no longer determined by impurities but could be controlled by doping. Unlike inorganic semiconductors, up to now, organic dyes are usually prepared in a nominally undoped form. However, controlled and stable doping is a prerequisite for the realization and the efficiency of many organic-based devices. If we succeed in shifting the Fermi level towards the transport states, this could reduce ohmic losses, ease carrier injection from contacts and increase the built-in potential of Schottky- or *p-n* junctions.

In this chapter, we study the electrical characteristics and doping effect of *p-* and *n*-doped organic layers by measuring current-voltage (*I-V*) curves and temperature-dependent AS. The fundamental theory of AS are describe in *Section 2.10*. Then, we also demonstrate the application of these conductivity-doped organic layers in OLED devices.

6.2   *n*-type doped system composed of PAK2-doped BPhen

Since the demonstration of the first double-layer OLED device in 1987 [4], a great deal of effort has been made to improve their performance. Improving the charge injection is one important way to enhance device performance. Efficient electron injection in OLED devices is more difficult to achieve without the use of low work-function metals. Using low work-function metals or alloys as cathode [4,5,6,7,8], remarkable improvements in device performance have been achieved. Unfortunately, the low work-function metals are readily oxidized

and limit the lifetime of the device. Despite its relatively high work function, an Al cathode is widely used due to its high resistance to corrosion, stability, and processibility.

Later, a number of groups have reported that electron injection can be significantly improved by inserting a thin layer of large band gap inorganic and organic salts or insulators at the organic/metal interface [7,9,10,11,12,13,14,15,16,17,18]. The improvements on the electron injection have been attributed to tunneling injection of electrons, as sufficient potential difference may be maintained between Al and Alq_3 in the presence of a thin insulating layer [9,19,20,21]. In these cases, a thin LiF is the most commonly used insulator to be inserted between Al and Alq_3 [10]. Another explanation for the mechanism of electron injection into the LiF/Al composite cathode is a chemical reaction between Al and LiF [22]. Another class of electron injection materials is organometallic complexes with reactive metals such as alkali metal carboxylates [23,24] and 2-(hydroxyl)quinoline lithium (Liq) [25]. However, the effectiveness of these electron injection materials is very sensitive to the choice of metal and only Al has been found to provide good device performance.

An alternative approach for efficient carrier injection is to introduce a *p-i-n* structure into an OLED device as described in *Section 1.4*. In 2004, Canon Inc. reported that cesium carbonate (Cs_2CO_3) [26], which can facilitate electron injection from a wide range of metal electrodes. However, fabrication can be performed only at the high deposition temperature of Cs_2CO_3 (around 500 ℃ under a vacuum). Therefore, finding a satisfactory *n*-type dopant with a low deposition temperature is important in developing OLEDs with low power consumption.

In this section, we developed an *n*-doped ETL that consists of dipotassium phthalate [$C_6H_4(COOK)_2$, abbreviation as PAK2 in this thesis] incorporated into BPhen, PAK2 can grow at a stable rate around 330 ^{0}C at a base vacuum of 10^{-6} torr, significantly facilitating the fabrication process. The electrical characteristics of this *n*-doped layer are also investigated by measuring current-voltage (*I-V*) curves and temperature-dependent AS and we also study the mechanism of the thermal evaporation process of PAK2 by quartz crystal microbalance (QCM) method and scanning auger spectroscopy.

6.2.1 Admittance measurements of PAK2-doped BPhen layer

A series of electron-only devices were also fabricated to study the electron injection and electrical characteristics of using PAK2 as *n*-type dopant. The structure of electron-only devices was ITO/Alq$_3$ (60 nm)/*n*-doped ETL (30 nm)/Al (150 nm), in which the *n*-doped ETL is composed of BPhen doped PAK2, and doping concentration of PAK2 were 0%, 5%, 10% and 20%, respectively.

Figure 6-1 plots the *I-V* characteristics of electron-only devices and reveals that the PAK2-doped devices all greatly outperform the undoped device, indicating that doping PAK2 into BPhen promotes the injection of electron from the Al cathode. The 5% PAK2-doped device B shows the best *I-V* characteristics amongst in all electron-only devices, even at small applied bias, probably due to the different extent of electron injection with various PAK2 doping concentration. The electrical properties of this *n*-doped layer were investigated by temperature-dependent AS with an equivalent circuit model to elucidate this phenomenon.
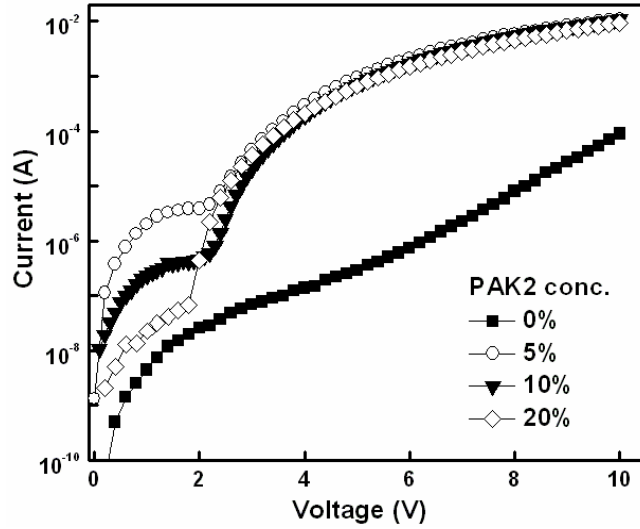
Figure 6-1 *I-V* characteristics of PAK2-doped electron-only devices.

Figure 6-2(a) shows the capacitance-frequency (*C-F*) and conductance/frequency-frequency (*G/F-F*) spectra of 5% PAK2-doped electon-only device measured at 1.8 V and room temperature. The spectra show two capacitance drops and *G/F* peaks at inflexion frequencies and around 22 kHz and 0.22 MHz, suggesting the presence of two geometric resistance-capacitance (*RC*) time constant effects. Based on these spectra, an equivalent circuit model as shown in Figure 6-2(b) is developed, where C_{Alq3}, R_{Alq3}, and C_{BPhen}, R_{BPhen} represent the geometric capacitance and resistance of the Alq$_3$ and BPhen layers, respectively, and *Rs* represent the series resistance which can be ascribed to parasitic effects due to lead/contact resistances [27].
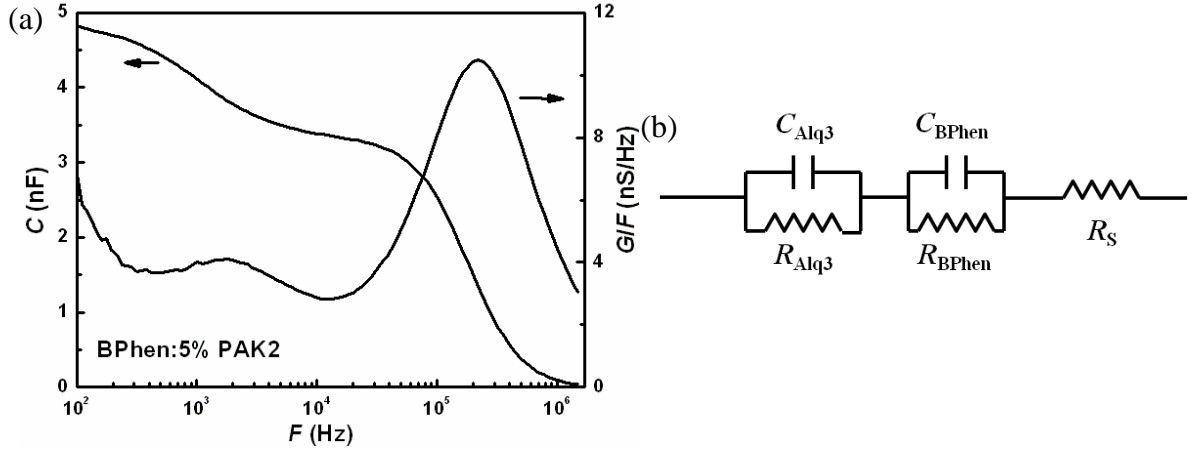
Figure 6-2 (a) *G/F-F* spectrum and capacitance-frequency *C-F* spectrum of 5% PAK2-doped device measured at 2 V and room temperature. (b) Schematic representation of equivalent circuit model.

In these electron-only devices, R_{Alq3} can be treated as an open circuit because it is much larger than R_{BPhen} and R_s, and R_{BPhen} can be also reasonably assumed to be larger than R_s. Based on this equivalent circuit, the total equivalent capacitance is related to *equation 2.11*, which is given by

$$C(\omega) = \frac{C_0}{1+(C_0 Rs\omega)^2} \tag{6.1}$$

where ω is frequency, and C_0 is

$$C_0 = \frac{C_{Alq3}C_{BPhen}}{C_{Alq3}+C_{BPhen}}\left[1+\frac{C_{Alq3}/C_{BPhen}}{1+\omega^2 R_{BPhen}{}^2 (C_{Alq3}+C_{BPhen})^2}\right] \tag{6.2}$$

From the equivalent capacitance *equations 6.1 and 6.2*, it can be found that $C(\omega)$ equals to C_{Alq3} when the frequency (ω) is low enough. As ω increases, $C(\omega)$ becomes a value of series combination of C_{Alq3} and C_{BPhen}. When ω further increases, $C(\omega)$ drops to zero due to series resistance *Rs*. As shown in Figure 6-2(a), the capacitance of 4.7 nF at 100 Hz is comparable to the value of 4.64 nF

determined from thickness of the Alq$_3$ layer according to the following parallel-capacitance model:

$$C = \varepsilon_r \varepsilon_0 A / d \tag{6.3}$$

where ε_r is 3.5 (the dielectric constant of Alq$_3$ [28]), ε_0 is 8.85 $\times$ 10^{-14} F/cm (the permittivity of free space), A and d are 0.09 cm^2 and 6 $\times$ 10^{-6} cm (the device active area and Alq$_3$ layer thickness), respectively.

As frequency increases, the carriers charging the BPhen layer cannot follow ac probing frequency and the capacitance drops at the inflexion frequency of ~2 kHz which equals to the inverse of the RC time constant of the BPhen layer by the relationship of

$$\omega_{inflexion} = \tau^{-1} = [R_{BPhen}(C_{Alq3} + C_{BPhen})]^{-1} \tag{6.4}$$

where the value of C_{BPhen} is 9.29 nF calculated from the same equation as C_{Alq3}. When frequency is increased beyond this inflexion frequency, the capacitance reaches a plateau with a value of 3.2 nF, which is also comparable to the calculated value of series combination of C_{Alq3} and C_{BPhen} ($C_{Alq3+BPhen}$) as shown below:

$$C_{Alq3+BPhen} = \frac{C_{Alq3} \times C_{BPhen}}{C_{Alq3} + C_{BPhen}} = \frac{4.64 \times 10^{-9} \times 9.29 \times 10^{-9}}{(4.64 + 9.29) \times 10^{-9}} = 3.1 \times 10^{-9} \tag{6.5}$$

As frequency further increases, the capacitance drops to zero due to the small value of series resistance R_s. The C-F spectrum shows excellent agreement with the results of equivalent circuit model. It is notable that the two inflexion frequencies can be more clearly observed in conductance/frequency-frequency (G/F-F) spectra.

Furthermore, we measured the conductance/frequency-frequency (G/F-F)

spectra of these electron-only devices at various biases as plotted in Figure 6-3, in which the distinct *G/F* peaks are proportional to the dielectric loss. The loss peak can be described by the classical Debye frequency response which is given by

$$\frac{G(F)}{F} = \frac{A/F_P}{1+(F/F_P)^2} \tag{6.6}$$

where the amplitude *A* is a temperature-dependent constant, F_p is the peak frequency. As shown in Figure 6-3, the undoped device only shows the bias-independent peak at high frequency region at 585 kHz, even at high applied bias, this peak is assigned to the resistance-capacitance (*RC*) time constant of parasitic series resistance as we discussed in previous paragraph. We attribute this result to the energy barrier between the work function of Al (4.2 eV) and the lowest unoccupied molecular orbital (LUMO) of BPhen (2.9 eV) in undoped device is too high to be measured by admittance spectroscopy.

On the other hand, the rest spectra of PAK2-doped devices all show two distinct *G/F* peaks: a bias-independent peak at high-frequency region of 0.16-0.22 MHz, which is assigned as the *RC* time constant of parasitic series resistance; a bias-dependent peak at low frequency region of ~1 kHz, which is associated with the *RC* time constant of PAK2-doped layer. Moreover, Figure 6-3 also reveals that the signal of PAK2-doped layer cannot be clearly observed at a bias of under 1 V, because a high energy barrier between Al and BPhen, limiting the AS measurements. We suggest that the energy barrier becomes negligible as the bias is increased over 1 V.
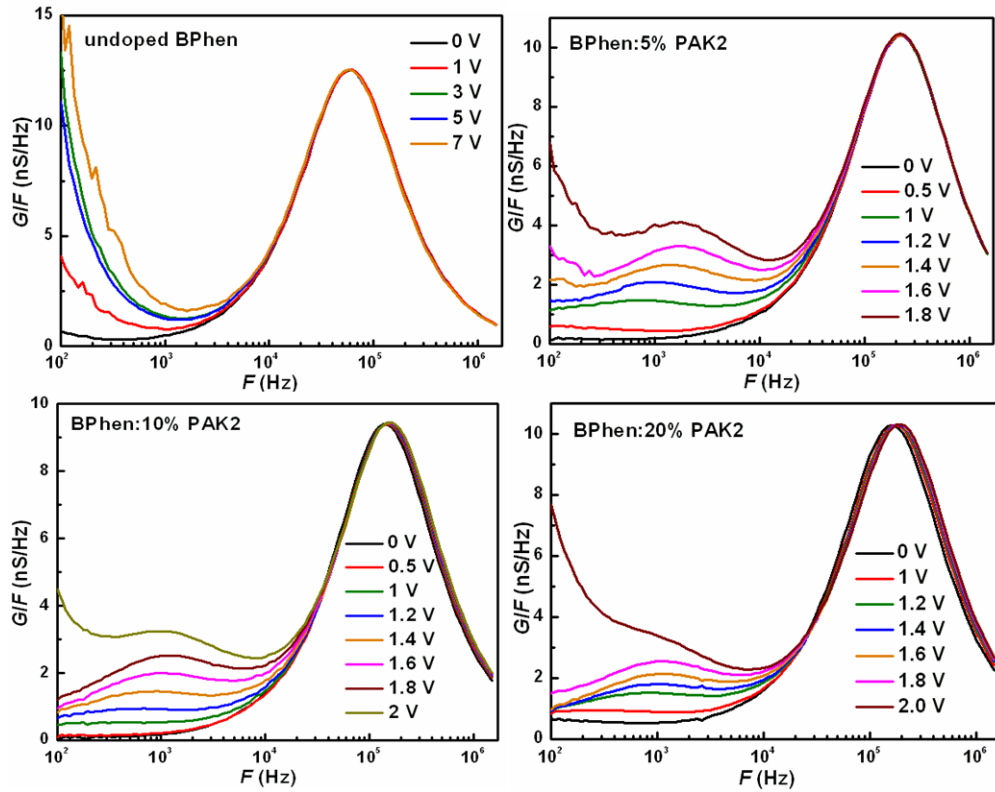
Figure 6-3 *G/F-F* spectra of PAK2-doped electron-only devices at various biases.

Furthermore, the electrical properties of PAK2-doped layer can be characterized from the temperature-dependent AS measurements. Figure 6-4 displays temperature-dependent *G/F-F* spectra of 5% PAK2-doped device measured at 1 V, 1.2 V, 1.6 V, and 1.8 V, respectively. It is evident that the signal of parasitic series resistance at high frequency region is temperature-independent and would not shift at different temperature. On the other hand, the signal of PAK2-doped layer at low frequency region is temperature-dependent, it would shift toward higher frequency region at high temperature.
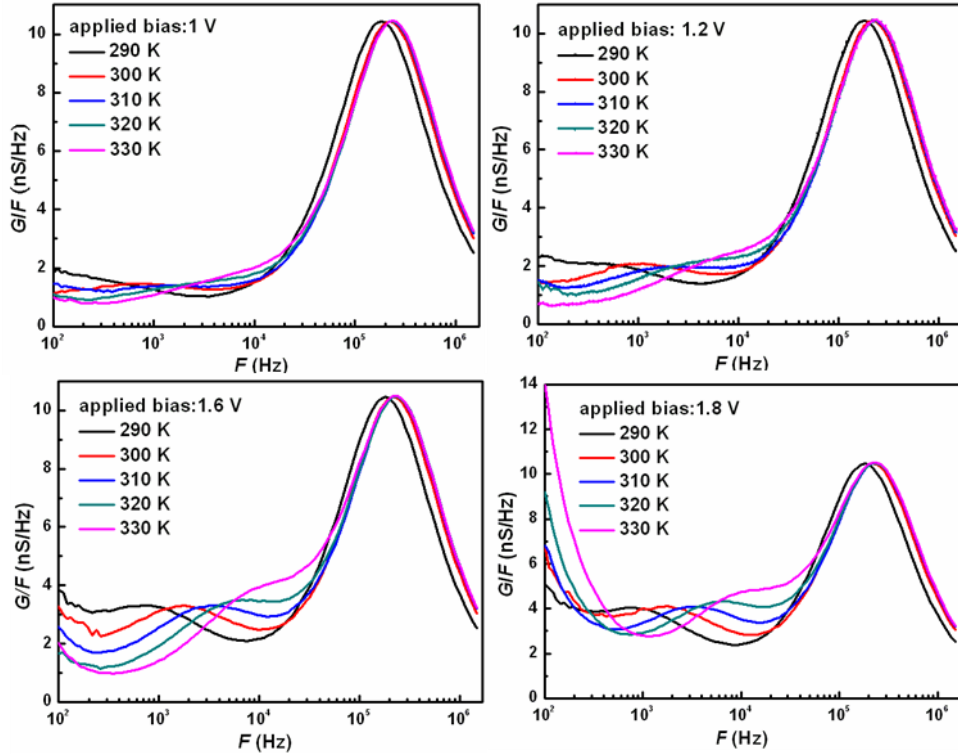
Figure 6-4 Temperature-dependent *G/F-F* spectra of 5% PAK2-doped devices measured at various biases.

The BPhen peak evidently depends significantly on temperature and the series-resistance peaks are all independent of temperature. Furthermore, the activation energy (E_a) can be obtained from these temperature-dependent peaks by a simple geometric equation derived from *equation 2.12*.

$$F = F_0 \exp(\frac{-E_a}{k_B T})$$
(6.7)

where F_0 is the pre-exponential factor, E_a is the activation energy which represents the energy separation between the edge of the Fermi level and the LUMO level of BPhen in this model, k_B is Boltzmann's constant and T is the temperature. Therefore, the E_a can be derived from the slope of relationship between of $\ln(F)$ and $1000/T$ as plotted in Figure 6-5(a).
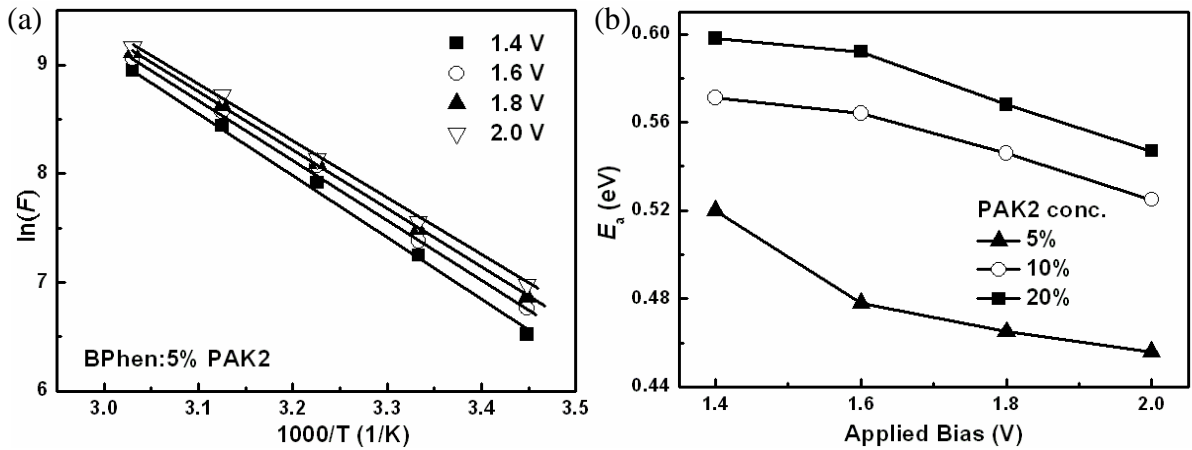
Figure 6-5 (a) Characteristics of ln(*F*) vs 1000/*T* of 5% PAK2-doped device at various biases derived from the low-frequency peaks in Figure 6-4. (b) Relationship between E_a and applied bias of PAK2-doped devices.

Figure 6-5(b) plots the relationship between E_a and applied bias of PAK2-doped devices. The calculated E_a values of the PAK2-doped devices are around 0.5~0.6 eV which is much smaller than the E_a (half band-gap, 1.7 eV) of pristine BPhen (The Fermi level of ideally pure organic semiconductors should be close to the middle of the gap) [29]. Based on these AS results, the incorporation of PAK2 into BPhen increases the Fermi level of BPhen from deep to shallow, further reducing the interface energy barrier and increasing the efficiency of electron injection from the Al cathode. Moreover, the 5% PAK2-doped device has the smallest E_a value, which fully agrees with the result of *I-V* measurement, indicating that increasing PAK2 concentration from 5% to 20% would not further improve the performance of electron injection, which might be attributable to some other effects of carrier quenching and defect generations.

6.2.2　　　Elucidation of the mechanism of thermal-evaporated PAK2 layer

In previous section, we studied the electrical characteristics of BPhen doped PAK2 layer from *I-V* curves and AS measurements and demonstrate the incorporation of PAK2 can reduce the electron injection barrier from Al cathode.

Similar result was reported for sodium acetate (CH_3COONa) used as an efficient EIL in OLED devices [24]. Furthermore, higher sodium (Na) content in overlaid Al cathodes was observed for $Alq_3/CH_3COONa/Al$ than $Alq_3/NaF/Al$ by x-ray photoelectron spectroscopy of detached Al cathodes [23]. It was also found by XPS that Na metal with a small amount of CH_3COONa was deposited during vapor deposition of CH_3COONa [30]. However, it is still a difficult task to evaluate the possibility of alkali metals formation by thermal decomposition.

For this purpose, the QCM is a simple and extremely sensitive method to measure the negative frequency shift caused by increasing mass during deposition of alkali metal salts. By using QCM, Ganzorig and Fujihira demonstrated the thermal decomposition of the Na salts of acetate and benzoate during vacuum vapor deposition [31]; Qiu also investigated the electron injection mechanism of evaporated Cs_2CO_3 [32]. To estimate the possible evaporation behavior of PAK2, we use QCM method to measure the negative frequency shift caused by the vacuum thermal evaporation of PAK2. In order to reduce the possible experimental errors, two thermally stable materials (NPB and MADN) were selected for comparison, and their slopes of the linear relationship (frequency shift *vs* mass loss) are compared to that of PAK2.

The frequency shift of the QCM (Δf) can be converted to the mass loss load on the surface of the quartz crystal wafer using the standard Sauerbrey formula

[33,34,35] as follows:

$$\Delta f = -2.26 \times 10^{-6} f^2 \Delta m / A \qquad (6.8)$$

where Δf (Hz) denotes the change in the oscillation frequency of the quartz crystal, f (Hz) is the resonance frequency of the quartz crystal, Δm (g) is the change in the mass and adsorbed onto the crystal, and A (cm^2) is the deposition area on the quartz crystal.

If the source material is assumed to be thermally stable during the evaporation, the mass adsorbed onto the crystal surface (Δm) would be in direct ratio the mass loss in the boat (ΔM):

$$\Delta m = -k\Delta M, (k \geq 0) \qquad (6.9)$$

Then, according to *equation 6.9*, the following equation can be obtained:

$$\Delta f = K\Delta M, K = -2.26 \times 10^{-6} f^2 k / A \qquad (6.10)$$

where K is a positive constant that is independent of the materials used. It can be seen that Δf is in direct ratio to ΔM. On the contrary, if the source material decomposes and only a fraction ($d\%$) is deposited, Δm would be in direct ratio to $d\% \times \Delta M$:

$$\Delta m = -k(d\%)\Delta M, (k \geq 0)$$

(6.11)

Thereby, according to *equation 6.11*, the following equation can be obtained:

$$\Delta f = (d\%)K\Delta M, K = -2.26 \times 10^{-6} f^2 k / A \qquad (6.12)$$

It is clear that the slope of the line (Δf *vs* ΔM) may decrease to $d\%$ of its initial value if the source material decomposes.

Approximately 10, 20, 30, and 40 mg of NPB, MADN, PAK2 were introduced into the tungsten boat in the vacuum chamber, respectively. The resistive heating was controlled by adjusting the source current of the power supply, which was increased by 5 A every 2 min. The resistive heating of the bare tungsten boat could have led to a positive (Δf) value when the current was increased, but the shift of the bare quartz crystal proved to be smaller than 25 Hz, which was negligible.

The negative frequency shift–current (Δf vs I) characteristics of these materials are shown in Figure 6-6. For NPB, MADN, and PAK2, the materials in the boat were not used up until the applied current became 50, 45, and 70 A (critical currents), respectively. The Δf values are therefore calculated from the frequencies at the critical currents and the frequencies at 0 A.

The Δf vs ΔM curves are plotted in Figure 6-7, reveal that the experimental data of each material can be fitted to a straight line ($\Delta f = K\Delta M + B$). The values of the slopes (K), intercepts (B), and linear correlation coefficients (r) are summarized in Table 6-1, show that Δf and ΔM have a good linear relationship for all the three materials. According to *Equations 6.10 and 6.12*, the intercept (B) should be zero, we attribute the experimental value of B is owing to the system errors. Note that the values of $K\Delta M$ are far form than those of B, therefore, the value of B can be omitted.
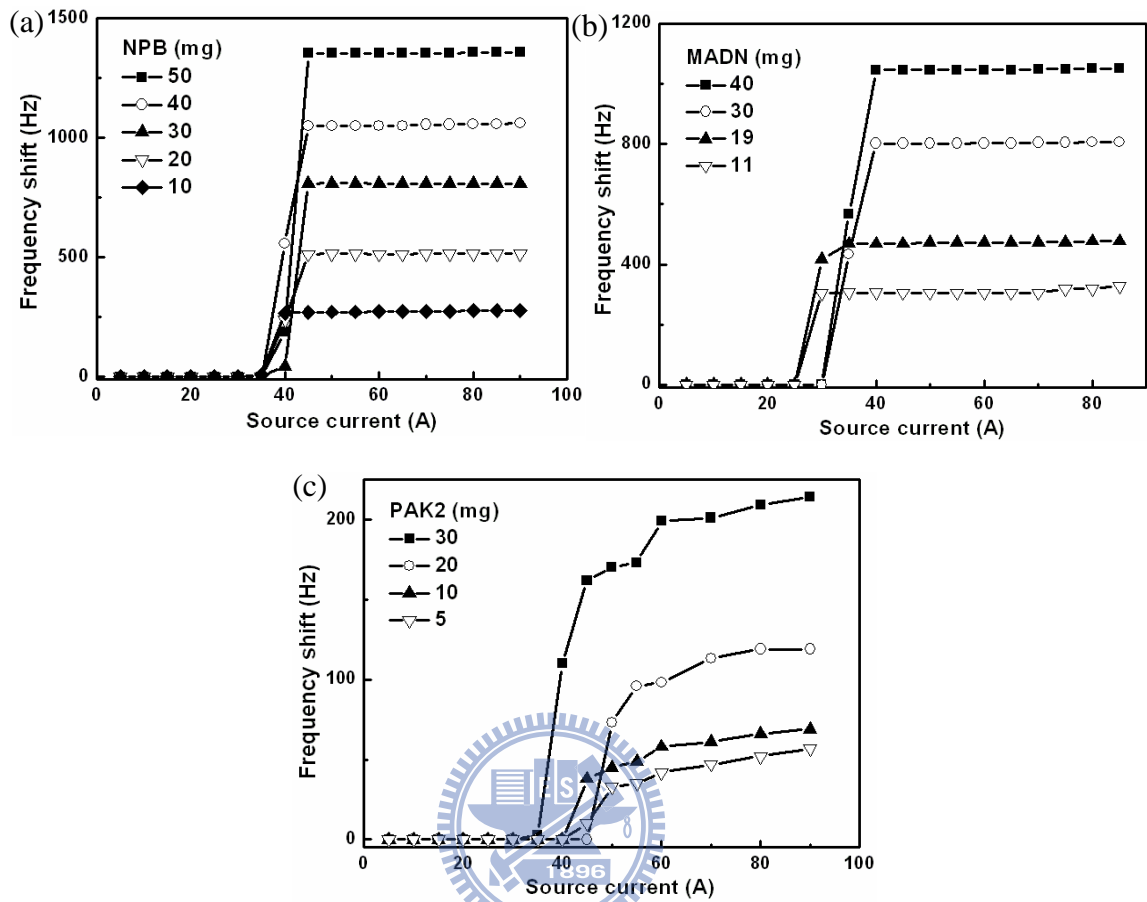
Figure 6-6 Δf *vs* I characteristics of (a) NPB, (b) MADN, and (c) PAK2.
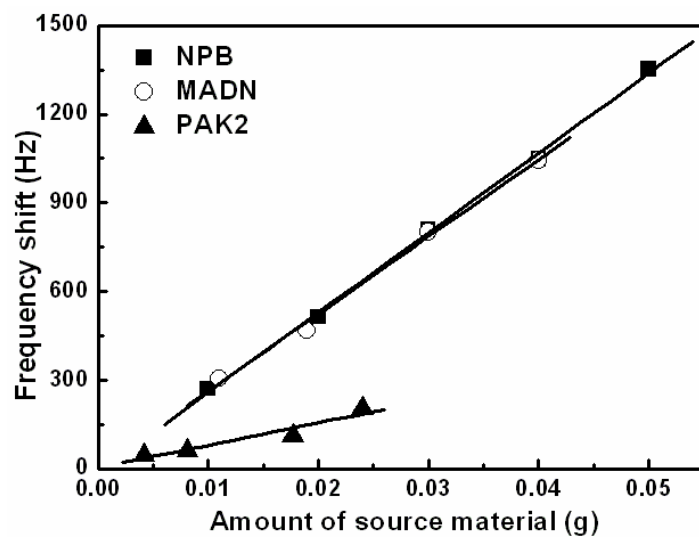
Figure 6-7 Δf *vs* ΔM characteristics of NPB, MADN, and PAK2.

Table 6-1 Parameters of the linear fitting ($\Delta f = K\Delta M + B$) from Figure 6-7 (r is the linear correlation coefficient).

Material	K (× 10^4 Hz/g)	B (Hz)	r	Fraction ($\Delta f/\Delta f$(NPB), %)
NPB	2.69	-10.5	0.99927	-
MADN	2.61	1.12	0.99788	-
PAK2	0.76	3.69	0.96289	28.3

In Table 6-1, it is found that the K values of NPB and MADN are almost identical when the measurement errors are considered, indicating that the behaviors of NPB and MADN fit *Equation 6.10* because they do not decompose during evaporation. In the case of PAK2, it is apparent that the negative Δf value is less than those of NPB and MADN, indicating that PAK2 is decomposed during thermal evaporation and the behavior of PAK2 also fits the *Equation 6.12*. Then, we consider the NPB as the standard material, and from the slopes (K) of NPB and PAK2, the d% of PAK2 can be determined to be 28.3%.

The weight percentage of potassium (K) atom in PAK2 molecule is 32.3%. Furthermore, it can be observed that the chamber pressure will suddenly rise to the order of 10^{-5} torr and then drop back to 10^{-6} torr when PAK2 is evaporated. According to the d% value of PAK2 from OCM measurements and the variation of chamber pressure, we suggest that PAK2 was partially decomposed during the thermal evaporation process, and some kind of gaseous byproducts are also generated, which are the reasons for the pressure variation. The result agrees with some reported observations [31].

In order to further confirm the mechanism of PAK2 deposition, we studied the depth profiling of PAK2 thin film (32 nm, deposited on silicon wafer) by

scanning auger spectroscopy. From Figure 6-8, which plots the characteristics of atomic percentage and etch time, shows the potassium (K) atoms are indeed deposited on the sample along with carbon (C) and oxygen (O) atoms. Based on the results of QCM measurements and depth profiling, we can conclude that the some species contain highly reactive potassium atom are generated during the evaporation process of PAK2. As a result, in the case of our *n*-doped layer composed of BPhen and PAK2, the those generated species with high dipole moments can reduce the electron injection barrier and further improve the electron injection from Al cathode.

We also tested the stability of PAK2 and compared the common used *n*-type material Cs_2CO_3, which absorbs easily the moisture in the ambient. The absorbing characteristics of PAK2 (23.6 mg, 9.7 $\times$ 10^{-5} mole) and Cs_2CO_3 (23 mg, 7.06 $\times$ 10^{-5} mole) were studied at a relative humidity of 60% and a temperature of 21 ^{0}C by a analytical balance in our clean room. The relationship between mass change (Δm) and the time of exposing the samples to the air is plotted in Figure 6-9, in which the smaller mass change can be observed for PAK2, assuring the advantages of using PAK2 into OLED devices.
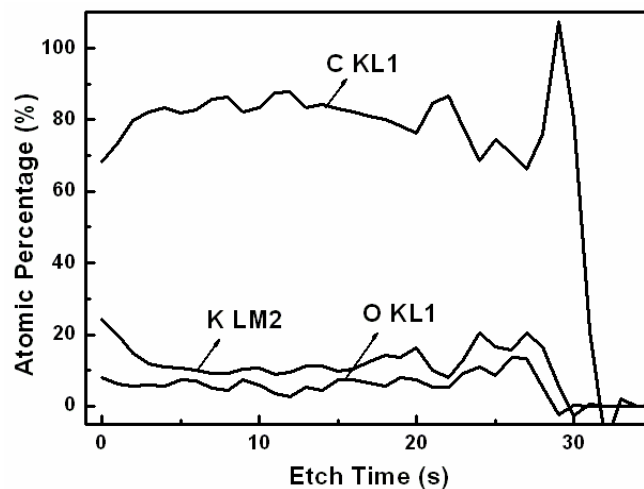
Figure 6-8 Depth profiling of PAK2-deposited film.
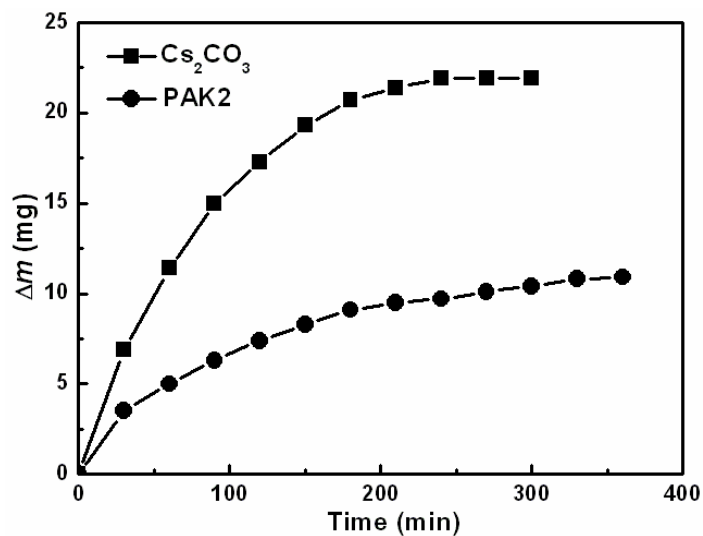
Figure 6-9 Relationship of mass change (Δm) *vs* time.
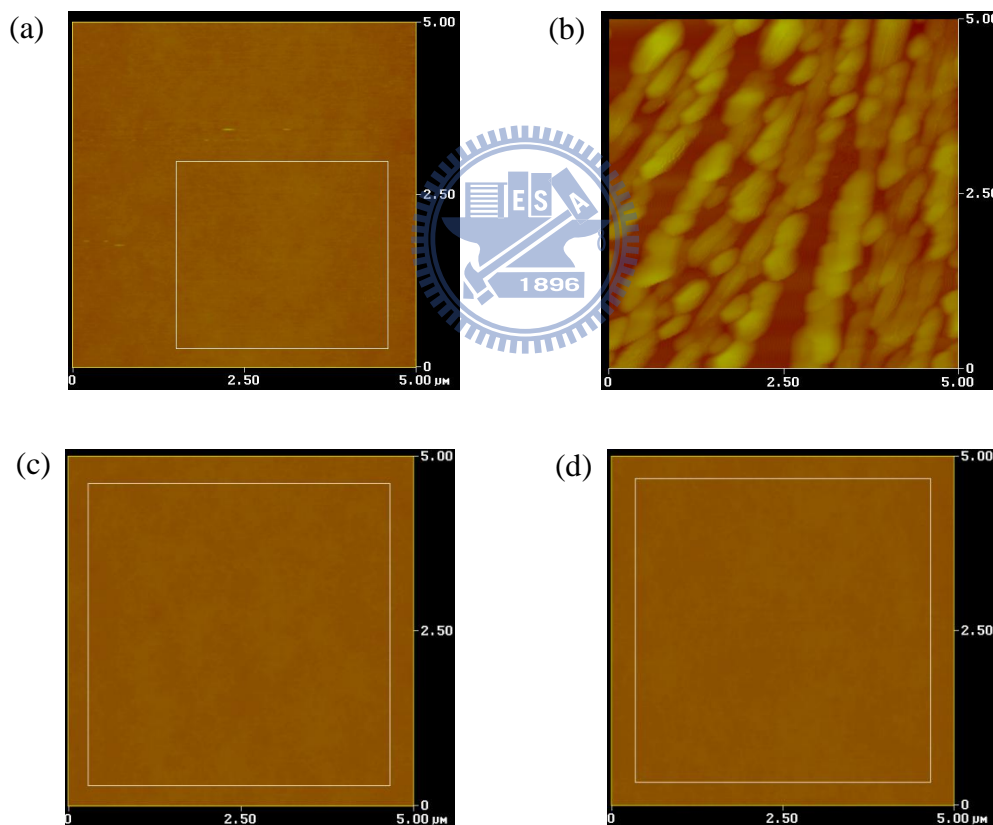
Figure 6-10 AFM topographic images of BPhen and 5% PAK2-doped BPhen thin films deposited on silicon wafers (50 nm). (a) BPhen before heating; (b) BPhen after heating; (c) 5% PAK2-doped BPhen before heating; (d) 5% PAK2-doped BPhen after heating (scanned area: 5 μm × 5 μm).

On the other hand, the thin film of BPhen is known to be morphologically unstable and has been found to affect device degradation [36]. Figure 6-10 pictures the results of AFM measurements, in which the root-mean-square surface roughnesses (R_{ms}) of unheated/heated BPhen films were 0.45 nm/48.8 nm, respectively, indicating the crystallization is evident in pristine BPhen film after heated at 80 °C for 30 min. However, the R_{ms} of unheated 5% PAK2-doped BPhen film was 0.38 nm, and the degradation of surface morphology is clearly suppressed even after heated (R_{ms} was 0.45 nm). Consequently, it is expected the PAK2-doped BPhen layer can improve the device operational stability as well as the electron injection.

6.2.3   Device performances of using *n*-doped layer composed of

PAK2-doped BPhen

To demonstrate PAK2 is more effective than the conventional LiF/Al composite cathode, following OLED devices were fabricated, Alq$_3$-based devices A and B: ITO/CF$_x$/NPB (60 nm)/Alq$_3$ (75 nm)/electron injection layer (EIL)/Al (150 nm), in which the EIL is LiF (1 nm) and BPhen: 5% PAK2 (5 nm), respectively. C545T-doped devices C, D and E: ITO/CF$_x$/NPB (60 nm)/Alq$_3$: 1% C545T (37.5 nm)/Alq$_3$ (37.5 nm)/EIL/Al (150 nm), in which the EIL is LiF (1 nm), BPhen: 5% PAK2 (5 nm), and BPhen: 5% Cs$_2$CO$_3$ (5 nm), respectively.

The detailed EL performances are summarized in Table 6-2. It is notable that devices B and D with PAK2-doped ETL can achieve higher power efficiency and at lower voltage as compared the standard devices A and C with conventional LiF/Al composite cathode. Figure 6-11 plots the power efficiency against luminance of these four devices, it can be observed that device D achieves a power efficiency of 10.9 lm/W at 1000 cd/m^2 and 4.6 V), which is

40% higher than that of conventional device C at 1000 cd/m^2 (7.8 lm/W at 5.2 V). These results clearly demonstrate that the *n*-doping effect of PAK2 in BPhen and further enhanced the electron injection. The dominant carrier in most Alq$_3$-based OLEDs is the injected hole [37]. The improvement of electron injection from the cathode not only reduces the drive voltage but also balances the carrier recombination in the device, which we believe is the main reason for the enhanced efficiency of the device. Moreover, it is notable that the device performances of device D are comparable to those of device E with the commonly used *n*-type dopant, Cs$_2$CO$_3$. In particular, the power efficiency of device D at 100 cd/m^2 can be as high as 14.6 lm/W (at 3.3 V), suggesting that the injection of electrons from the cathode of this PAK2-doped ETL is efficient even at low drive voltage.

Table 6-2 EL performances of OLED devices at 20 mA/cm^2.

Device	Voltage (V)	Current Eff. (cd/A)	Power Eff. (lm/W)	E. Q. E. (%)	CIE$_{x,y}$
A	6.3	3.6	1.8	1.1	(0.36, 0.55)
B	5.3	3.6	2.1	2.1	(0.35, 0.55)
C	6.3	13.3	6.7	3.5	(0.32, 0.64)
D	5.7	15.7	8.7	4.2	(0.30, 0.64)
E	5.7	14.3	7.9	3.8	(0.32, 0.64)
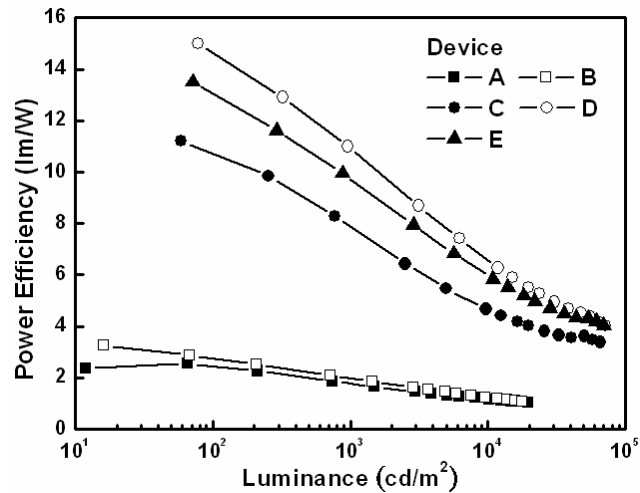
Figure 6-11 Power efficiency *vs* luminance characteristics of OLED devices.

The operational lifetimes of devices C and D under a constant current density of 20 mA/cm^2 was also measured in a dry box, as shown in Figure 6-12. The t_{70} (time for the luminance to decline to 70% of the initial luminance) values of both devices are approximately 500 hrs. In addition, the drive voltage of both devices increased only 0.5 V with continuous operation after 500 h. Based on the assumption of scalable coulombic degradation [38], the half-lives ($t_{1/2}$) of devices C and D can be projected to 28900 hrs and 36200 hrs at 100 cd/m^2, respectively. The operational stability of device D with *n*-doped ETL is clearly comparable to that of conventional device C.
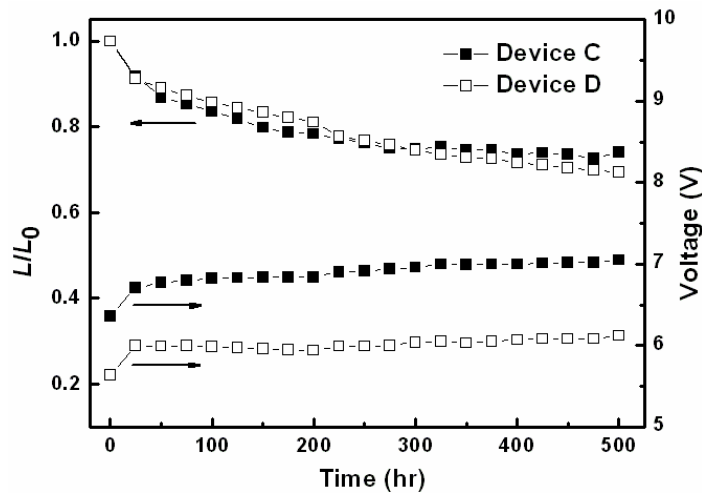
Figure 6-12 Device operational stability of devices C and D.

In summary, *I-V* measurement and temperature-dependent AS indicated that the incorporation of PAK2 into BPhen increases the Fermi-level to only around 0.5 eV below BPhen's LUMO band, further enhancing the efficiency of electron injection from Al cathode. Additionally, the low deposition temperature of PAK2 substantially facilitates the fabrication processes. When this *n*-doped layer is incorporated in the OLED device, the C545T-doped device achieves a current efficiency of 16 cd/A and a power efficiency of 10.9 lm/W at 1000 cd/m^2.

6.3   *p*-type doped system composed of WO$_3$-doped MADN

From the CV curve as shown in Figure 6-13, MADN shows a reversible and stable oxidation and reduction peaks in CV even after repeated scans. This result suggests that MADN possesses stable oxidation and reduction states and is capable of generating free holes and electrons in the presence of *p*-type and *n*-type dopants, indicating that MADN has the potential to be a host for *p*-type and *n*-type dopants in OLED devices.
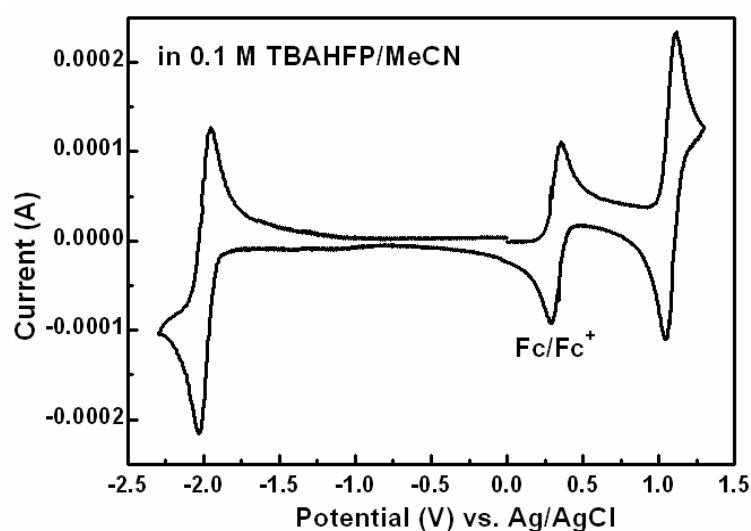
Figure 6-13 Cyclic voltammogram of MADN by using 0.1M tetrabutylammonium hexafluorophosphate as the supporting electrolyte in dichloromethane.

In this section, we develop the p-HTL composed of MADN and WO$_3$, in which WO$_3$ is used as p-type dopant [39]. The carrier injection properties and the effect of WO$_3$ incorporation into MADN are investigated by measuring I-V curves and temperature-dependent AS. The result demonstrates that the incorporation of WO$_3$ into MADN can reduce the resistance and activation energy of MADN layer, which in turn reduces energy barrier of hole injection from ITO anode to MADN layer and ohmic loss of the device. We also demonstrate the application of this p-doped organic layer in OLED devices.

6.3.1   Admittance measurements of WO$_3$-doped MADN layer

In our experiments, a series of hole-only devices were fabricated for studying the effect of hole injection and electrical characteristics. The hole-only device structure was ITO/p-doped HTL (60 nm)/Alq$_3$ (60 nm)/ Al (150 nm), in which the doping concentration of WO$_3$ in MADN are 0%, 10%, 20% and 33%, respectively.

Figure 6-14 plots the I-V characteristics of the hole-only devices. It is shown that the WO$_3$-doped hole-only devices all greatly outperform the undoped device, indicating that doping WO$_3$ into MADN promotes the injection of hole from ITO anode. At a small applied bias, the device with 33% WO$_3$ has the best I-V characteristics than most of the other WO$_3$-doped devices.
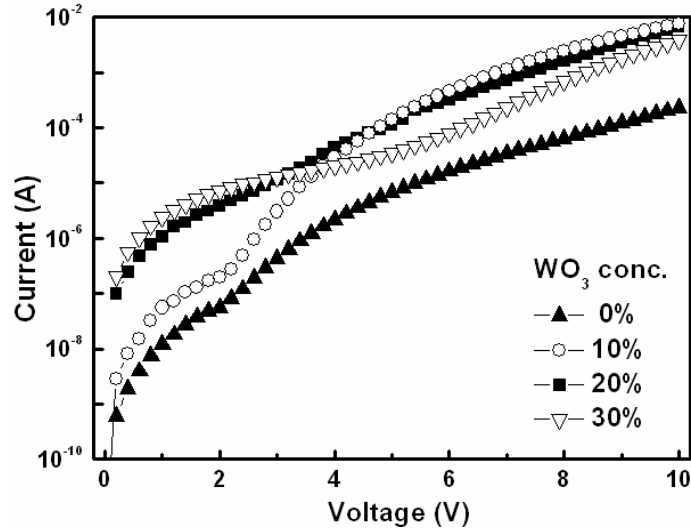
Figure 6-14 *I-V* characteristics of WO_3-doped hole-only devices.

To understand the electrical doping phenomena, the hole-only devices are further investigated by AS as shown in Figure 6-15. As we discussed in the PAK2 case (*Section 6.2.1*), the low-frequency peaks (*G/F* peaks at 250 Hz for undoped device, and 20 kHz for 10% WO_3 device) are assigned to be associated with a single *RC* time constant of the *p*-doped MADN layer and high-frequency peaks (*G/F* peaks at 0.34-0.58 MHz for all devices) are associated with the single *RC* time constant of parasitic series resistance [27]. It can also be observed in Figure 6-15, the *G/F* peak of *p*-doped MADN layer gradually shifts toward the high frequency region and finally mixes with the series resistance peak as WO_3 percentage is increased from 0% to 20%. This result indicates that doping WO_3 into MADN can greatly reduce the resistance of *p*-doped MADN layer according to the relationship of $2\pi f = (RC)^{-1}$.
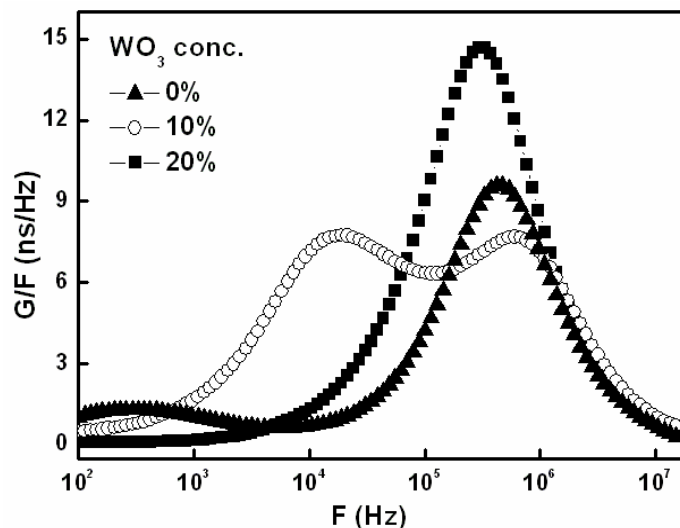
Figure 6-15 *G*/*F*-*F* spectra at zero bias and room temperature of hole-only devices with various WO_3 doping concentration.

Figure 6-16 plots the temperature-dependent *G/F*-*F* spectra measured at zero bias of these hole-only devices, it is found that the high-frequency peak is temperature-independent and the low-frequency peak is temperature-dependent. Furthermore, the E_a of *p*-doped MADN layer can be derived from the slope of relationship between of $\ln(F)$ and $1000/T$ as plotted in Figure 6-17(a). In this case, E_a represents the energy separation between the edge of the HOMO level and Fermi level of MADN as shown in Figure 6-17(b).
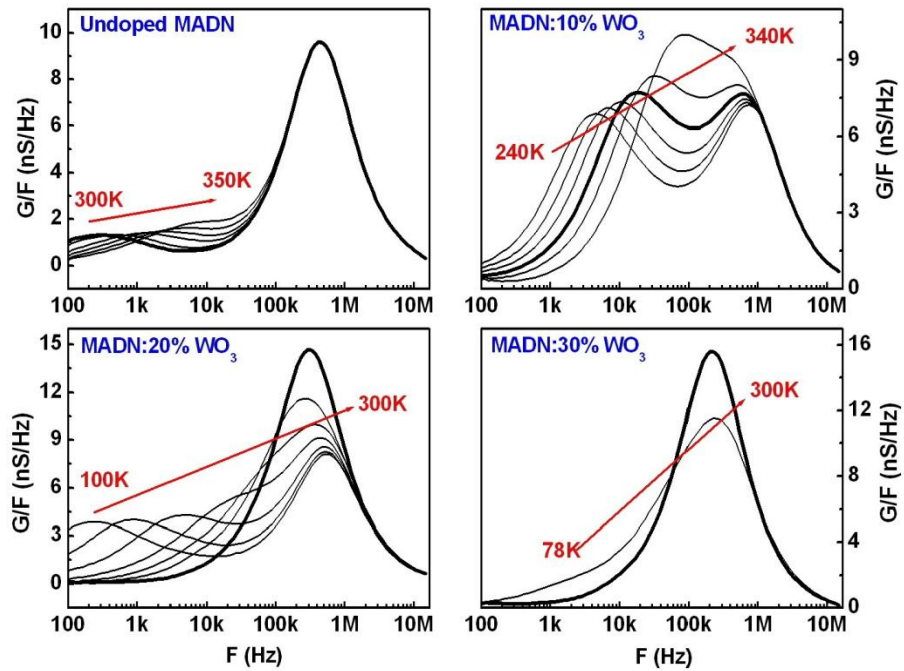
Figure 6-16 Temperature-dependent *G/F-F* spectra at zero bias of hole-only devices with various doping concentration.
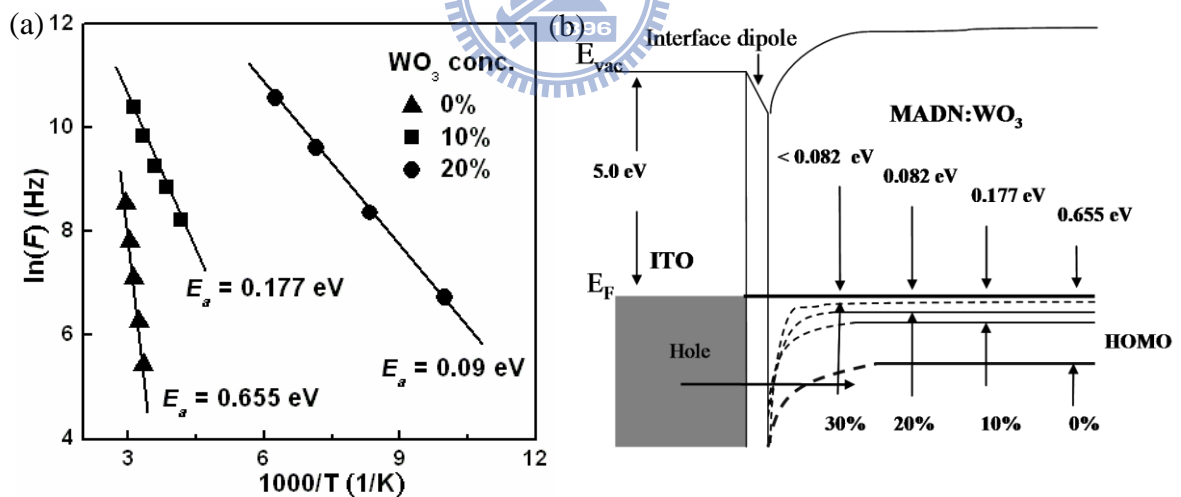
Figure 6-17 (a) Characteristic of ln(*F*) vs 1000/*T* of WO$_3$-doped devices derived from the low-frequency peaks in Figure 6-16. (b) Schematic energy diagram of ITO/*p*-doped MADN interface.

As shown, when the doping concentration of WO_3 is increased from 0% to 10% and then to 20%, the E_a of MADN could be greatly reduced from 0.655 eV to 0.177 eV and then to 0.09 eV. However, as the doping concentration further increases to 33%, the *p*-doped MADN peak still cannot be resolved from the series resistance peak even at a temperature of 78 K. As a result, the E_a cannot be obtained exactly, but it could be estimated to be less than 0.09 eV. Owing to that the E_a represents the energy separation between the edge of HOMO level and Fermi level, the decrease of E_a indicates that the WO_3 incorporation reduces this separation, which lowers the hole injection energy barrier between MADN and ITO, thus improves the hole injection from ITO to MADN.

The improvement can be demonstrated in Figure 6-14, where the room-temperature *I-V* characteristics of the hole-only devices in logarithm scale are plotted. As is shown, the current is gradually improved from the undoped device to the device doped with 33% WO_3 at a small applied bias which agrees well with the results concluded from Figure 6-17(a). Because the current condition of the hole-only device at the small applied bias is mainly dominated by hole injection from ITO to HTL layer, the enhanced current condition at the small applied bias can be ascribed to the reduced width of energy barrier between MADN and ITO as well. At the high applied bias, however, the device doped with 10% WO_3 outperforms the other devices, suggesting that the hole injection barrier becomes negligible at the high applied bias. Consequently under high bias, it is likely that the current conduction is dominated by the carrier transport in the bulk of hole-only device instead. In the heavy doping consideration, the WO_3 could be diffused into the Alq_3 layer resulting in creating trap center near the interface between MADN and Alq_3 which limits the carrier

transport via the interface between MADN and Alq$_3$. As a result, the device doped with 33% WO$_3$ shows a worse current condition than that of the devices doped with 10% and 20% at high applied bias. Following this study, we conclude that the *p*-doped MADN layer is expected to improve hole injection and reduce ohmic loss in OLED devices.

6.3.2 **Device performance of using *p*-doped layer composed of MADN and WO$_3$**

In our experiments, we fabricated the OLED devices with the *p*-doped HTL composed of MADN doped with WO$_3$ with structure of ITO/*p*-type HTL (50 nm)/MADN (10 nm)/Alq$_3$ (75 nm)/LiF (1 nm)/Al (150 nm), in which the doping concentration of WO$_3$ are 0%, 10%, 20%, and 33%, respectively.

Figure 6-18 depicts the *L-J-V* characteristics of these WO$_3$-doped devices. It is notable that higher current density and luminance can be achieved at lower applied bias by using WO$_3$ as *p*-dopant. The overall EL performances of these devices are summarized in Table 6-3. Device with 10% WO$_3$ doping achieved a power efficiency of 2.4 lm/W at 20 mA/cm^2, which is 40% higher than that of undoped device. The results show excellent agreement with the conclusions obtained from the study of hole-only device and clearly demonstrate that the MADN doped with WO$_3$ could be adopted for an efficient *p*-HTL in OLEDs device.
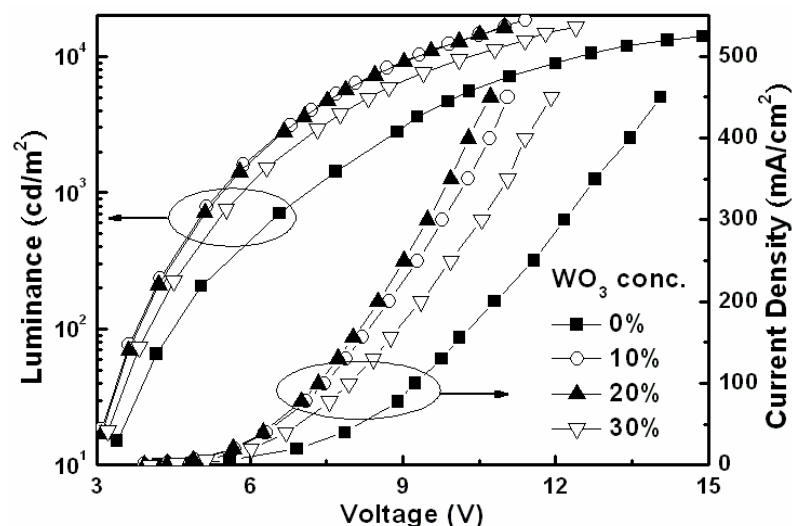
Figure 6-18 *L-J-V* characteristics of the WO$_3$-doped devices.

Table 6-3 EL performances of OLED devices at 20 mA/cm^2.

WO$_3$ conc. (%)	Voltage (V)	Current Eff. (cd/A)	Power Eff. (lm/W)	E. Q. E. (%)	CIE$_{x,y}$
0	6.6	3.5	1.7	1.4	(0.35, 0.56)
10	5.2	4.0	2.4	2.1	(0.35, 0.55)
20	5.3	3.5	2.1	3.5	(0.30, 0.65)
33	5.4	3.9	2.3	5.8	(0.30, 0.64)

In summary, we demonstrated that the MADN doped with WO$_3$ decreases the resistance of MADN and the hole injection energy barrier between MADN and ITO resulting in improving the ohmic loss and hole injection. In Alq$_3$ based OLEDs, using MADN doped with WO$_3$ as *p*-HTL can achieve a current efficiency of 4.0 cd/A and a power efficiency of 2.4 lm/W.

6.4   *n*-type doped system composed of CsF-doped MADN

In this section, we further report the development of the *n*-doped transport layers using MADN as a host, in which cesium fluoride (CsF) is used as *n*-dopant, repectively. The carrier injection property and the effect of CsF

incorporation into MADN are investigated by measuring *I-V* curves and temperature-dependent AS. The AS results show that the incorporation of CsF into MADN can greatly reduce the resistance and activation energy of MADN layer resulting in improving electron injection. We also demonstrate the application of the *n*-doped organic layer of MADN doped CsF in OLED devices.

6.4.1   Admittance measurements of CsF-doped MADN layer

In our experiments, a series of electron-only devices were fabricated for studying the effect of electron injection and electrical characteristics. The electron-only device structure was ITO/Alq$_3$ (80 nm)/*n*-doped ETL (10 nm)/Al (150 nm), in which the doping concentration of CsF in MADN are 0%, 10%, 20% and 30%, respectively.

Figure 6-19 plots the *I-V* characteristics of these electron-only devices. Lower operational voltage and higher current density dependency were observed in CsF doped electron-only device as compared to that of undoped device, which indicate that the electron injection from Al cathode can also be improved by doping CsF into MADN.
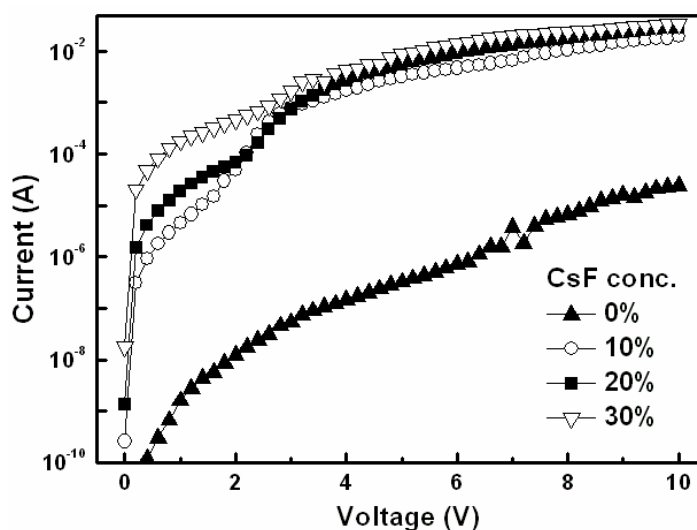
Figure 6-19 *I-V* characteristics of CsF-doped electron-only devices.

To understand the electrical doping phenomena, the electron-only devices are further investigated by AS as shown in Figure 6-20. As we discussed in the PAK2 case (*Section 6.2.1*), the low-frequency peaks (*G/F* peaks at 200-4000 Hz) are assigned to be associated with a single *RC* time constant of the *n*-doped MADN layer and high-frequency peaks (*G/F* peaks at 0.13-0.15 MHz) are associated with a single *RC* time constant of parasitic series resistance [27]. It is also found that the high-frequency peak is temperature-independent and the low-frequency peak is temperature-dependent. Furthermore, the E_a of *n*-doped MADN layer can be derived from the slope of relationship between of ln(*F*) and 1000/*T* as plotted in Figure 6-21(a), when the doping percentage of CsF was increased from 10%, to 20%, and 30%, the activation energy (E_a) of MADN could be greatly reduced from 0.157 eV to 0.145 eV and then to 0.099 eV. In this case, E_a represents the energy separation between the edge of the LUMO level and Fermi level of MADN as shown in Figure 6-21(b), the decrease of E_a indicates that the Cs_2CO_3 incorporation reduces this separation, which lowers the electron injection energy barrier between MADN and Al, thus improves the electron injection from Al cathode to MADN.
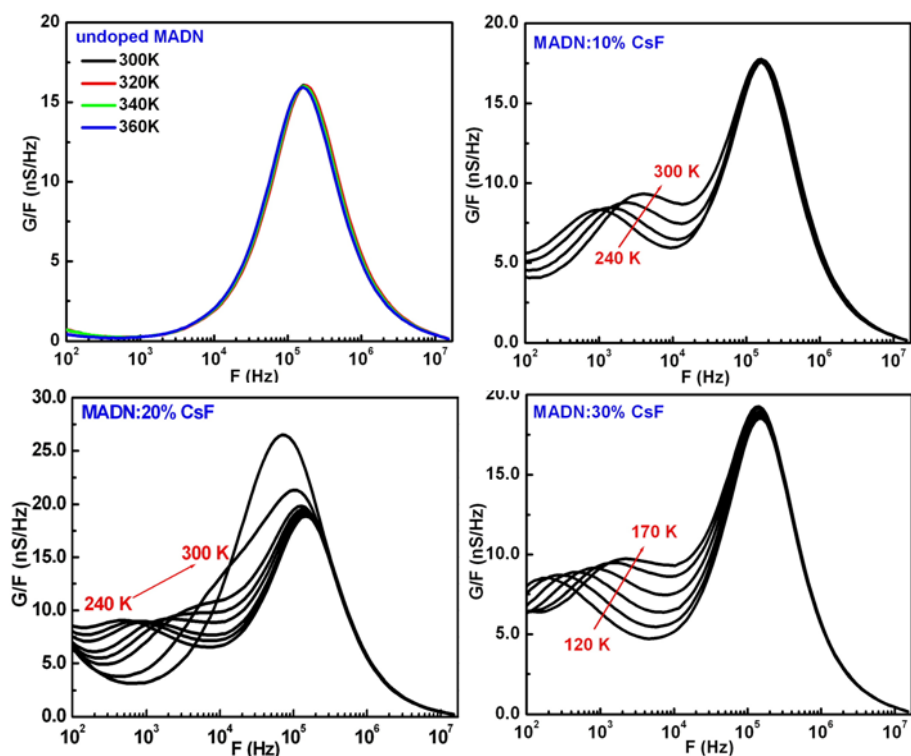
Figure 6-20 Temperature-dependent *G/F-F* spectra at zero bias of electron-only devices with various doping concentration.
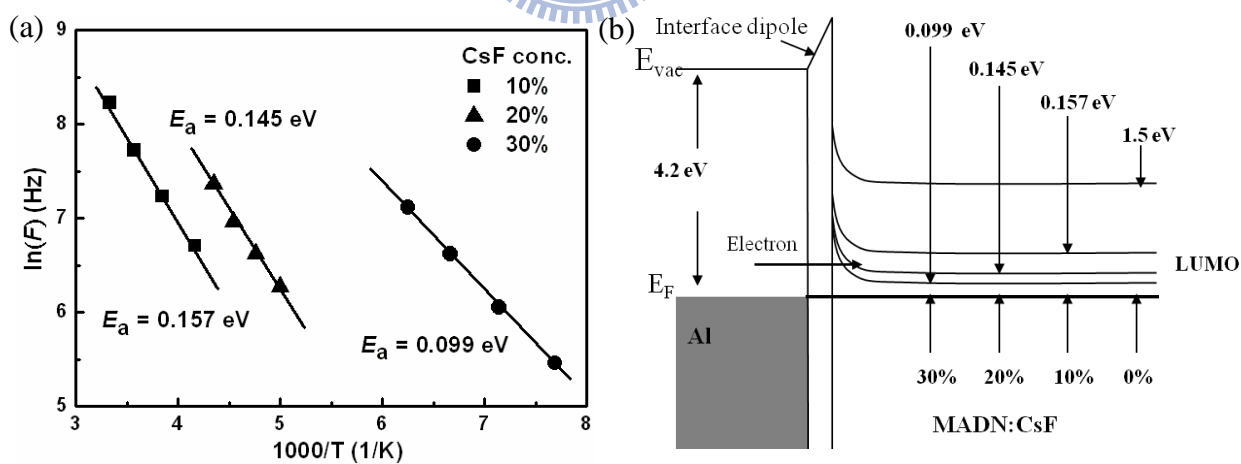
Figure 6-21 (a) Characteristic of ln(*F*) vs 1000/*T* of CsF-doped devices derived from the low-frequency peaks in Figure 6-20. (b) Schematic energy diagram of Al/*n*-doped MADN interface.

6.4.2 Device performances of using *n*-doped layer composed of CsF-doped MADN

As illustrated in Figure 6-22, three following devices are fabricated to test the efficacy of the *n*-doped ETL composed of MADN doped with CsF. First one is the standard device with conventional structure of ITO ITO/CF$_x$/NPB (60 nm)/Alq$_3$ (75 nm)/LiF (1 nm)/Al (150 nm), second and third are i-i-*n* devices with structures of ITO/CF$_x$/HTL (60 nm)/Alq$_3$ (65 nm)/MADN: 30% CsF (10 nm)/Al (150 nm), in which NPB and MADN were used as HTL, respectively.
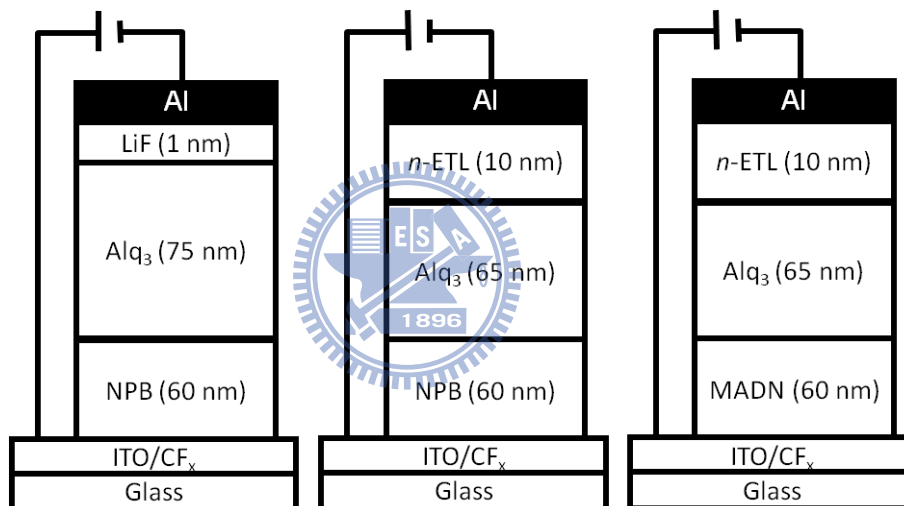
Figure 6-22 Device architecture of standard device and i-i-*n* devices.

The EL performances are summarized in Table 6-4, it is apparent that i-i-*n* devices with MADN doped CsF layer can achieve higher efficiency and low drive voltage at 20 mA/cm^2. Significantly, inducing the *n*-doped layer of MADN doped CsF can improve the electron injection from Al cathode, which fully agrees the results of *I-V* characteristic and AS measurement. These results indicate that MADN can be used as an efficient host for *n*-type dopant CsF and reduce the drive voltage in OLED devices. Furthermore, the performance of

i-i-*n* device with MADN as hole transport layer (HTL) can boost up to 6.1 cd/A as shown in Figure 6-23, the enhancement of device performance agrees the result of the utilization of MADN as HTL, which we will discuss in *Section 7.3*.

Table 6-4 EL performances of OLED devices at 20 mA/cm^2.

Device (HTL)	Voltage (V)	Current Eff. (cd/A)	Power Eff. (lm/W)	E. Q. E. (%)	CIE$_{x,y}$
Standard	6.3	3.6	1.8	1.1	(0.36, 0.55)
i-i-*n* (NPB)	5.2	3.3	2.0	1.1	(0.36, 0.55)
i-i-*n* (MADN)	5.5	6.1	3.5	1.9	(0.38, 0.55)
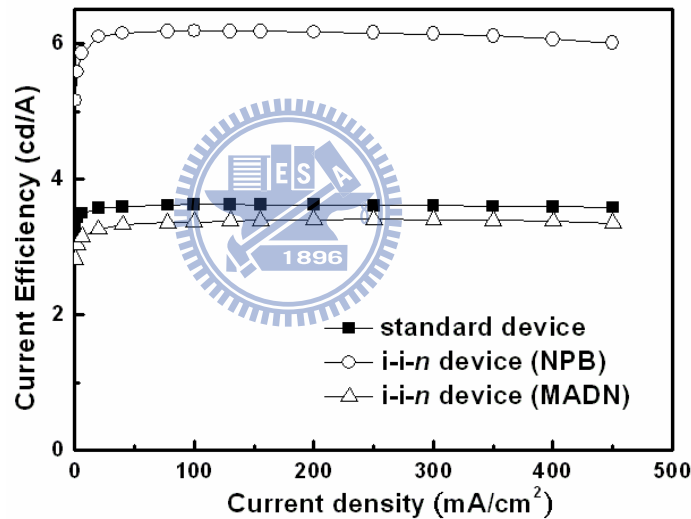
Figure 6-23 Current efficiency *vs* current density characteristics of OLED devices.

6.5 Summary

In this chapter, we study the electrical characteristics and doping effect of *p*-doped (WO$_3$-doped MADN) and *n*-doped (PAK2-doped BPhen and CsF-doped MADN) organic layers by measuring *I-V* curves and temperature-dependent AS. The results indicate that incorporations of *p*-type

(WO$_3$) and *n*-type (PAK2 and CsF) dopants can reduce the activation energy, which represents the energy separation of between the Fermi level and the HOMO level for *p*-type case, the LUMO level for *n*-type cases, respectively, and can further improve the carrier injection from the electrodes.

On the other hand, the results of PAK2 case also show that potassium metal carboxylates are also useful for *n*-type doping with an easy and stable evaporation process as compared to inorganic salts. However, the mechanism of thermal deposition of these kind of materials is still not well understood, even we investigated this phenomenon by QCM.

Moreover, the results of MADN cases imply that MADN can be a host for both *p*-type (WO$_3$) and *n*-type (CsF) dopants and these *p*-doped and *n*-doped MADN layers can effectively applied to OLED devices, which is an useful information for simplifying the OLED device architecture by multifunctionally utilizing MADN, and the further experiments are described in next chapter.

References

[1] S. R. Forrest, *Chem. Rev.* **97**, 1793 (19997).

[2] N. Karl, *Defect Control in Semiconductors, Vol. II*, North Holland: Amsterdam (1990).

[3] C. W. Tang, *Appl. Phys. Lett.* **48**, 183 (1986).

[4] C. W. Tang, S. A. Van Slyke, *Appl. Phys. Lett.* **51**, 913 (1987).

[5] J. Kido, K. Nagai, Y. Okamoto, *IEEE Trans. Electron Devices* **40**, 1342 (1993).

[6] I. D. Parker, *J. Appl. Phys.* 75, 1656 (1994).

[7] T. Wakimoto, Y. Fukuda, K. Nagayama, A. Yokoi, H. Nakada, M. Tsuchida,

IEEE Trans. Electron Devices **44**, 1245 (1997).

[8] E.I. Haskal, A. Curioni, P.F. Seidler, W. Andreoni, *Appl. Phys. Lett.* **71**, 1151 (1997).

[9] Y. E. Kim, H. Park, J. J. Kim, *Appl. Phys. Lett.* **69**, 599 (1996).

[10] L. S. Hung, C. W. Tang, M. G. Mason, *Appl. Phys. Lett.* **70**, 152 (1997).

[11] G. E. Jabbour, Y. Kawabe, S. E. Shaheen, J. F. Wang, M. M. Morrell, B. Kippelen, N. Peyghambarian, *Appl. Phys. Lett.* **71**, 1762 (1997).

[12] S. E. Shaheen, G. E. Jabbour, M. M. Morrell, Y. Kawabe, B. Kippelen, N. Peyghambarian, M. F. Nabor, R. Schlaf, E. A. Mash, N. R. Armstrong, *J. Appl. Phys.* **84**, 2324 (1998).

[13] C. H. Lee, *Synth. Met.* **91**, 125 (1997).

[14] F. Li, H. Tang, J. Anderegg, J. Shinar, *Appl. Phys. Lett.* **70**, 1233 (1997).

[15] H. Tang, F. Li, J. Shinar, *Appl. Phys. Lett.* **71**, 2560 (1997).

[16] Y. Park, J. Lee, S. K. Lee, D. Y. Kim, *Appl. Phys. Lett.* **79**, 105 (2001).

[17] J. Lee, Y. Park, S. K. Lee, E. J. Cho, D. Y. Kim, H. Y. Chu, H. Lee, L. M. Do, T. Zyung, *Appl. Phys. Lett.* **80**, 3123 (2002).

[18] J. Liu, A. R. Duggal, J. J. Shiang, C. M. Heller, *Appl. Phys. Lett.* **85**, 837 (2004).

[19] T. Mori, H. Fujikawa, S. Tokito, Y. Taga, *Appl. Phys. Lett.* **73**, 2763 (1998).

[20] E. Ettedgui, H. Razafitrimo, Y. Gao, B. R. Hsieh, *Appl. Phys. Lett.* **67**, 2705 (1995).

[21] J. Yoon, J. J. Kim, T. W. Lee, O. O. Park, *Appl. Phys. Lett.* **76**, 2152 (2000).

[22] P. He, S. D. Wang, S. T. Lee, L. S. Hung, *Appl. Phys. Lett.* **82**, 3218 (2003).

[23] C. Ganzorig, M. Fujihira, *Jpn. J. Appl. Phys. Part 2* **38**, L1348 (1999).

[24] C. Ganzorig, K. Suga, M. Fujihira, *Mater. Sci. Eng. B* **85**, 140 (2001).

[25] S. H. Kim, J. Jang, J. Y. Lee, *Appl. Phys. Lett.* **91**, 103501 (2007).

[26] T. Hasegawa, S. Miura, T. Moriyama, T. Kimura, I. Takaya, Y. Osato, H. Mizutani, *Proceedings of SID'04*, p. 154, May 23-28 (2004), Seattle, Washington, USA.

[27] W. Brütting, H. Riel, T. Beierlein, W. Riess, *J. Appl. Phys.* **89**, 1704 (1994).

[28] S. Odermatt, N. Ketter, B. Witzigmann, *Appl. Phys. Lett.* **90**, 221107 (2007).

[29] M. Pfeiffer, K. Leo, and N. Karl, J. Appl. Phys. **80**, 6880 (1996).

[30] Y. Matsuda, C. Ganzorig, K. Suga, M. Fujihira, *Ext. Abstracts, 50ᵗʰ Spring Meeting, Jpn. Soc. Appl. Phys. and Related Soc.* p. 1404, 27p-A-4 (2003).

[31] C. Ganzorig, M. Fujihira, *Appl. Phys. Lett.* **85**, 4774 (2004).

[32] Y. Li, D. Q. Zhang, L. Duan, R. Zhang, L. Duo, Y. Qiu, *Appl. Phys. Lett.* **90**, 012119 (2007).

[33] G. Z. Sauerbrey, Z. Phys. Chem. (Munich) **155**, 206 (1959).

[34] H. Jiming, L. Lijia, B. Danielsson, X. Zhou, L. Wang, *Anal. Chim. Acta* **423**, 215 (2000).

[35] A. B. Daniel, D. W. Michael, *Chem. Rev. (Washington, D.C.)* **92**, 1355 (1992).

[36] B. W. D'Andrade, S. R. Forrest, and A. B. Chwang, *Appl. Phys. Lett.* **83**, 3858 (2003).

[37] H. Aziz, Z. D. Popovic, N.-X. Hu, A. M. Hor, G. Xu, *Science* **283**, 1900 (1999).

[38] S. A. Van Slyke, C. H. Chen, C. W. Tang, *Appl. Phys. Lett.* **69**, 2160 (1996).

[39] C. C. Chang, M. T. Hsieh, J. F. Chen, S. W. Hwang, C. H. Chen, *Appl. Phys. Lett.*, **89**, 253504 (2006).

Chapter 7

Organic Light-Emitting Diodes based on one Multifunctional

Bipolar Material

7.1   Introduction

Since Tang and Van Slyke developed the multi-layer OLEDs [1], tremendous efforts have been directed toward improving the device performance and operational lifetime. It was recognized that E. Q. E. of OLEDs depends heavily on the efficiency of carrier injection, transport and recombination as well as the balance of the holes and electrons [2], however, the mechanism underlying these key performance parameters are not well understood.

The basic OLED device has a bilayer organic thin-film structure such as ITO/NPB/Alq$_3$/LiF/Al, where ITO is the anode, LiF/Al is the cathode, NPB and Alq$_3$ are the HTL and ETL, respectively. During operation, the injected holes and electrons recombine at or near the HTL/ETL interface, producing EL. However, this typical NPB/Alq$_3$ structure in general does not necessarily provide the configuration to achieve a balanced carrier injection/transportation that leads to recombination. One of the reasons is that the excess holes would accumulate at HTL/ETL interface and generate NPB$^+$ and Alq$_3^+$ radical cations. It has been suggested that exciton quenching at the NPB/Alq$_3$ interface due to the accumulation of NPB$^+$ radical cations at the interface impacts significantly on the current efficiency [3,4]. Moreover, it has also been reported that Alq$_3$ cationic species would easily be produced when hole carriers exist excessively, resulting in deterioration of device lifetime [5,6,7].

It has been shown that much improved OLED performance can be realized

using a HIL/HTL structure, where HIL is the "hole-injection" layer inserted between the anode and the HTL. For example, with CuPc [8] as the HIL as in CuPc/NPB/Alq$_3$ where Alq$_3$ also functions as the emissive layer, long-lived OLEDs have been obtained. Another common HIL material is 4,4',4"-*tris*[*N*-(3-methylphenyl)-*N*-phenylamino] triphenylamine (MTDATA) [9], with which enhanced current efficiency and operational stability have been demonstrated. High-efficiency OLEDs have also been reported in various HIL/HTL configurations [10,11,12,13,14]. Furthermore, low-voltage and high-efficiency OLEDs can be realized with a *p*-doped HTL [15,16,17], in which the layer thickness can be readily adjusted for optimal light extraction. It has been suggested that the enhanced performance in HIL/HTL devices is due to a sequence of cascaded hole-injection barriers present in the HIL/HTL/ETL structure, which produces a "balanced" electron-hole recombination at the HTL/ETL interface [18,19].

Consequently, finding a way of reducing the number of holes or increasing the number of electrons reaching the emission layer is considered one of the most direct and economic solutions to improve device efficiency. Recently, it was found that the hole mobility can be efficiently controlled by incorporating the composite hole transporting layer (*c*-HTL) of NPB: copper phthalocyanin (CuPc) (1:1) to balance the charge carriers [20] from which the device efficiency can be significantly enhanced. However, the fabrication process is complicated, which requires precise control and in particular, using the environmentally unfriendly CuPc.

In addition to the well-known property of large bandgap and high fluorescence quantum yield, anthracene-based derivatives have been shown to

possess bipolar character and moderate-to-high carrier mobilities. In this chapter, we summarize examples of anthracene-based compounds that have successfully been used as charge transport materials both for hole and electron transport layers, respectively. We also demonstrate the bipolar nature of MADN by studying the electrical characteristics of carrier-only devices and further simplify the OLED device structure by taking the advantage of this bipolar nature.

7.2   Review of anthracene-based materials used in HTL of OLED devices

As early in 2002, Shi and Tang at Kodak had claimed in a US patent in which anthracene-based derivatives were found to be useful as hole transport layer in producing efficient OLED devices [21]. Representative structures are shown in Figure 7-1. In the past, although arylamines have been used extensively as hole transport materials in OLED devices, they do have a number of deficiencies. First, as a class of organic materials, they are relatively strong electron donors, meaning that they can be readily oxidized and may be unstable in ambient environments. Second, when placed adjacent to an ETL as HTL in a OLED device, the arylamines may interact with the strongly accepting electron transport layer to produce non-emissive charge-transfer species which will result in a loss of EL. Third, because of the low ionization potential of the arylamines HTL and the hole-blocking ETL will cause the holes to localize in the arylamines to form the non-emissive amine radical cations which will also lead to quenching. To alleviate the aforementioned shortcomings in HTL, anthracene-based derivatives have been used recently for improving the OLED device performance.
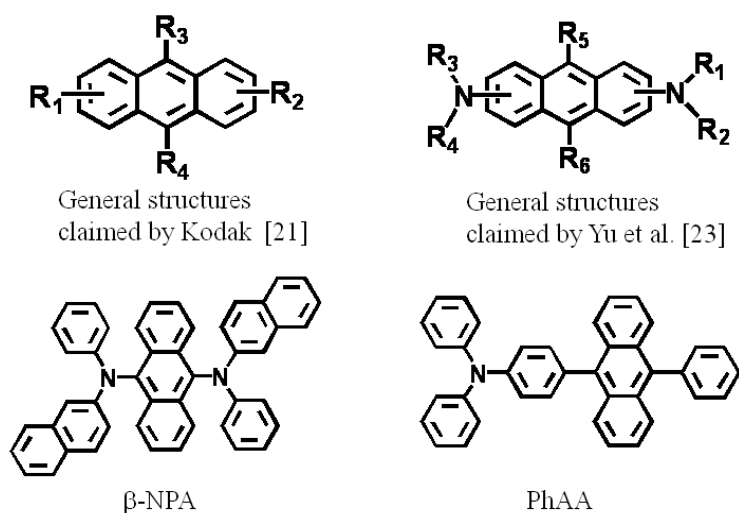
Figure 7-1 Chemical structures of anthracene-based HTLs.

In 2002, Tao et al. [22] synthesized a series of diaminoanthracene derivatives and used them as hole transport material in a green emitter. The structure of 9,10-*bis*(2-naphthylphenylamino)anthracene (β-NPA) is depicted in Figure 7-1 as well. The β-NPA-based device, with structure of ITO/β-NPA (40 nm)/Alq$_3$ (50 nm)/Mg:Ag alloy (10:1, 55 nm), achieved an EL efficiency of 7.7 cd/A and 5.4 lm/W with an EL peaking at 530 nm and CIE$_{x,y}$ of (0.31, 0.63). In particular, the device has an extremely low turn-on voltage of 2.6 V without any *p*-dopant, suggesting that diaminoanthracene derivatives are excellent for hole transport layer with HOMO of 5.54 eV. After that, there was another patent by Yu et al. [23] claiming that the introduction of diarylamino groups on 2-/6- positions of anthracene moiety could improve hole transport property considerably and is useful as hole transport layer in OLEDs.

Later, triphenylamine end-capped anthracene derivatives have also been characterized for efficient blue emitter as well as HTL [24] whose typical structure of 9-Phenyl-10-(4-triphenylamine)anthrancene (PhAA) is also shown in Fig. 7-1. These type of materials show high T_g of 104-162 °C with good

thermal stability, and strong blue emission of quantum yields of 0.44-0.48. Based on these compounds, efficient deep-blue emissions have been achieved by using a simplified two-layer device architecture of ITO/PhAA (50 nm)/TPBI (30 nm)/LiF/MgAg with maximum efficiency of 3.0 cd/A (2.4 lm/W) and $CIE_{x,y}$ of (0.14, 0.14).

7.3   Using MADN as HTL

In our previous work, MADN has been found to be an efficient blue host material which forms stable thin-film morphology upon thermal evaporation and has a wide energy bandgap [25]. Moreover, the hole mobility of MADN has been measured to be (3-9) $\times$ 10^{-3} cm^2/Vs by TOF technique and discussed in *Section 5.3.2*, which is even higher than that of common-used hole transport material NPB (5.1 $\times$ 10^{-4} cm^2/Vs) [26], indicating that MADN can be used as a hole-transport material in OLED devices.

In this section, we study the electrical characteristics of *I-V* dependence and AS of devices in which the conventional HTL, NPB, is replaced with MADN and find that it could simultaneously improve the carrier recombination in the device and significantly enhance the device efficiency and operational lifetime as well.

7.3.1   Admittance measurements of MADN/Alq$_3$ bilayer structure

For studying the transport phenomenon and electrical characteristics, two additional hole-only devices were also fabricated. The structure of hole-only devices were ITO/CF$_x$/MADN (30 nm)/Alq$_3$ (60 nm)/Al (150 nm) and ITO/CF$_x$/NPB (30 nm)/Alq$_3$ (60 nm)/Al (150 nm), respectively. Figure 7-2 shows the *I-V* characteristics of the hole-only devices. Higher operational voltage and smaller current density dependency were observed in device B with

MADN as compared to that of the device A. For instance, the turn-on voltage of hole-only devices A and B are 2.4 V and 3.0 V, respectively. We attribute the high drive voltage of MADN device to the large energy gap between MADN and ITO anode as compared to those of NPB hole-only device. (The HOMO levels of MADN and NPB are 5.8 eV and 5.4 eV, respectively.) The electrical properties of the hole-only devices are further investigated by temperature-dependent AS.
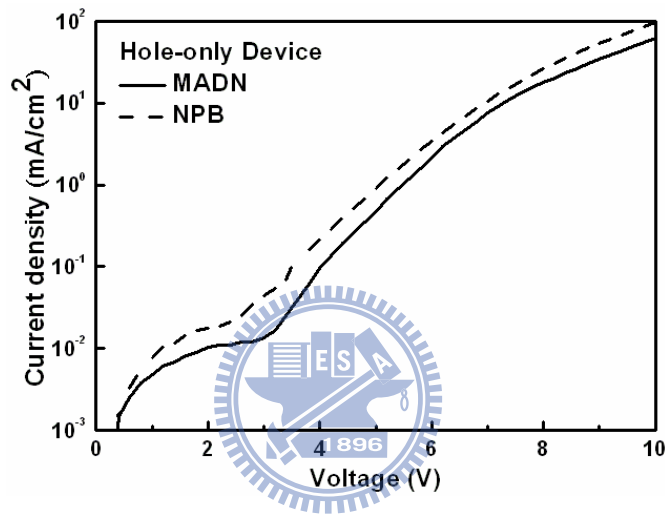
Figure 7-2 *I-V* characteristics of hole-only devices.

The fundamental theory of AS are describe in *Section 2.10*. Figure 7-3(a) plots the temperature-dependent *G/F-F* spectra measured at zero bias of the hole-only device of MADN, in which shows two distinct *G/F* peaks which are proportional to the dielectric loss. The loss peak can be described by the classical Debye frequency response which is given by

$$\frac{G(F)}{F} = \frac{A/F_P}{1+(F/F_P)^2} \tag{7.1}$$

where the amplitude A is a temperature-dependent constant, F_p is the peak frequency. It is evident that the high-frequency peak is temperature-independent

172

and would not shift at different temperature. On the other hand, the low-frequency peak is temperature-dependent, it will shift toward lower frequency region at low temperature. According to the results of PAK2 case (*Section 6.2.1*), the high-frequency peak (*G/F* peak at 0.45 MHz) is associated with the *RC* time constant of parasitic series resistance and the low-frequency loss peaks (*G/F* peaks at 250-7300 Hz) are assigned to be associated with the single *RC* time constant of MADN layer. Similar result can be also observed in the hole-only device of NPB as depicted in Figure 7-3(b).
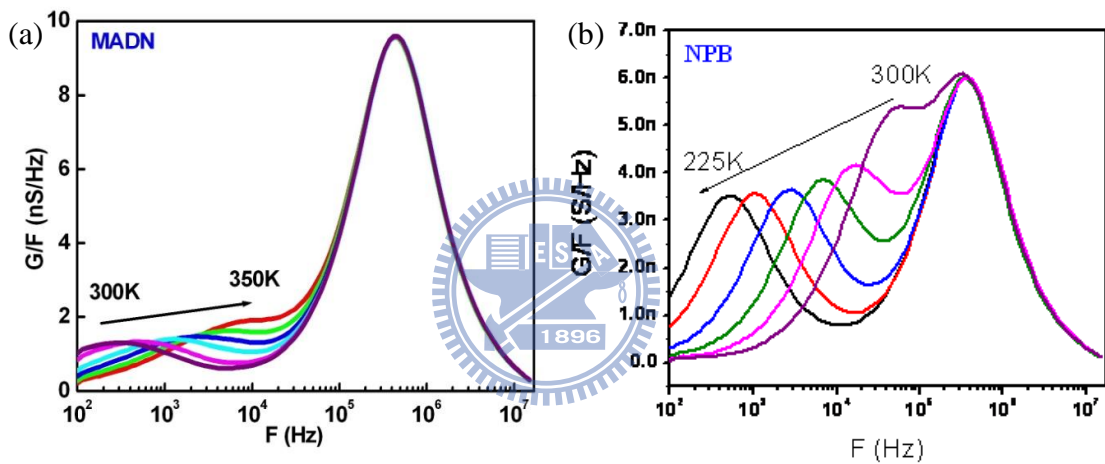
Figure 7-3 Temperature-dependent *G/F-F* spectra at zero bias of hole-only devices (a) MADN and (b)NPB.

In addition, as the results we discussed in PAK2 case (*Section 6.2.1*), the E_a can also be derived from the slope of relationship between of ln(*F*) and 1000/*T* as plotted in Figure 7-4(a), in which in the E_a value of MADN is found to be 0.655 eV and is larger than that of NPB (0.238 eV). In this case, E_a represents the energy separation between the edge of HOMO level and Fermi level of MADN as illustrated in Figure 7-4(b), thereby, larger E_a value represents the larger injection barrier for holes from ITO anode to organic layers and also the

amount of holes injected from ITO anode is reduced, which agrees with the results of *I-V* characteristics of hole-only devices as plotted in Figure 7-2. On the other hand, with the lower-lying HOMO of MADN which creates a small barrier (0.2 eV) for holes at the interface between HOMOs of MADN and Alq_3 (5.7 eV), there would be fewer holes accumulated at MADN/Alq_3 interface as compared to the NPB/Alq_3 interface. Therefore, it is expected that the issues of excess hole carriers mentioned earlier can be circumvented by introducing MADN as HTL in OLED devices.
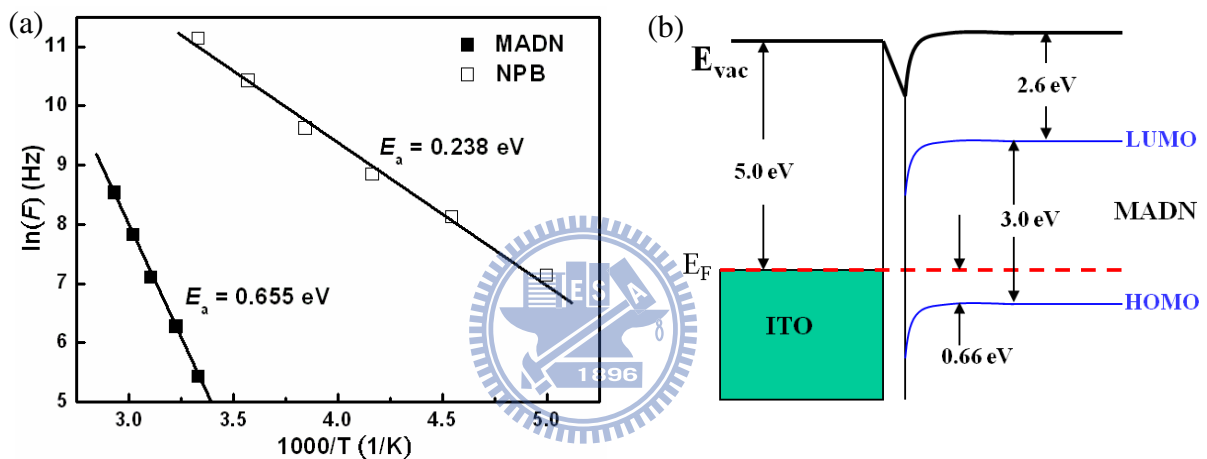
Figure 7-4 (a) Characteristic of $\ln(F)$ vs $1000/T$ of hole-only devices derived from the low-frequency peaks in Figure 7-3. (b) Schematic energy diagram of ITO/MADN interface.

7.3.2 Device performances of using MADN as HTL

In our experiments, four OLED devices are fabricated to demonstrate the efficacy of utilizing MADN as HTL with following structures, Alq_3-based devices A and F: ITO/CF_x/HTL (60 nm)/Alq_3 (75 nm)/LiF (1 nm)/Al (150 nm); C545T-doped devices C and G: ITO/CF_x/HTL (60 nm)/$Alq_{3:}$ 1% C545T (37.5 nm)/Alq_3 (37.5 nm)/LiF (1 nm)/Al (150 nm). For comparison, the HTL of

devices A and C is NPB and the HTL of devices F and G is MADN, respectively.

The detailed EL performances are summarized in Table 7-1. It is noted that the voltage required at a given current density of device with MADN as HTL is higher than that of the standard device, which is in complete agreements with the results derived from I-V measurement and AS. Although the drive voltage was slightly increased by using MADN as HTL, the performance of devices F and G were considerably enhanced. For instance, the luminance of devices C and G at 20 mA/cm^2 were 2668 cd/m^2 (at 6.3 V) and 4367 cd/m^2 (at 6.6 V), respectively.

Table 7-1 EL performances of OLED devices at 20 mA/cm^2.

Device	Voltage (V)	Current Eff. (cd/A)	Power Eff. (lm/W)	E. Q. E. (%)	CIE$_{x,y}$
A	6.3	3.6	1.8	1.1	(0.36, 0.55)
F	6.6	6.7	3.7	2.1	(0.35, 0.55)
C	6.3	13.3	6.7	3.5	(0.32, 0.64)
G	6.6	21.8	10.4	5.8	(0.30, 0.64)

The current efficiencies of devices F and G (6.7 cd/A and 21.8 cd/A) are improved by 86% and 65% as compared to those of standard devices A and C (3.6 cd/A and 13.3 cd/A) as shown in Figure 7-5. Furthermore, the utilization of MADN as HTL would not impact on the emission color, the CIE$_{x,y}$ coordinates are essentially identical to those of the standard devices as summarized in Table 7-1. It can also be observed that the current efficiency of device G is sustained at 21.3 cd/A even at 450 mA/cm^2 suffers essentially no current-induced quenching, and there is no color shift with respect to varying drive currents as the CIE$_{x,y}$

coordinates only shift from (0.304, 0.647) at 2 mA/cm^2 to (0.303, 0.637) at 450 mA/cm^2 with $\Delta CIE_{x,y} = \pm(0.001, 0.01)$. The enhancement of device performance and the apparent resistance to changes of both current efficiency and emission color under various drive current densities can be attributed to the well-balanced charge carriers for recombination in the devices with MADN as HTL.
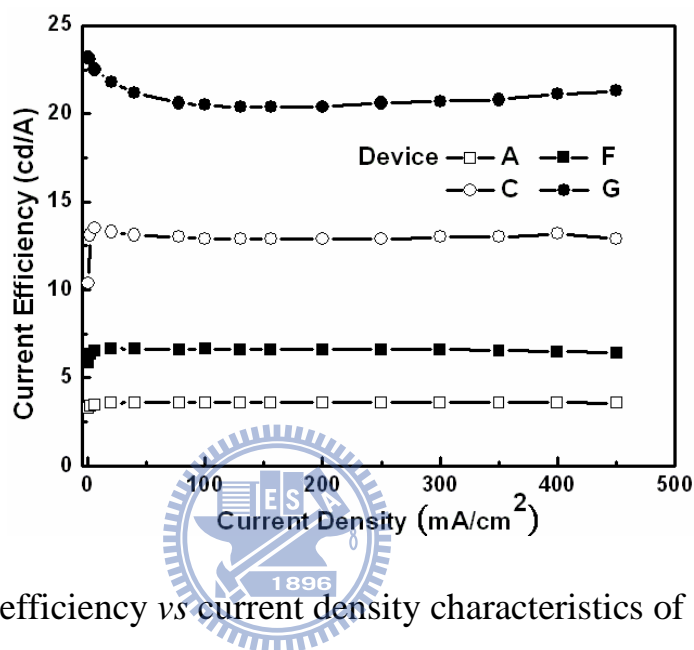
Figure 7-5 Current efficiency *vs* current density characteristics of devices A, B, F, and G.

We also measured the absorption spectrum of MADN$^+$ in methyl cyanide (MeCN) solution as shown in Figure 7-6. As compared to the absorption of neutral MADN, MADN$^+$ radical cation shows stronger absorption at 328 nm, 436 nm, 604 nm, 664 nm, and weaker absorption at 361 nm, 377 nm, and 397 nm, respectively. Importantly, there is no significant enhancement of absorption in the range of 450 ~ 550 nm, indicating that MADN$^+$ radical cation would not be a strong quencher of green and sky-blue fluorescence as compared to NPB$^+$ radical cations [4]. We believe that the smaller extinction coefficient of MADN radical cations is another reason for the enhanced device efficiency in addition

to the more balanced carrier recombination.
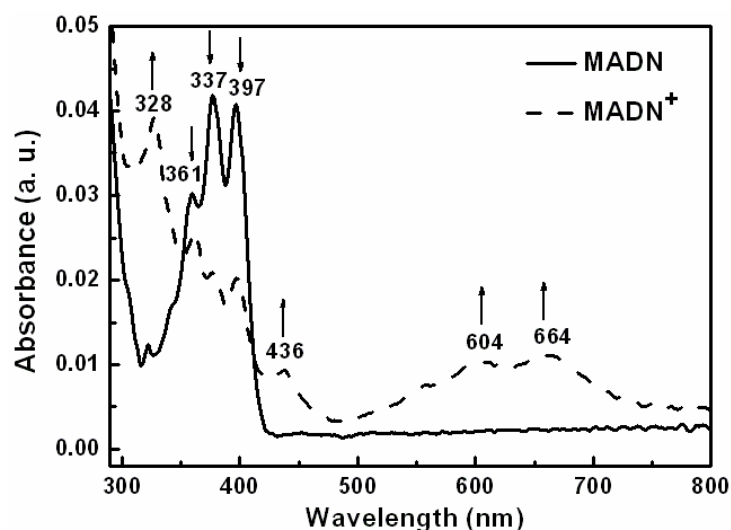
Figure 7-6 Absorption spectra of MADN and MADN radical cation in MeCN solution.

Device G with MADN as HTL also showed exceptionally long operational stability as shown in Figure 7-7. The $t_{1/2}$ [the time for the luminance to drop to 50% of initial luminance (L_0)] of device II measured at constant current densities of 20 mA/cm^2 ($L_0 = 4366$ cd/m^2), 40 mA/cm^2 ($L_0 = 8469$ cd/m^2), and 60 mA/cm^2 ($L_0 = 12387$ cd/m^2) were 612 hrs, 202 hrs, and 110 hrs, respectively. Assuming scalable Coulombic degradation of ($L_0^n \times t_{1/2} = $ constant) under accelerated drive conditions [27] and by estimation of extrapolated profile, the $t_{1/2}$ of device F driving at a L_0 value of 500 cd/m^2 is projected to be about 22000 hrs. The remarkably long operational lifetime is attributed to the improved recombination probability of charge carriers in the emission layer that leads to much reduced fluorescent quencher of Alq$_3$ cationic radical produced by excess hole in the emitter.
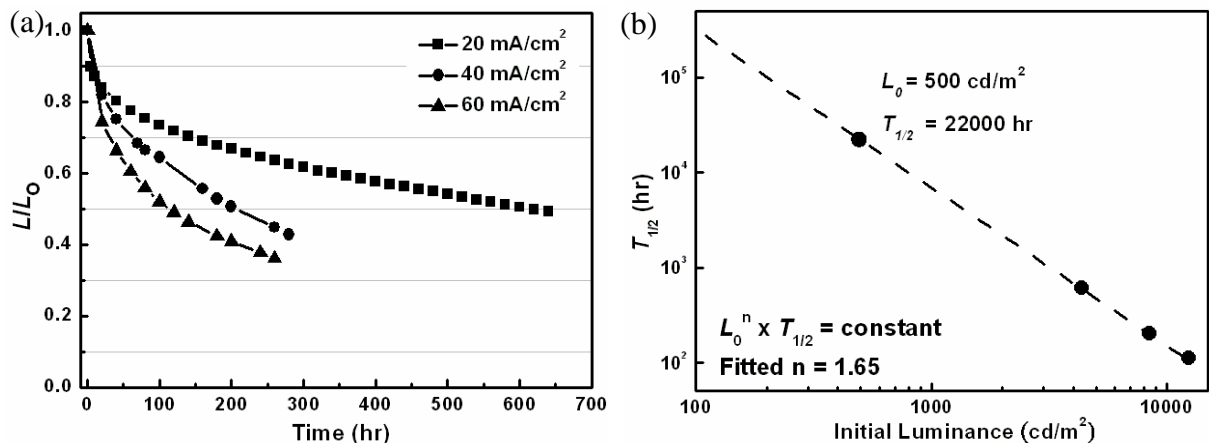
Figure 7-7 (a) Device operational stability of device G measured at different current densities. (b) Extrapolated half life of device G.

In summary, carrier recombination, as well as the balance of holes and electrons, is considered to be one of the most important factors that determine the E. Q. E. of OLEDs. Here, we make use of the high hole mobility of MADN and introduce MADN to be used as HTL in OLED devices. In addition, the results of *I-V* measurement and AS indicate that MADN layer has higher resistance and higher energy barrier (E_a) with respect to ITO anode, which can efficiently reduce the excess injected holes and further improve the hole/electron recombination efficiency, giving rise to the remarkably high E. Q. E. and current efficiency of 5.8% and 21.8 cd/A and a long operational lifetime of C545T-doped OLED device.

7.4   Review of anthracene-based materials used in ETL of OLED devices

To date, the widely used ETL and host emitting material in OLEDs appears to be Alq_3. This is because Alq_3 is thermally and morphologically stable to be evaporated into thin films, easily synthesized, commercially available in bulk quantities, molecularly shaped to avoid exciplex formation (e.g., with adjacent

hole transport NPB at the interface), and a commonly accepted green and red fluorescence host emitter. But, it has also many shortcomings such as low quantum efficiency, the ashing issue during sublimation, particularly, its low electron mobility in the ranges of 10^{-7} to 10^{-6} cm^2/Vs [28,29] (three orders lower than that of NPB) which often impacts on the balance of carrier recombination in the emitter and causes the drive voltage to increase. Moreover, it has been reported that the fluorescence quencher of oxidized Alq$_3$ radical cationic species would easily be produced when considerable quantities of hole carriers exist, resulting in the deterioration of the device lifetime [5,6,7]. Therefore, the development of efficient ETL is of high priority as the power consumption of ETL has been estimated to be the highest (~35.9%) among all the layers in the multi-layered OLEDs [30].

There have been many reports about utilizing anthracene-based materials as ETL in OLED in industry and academia. For example, Kodak research group has published work by using PADN as ETL as described in the previous section [31,32]. LG and Idemitsu also recently disclosed patents about the same design based on anthracene derivatives with one or two nitrogen-containing heterocyclic groups introduced to 2-/ 6- positions of 9,10-substituted anthracene [33,34] whose structures are shown in Figure 7-8.

Other notable example was disclosed by Sanyo group [35], they used 9,10-*bis*[4-(6-methylbenzothiazol-)2-yl]phenyl anthracene (DBzA) as ETL in green C545T-doped device with 9,9',10,10'-tetraphenyl-2,2'-bianthracene (TPBA) as host material. The green device achieved a very high EL efficiency of 29.8 cd/A and 26.2 lm/W at 20 mA/cm^2 and exhibited very high E. Q. E. of nearly 10% maintained through a wide drive current-density range of 2-100

mA/cm^2, which was among the highest reported fluorescent OLEDs then. DBzA was also shown to be just as good as applied in red OLED device [36]. The E. Q. E. of the red OLED improved from 1.7% to 4.7% by changing from Alq$_3$ into DBzA for the ETL. Recently, a series of new anthracene-based derivatives have also been synthesized for electron transport materials [37], in which the 9- and 10- positions of anthracene have been directly substituted by phenyloxadiazole groups [a representative structure of 5,5'-(2,6-di-*tert*-butylanthracene-9,10-diyl) *bis*(2-phenyl-1,3,4-oxadiazole) is shown in Figure 7-8]. These compounds possess electron affinity of 3.1-3.2 eV and ionization potential around 5.9-6.0 eV, comparable to those of Alq$_3$, and show high efficiency as ETL in green phosphorescence OLED devices.

PADN (Kodak)　　ETM of LG [33]　　ETM of Idemitsu of [34]

DBzA (Sanyo)　　5,5'-(2,6-di-*tert*-butylanthracene-9,10-diyl)bis(2-phenyl-1,3,4-oxadiazole)　　POAn
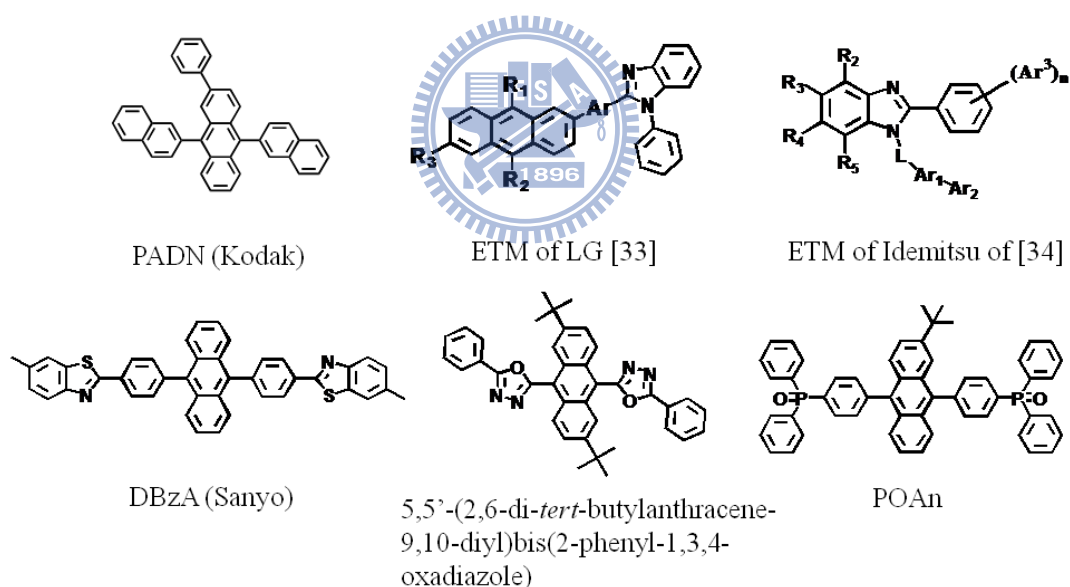
Figure 7-8 Chemical structures of anthracene-based ETLs.

Chien et al. [38] reported a new blue-light emitter, 2-tert-butyl-9,10-bis[40-(diphenylphosphoryl) phenyl]anthracene (POAn) which comprises electron-deficient triphenylphosphine oxide side groups appended to the 9- and 10-positions of a 2-*tert*-butylanthracene core. POAn possesses good

morphological stability and high quantum efficiency due to its non-planar configuration. Notably, in addition to serving as an electron-transporting blue-emitting material, POAn also was found to facilitate electron injection from the Al cathode directly to itself. Consequently, a very simple double-layer device with structure of ITO/9,9-*bis*[4-(N,N-diphenylamino)phenyl]fluorene (BPAF, 30 nm)/POAn (70 nm)/Al (100 nm) achieved an EL efficiency of 2.7 cd/A and EQE of 4.1% with CIE coordinates of (0.15, 0.07) at 100 cd/m^2.

7.5   Using MADN as ETL

Although the electron mobility of MADN cannot be obtained from TOF measurements as we discussed in *Sections 5.3.2 and 5.3.5*, we still demonstrate the advantage of utilized MADN as ETL by studying the electrical properties of electron-only devices in this section.

7.5.1   Electrical characteristics of electron-only devices

Before we fabricated OLED devices with using MADN as ETL, the electron injection should be considered. The HOMO/LUMO levels of MADN are 5.6/2.6 eV, respectively. It is expected that the electron injection from Al cathode with a work function of 4.2 eV to the LUMO level of MADN is difficult. As a result, two electron-only devices with MADN as ETL and different electron injection layers (EIL) with structures of ITO/BPhen (20 nm)/MADN (80 nm)/electron injection layer (EIL)/Al (120 nm) are fabricated, in which the EIL were LiF (1 nm) and BPhen: 5% Cs_2CO_3 (10 nm), respectively. From comparison, two additional electron-only devices with Alq_3 as ETL are also fabricated, in which the EIL were LiF (1 nm) and BPhen: 5% Cs_2CO_3 (10 nm), respectively. Here, we not only compare the electron transport property of MADN and Alq_3 also the compare

the electron injection efficacy of LiF and n-doped EIL composed of BPhen and Cs$_2$CO$_3$ to understand which one is more adequate for MADN.

As shown in Figure 7-9, the current of the devices with n-doped EIL are much higher than that of devices with LiF, it suggests the electron injection efficacy of n-doped EIL is better than LiF, even in the case of Alq$_3$ devices. Besides, the *I-V* characteristics of the LiF-devices also indicate that MADN cannot effectively react with LiF and Al cathode as the reaction between Alq$_3$, LiF, and Al [39]. However, using a n-doping EIL can overcome the energy mismatch between MADN's LUMO and Al's work function and thus, dramatically improved electron injection from Al cathode to MADN layer.

On the other hand, it shows the current of MADN device with n-doped EIL is slightly smaller but comparable to that of Alq$_3$ device with n-doped EIL, this result confirms the bipolar nature of MADN. The high drive voltage of MADN device is attributed to the large energy gap between the LUMO level of MADN and Al cathode anode as compared to that of Alq$_3$ device (The LUMO level of Alq$_3$ is 2.9 eV).
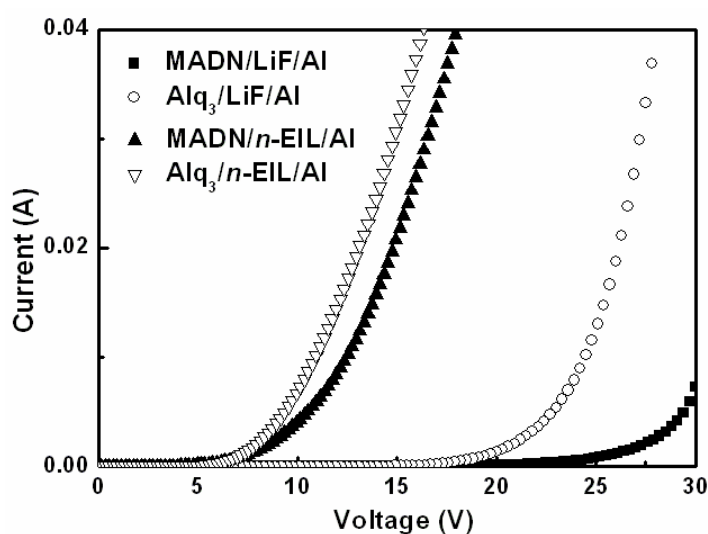
Figure 7-9 *I-V* characteristics of electron-only devices.

7.5.2 Device performances of using MADN as ETL

The results of *I-V* characteristics of electron-only device indicate MADN can be used as an ETL, albeit the electron injection barrier is too high due to the high-lying LUMO of MADN. Thereby, We further fabricated a green C545T-doped OLED device by utilizing MADN as ETL with a structure of ITO/CF$_x$/NPB (60 nm)/Alq$_3$: 1% C545T (35 nm)/MADN (20 nm)/BPhen: 5% Cs$_2$CO$_3$ (10 nm)/Al. Figure 7-10 plots the *L-J-V* characteristics of this device, which produces a respectable EL efficiency of 8.8 cd/A and 5.2 lm/W at 20 mA/cm^2. The low drive voltage of 5.3 V at 20 mA/cm^2 coupled with a good *J-V* response gives ample evidence that MADN can indeed be used as an effective ETL.
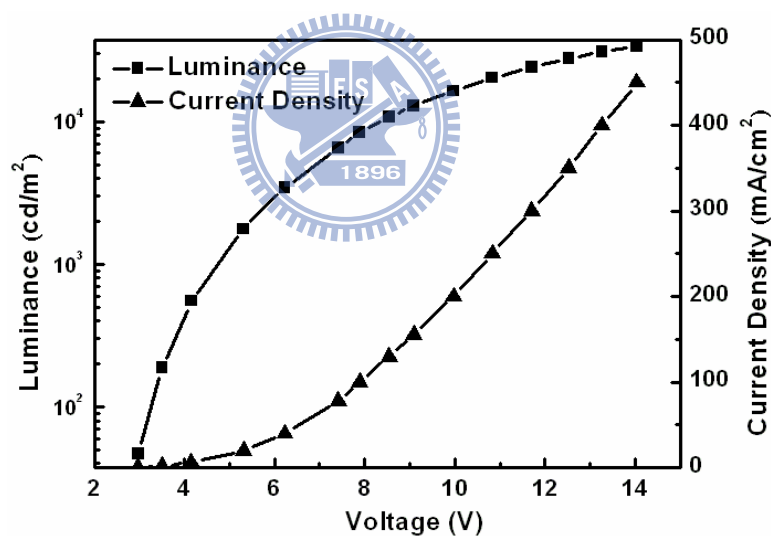
Figure 7-10 *L-J-V* characteristics of green C545T-doped device utilizing MADN as ETL.

7.6 Single-layer OLED devices based on multifunctional bipolar MADN

To enhance the commercial viability of OLEDs for various applications, the

simplification of the device structure and the manufacturing processes to reduce cost is always an important consideration. Therefore, increasing efforts have been directed toward the exploration of single-layer small molecule devices which would simplify OLED structure/fabrication [40,41,42,43,44,45,46]. Various OLEDs, either fluorescence or phosphorescence, had been reported using either single ambipolar carrier-transport host materials [42-45] or mixtures of hole- and electron-transporting as virtual host materials [40,41]. Clearly, there is a need to look for a material with a wide bandgap, appropriate HOMO/LUMO energy levels, and more balanced carrier (hole and electron) mobilities. With a wide bandgap host, it is possible to sensitize red, green and even blue dopants. With a material possessing appropriate HOMO/LUMO energy levels and balanced carrier mobilities, the carriers can efficiently inject from the commonly used ITO anode and Al cathode in OLED device architectures which may also improve carrier recombination in the emitter. These requirements indeed underscore the need for a large-bandgap bipolar charge transport material.

According to those results described in our previous experiments, MADN has been proven to be both an efficient hole and electron transport materials, therefore, one green OLED device with structure of ITO/ITO/CF$_x$/MADN (60 nm)/Alq$_3$: 1% C545T (35 nm)/MADN (10 nm)/BPhen: 5% Cs$_2$CO$_3$ (5 nm)/Al is fabricated to demonstrate the bipolar nature of MADN, in which MADN is used as HTL and ETL. Furthermore, by taking advantage of bipolar property along with the wide bandgap and stable thin-film morphology of MADN, a single-layer blue OLED device was fabricated with structure of ITO/CF$_x$/MADN (70 nm)/MADN: 3% *p*-bis(4-(*N,N*-(2-methyl-6-ethylphenyl)(phenyl) aminostryl) benzene (BUBD-1,

structure can be found in Table 2.1) [47] (30 nm)/MADN (10 nm)/BPhen: 5% Cs_2CO_3 (5 nm)/Al, in which MADN is multi-functionally adopted simultaneously as HTL, host of emitting layer, and ETL. The device structures are illustrated in Figure 7-11.
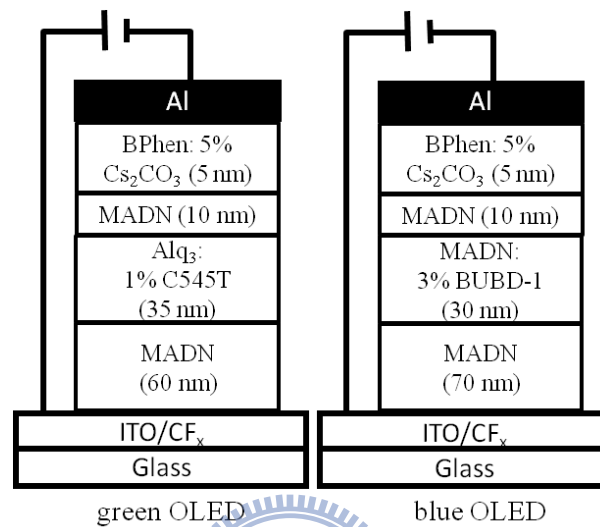
Figure 7-11 Device architecture of green and blue OLED devices with MADN as HTL and ETL.

The detailed EL performances are summarized in Table 7-2. The drive voltage of these two devices are 5.7 V and 4.7 V at mA/cm^2, respectively, the low drive indicates that MADN can indeed be used for both hole an electron transporting because of its bipolar nature. Moreover, as compared to the green device, the lower drive voltage of the single-layer blue device is attributed to the fewer interface inside the device, in which MADN is multifunctional utilized. The single-layer *common-host* blue OLED can also achieve promising performances and is comparable to those of conventional multilayered blue OLED devices composed of many different materials. The EL efficiency of this single-layer device achieved 8.5 cd/A and 5.7 lm/W at 20 mA/cm^2 with $CIE_{x,y}$ of

(0.16, 0.25) and a high E. Q. E. of 4.9%. Based on this work, it is anticipated that OLEDs fabrication process can be considerably simplified and the bill of materials reduced by using one common large bandgap and bipolar material for both carrier transport layers and emission layer.

Table 7-2 EL performances of OLED devices at 20 mA/cm^2.

Device	Voltage (V)	Current Eff. (cd/A)	Power Eff. (lm/W)	E. Q. E. (%)	CIE$_{x,y}$
green	5.7	13.8	7.6	3.7	(0.13, 0.63)
blue	4.7	8.5	5.7	4.9	(0.16, 0.25)

7.7   Stable and efficient *p*-i-*n* OLED devices with a single common host of MADN

According to the previous results, MADN has been demonstrated to be an efficient carrier transport material for both holes and electrons. However, the carrier injection from both electrodes are still problems owing the appropriate HOMO/LUMO levels of MADN as respect to the work functions of ITO anode and Al cathode. In addition, from the AS results discussed in *Sections 6.3 and 6.4*, the incorporation of WO$_3$ and CsF into MADN can greatly reduce the energy barrier for carrier injection. Based on these AS results, the OLED device structure can be further simplified by a common host of MADN for *p*-doped and *n*-doped layers as well as EML.

7.7.1   *p*-i-*n* blue OLED device based on MADN

The common host p-i-n blue OLED device based on MADN can be realized and Figure 7-12 illustrates device architecture and energy diagram. The device structure is ITO/MADN: 10% WO$_3$ (60 nm)/MADN (10 nm)/MADN: 3%

BUBD-1 (30 nm)/MADN (10 nm)/MADN: 30% CsF (10 nm)/Al (120 nm), in which MADN is used as hosts for both *p*-type HTL and *n*-type ETL; WO$_3$ and CsF are used as *p*-type dopant and *n*-type dopant, respectively.
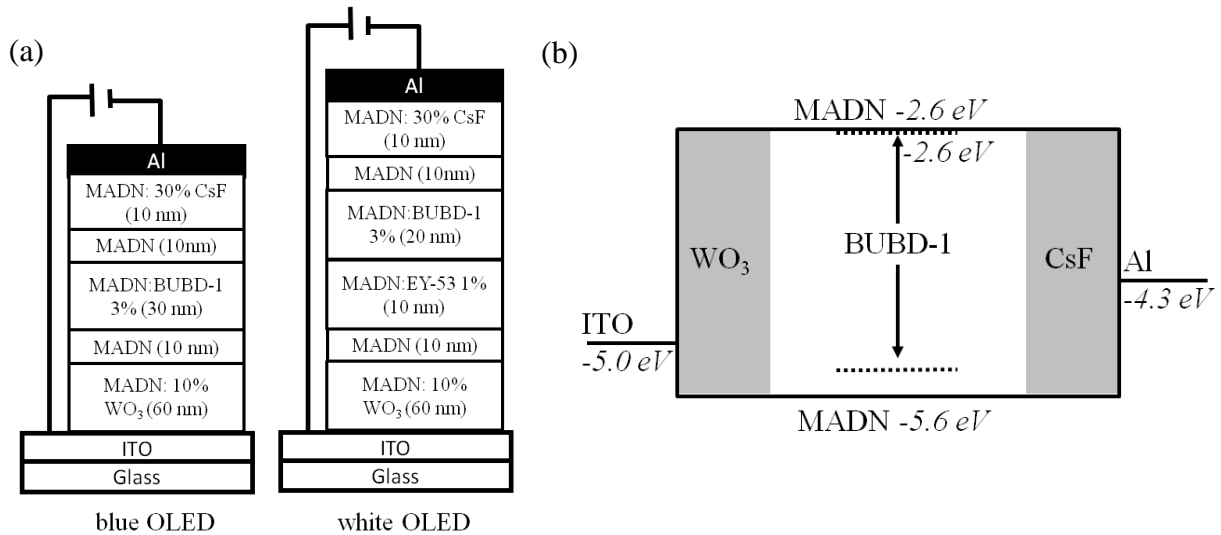
Figure 7-12 (a) Device architecture and (b) energy diagram of *p*-i-*n* OLEDs with a single common host.
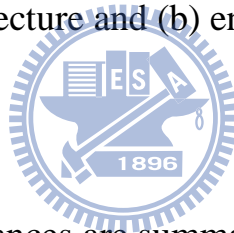
The detailed EL performances are summarized in Table 7-3. By virtue of the common host, this novel device is effectively a *p*-i-*n* OLED without interface between organic layers and can achieve an EL efficiency of 8.6 cd/A and 5.7 lm/W at 20 mA/cm^2 with CIE$_{x,y}$ of (0.17, 0.33) and a high E. Q. E. of 4.1%. Most importantly, as compared to a standard *p*-i-*n* device with structure of ITO/NPB: 30% WO$_3$ (60 nm)/NPB (10 nm)/MADN: 3% BUBD-1 (30 nm)/BPhen (10 nm)/BPhen: 5% Cs$_2$CO$_3$ (10 nm)/Al (120 nm), in which NPB doped WO$_3$ and BPhen doped Cs$_2$CO$_3$ were used as the *p*-doped and *n*-doped layers, respectively. The simplified *p*-i-*n* device with the common host is more stable (as shown in Figure 7-13). The t_{70} [time for the luminance to drop to 70% of initial luminance (L_0)] at the initial luminance of $L_0 = 3000$ cd/m^2 is 500 hrs.

The remarkably long operational lifetime is attributed to the device without apparent interface and charge accumulation in the organic layers.

Table 7-3 EL performances of OLED devices at 20 mA/cm^2.

Device	Voltage (V)	Current Eff. (cd/A)	Power Eff. (lm/W)	E. Q. E. (%)	CIE$_{x,y}$
blue	4.7	8.6	5.7	3.7	(0.17, 0.31)
white	4.5	9.0	6.3	3.7	(0.37, 0.40)
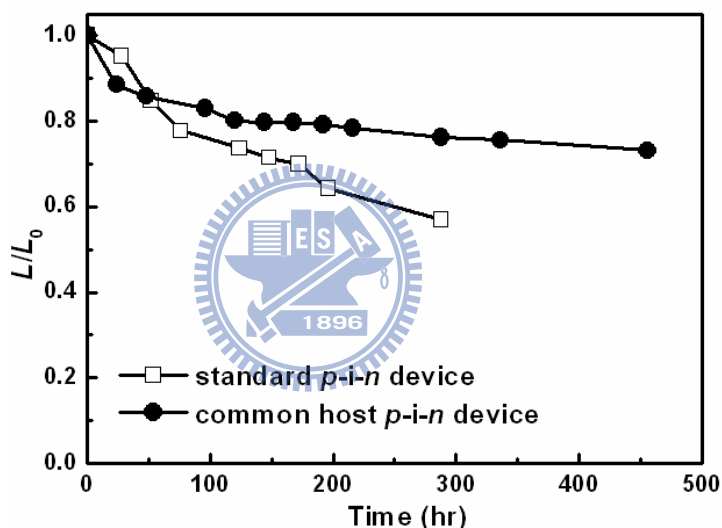
Figure 7-13 Device operational stability of standard *p*-i-*n* devices and common host *p*-i-*n* device.

7.7.2   *p*-i-*n* WOLED device based on MADN

To further take the advantage of the wide bandgap of MADN, a common host *p*-i-*n* WOLED device based on MADN was fabricated with structure of ITO/MADN: 10% WO$_3$ (60 nm)/MADN (10 nm)/MADN: 1% EY-53 (10 nm)/MADN: 3% BUBD-1 (20 nm)/MADN (10 nm)/MADN: 30% CsF (10

nm)/Al (120 nm), in which EY-53 is used as yellow dopant and purchased from e-Ray Optoelectronic Co. Ltd.

This *p*-i-*n* white OLED can achieve the EL efficiency of 9.0 cd/A and 6.3 lm/W at 20 mA/cm^2 and 4.5 V with CIE$_{x,y}$ of (0.38, 0.40) and an E. Q. E. of 3.7%. Under different current densities, this white device also reveals a stable EL color with ΔCIE$_{x,y}$ of ±(0.001, 0.003) from (0.370, 0.393) to (0.371, 0.396) at a broad range from 2 mA/cm^2 to 100 mA/cm^2 as depicted in Figure 7-14(a). In addition, the drive voltage of this white device increases only 0.5 V with continuous operation after 800 hrs as shown in Figure 7-14(b).
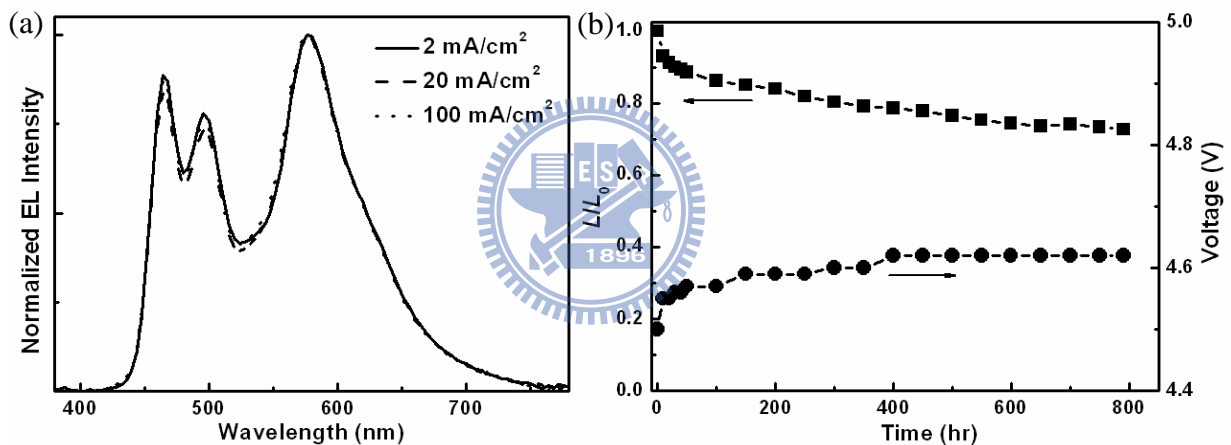
Figure 7-14 (a) EL spectra at different current densities and (b) operational stability of common host *p*-i-*n* WOLED device.

7.8   Summary

In general, OLED device with a multi-layer structure often needs many different materials individually optimized for each layer to achieve the best device performance. As a result it tends to complicate the fabrication process and at the same time increases the bill of materials. By taking the advantage of the large bandgap and bipolar nature of MADN, we demonstrate that simplified

fabrication process is possible for fabricating an efficient and stable *p-i-n* OLEDs by incorporation of WO_3 and CsF as *p-* and *n*-dopants into MADN.

References

[1] C. W. Tang, S. A. Van Slyke, *Appl. Phys. Lett.* **51**, 913 (1987).

[2] J. Kido, Y. Iizumi, *Appl. Phys. Lett.* **73**, 2721 (1998).

[3] M. Sims, S. W. Venter, I. D. Parker, *Proceedings of SID2008*, p. 223, May 20-23 (2008), Los Angeles, CA, USA.

[4] R. H. Young, J. R. Lenhard, D. Y. Kondakov, T. K. Hatwar, *Proceedings of SID2008*, p. 705, May 20-23 (2008), Los Angeles, CA, USA.

[5] H. Aziz, Z. D. Popovic, N. X. Hu, A. M. Hor, G. Xu, *Science* **283**, 1900 (1999).

[6] Z. D. Popovic, H. Aziz, A. Ioannidis, N. Hu, P. N. M. dos Anjos, *Synth. Met.* **123**, 179 (2001).

[7] Z. D. Popovic, H. Aziz, N. Hu, A. Ioannidis, P. N. M. dos Anjos, *J. Appl. Phys.* **89**, 4673 (2001).

[8] S. A. VanSlyke, C. H. Chen, C. W. Tang, *Appl. Phys. Lett.* **69**, 2160 (1996).

[9] Y. Shirota, Y. Kuwabara, H. Inada, T. Wakimoto, H. Nakada, Y. Yonemoto, S. Kawami, K. Imai, *Appl. Phys. Lett.* **65**, 807 (1994).

[10] Z. B. Deng, X. M. Ding, S. T. Lee, W. A. Gambling, *Appl. Phys. Lett.* **74**, 2227 (1999).

[11] H. Jiang, Y. Zhou, B. S. Ooi, Y. Chen, T. Wee, Y. L. Lam, J. Huang, S. Liu, *Thin Solid Films* **363**, 25 (2000).

[12] D. Liu, C. G. Zhen, X. S. Wang, D. C. Zou, B. W. Zhang, Y. Cao, *Synth. Met.* **146**, 85 (2004).
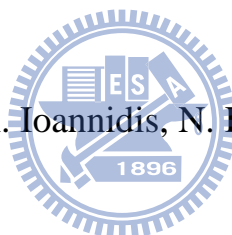
[13] S. F. Chen, C. W. Wang, *Appl. Phys. Lett.* **85**, 765 (2004).

[14] J. Li, C. Ma, J. Tang, C. S. Lee, S. Lee, *Chem. Mater.* **17**, 615 (2005).

[15] X. Zhou, M. Pfeiffer, J. Blochwitz, A. Werner, A. Nollau, T. Fritz, K. Leo, *Appl. Phys. Lett.* **78**, 410 (2001).

[16] J. S. Huang, M. Pfeiffer, A. Werner, J. Blochwitz, K. Leo, S. Y. Liu, *Appl. Phys. Lett.* **80**, 139 (2002).

[17] G. He, O. Schneider, D. Qin, X. Zhou, M. Pfeiffer, K. Leo, *J. Appl. Phys.* **95**, 5773 (2004).

[18] J. Staudigel, M. Stossel, F. Steuber, J. Simmerer, *J. Appl. Phys.* **86**, 3895 (1999).

[19] C. Giebeler, H. Antoniadis, D. D. C. Bradley, Y. Shirota, *J. Appl. Phys.* **85**, 608 (1999).

[20] C. H. Liao, M. T. Lee, C. H. Tsai, C. H. Chen, *Appl. Phys. Lett.* **86**, 203507 (2005).

[21] J. Shi, C. W. Tang, K. P. Klubek, *US Patent* 6465115 (2002).

[22] M. X. Yu, J. P. Duan, C. H. Lin, C. H. Cheng, Y. T. Tao, *Chem. Mater.* **14**, 3958 (2002).

[23] C. P. Yu, C. W. Ko, *US Patent* 0260442 (2005).

[24] S. Tao, Y. Zhou, C. S. Lee, S. T. Lee, D. Huang, X. Zhang, *J. Phys. Chem. C* ***112***, 14603 (2008).

[25] M. T. Lee, H. H. Chen, C. H. Tsai, C. H. Liao, C. H. Chen, *Appl. Phys. Lett.* **85**, 3301 (2004).

[26] B. Chen, C. S. Lee, S. T. Lee, P. Webb, Y. C. Chan, W. Gambling, H. Tian, W. Zhu, *Jpn. J. Appl. Phys.* **39, 1**190 (2000).

[27] R. Meerheim, K. Walzer, M. Pfeiffer, K. Leo, *Appl. Phys. Lett.* **89**, 061111

(2006).

[28] G. G. Malliaras, Y. Shen, D. H. Dunlap, H. Muratac, Z. H. Kafafi, *Appl. Phys. Lett.* **79**, 2582 (2001).

[29] S. C. Tse, H. H. Fong, S. K. So, *J. Appl. Phys.* **94**, 2033 (2003).

[30] P. Kathirgamanathan, V. Arkley, S. Surendrakumar, Y. F. Chan, J. Antipan-Lara, S. Ganeshamurugan, *Proceedings of SID2008*, p. 701, May 20-23 (2008), Los Angeles, CA, USA.

[31] D. Y. Kondakov, *J. Soc. Inf. Disp.* **17**, 137 (2009).

[32] V. V. Jarikov, D. Y. Kondakov, C. T. Brown, *J. Appl. Phys.* **102**, 104908 (2007).

[33] S. H. Yoon, J. S. Bae, Y. G. Lee, S. G. Im, J. C. Lee, J. E. Kim, K. K. Kim, S. H. Son, Y. K. Han, *US Patent* 6868469 (2005).

[34] H. Hamamoto, M. Matsuura, M. Kubota, Kawamura, *US Patent* 0267970 (2007).

[35] K. Okumoto, H. Kanno, Y. Hamaa, H. Takahashi, K. Shibata, *Appl. Phys. Lett.* **89**, 063504 (2006).

[36] K. Okumoto, H. Kanno, Y. Hamada, H. Takahashi, K. Shibata, *Appl. Phys. Lett.* **89**, 013502 (2006).

[37] M. A. Reddy, A. Thomas, K. Srinivas, V. J. Rao, K. Bhanuprakash, B. Sridhar, A. Kumar, M. N. Kamalasanan, R. Srivastavad, *J. Mater. Chem.* **19**, 6172 (2009).

[38] C. H. Chien, C. K. Chen, F. M. Hsu, C. F. Shu, P. T. Chou, C. H. Lai, *Adv. Funct. Mater.* **19**, 560 (2009).

[39] P. He, S. D. Wang, S. T. Lee, L. S. Hung, *Appl. Phys. Lett.* **82**, 3218 (2003).

[40] J. Littman, P. Martic, *J. Appl. Phys.* **72**, 1957 (1992).

[41] V. E. Choong, S. Shi, J. Curless, C. L. Shieh, H. C. Lee, F. So, J. Shen, J. Yang, *Appl. Phys. Lett.* **75**, 172 (1999).

[42] Z. Zhao, J. H. Li, P. Lu, Y. Yang, *Adv. Funct. Mater.* **17**, 2203 (2007).

[43] K. R. J. Thomas, M. Velusamy, J. T. Lin, Y. T. Tao, C. H. Chuen, *Adv. Funct. Mater.* **14**, 387 (2004).

[44] T. H. Huang, J. T. Lin, L. Y. Chen, C. C. Wu, *Adv. Mater.* **18**, 602 (2006).

[45] M. Y. Lai, C. H. Chen, W. S. Huang, J. T. Lin, T. K. Ke, L. Y. Chen, M. H. Tsai, C. C. Wu, *Angew. Chem. Int. Ed.* **47**, 581, (2008).

[46] T. Matsushima, C. Adachi, *Appl. Phys. Lett.* **89**, 253506 (2006).

[47] M. F. Lin, L. Wang, L. W. K. Wong, K. W. Cheah, H. L. Tam, M. T. Lee, C. H. Chen, C. H. *Appl. Phys. Lett.* **89**, 121913 (2006).
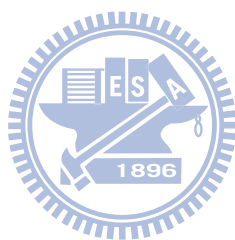
Chapter 8

Conclusions and Future Works

8.1   Conclusions

In this thesis, we introduced the *p*-doped (WO$_3$-doped NPB) and *n*-doped (Cs$_2$CO$_3$-doped BPhen) organic layers into conventional *di*-chromatic WOLED device architecture and carefully controlled the carrier recombination zone in a thin thickness (15 nm) by a DEML system. The *p*-i-*n* *di*-chromatic WOLED device with the refined exciton confinement can achieve high performances of 10 cd/A and 9.3 lm/W at 1000 cd/m^2 with a stable white CIE$_{x,y}$ of (0.32, 0.43) under various drive conditions. A high-brightness *p*-i-*n* tandem WOLED device by utilizing doped organic *p*-*n* junction of BPhen: Cs$_2$CO$_3$/NPB: WO$_3$ as connecting layer has also been demonstrated, giving rise to the EL efficiency of 23.9 cd/A and 7.8 lm/W with a white CIE$_{x,y}$ of (0.30, 0.43).

In addition, we developed α,α-MADN as an effective wide bandgap host material for the doped deep blue OLED device. It is found that α,α-MADN can be more efficient in Förster energy-transfer to the deep blue dopant SA-BiPh, the EL efficiencies of 3.3 cd/A and a saturate blue CIE$_{x,y}$ color coordinates of (0.15, 0.13) can be achieved. When this deep blue system is adopted in *tri*-chromatic WOLED device, the color gamut and color rendering index are improved to 73.2% and 87, respectively.

The hole mobilities of MADN and TBADN were also measured by TOF technique, and we found that ADN-type materials have high hole mobilities in the ranges of 2×10^{-3} to 9×10^{-3} cm^2/Vs, and have almost identical and small Poole-Frenkel factors. C60 has also been shown to be a useful charge generation

layer for TOF measurements for hole mobilities of ADN-type materials.

We further developed new *p*-doped (WO$_3$-doped MADN) and *n*-doped (PAK2-doped BPhen and CsF-doped MADN) organic layers and investigated their electrical characteristics by measuring *I-V* curves and temperature-dependent AS. The results show the conductive-doping can reduce the injection barrier and drive voltage when they are adopted in OLED devices.

Finally, according to all results from previous chapters and by taking the advantages of large bandgap, stable thin-film morphology, reversible electrochemical properties, and bipolar charge transport nature of MADN, efficient and stable blue and white OLED devices with simplified device architecture based on a single common host of MADN have been demonstrated.

8.2   Future works

The studies of OLED technique have already had a history of about 25 years since Tang and Van Slyke demonstrated multilayer structure [1]. In recent years, several high resolution full-color active matrix OLED displays have been demonstrated [2,3,4], indicating OLED technique is getting mature and already on the display market, and also are entering the solid state lighting (SSL) market. In order to pursuit and make these dreams come true as soon as possible, the development of highly efficient and stable WOLEDs is necessary and it inevitably must adopt phosphorescent emitters. However, the undesirable color saturation and operational lifetime of blue phosphorescent emitters is always an issue. Moreover, blue fluorescence emitter is of particular importance as it has been shown that triplet-triplet annihilation is a significant contributor to the enhancement of luminous efficiency in OLED [5,6], thereby, it is expected that hybrid system [7,8] will be widely used in most OLED products. As a result,

developing efficient and stable fluorescent blue system is still an important topic for OLEDs.

On the other hand, how to cost down OLED technique is another issue should be kept in mind. The most straight forward way is to simplify the OLED device architecture. Nowadays, OLED device with a multi-layer structure often needs many different materials individually optimized for each layer to achieve the best device performance. Hence, it is a worth and significant research direction for material scientists and engineers to develop multi-function materials, for instance, hole and electron transport and light emission. It is anticipated that OELDs fabrication process can be considerably simplified and the bill of materials reduced by using such multi-function materials.

Lastly, materials with anthracene core structure have been found to be very useful in many types of OLED devices as we reviewed and discussed in this thesis. Seeing how to utilize the superb advantages of anthracene-based materials along with constructing hybrid WOLEDs with green and red phosphorescent emitter system, and then further apply to OLED displays and lighting products would be an excellent avenue to pursue.

References

[1] C. W. Tang, S. A. Van Slyke, *Appl. Phys. Lett.* **51**, 913 (1987).

[2] T. Urabe, T. Sasaoka, K. Tatsuki, J. Takaki, *Proceedings of SID2007*, p. 161, May 19-25 (2007), Long Beach, CA, USA.

[3] M. H. Lee, S. M. Seop, J. S. Kim, J. H. Hwang, H. J. Shin, S. K. Cho, K. W. Min, W. K. Kwak, S. I. Jung, C. S. Kim, W. S. Choi, S. C. Kim, E. J. Yoo, *Proceedings of SID2009*, p. 802, May 31- June 5 (2009), San Antonio, TX,

USA.

[4] M. Noda, N. Kobayashi, M. Katsuhara, A. Yumoto, S. Ushikura, R. Yasuda, N. Hirai, G. Yukawa, I. Yagi, K. Nomoto, T. Urabe, *Proceedings of SID2010*, p. 786, May 23-28 (2010), Seattle, WA, USA.

[5] D. Y. Kondakov, *J. Appl. Phys.* **102**, 114504 (2007).

[6] D. Y. Kondakov, *J. Soc. Inf. Disp.* **17**, 137 (2009).

[7] Y. Sun, N. C. Giebink, H. Kanno, B. Wa, M. E. Thompson, S. R. Forrest, *Nature* **440**, 908 (2006).

[8] H. Kanno, N. C. Giebink, Y. Sun, S. R. Forrest, *Appl. Phys. Lett.* **89**, 023503 (2006).

Curriculum Vitae

Meng-Huan Ho was born in Taiwan in 1981. He received a Bachelors of Science degree and Masters of Science degree in Applied Chemistry from National Chiao Tung University (NCTU), Taiwan, in 2003 and 2005, respectively. He joined NCTU OLED research group in 2001. The topic of his master thesis is "Development and Application of Novel Deep Blue Fluorescent Dopants for Organic Electroluminescent Devices". Then he pursued his doctorate in Applied Chemistry of NCTU, Taiwan, under the joint supervision of Profs. Chin H. Chen and Teng-Ming Chen. Having been awarded an oversea scholarship from National Science Council of Taiwan, he went to study for one year at the University of Rochester, New York with Prof. Ching W. Tang in 2009. His current research interests include organic functional materials and organic electronic devices.
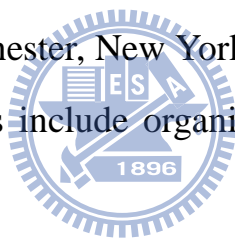
Publication Lists

A. Journal Paper

1. "New dopant and host materials for blue phosphorescent organic electroluminescent devices" -S. J. Yeh, W. C. Wu, C. T. Chen; Y. H. Song, Y. Chi, <u>M. H. Ho,</u> S. F. Hsu, C. H. Chen, *Adv. Mater.* **17**, 285 (2005).

2. "*Ab initio* Molecular Orbital Study of 1,3,5-Triazine Derivatives for Phosphorescent Organic Light Emitting Devices"-T. Y. Chu, <u>M. H. Ho</u>, J. F. Chen, C. H. Chen, *Chem. Phys. Lett.* **415**, 137 (2005).

3. "Efficient and Bright Blue-Emitting Phosphorescent Materials"-S. J. Yeh, C. T. Chen, Y. H. Song, Y. Chi, <u>M. H. Ho</u>, *J. Soc. Inf. Disp.* **13**(10), 857 (2005).

4. "Phosphorescence of red Os(fppz)$_2$(PPh$_2$Me)$_2$ doped organic light-emitting devices with *n*- and *p*-hosts"-T. H. Liu; S. F. Hsu, <u>M. H. Ho</u>, C. H. Liao, Y. S. Wu, C. H. Chen; Y. L. Tung, P. C. Wu, Y. Chi, *Appl. Phys. Lett.* **88**, 06358 (2006).

5. "Highly efficient deep blue organic electroluminescent device based on 2-methyl-9,10- di(1-naphthyl)anthracene"-<u>M. H. Ho</u>, Y. S. Wu, S. W. Wen, M. T. Lee, T. M. Chen, C. H. Chen, K. C. Kwok, S. K. So, K. T. Yeung, Y. K. Cheng, Z. Q. Gao, *Appl. Phys. Lett.* **89**, 252903 (2006).

6. "Highly efficient and stable white light organic light-emitting devices" -M. F. Lin, L. Wang, W. K. Wong, K. W. Cheah, H. L. TAM, M. T. Lee, <u>M. H. Ho</u>, C. H. Chen, *Appl. Phys. Lett.* **91**, 073517 (2007).

7. "Efficient deep blue emitters for organic electroluminescent devices"-<u>M. H. Ho</u>, Y. S. Wu, W. S. Wen, T. M. Chen, C. H. Chen, *Appl. Phys. Lett.* **91**, 083515 (2007).   (Highlighted by news report in Photonic Spectra, November 2007)

8. "White *p-i-n* organic light-emitting devices with high power efficiency and

stable color"-<u>M. H. Ho</u>, S. F. Hsu, J. W. Ma, S. W. Hwang, P. C. Yeh, C. H. Chen, *Appl. Phys. Lett.* **91**, 113518 (2007).

9. "Highly efficient *p-i-n* white organic light emitting devices with tandem structure"-<u>M. H. Ho</u>, T. M. Chen, P. C. Yeh, S. W. Hwang, C. H. Chen, *Appl. Phys. Lett.* **91**, 233507 (2007).

10. "Iminodibenzyl-substituted Distyrylarylenes as Dopants for Blue and White Organic Light Emitting Devices"-<u>M. H. Ho</u>, C. M. Cheng, T. Y. Chu, T. M. Chen, C. H. Chen, *Org. Electron.* **9**, 101 (2008).

11. "A Morphologically Stable Host Material for Efficient Phosphorescent Green and Red Organic Light Emitting Devices"-<u>M. H. Ho</u>, B. Balaganesan, T. Y. Chu, T. M. Chen, C. H. Chen, *Thin Solid Films* **517**, 943 (2008).

12. "Electrical characterization of organic light-emitting diodes using dipotassium phthalate as *n*-type dopant"-<u>M. H. Ho</u>, M. T. Hsieh, T. M. Chen, J. F. Chen, S. W. Hwang, C. H. Chen, *Appl. Phys. Lett.* **93**, 083505 (2008).

13. "Study of efficient and stable organic light-emitting diodes with 2-methyl-9,10-*di*(2-naphthyl)anthracene as hole-transport material by admittance spectroscopy"-<u>M. H. Ho</u>, M. T. Hsieh, K. H. Lin, T. M. Chen, J. F. Chen, C. H. Chen, *Appl. Phys. Lett.* **94**, 023306 (2009).

14. "Study of electrical characterization of 2-methyl-9,10-*di*(2-naphthyl) anthracene doped with tungsten oxide as hole-transport layer"-M. T. Hsieh, <u>M. H. Ho</u>, K. H. Lin, T. M. Chen, J. F. Chen, C. H. Chen, *Appl. Phys. Lett.* **95**, 033501 (2009).

15. "Flexible Inverted Bottom-Emitting Organic Light-emitting Devices with a Semi-transparent Metal-assisted Electron Injection Layer"-C. Y. Wu, <u>M. H. Ho</u>, S. Y. Su, C. H. Chen, *J. Soc. Inf. Disp.* **18**(1), 76 (2010).

16. "Study of electric characteristics and diffusion effects of 2-methyl-9,10-*di*(2-naphthyl) anthracene doped with cesium fluoride by admittance spectroscopy"-M. T. Hsieh, <u>M. H. Ho</u>, K. H. Lin, T. M. Chen, J. F. Chen, C. H. Chen, *Appl. Phys. Lett.* **96**, 033501 (2010).

17. "Fabrication of Cd1-xZnxS films with controllable zinc doping using a vapor zinc chloride treatment"-W. Xia, J. Welt, H. Lin, H. N. Wu, <u>M. H. Ho</u>, C. W. Tang, *Sol. Energy Mater. Sol. Cells* (2010) (accepted).

18. "Efficient and color-saturated inverted bottom-emitting organic light-emitting devices with a semi-transparent metal-assisted electron injection layer" - <u>M. H. Ho</u>, C. Y. Wu, T. M. Chen, C. H. Chen, *J. Lum.* (in revision).

B. Chinese Journal

1. "有機電激磷光材料與 OLED 磷光元件之發展近況" -<u>何孟寰</u>、黃孝文、陳金鑫,*化學*, **63**(3), 443 (2005). (九十四年『化學』論文獎)

2. "有機光電材料之電腦模擬計算與分析－OLED 應用"-朱達雅、<u>何孟寰</u>、陳金鑫,*光學工程*, **94**, 33 (2006).

3. "磷光白光有機電激發光二極體之發展與現況" -張繼聖、蘇尚裕、<u>何孟寰</u>、陳金鑫,*電子月刊*, **156**, 98 (2008).

C. Patent

1. "藍光有機化合物和有機電激發光元件裝置"-陳金鑫、吳曜杉、<u>何孟寰</u>、溫世文 (專利申請號碼 96117874,申請中)

D. Selected Conference Paper

1. "Organic Electroluminance Materials Study by Computational Simulation"-T. Y. Chu, <u>M. H. Ho</u>, Y. S. Wu, J. F. Chen, C. H. Chen, *Proceedings of The 4ᵗʰ International OLED and PLED Workshop in Taipei,* P3, Taipei, Taiwan (2005). (Best Student Poster Award)

2. "Highly Efficient Beep Blue Organic Electroluminescent Devices"-<u>M. H. Ho</u>, Y. S. Wu, S. W. Wen, C. H. Chen, *Proceedings of Society for Information Display 2007 (SID 2007)*, P. 1768, Long Beach, USA (2007). (oral presentation)

3. "Stable and efficient organic light emitting diodes based on a single host of p-doped and n-doped layers"-<u>M. H. Ho</u>, K. H. Lin, C. H. Chen, M. T. Hsieh, J. F. Chen, *Proceedings of Society for Information Display 2009 (SID 2009)*, p. 503, San Antonio, USA (2009). (oral presentation)

4. "Efficient Single-Layer Small Molecule Blue OLEDs Based on a Multifunctional *Bi*polar Transport Material"-<u>M. H. Ho</u>, M. Y. Liu, K. H. Lin, C. H. Chen, C. W. Tang, *Proceedings of Society for Information Display 2010 (SID 2010)*, p. 552, Seattle, USA (2010). (oral presentation)